



<https://theses.gla.ac.uk/>

Theses Digitisation:

<https://www.gla.ac.uk/myglasgow/research/enlighten/theses/digitisation/>

This is a digitised version of the original print thesis.

Copyright and moral rights for this work are retained by the author

A copy can be downloaded for personal non-commercial research or study,
without prior permission or charge

This work cannot be reproduced or quoted extensively from without first
obtaining permission in writing from the author

The content must not be changed in any way or sold commercially in any
format or medium without the formal permission of the author

When referring to this work, full bibliographic details including the author,
title, awarding institution and date of the thesis must be given

Enlighten: Theses

<https://theses.gla.ac.uk/>
research-enlighten@glasgow.ac.uk

THE DENSITY OF GAP STATES IN
MAGNETRON SPUTTERED HYDROGENATED
AMORPHOUS SILICON.

BY MOHAMMED CHAHDI, D.E.S., MSc.

SUBMITTED FOR THE DEGREE OF Ph.D.

DEPARTMENT OF PHYSICS AND ASTRONOMY,
UNIVERSITY OF GLASGOW.

NOVEMBER, 1986.

ProQuest Number: 10991894

All rights reserved

INFORMATION TO ALL USERS

The quality of this reproduction is dependent upon the quality of the copy submitted.

In the unlikely event that the author did not send a complete manuscript and there are missing pages, these will be noted. Also, if material had to be removed, a note will indicate the deletion.



ProQuest 10991894

Published by ProQuest LLC (2018). Copyright of the Dissertation is held by the Author.

All rights reserved.

This work is protected against unauthorized copying under Title 17, United States Code
Microform Edition © ProQuest LLC.

ProQuest LLC.
789 East Eisenhower Parkway
P.O. Box 1346
Ann Arbor, MI 48106 – 1346

DECLARATION

I, the undersigned, hereby certify that I am the author of this thesis, that the work in this thesis was done by me except where explicitly mentioned in the text when a reference is given, and that this work has not been previously accepted for a higher degree.

Mohammed Chahdi.

CONTENTS.

Acknowledgements	i.
Abstr.	ii
List of symbols	iii
Chapter 1. Introduction	<u>1.</u>
1.1 The Present work.	
Chapter 2. Theoretical Review	
2.1.1. Localization in Amorphous semiconductors	<u>4</u>
2.1.2. The Space Charge Region	<u>7</u>
2.2. The Role of the surface depletion in transverse field effect analysis	<u>12</u>
2.2.1. The Procedure	<u>12</u>
2.2.2. Improved analysis of field effect experiment	1
2.2.3. The density of states	<u>17.</u>
2.2.4. Limitations of field effect measurements	<u>17</u>
2.3 Capacitance Measurements on surface charged layers	<u>19</u>
2.3.1. Capacitance-Voltage measurements on MIS structures	<u>19</u>
2.3.2. The Schottky Barrier	<u>21</u>
2.3.2.1. Current transport mechanisms	<u>21</u>
2.3.2.2. Capacitance Measurements on crystalline Schottky barriers	<u>26</u>
2.3.2.3. Capacitance Measurements on Amorphous Schottky barriers	<u>27</u>
2.3.2.3.1. Capacitance Voltage Measurements	<u>29</u>
2.3.2.3.2. Capacitance Frequency Measurements	<u>29</u>
2.4 Other Capacitance Measurements	<u>32</u>
2.4.1. D.L.T.S. Measurements	<u>33</u>
2.4.2. D.L.T.S. Measurements on a-Si:H	<u>35</u>

2.4.3.	The Density of States	<u>35</u>
2.5	S.C.L.C. Measurements	<u>37</u>
CHAPTER 3.	Experimental Techniques	<u>43</u>
3.1.	Sample Preparation	<u>43</u>
3.1.1.	A review of the sputtering process	<u>43</u>
3.1.2.	R.F. Magnetron Sputtering	<u>46</u>
3.1.3.	The R.F. System	<u>48</u>
3.2	The Gas Mixture	<u>50</u>
3.3.	Thermal Evaporation	<u>52</u>
3.4	The Insert	
3.5.	Sample Geometry	<u>54</u>
3.5.1.	Schottky Barrier structure	<u>54</u>
3.5.2.	SCLC structure	<u>55</u>
3.5.3.	The Measuring circuit	<u>56</u>
3.6	Thickness Measurements	<u>58</u>
3.6.1	Varian \AA scope	<u>58</u>
3.6.2.	Thickness Measurement using optical response	<u>59</u>
3.6.3.	Mechanical Method	<u>59</u>
3.7	Other Measurements	<u>60</u>
3.7.1.	Electron Microscopy Analysis	<u>60</u>
3.7.2.	I.R. Absorption	<u>61</u>
3.7.3.	Optical Measurement	<u>61</u>
3.7.3.1.	Experimental arrangement	<u>63</u>
3.7.4.	Hydrogen Evolution Apparatus	<u>64</u>
3.7.4.1.	The Insert	<u>65</u>
CHAPTER 4.	FILM CHARACTERISATION	
4.1	General Description	<u>67</u>
4.2.	The effect of hydrogen on transport properties of a-Si	<u>68</u>
4.3	Hydrogen Evolution	<u>71</u>
4.4	I.R. Absorption	<u>73</u>

4.5	Analysis by Electron Microscopy	<u>75</u>
4.6	Optical Absorption	<u>77</u>
CHAPTER 5	SCHOTTKY BARRIERS	<u>80</u>
5.1	D.C. properties of Schottky barriers	<u>80</u>
5.2	A.C. properties of Schottky barriers	<u>86</u>
5.3	The Equivalent Circuit	<u>93</u>
5.4	Analysis of A.C. Results	<u>99</u>
5.5.	Temperature Dependence	<u>104</u>
5.5.1	Attempt to escape frequencies and trapping cross sections	<u>109</u>
CHAPTER 6	SCLC EXPERIMENT	<u>114</u>
6.1.1.	SCLC Mechanism	<u>114</u>
6.1.2.	SCLC Formulation	<u>115</u>
6.2	Deduction of the Density of States	<u>118</u>
6.2.1.	The Direct Method	<u>118</u>
6.2.2.	Deduction of the Density of states from SCLC Characteristics (Inversion procedure)	<u>120</u>
6.2.3.	The role of the states away from the fermi level in determining SCLC characteristics	<u>123</u>
6.2.4.	The influence of spatial non uniformities in the film on the SCLC characteristics	<u>126</u>
6.3	Analysis of Results	
6.3.1.	Sample Description and Measurements	<u>129</u>
6.3.2.	High Activation Energy Samples	<u>131</u>
6.3.3.	Low Activation Energy Samples	<u>133</u>
6.3.4.	Summary of SCLC Results.	<u>137</u>
CHAPTER 7.	SUMMARY AND CONCLUSIONS	<u>140</u>
REFERENCES		<u>147</u>

Acknowledgements.

My gratitude goes to my supervisor Dr. A.R. Long for his guidance, encouragement and valuable discussions during this project.

I am also grateful to the Algerian "Ministere de l'Enseignement superieur et de la recherche scientifique" for the financial support.

It is a pleasure to thank many people in the department of Natural Philosophy, especially my colleague M. Holland and the technical staff M. MacDonald and A.M. Young for creating a pleasant atmosphere during this work.

Finally, I would like to thank Mrs. Liz Hughes for typing this thesis.

ABSTRACT

The main objective of this project was to measure the density of states in magnetron sputtered hydrogenated amorphous silicon and compare it with that obtained from material prepared by the conventional R.F. sputtering method and to try to decide on the critical factors which may influence it. It was also intended to compare the results to the well known density of states of glow discharge amorphous silicon. To this end, two types of experiments were used: the admittance-frequency measurements on Schottky barriers and space charge limited current measurements. In the case of the Schottky barrier analysis, the results were analysed using a trap release model and the temperature-frequency dependence of the A.C. response of Schottky barriers was investigated. The results obtained from several samples give densities of states around $10^{16} \text{ eV}^{-1} \text{ cm}^{-3}$, significantly lower than the values quoted for non-magnetron material reported in literature. For SCLC experiment, the results obtained indicate densities of states near the fermi level of 10^{15} - $10^{16} \text{ eV}^{-1} \text{ cm}^{-3}$. Experimental data showed that the surface layers at front and back contacts were different, clearly indicating surface properties of the film. Therefore, it becomes clear that a complete description of the material requires the surface states to be included in the analysis and a computer program was developed for this. It was concluded that the true bulk density of states of the material could be substantially reduced if surface states were considered. The temperature dependence of SCLC characteristics was also investigated and it was found that tail states could be detected by the SCLC technique. The values of the density of states obtained suggest that, as far as bulk properties of

of magnetron sputtered a-Si:H are concerned, these are not distinguishable from those of glow discharge material. However, significant evidence was found for the presence of surface layers and their related effects.

LIST OF SYMBOLS.

A	area
C_g	geometrical capacitance of Schottky barrier sample
C_m	measured capacitance of Schottky barrier sample
C_o	DC capacitance of Schottky barrier
C_S	capacitance of Schottky barrier
d	thickness of the sample
e	electronic charge
E_C	bottom of conduction band energy level
E_i	intrinsic energy level
E_V	top of Valence band energy level
E_A	activation energy for DC conductivity
E_F	fermi level
F	electric field
f	reduced form of F
G_m	measured conductance of Schottky barrier
G_S	conductance of Schottky barrier
J	current density
j	reduced form of J
I	current
K	Boltzmann constant
L	Debye length
$g(E)$	Density distribution of localised states
g_o	constant density of states
n	ideality factor
$n(x)$	Density distribution of mobile electrons
P_A, P_H	Argon and hydrogen partial pressure
$p(x)$	Density distribution of mobile holes
Re	Reflectance
T	Absolute temperature

T_r transmittance
 v_{th} carrier thermal velocity
 $V(x)$ electrostatic potential profile
 v reduced form of V
 V_S value of potential at metal semiconductor interface
 V_C onset voltage in SCLC region
 W Schottky barrier thickness
 ϵ a-Si:H permittivity
 ϵ_1, ϵ_2 real, imaginary a-si:H dielectric constant
 K_1, K_2 real, imaginary refractive index.
 λ wavelength
 ν frequency
 ρ charge density function
 S_n trap capture cross section for electrons
 τ trap release time
 τ'_0, τ''_0 Release time for traps at onset of barrier, metal surface.
 ϕ_b Schottky barrier height
 ϕ_t barrier height for maximum thermionic field emission
 $\Delta(x)$ Fermi level shift
 ω angular frequency

CHAPTER 1.

INTRODUCTION

There has been growing interest in amorphous materials during the last fifteen years and a significant progress has been made in the fundamental understanding of them. This progress has been both of theoretical and experimental nature. A direct result of this achievement is the rapid development of device applications. In this, amorphous silicon is the most promising thin film semiconductor. Although a full characterisation of this material has not yet been achieved, advancement in the technological field has been considerable. This aspect of the subject has been the incentive behind the idea of carrying out the present work.

The Present Work

Fundamental to amorphous materials is localisation. Therefore a precise knowledge of the density of localised gap states and their behaviour is crucial to the physical understanding of these materials.

Given the number and range of measurements of the density of states which have been performed, it should now be possible to draw definitive conclusion about its magnitude and shape. Surprisingly, the shape of $g(E)$ which emerges from various measurement techniques has been the subject of conflicting ideas. Much of the previous work has been done on glow discharge amorphous silicon, and, to a lesser extent, R.F. sputtered amorphous silicon. The

results obtained so far suggest that the question of localisation and the exact form of $g(E)$ is still open to debate. For material prepared by the R.F. magnetron sputtering technique the amount of information available is very limited. Our interest in the subject has been to understand the properties of sputtered material, in general, and to decide on the critical preparation factors in order to improve its quality.

It was the aim of this project to investigate the density of states $g(E)$ for magnetron sputtered a-Si:H over as wide an energy range as possible and as large a number of preparation conditions as possible. It was then hoped to compare the results with those obtained from material prepared by the conventional method and to a lesser extent with those of the well known glow discharge material. Finally, in following these lines, we hoped to draw decisive conclusions about the deposition methods used.

The layout of this thesis is as follows : In the first part of the thesis we give a brief review of some theoretical work. We also present a description of the various experimental methods used to estimate $g(E)$ for amorphous silicon. In Chapter 3, we give a description of sample preparation techniques. Also given in this chapter are details of measurement techniques used in this work. Chapter 4 is concerned with various experiments carried out to characterise the magnetron sputtered material. In Chapter 5, we present the study of D.C. and A.C. behaviour of an amorphous Schottky barrier. In Chapter 6 we present

the theory and analysis of SCLC experiment. Also given is our analysis scheme for SCLC mechanisms developed to analyse the experimental data obtained. Finally we give a summary and conclusions of the work in Chapter 7.

CHAPTER 2.

Theoretical Review

This chapter is concerned with the presentation and the discussion of the relevant work conducted in past experiments aimed at characterisation and identification of localized states in amorphous silicon. The first section deals with various models proposed to explain localization, followed by a discussion of the surface depletion effects in crystalline semiconductors and the corresponding amorphous effects. In the following sections, we present a review of the most important techniques used to study localized states in hydrogenated amorphous silicon (a-Si:H). In this, special attention is paid to the formation of Schottky barriers. Finally, a survey of the SCLC technique is presented.

2.1.1 Localization in Amorphous Semiconductors

Despite the significant progress made in the study of amorphous materials, the magnitude and energy distribution of localized states remain somewhat uncertain. The nature and the characteristics of these states are also still the subject of conflicting reports. In this section, we present some of the relevant points. We consider broadly the type of electronic states one might expect in an amorphous material. Figure (2.1.a) shows a general energy distribution between the conduction band edge E_C of the upper band and the valence^{band} edge E_V of the lower part of the gap. The energy spectrum can be divided according to the electronic character of the states, into extended states, band tail states, and gap states. It is generally believed

that the tail states of conduction and valence bands are associated with the disordered structure of the network, whereas, the states in the gap are produced by defects.

Following Anderson's theory ⁽²⁾, Mott (1) suggested that electron wavefunctions will be spatially localized in the energy range lower than a particular value E_c at the conduction band edge and extended above it. Mott, also proposed the equivalent transition at the valence band edge, thus introducing a separation between the energy range where the mobility is finite from that where it is vanishingly small in the limit of zero temperature. This is termed the mobility edge.

Fundamental to amorphous materials is the concept of localization. It occurs with increasing potential disorder V_0 . To quantify this perturbation, the exchange integral H is introduced as a measure of the wavefunction overlap of electron states on nearest neighbour atoms. When the ratio $\frac{V_0}{H}$ exceeds a critical value B , then all states will be localized and the ensemble average over a transport quantity such as conductivity must vanish i.e. $\langle \sigma \rangle = 0$ at $T = 0$ (2)

The exponential energy distribution of band tail states is due mainly to the absence of long range order and as such they represent a universal property of amorphous silicon.

Illustrated in Figure (2.1.b) is the CFO model, put forward by COHEN, FRITZSCHE and OVSHINSKY (3). In this case, valence and conduction band tails are envisaged as overlapping forming a broad distribution throughout the gap. It does describe adequately several important effects observed in amorphous semiconductors. However, later theoretical work and experimental results (4) showed that this model does not describe

accurately the magnitude of band tail state density observed in these materials.

A number of studies of the recombination process (5) (6) (7) (8) led to the determination of the nature of the dominant recombination process and the position within the mobility gap of the recombination centres. Despite the existence of some unspecified defects, it became conclusive that deep trapping in amorphous silicon (a-Si) is predominantly associated with states formed by dangling bonds centres. The evidence is based on ESR results (Street et al (9) (10) and Dersch et al (11) (12)).

Several effects of dangling bonds were pointed out. The most interesting feature of these is that they assist recombination of electron and holes. A better understanding of dangling bonds properties can be gained from Mott (13). Since the environment of a dangling bond centre in a non-crystalline material changes from one such defect to another, the energies of the electrons at the defect will be spread over a certain range. More precisely, if one electron is removed, the resulting hole, in its motion from one centre to the next, has a range of energies. In the same way, if one electron is added to one of the centres, it has a range of energies too, leading to the form of state energy distribution proposed by Mott and shown in Figure (2.1.c).⁽¹⁴⁾ In this model, a defect centre can act both as a donor and an acceptor, thus giving rise to two overlapping band peaks in the gap separated by the Hubbard gap U . The meaning of this is that in equilibrium and at zero temperature, some

centres are positively charged and an equal number negatively charged. As a result, the density of states at the Fermi level E_F must be finite, and not zero as expected in an intrinsic crystalline semiconductor.

2.1.2. The Space Charge Region

In many experiments involving band bending in semiconductors, a surface layer can become charged, as electronic states within it are filled or emptied. A detailed knowledge of the space charge region is essential to understand many semiconductor properties in which we are interested. This involves the solution of Poisson's equation.

In this section we start with an investigation of the crystalline case^(15,16), then we outline the modifications necessary for the amorphous situation.

We start from Poisson's equation

$$\frac{d^2V(x)}{dx^2} = \frac{-\rho(x)}{\epsilon} \quad (2.1)$$

where $V(x)$ is the electrostatic potential characterising the band bending

$\rho(x)$ is the induced charge density distribution
and ϵ is the semiconductor permittivity.

In the crystalline case two types of contribution to the charge density $\rho(x)$ are expected (McKelvey, J.P.(15)).

1) The contribution of mobile charge carriers in the conduction and valence bands reflected in the following expressions:

$$n(x) = n_i \exp \frac{(E_F - E_i) - eV(x)}{kT} \quad (2.2)$$

$$p(x) = n_i \exp \frac{(E_i - E_F) + eV(x)}{kT} \quad (2.3)$$

where $n(x)$ and $p(x)$ are respectively electron and hole concentrations and n_i is the electron concentration at the intrinsic Fermi level E_i .

2) The second contribution is attributed to fixed charge from any ionized donor or acceptor present in the system at sufficiently high temperature and low impurity concentration. Considering all impurities to be ionized, $\rho(x)$ becomes

$$\rho(x) = [p(x) - n(x) + N_d - N_a] \quad (2.4)$$

where N_d and N_a are respectively donor and acceptor concentrations.

In this case, equation (2.1) is written in a general form (15)

$$\frac{d^2 u(x)}{dx^2} = \frac{2}{L_i} \sinh\left[-\frac{(E_F - E_i)}{kT} + u(x)\right] - \frac{N_d - N_a}{2n_i} \quad (2.5)$$

where $u(x) = \frac{eV(x)}{kT}$ and $L_i = \left[\frac{\epsilon kT}{e^2 n_i}\right]^{\frac{1}{2}}$ is the intrinsic Debye length.

This general equation cannot be solved explicitly to give the spatial form of $u(x)$ except under specific conditions.

The formation of a depletion region at a metal-semiconductor contact, the Schottky barrier, is a particularly important case. For this case "the depletion approximation" is usually used to solve Poisson's equation. In this approximation, the free carrier density is assumed to fall abruptly from its bulk value (where there is a balance of charge) to a value which is negligible compared with the donor (or acceptor) concentration, at a distance W from the metal-semiconductor interface. This distance defines the thickness of the barrier region. The charge density distribution is therefore simplified, in the case of an n-type semiconductor to the following form.

$$\begin{aligned} \rho(x) &= eN_d & 0 < x < W \\ &= 0 & \text{for } x > W \end{aligned} \quad (2.6)$$

To treat this case properly, one has to bear in mind that abrupt transition assumed occurs over a finite but small distance. Considering the simplified form of $\rho(x)$, the barrier profile becomes

$$V(x) = \frac{eN_d}{2\epsilon} (W-x)^2 \quad (2.7)$$

Most of the formalism developed for crystalline semiconductors can be transferred and applied to amorphous semiconductors. Thus the features summarised in Figure (2.2) for the crystalline case, can equally be found in the amorphous case. The main difference comes from the form of the charge density $\rho(x)$ which is strongly influenced by deep localized states in the Fermi-level region. Shallow donor and acceptor levels can be adequately treated by crystal like techniques. However for the deep states characteristic of amorphous semiconductors new procedures are required.

In early work by Barbe (17), on the basis of CFO model, it was suggested that the density of states near the Fermi level region might be constant, though consisting of the sum of acceptor-like and donor-like band tails. In addition, he postulated that the filling and emptying of these states as the Fermi level moved through the gap, was the source of space charge, neglecting mobile charge effects. According to this model, the charge density can be expressed in this form i.e.,

$$\rho(x) = -e \int_0^{eV(x)} (N_A + N_D) dE \quad (2.8)$$

where N_A and N_D are respectively the acceptor-like and donor-like localized state distributions.

This was followed by another approximation in the

analysis i.e. the assumption that there is a sharp cut off in occupancy of the localized states above E_F . Using this form for $\rho(x)$ and considering $N_A + N_D$ to be constant, the solution of Poisson's equation becomes

$$V(x) = V_s \exp\left(-\frac{x}{L}\right) \quad (2.9)$$

$$\text{where } L = \left[\frac{\epsilon}{e^2 (N_A + N_D)} \right]^{\frac{1}{2}} \quad (2.10)$$

This simple form has been used extensively by many groups (18) (19) (20) (21) (22) and also refined and developed by others. Mahan and Bube (23) extend the formalism and include a contribution to $\rho(x)$ from mobile majority carriers leading to the form of $\rho(x)$ for a p-type material given by:

$$\rho(x) = -e [g(E_F) \Delta E_F(x) + (p(x) - p_b)] \quad (2.11)$$

where $g(E_F)$ is the density of states at Fermi level.

$\Delta E_F(x)$ is the shift in the Fermi level with respect to the valence band.

p_b is the neutral bulk hole concentration.

$p(x)$ is the mobile hole density and given by:

$$p(x) = N_v \exp\left(-\frac{E_F(x)}{kT}\right)$$

The authors established this form of $\rho(x)$ then analysed it in the limits of either space charge or mobile charge being dominant. For the former, the equation giving the barrier profile is reproduced, but for the latter case, exact solutions could not be found except in the "small signal" limit, where again, the solution is given by equation (2.9) but with a modified Debye length similar to that obtained previously in the crystalline case.

$$L_i = \left[\frac{\epsilon kT}{e^2 (n_b^2 + p_b^2)} \right]^{\frac{1}{2}} \quad (2.12)$$

A new model was proposed by Neudeck and Malhotra (24) and inspired from Barbe's work. In this new model, additional terms were included to describe the exponential rise of the band tails and the general form of the charge density is written as:

$$\rho(x) = -e \int_0^{eV(x)} g(E) dE + ep_b \exp\left(\frac{-eV(x)}{kT}\right) - en_b \exp\left(\frac{eV(x)}{kT}\right) \quad (2.13)$$

where p_b is the hole concentration in the bulk,
 n_b is the electron concentration in the bulk
 and $g(E) = N_D(E) + N_A(E)$

For movement of the Fermi level, less than a certain energy E_a away from its bulk position, $g(E)$ is assumed constant at a value g_0 and the charge density becomes

$$\rho(x) = -e \left(eg_0 V(x) + n_b \exp\left(\frac{eV(x)}{kT}\right) - p_b \exp\left(\frac{-eV(x)}{kT}\right) \right) \quad (2.14)$$

Outside this region of band bending, the density of states $g(E)$ becomes more complex i.e.

$$g(E) = g_0 \exp\left\{ m(eV(x) - E_a) \right\} \quad (2.15)$$

where m is a modelling parameter controlling the rate of rise of the state distribution.

Replacing equation (2.15) in equation (2.13) $\rho(x)$ becomes

$$\rho(x) = -e \left(g_0 E_a + \left(\frac{g_0}{m}\right) \left(\exp\left(m \left[eV(x) - E_a \right] \right) - 1 \right) + n_b \exp\left(\frac{eV(x)}{kT}\right) - p_b \exp\left(\frac{-eV(x)}{kT}\right) \right) \quad (2.16)$$

In this model the spatial variation of the band bending potential was derived but no full solution of Poisson's equation was obtained. Using the charge density described by equation (2.14) leads to:

$$\frac{dV(x)}{dx} = - \left(\frac{2e^2}{\epsilon} \left\{ \frac{1}{2} g_o (eV)^2 + n_b kT \exp\left(\frac{eV(x)}{kT} - 1\right) + p_b kT \exp\left(\frac{-eV(x)}{kT} - 1\right) \right\} \right)^{\frac{1}{2}} \quad (2.17)$$

Such forms of Poisson's equation enable one in principle to analyse most surface layer problems. However the way in which this treatment is applied depends on the type of measurements involved. We now go on to discuss firstly the development of surface layers by a transverse field in field effect experiment (section 2.2) and then capacitance effects (section 2.3).

2.2 The Role of the Surface Depletion in Transverse Field effect analysis.

2.2.1 The Procedure

The quantitative knowledge of states distribution in amorphous silicon came from the field effect experiment developed by the Dundee group (25,26,27,28,29). In this measurement the localized state distribution is investigated by displacing it with respect to the Fermi level E_F . This is done by means of an external electric field, applied in a direction normal to the surface of the film to be studied. The procedure employed (27,28) is illustrated in Figure (2.3a), the gate electrode, G, is deposited first then covered by a thin layer of Si_3N_4 ($\sim 1\mu m$ thick), produced by glow discharge decomposition. This is followed by the a-Si film to be investigated. Finally, surface electrodes are evaporated to form source (S) and drain (D) used in this configuration. The thin layer of silicon nitride presented a significant improvement over the thin glass used in earlier experiments (25). As a result, much higher fields

could be applied with comparatively low voltages.

The measurement consists of applying a relatively small constant voltage V_{SD} between the source (S) and drain (D) and measuring the collected current I_D .

The process involved is illustrated in Figure (2.3b). As shown, the extended electrons states above E_C are pulled towards the Fermi level E_F in a region that extends from the dielectric/a-Si interface ($x=0$) to $x=\lambda$ in the a-Si film; λ depends on V_G and $g(E)$ and varies between 100 to 1000 \AA . The charge Q , induced in the a-Si, consists mainly of electrons confined into localized states which have been moved below E_F when V_G is applied. It is obvious that for a given V_G , the increase in I_D will be largest for samples with lowest $g(E)$ in the energy range probed. From a computerised analysis of the density of charge induced and discussed in the previous sections, $g(E)$ is obtained.

The methods proposed so far for analysing band bending in amorphous semiconductors and its related problems involve procedures whereby a theoretical form of the charge density using analytical functions is constructed, then using these functions to solve Poisson's equation either explicitly or numerically and adjusting some parameters to fit the experimental data. A more flexible approach uses numerical integration of the experimental data and iteration to construct a point by point energy distribution of gap states.

The pioneering work of Spear and Le Comber on amorphous silicon (25) showed for the first time that, if some

simplifications were made, then the analysis scheme based on numerical integration could provide valuable information about the density of states. The first of these simplifications was the assumption of zero temperature statistics, (this is a common assumption often mentioned in the literature). In their second simplification, the charge density was assumed to be constant over a certain distance λ from the surface ^{and} zero elsewhere. This is similar to the abrupt depletion approximation used in the crystalline case (30) and led, similarly, to a parabolic solution of Poisson's equation. As the surface potential is changed step by step, λ also changes as a function of the charge density. The third approximation consisted of varying λ for all values of V_S while retaining the parabolic form. This original method did not include an iteration step to improve the correlation between predicted and experimental points. However, in their following work (Madan and Le Comber (26), Spear and Le Comber (29)), this step was added and the two initial approximations discussed above also removed. This led to an overall increase in the magnitude of the density of states $g(E)$, whereas the shape of $g(E)$ remained the same.

The clearest picture of the energy distribution of states, so far, comes from the results of the Dundee Group. Their ability to perform this analysis scheme gave a new dimension to the challenging problem of localized states in amorphous semiconductors and, ever since, a great deal of effort has been made to gain better understanding of their properties.

A more general approach has been proposed for field effect analysis (31,32,33,34). This approach removes

all the assumptions. Moreover, several groups have presented theoretical modelling of the detailed correspondence between field effect data and $g(E)$ (31,33,34). The general form of the charge density is written as:

$$\rho(x) = -e \int_{-\infty}^{+\infty} g(E) \left[h(E - eV(x)) - h(E) \right] dE \quad (2.18)$$

which reduces to

$$\rho(x) = \int_0^{eV(x)} g(E) dE. \quad (2.19)$$

in the limit of zero temperature statistics.

2.2.2 Improved analysis of field effect experiment

Considering the form of the charge density described by equation (2.18), Goodman and Fritzsche (31) solved Poisson's equation in terms of the variable x , but the method has been proven to be complex and involves a lot of computing. Instead, in a different approach by Powell (33) the equations were manipulated to make the potential V the independent variable, since in a uniform semiconductor the charge density is not a function of V and x independently. This method makes the calculations simpler. Poisson's equation becomes:

$$\frac{d}{dV} (F^2) = - \frac{2}{\epsilon} \rho(V) \quad (2.20)$$

where $F = - \frac{dV}{dx}$ is the electric field at any point.

As we shall see in Chapter 6, equation (2.20) is also relevant to SCLC analysis.

Using zero temperature statistics, the charge density

is written as: . . .

$$\rho(V) = - e^2 \int_0^V g(E_F + eV) dV \quad (2.21)$$

In the case of a uniform semiconductor, the Poisson's equation can be solved for the surface leading to a relation between surface field and surface potential, and subsequently the band bending can be constructed for any surface potential. This analysis shows that a small perturbation in surface potential dV_S merely shifts the potential $V(x)$ rigidly a distance dx controlled by the surface field ($F_S = - \frac{dV}{dx} \text{ at } x=0$). This type of approach does assume that the field decreases to zero in the film which is reasonable for a film of sufficient thickness.

Following Powell's analysis (33), the change in conductance from the flat band conditions due to the band potential $V(x)$ is described by the following expression:

$$\frac{d}{dV} \frac{G-G_0}{G_0} d(1+\alpha) = \left[\frac{\exp\left(\frac{-eVs}{kT}\right) - 1}{F(V)} + \alpha \frac{\exp\left(\frac{eVs}{kT}\right) - 1}{F(V)} \right] \quad (2.22)$$

where G_0 denotes the sheet conductance for $V(x)=0$

d is the sample thickness

α is the ratio of the hole to electron mobilities.

The experimentally measured quantities are $M(V) = \frac{G-G_0}{G_0} d(1+\alpha)$ and the surface field F_S which is related to the gate voltage by:

$$F_S = \frac{\epsilon \epsilon_{OX}}{d_{OX}} (V_G - V_{FB}) \quad (2.23)$$

where ϵ_{OX} and d_{OX} are the dielectric constant and the thickness of the insulator.

V_{FB} is the voltage applied to the gate to produce flat bands.

2.2.3 The Density of States

Shown in Figure (2.4) is the classical density of state distribution obtained by the Dundee Group for glow discharge silicon. The defect band structure near $E_C - 0.4$ eV and $E_V + 0.6$ eV are clearly visible. It is, perhaps, worth mentioning that these results were obtained from a series of samples with different phosphorous and boron doping enabling the scan of $g(E)$ over such a large energy spectrum. Ever since this revolutionary work, many investigations of this type have been conducted (31,32,33,34).

Additional evidence consistent with field effect density of states is provided by the results of a number of independent experiments such as drift mobility (Spear and Le Comber (35)). The spectral dependence of photoconductivity and optical absorption (Loveland et al (36)), was interpreted to resolve the controversy about the E_V peak located at 1.2 eV below E_C . Similarly, the results of photoconductivity and recombination (Anderson and Spear (37)), allowed the clarification of the issue raised about the E_X peak.

Other authors dispute details of field effect density of states within the gap region. More recent work using alternative direct techniques led to important discrepancies. These are discussed in the following sections.

2.2.4 Limitations of Field Effect Measurement

Refinement of field effect analysis (31,32,33,34). (see section 2.2.2) removed many assumptions implicit in early work. However even these analyses still involve certain critical assumptions.

- 1) The semiconductor is perfectly homogeneous

2) No change in trapped charge density occurs at the interface.

3) The insulator is perfect without trapped charge. All these assumptions have been found difficult to prove.

Moreover, the sensitivity of field effect measurements is seen to be spatially limited, only a region typically between 20 to 100\AA from the insulator interface is probed by this technique (Fritzsche, (38)). This indicates that potential problems remain unsolved in interpreting the field effect data to give a bulk density of states in a-Si:H. Hence, its ability to determine the true bulk properties is questionable!

A number of studies have indicated anomalous behaviour of a-Si:H films, close to the sample surface (Solomon et al. (20), Tanielien et al. (39), Ast and Brodsky, (40), Solomon and Brodsky (41), Rehm et al. (42)). Anomalous behaviour attributed to the existence of a large number of surface states was also suggested (Knights and Bergelen, (43)). The problem of surface states was discussed by Goodman and Fritzsche who have shown that not only do the surface states lead to an upper limit of bulk densities of states but they can even undermine much of the theory and its interpretation. In this context, Weisfield (34) has interpreted his results from sputtered silicon in terms of surface effects.

Another criticism involves the effect of the approximations used in developing the analysis scheme used. Goodman and Fritzsche (31), and later Powell (33) have examined the effect of various commonly used approximations by re-analysing the data, using analysis schemes containing

various levels of approximation. They have shown that considerable variations do occur and mostly affected are the defect bands displayed in the classical curve calling into question the prominent peak E_x .

Schweitzer et al (44) have shown that the classical density of states is completely altered when correlation effects are considered. The authors have analysed the density of gap states obtained from field effect experiments in terms of a model which incorporates electron correlation effects. Due to the positive Hubbard energy U , the density of states deduced differs appreciably from the traditional gap state distribution. Besides the lack of the E_x and E_y peaks commonly reported in field effect measurements the minimum density of states is found to be between 10^{15} and $10^{16} \text{ eV}^{-1} \text{ cm}^{-3}$.

2.3. Capacitance Measurements on Surface Charged Layers.

Another method used to study semiconductors properties is based on capacitance effects. In the following sections we discuss these effects.

2.3.1 Capacitance-Voltage measurements on MIS structures.

The development of the capacitance technique as a tool to investigate the space charge Schottky barrier or MOS structures to obtain information about the density of states in crystalline semiconductors was first discussed by Goodman (45) for measurements of capacitance as a function of applied voltage (C-V). This was followed by studies in great details by Roberts and Crowell (46), Beguwala and Crowell (47) and Losee (48). The use of low frequency capacitance versus voltage (C-V) measurements to study gap states in a-Si:H was

first presented by Dohler and Hirose (49) and by Spear et al (50). Later several groups carried out similar experiments in order to characterise states in a-Si:H (51,52,53).

In general, at a low frequency where all the states respond to the applied field (see section 2.3.2.2) the differential capacitance (per unit area) due to the band bending in the semiconductor is (16)

$$C = \frac{dQ_s}{dV_s} \quad (2.24)$$

where dQ_s is the charge in space charge per unit area and $dQ_s = \epsilon F_s$ for a change in the surface potential of dV_s . F_s is the surface field and $F_s = -\left. \frac{dV}{dx} \right|_{x=0}$

Following the work by Dohler and Hirose (49) and Powell and Dohler (54), the general form for capacitance for a uniform semiconductor is expressed as:

$$C = \frac{\rho_s}{F_s} \quad (2.25)$$

where ρ_s is the surface charge density and $\rho_s = \rho(E_F + eV_s)$.

Because of the presence of the oxide layer, the measured capacitance C_m takes the following form:

$$C_m = \frac{C_1 \cdot C}{C_1 + C} \quad (2.26)$$

which shows the series combination of the barrier capacitance with the oxide capacitance $C_1 = \frac{\epsilon_{ox}}{d_{ox}}$.

A more important system on which to study capacitance effects in the metal-semiconductor with a depletion layer is

the Schottky barrier which we now discuss.

2.3.2 The Schottky Barrier

2.3.2.1 Current transport mechanisms.

The formation of a barrier occurs when a metal and a semiconductor are brought in intimate contact. The resulting phenomena are illustrated in Figure (2.5.a). When these are connected electrically, a transfer of charge takes place and the two Fermi levels coincide at thermal equilibrium (in general, this does not happen when the two materials are apart). The charge in the semiconductor is accommodated in band bending at surface.

According to the classical theory (Mott, 1938), the built-in surface potential is equal to the difference between the work functions of the two materials. This presents too simplified a picture, ignoring the effects of interfacial states and any interfacial layer. When band bending occurs, two situations may arise. First, if accumulation of mobile charges results in a barrier region of small resistance compared with the bulk then the contact is described as ohmic. Secondly, if, on the other hand, the region is depleted of carriers and the barrier region is appreciably resistive then it is described as a Schottky barrier and the contact has rectifying properties.

If a bias voltage is applied to the contact so that the metal is positive, the bands in the semiconductor are raised in energy relative to those in the metal and the electric field in the barrier is reduced. The decrease in the electric field is significant only within the semiconductor region causing a greater flow of electrons into the metal. This is defined

as the forward polarity Figure (2.5.b). If, on the other hand, the voltage is reversed Figure (2.5.c), the bands in the semiconductor are lowered relative to those in the metal and V_{bi} increases. The resulting effect is to cut off the current in the forward direction. Since the flow of carriers from the metal to the semiconductor remains constant (as the barrier height ϕ_b is unchanged) a net rectifying behaviour is observed.

As mentioned above, the classical school of thought suggested that V_{bi} and ϕ_b were likely to be sensitive to the work function of the metal contact. This has not been found to be the case in either crystalline or amorphous semiconductors. The more likely reason is attributed to the interface states, the role of which is seen to screen the semiconductor from the electric field.

The transport of majority carriers from the bulk of the semiconductor to the interface is governed, first, by the usual mechanism of diffusion and drift in the electric field of the barrier region. Secondly, at the interface, the emission into the metal is controlled by the number of available Bloch states which can communicate with states in the semiconductor. These two processes are effectively in series and are treated accordingly by diffusion and thermionic emission theories. The predicted behaviour in both cases is almost identical and described by the following equation:

$$J = J_0 \left[\exp\left(\frac{eV}{kT}\right) - 1 \right] \quad (2.27)$$

However, the form of J_0 the saturation current density expected in the two cases is different.

In diffusion theory, J_0 is described by:

$$J_0 \propto \exp\left(\frac{-e\phi_b}{kT}\right) \quad (2.28)$$

whereas, in thermionic emission theory J_0 takes the following form:

$$J_0 \propto T^2 \exp\left(\frac{-e\phi_b}{kT}\right) \quad (2.29)$$

where ϕ_b is the metal-semiconductor barrier height defined in Figure (2.5).

In practice, it has been found difficult to decide

which of these processes is dominant.

According to the Bethe criterion(55), for thermionic emission to be valid, the electron free path δ must be greater than a given distance y in which the barrier maximum decreases by an amount $\frac{kT}{e}$. On the contrary, for $\delta \ll y$ diffusion theory prevails. For crystalline semiconductors, experimental results indicate that thermionic emission is more likely to reflect the true properties of the transport mechanism due to high carrier mobilities in these materials which imply long free paths. This has been confirmed by theoretical studies (56). For amorphous semiconductors the reported results have been ambiguous. Early results by Wronski et al (57) on glow discharge silicon were interpreted in terms of diffusion theory. Deneuille and Brodsky (58) have reported data for glow discharge silicon which suggest that neither mechanism dominates the current flow. Despite the conflicting reports on the subject, Thompson et al (59) and Gibb et al (22) have produced evidence for thermionic emission theory being valid at high temperatures for their sputtered material, whereas a tunnelling mechanism becomes important at

low temperatures. This is an unexpected conclusion given the low mobilities in amorphous materials. Our own data are discussed in Chapter 5.

Important to the characteristics of transport mechanisms is the concept of quasi-Fermi level ξ_e introduced to describe the electron behaviour under non-equilibrium conditions i.e. under bias. The behaviour of this quantity, as predicted in each case, is variable according to which theory is valid. In thermionic emission theory, since the main impedance to the current is at the interface, ξ_e is flat throughout the semiconductor right upto and beyond the interface where it drops abruptly to the Fermi level position. In diffusion theory, on the other hand, the quasi Fermi level ξ_e is constant throughout the bulk of the semiconductor then decreases smoothly across the depletion region as illustrated in Figure (2.6). The corresponding quasi-Fermi level for holes ξ_h is essentially flat throughout the depletion region and remains continuous with E_F in the metal across the interface in both theories.

For ideal behaviour of a Schottky barrier, the expected current voltage dependence is as described by equations (2.27 - 2.29). However, various effects may cause deviations from this ideal characteristic including the possibility of other transport mechanisms across the barrier region as shown in Figure (2.7).

The ideality factor n is introduced to model the effects of certain deviations from the idealized behaviour, particularly those caused by an interfacial layer or image force lowering of the barrier. In this case, the general equation for both theories becomes

$$J = J_0 \exp\left(\frac{eV}{nkT}\right) \left(1 - \exp\left(\frac{-eV}{kT}\right)\right) \quad (2.30)$$

where n is the ideality factor describing the rate of change of ϕ_b with bias and n is defined by (Crowell and Beguwala)

$$\frac{1}{n} = \left(\frac{kT}{e}\right) \frac{d}{dV} \left[\ln \frac{J}{1 - \exp\left(\frac{-eV}{kT}\right)} \right]$$

The more general form is often written as:

$$J = J_0 \left(\exp\left(\frac{eV}{nkT}\right) - 1 \right) \quad (2.31)$$

which holds for $V > \frac{3kT}{e}$. It follows that a plot of $\ln \frac{J}{1 - \exp\left(\frac{-eV}{kT}\right)}$ versus V , has a gradient of slope $\frac{e}{nkT}$.

Due to the presence of localized gap states, particularly the surface states, tunnelling probabilities are much enhanced over those for crystalline semiconductors (60). This becomes clear by examining the temperature dependence of J_0 . The number of electrons having sufficient energy to cross the barrier by thermal emission will be reduced as the temperature decreases allowing tunnelling conduction processes to take place and, eventually, become significant (B and C in Figure 2.7). In particular, thermionic field emission tunnelling will become the dominant conduction mechanism, at sufficiently low temperatures. Also due to filled localized states at the amorphous semiconductor Fermi level, a tunnelling current can flow between the two levels at either polarity of bias. This is shown in Figure (2.7) for reverse bias.

In the theory of thermionic field emission formulated by Crowell and co-workers (56,61,62), it has been shown that for an ideal J-V characteristic, the barrier height ϕ_b must be replaced by an energy barrier ϕ_t at which the tunnelling current is maximum at any particular temperature. However,

since this quantity is temperature dependent, a plot of $\ln J_0$ versus reciprocal temperature is not expected to be linear giving no clue on activation energy. This type of behaviour is indicative of thermionic field emission tunnelling. In this case, the high temperature extrapolation of the data points should give a lower limit for ϕ_b . As discussed above, this characteristic is an indication of large gap state densities.

2.3.2.2 Capacitance Measurements on Crystalline Schottky barriers.

In crystalline semiconductors or any semiconductor in which the space charge is dominated by the shallow donor or acceptor concentrations, ^{the} capacitance is independent of the applied frequency or temperature provided that the dielectric relaxation time is short enough compared to the measuring frequency (see discussion in 2.3.2.3). This is a crucial point since the movement of charge at the edge of the depletion region and hence the contribution to charge density is measured on this time scale. An alternative for crystalline semiconductor investigation is the exploration of capacitance voltage measurements.

For the regime of band bending where the abrupt depletion approximation is valid (30), the relation between C and V is simply described by the following equation:

$$C = \frac{\epsilon}{w} \left[\frac{e\epsilon N_d}{2V} \right]^{1/2} \quad (2.32)$$

where N_d is the donor concentration (n-type).

In this case, details about the barrier are obtained from

the plot of $\frac{1}{C^2}$ versus V . The gradient of the predicted straight line is directly related to the charge density N_d while the intercept with the voltage axis gives the built-in potential V_{bi} .

In the case of a non-uniform charge density, the plot is no longer linear, but the relation between the gradient and the charge density at the edge of the depletion region still holds allowing doping profiles to be measured.

As mentioned above, under specific conditions, the frequency is unlikely to play any role in characterising these materials as in the MIS structure, but there is a real possibility of making use of the capacitance-frequency dependence i.e. when deep traps are present (as in amorphous semiconductors). Since these are not totally ionized at room temperature, their occupation is being controlled by the Fermi level. Therefore, any perturbing signal may influence their occupation leading to an extra capacitance which modifies the overall capacitance.

2.3.2.3 Capacitance Measurement on Amorphous Schottky barriers.

The first attempts at interpreting capacitance-voltage measurements on amorphous semiconductors were made by Wronski (63), who used the theory formulated for crystalline systems followed by Dohler and Hirose (49) who formulated the basic theory for amorphous semiconductors.

In a thorough study of amorphous barriers, Spear et al (50), following along the lines presented by Roberts and Crowell (46), pointed out that, unlike crystalline semiconductors, in amorphous ones, the charge density is not

uniform but it is a function of both position and energy, because of the presence of localized states in the latter which contribute to the charge density. Thus a fundamental difference does exist between the two cases. The authors extended their analysis to include the dependence of amorphous barrier capacitance on the measuring frequency giving rise to a relevant question of how quickly do states respond to a modulation. Using a thermal release time model, Spear et al (50) have shown that states deeper than 1eV below the conduction band (typical value for a Schottky barrier) require $\sim 10^4$ S at room temperature to respond to a perturbation and can be even greater for states deeper than this energy level. This highlights the fact that at a typical measurement frequency, one may possibly not observe the total response of the system because of non-contributing states.

To model this phenomena, Spear et al (50) imposed a cut off energy in the barrier space charge density distribution beyond which the distribution was either constant or increased slowly & linearly. However, they did not express the capacitance explicitly in terms of the total density of states in the gap. Instead they constructed the barrier charge distribution by de-convoluting the density of states distribution obtained from field effect measurement into acceptor and donor like bands. This procedure enabled band bending profiles to be constructed for doped as well as undoped materials. On the basis of these model calculations they concluded that amorphous semiconductors differ from their counterpart crystals, and therefore must be treated differently.

2.3.2.3.1 Capacitance-Voltage Measurements.

Capacitance-voltage measurements have not been widely used. Early results reported by Hirose et al (64) on glow discharge silicon showed a smooth variation of $g(E)$ with energy without peak structures and a minimum between 10^{16} - $10^{17} \text{ eV}^{-1} \text{ cm}^{-3}$. The density of states derived from field effect analysis, also performed on the same sample, was higher than ^{the measurement} for $C-V$ and indicated a hint of the $E_c - 0.4 \text{ eV}$ peak reported in some other field effect experiments.

In their analysis, Spear et al (50) have used their well established model of density of states to predict the capacitance-voltage behaviour. They used the formula normally used in crystalline cases, but taking into consideration the frequency dependence of states, and deduced a value of charge density $\sim 10^{16} \text{ cm}^{-3}$ in agreement with their prediction.

Surprisingly, in view of the details presented above, Wronski (63), has reported data on glow discharge material which fits the usual linear plot of C^{-2} versus V usually used for crystalline materials. These fits give V_{bi} values which agree with D.C. measurements and also give space charge density of $\sim 5 \cdot 10^{15} \text{ cm}^{-3}$ in the barrier. The author estimates also a surface state density of $\sim 10^{13} \text{ eV}^{-1} \text{ cm}^{-2}$.

2.3.2.3.2 Capacitance-Frequency Measurements.

The most important feature in the Spear et al (50) formulation is that of non-contributing states. From a well known average thermal release time of an electron lying at certain energy levels and using reasonable values for the quantities involved, the authors estimated the measuring

frequency beyond which states cease to contribute to the differential capacitance. Equally important is this dual relation between frequency and energy. Having established this relationship, the problem of localized states can be seen, now, in a new dimension.

Indeed, since the measured capacitance is related to the density of localized states, the measurement of capacitance as function of frequency is equivalent to a measurement of the density of states $g(E)$ as function of E .

To examine this type of experiment, a theoretical platform is needed. As usual, the method involves analytical forms of the density of localized states. The most commonly used is the constant density of states approximation.

Two methods have been proposed to model the kinetics of charge movement in the depletion region. The first is that due to Beichler et al (18), where the frequency dependence of capacitance measurement is attributed entirely to a distribution of electron traps. In this model, the charge motion during the process of filling and emptying these traps is characterized by its thermal release time described by the following relation:

$$\tau = \tau_0 \exp \left(\frac{E_c(x) - E_F}{kT} \right) \quad (2.33)$$

where $E_c(x) = E_{c_{bulk}} + eV(x)$.

$$\tau_0^{-1} = N_c v_{th} S_n$$

N_c is the number of states within kT of the conduction band edge.

v_{th} is the carrier thermal velocity.

S_n is the trap capture cross section (assumed constant with energy)

The procedure consists of perturbing the trap population by an A.C modulation and the resulting response is modelled by a parallel combination of a capacitor and a conductance, both of which are frequency dependent. Using the constant density of states approximation, Beichler et al obtain the following expression for capacitance-frequency dependence

$$C(\omega) = C_0 \left[1 - \frac{kT}{2eV_s} \cdot \ln \frac{1 + \omega^2 \tau_0^2 \exp \left[\frac{2(E_C - E_F + eV_s)}{kT} \right]}{1 + \omega^2 \tau_0^2 \exp \left[\frac{2(E_C - E_F)}{kT} \right]} \right] \quad (2.34)$$

where C_0 is the D.C. capacitance of the depletion layer $C_0 = \frac{\epsilon}{L}$, V_s is the surface potential ($V_s = V_{bi}$ under zero bias) and ω is the angular frequency

The analysis scheme has been developed to take into consideration the bulk contributions. These are considered frequency independent and are represented by a simple combination of capacitance and conductance. Thus, at high frequencies, the response becomes simply the geometrical capacitance of the sample, whereas, at low frequency, the capacitance is related purely to the barrier response.

A similar approach has been proposed by Tiedje et al (65) but with a more complex density of states distribution.

The second approach is that of Viktorovitch et al (21) (66) who proposed a much more complex model which not only considers trap contributions but includes also resistive elements describing charge transport in the bands and geometrical capacitances. To explain all these processes, the authors construct a lumped R.C. circuit based on the analysis of Beguwala and Crowell (47). This leads again as shown by Beguwala et al to a more complicated equivalent

circuit. By making appropriate simplifications and using the constant density of states approximation, Viktorovitch et al derived the following expression for capacitance-frequency dependence

$$C(\omega) = \frac{\epsilon}{L} \left[1 + \ln \frac{eV_s/kT}{1 + \ln(\omega_0/\omega)} \right]^{-1} \quad (2.35)$$

where ω_0 is the angular frequency corresponding to the state kT above the onset of the barrier.

In developing their theory, Viktorovitch et al (21), initially ignored diffusive elements in their model and suggested that the thermionic approximation was valid to describe the mechanisms involved, but the author concluded later that diffusion theory not thermionic theory was appropriate to describe the transport of electrons. However, the analysis formula was not affected by this conclusion. This, again, outlined the problem of differentiating the two effects.

Viktorovitch (67) has demonstrated that in certain circumstances the total response of the barrier is unlikely to be detected because of shorting conductance effects at the surface, in particular from the contact resistance.

Snell et al (51), have also warned of this problem which they related to minority carrier conductance due to weak inversion at the surface.

2.4 Other Capacitance Measurements

Transient junction capacitance methods which include deep level transient spectroscopy (D.L.T.S.) (68, 69, 70), thermally stimulated capacitance (T.S.C.) (68), photocapacitance (71), and the drive-level capacitance profiling technique all lead to $g(E)$ curves similar to those observed by D.L.T.S (72)

as illustrated in Figure (2.8b). They are all sensitive to bulk gap states in a limited region near the edge of the depletion region.

2.4.1 D.L.T.S. Measurements

The main feature of D.L.T.S. measurements is the existence of an emission rate window which, once set, allows only transient signals with rates within this window to be detected. Usually these rates are thermally activated, and hence vary strongly with temperature.

In this technique, the measurement consists of returning a reverse biased Schottky or p-n junction to approximately the zero bias condition with a short voltage pulse, then going back to the original bias. During this procedure, traps which are empty under reverse bias, are filled. They then empty again by thermal emission.

The transient response is detected at two fixed times t_1 and t_2 after perturbation. These times t_1 and t_2 are defined by the rate window $\frac{1}{\tau_{\max}}$ to which the measurement is most sensitive.

The emptying process can be measured either as capacitance or current transient and the difference in signal $S(T)$ is measured as a function of temperature and is written as:

$$S(T) = \frac{\Delta C(t_1) - \Delta C(t_2)}{\Delta C(o)} \quad (2.36)$$

where $\Delta C(o)$ is the capacitance change due to the pulse at $t=0$.

For an exponential transient response the expression becomes:

$$S(T) = \exp(-t_1/2) - \exp(-t_2/2) = \exp(-t_1/2) \left[1 - \exp(+\Delta t/2) \right] \quad (2.37)$$

where $\Delta t = t_2 - t_1$

The relationship between τ_{\max} and t_1 , and t_2 is written as:

$$\tau_{\max} = \frac{t_1 - t_2}{\ln t_1/t_2} \quad (2.38)$$

The experiment was very successful in the study of trap levels in crystalline semiconductors. Typical data of D.L.T.S. measurement is illustrated in Figure (2.8a). From that data, the emission rate corresponding to the maximum of a trap observed in D.L.T.S. thermal scan is quantified and along with the temperature of the peak maximum, a semi-log energy plot is constructed. At the maximum of the signal one can measure the temperature and calculate τ_{\max} from equation (2.38) to get one point of the plot. Other points can be similarly obtained from other scans made with different window settings, and therefore different values of τ_{\max} and different trap peak positions. The magnitude of the peak maximum can be determined from equations (2.36 - 2.38) and thus trap concentration can be derived i.e.,

$$N = \frac{2\Delta C}{C} (N_A - N_D) \quad (2.39)$$

where ΔC is the capacitance change at $t=0$ due to a saturating injection pulse.

C is the capacitance of the diode under quiescent reverse biased condition.

$(N_A - N_D)$ is the net acceptor concentration on the p-side of the p-n junction.

Because of the well defined D.L.T.S. line spectra in crystalline case, it is straightforward to analyse the data to give the temperature dependence of the emission rate from

the corresponding trap (see fig. 2.8a)

2.4.2 D.L.T.S. Measurements on a-Si:H

Several effects may occur when the D.L.T.S. technique is applied to a-Si:H and major complicating factors emerge. The filling pulse may generate a capacitance transient which is large compared with the background, profoundly modifying the barrier shape and making the experiment difficult to analyse. The deep trap states are broadly distributed with no pronounced features. In this case, the activation energy of each component cannot be measured directly by a set of Arrhenius plots as in the crystalline case. This feature undermines the energy calibration.

To measure the capacitance accurately requires an equivalent circuit with the time constant satisfying the following relation:

$$\omega \ll \frac{1}{R_b C}$$

where R_b is the bulk resistance of the diode, otherwise, there will be no charge transfer to the barrier under investigation. Hence, it is necessary to work with doped material having a low value of R_b . Even so, it is necessary to measure at a much lower frequency, 1-100 KHz and with a smaller rate window $10s^{-1}$, than in the crystalline case.

2.4.3 The Density of States

A summary of the density of states results is presented in Figure (2.8b). As shown $g(E)$ covers much of the gap and differs in form and magnitude from the equivalent

field effect data. The discrepancies are very large and cannot be explained by the possible errors in field effect analysis. The conflicting pictures of $g(E)$ obtained by these two methods show that fundamental differences do exist. Values of $g(E)$ as low as $5 \times 10^{15} \text{eV}^{-1} \text{cm}^{-3}$ were obtained by D.L.T.S. measurements.

The most striking feature is that, instead of a peak in the distribution at 0.4 eV below E_c , a minimum is observed at ~ 0.5 eV from E_c . Such a large difference both in magnitude and distribution is attributed by most authors to the inherent characteristic of field effect experiment being very sensitive to the surface if not entirely surface in origin. In general, coplanar transport measurements are highly susceptible to a high density of trap states near the surface because a drifting carrier cloud is likely to sample such traps during the course of its motion. This is particularly important for field effect measurements, where transport is restricted to surface layers $< 100\text{\AA}$ thick (38). From this point of view, the D.L.T.S. technique reflects the true properties of bulk material and can indeed be used to measure the spatial variation in the density of states (by varying the fill voltage) over a distance of 0.1 μm to 0.6 μm from the surface (70). The low magnitude seen in D.L.T.S. may well be justified in many cases (Weisfield (73)). The results of an independent measurement of space charge limited current (S.C.L.C.) tend to support the figures reported by D.L.T.S. though not the energy dependence of $g(E)$. There are, however, many approximations in the analysis of D.L.T.S. experiments some of which are not

obviously true. The issue was raised by Viktorovitch and Moddel (21) and calls into question some of the assumptions made in developing the D.L.T.S analysis scheme. In their discussion, they argued that the dynamic response of an a-Si:H Schottky barrier is controlled by carrier transport and not by capture and emission at states in the gap. If true, it presents a severe handicap for the D.L.T.S. method.

As we shall see in Chapter 6, our results of S.C.L.C. measurements, carried out on magnetron sputtered a-Si:H indicate that the low values of the density gap states may well be justified. However, there is, evidence that the S.C.L.C experiment is not only restricted to bulk properties (as thought in the past) but is influenced by surface properties as well.

2.5 The Space Charge Limited Current (S.C.L.C) Measurements.

This technique was initially developed to study the continuously distributed electronic density of states in the gap of insulators (74, 75, 76). In this experiment a non-equilibrium density of charge is injected at higher voltages. In principle, this density of charge extends throughout the sample and a large part of it populates the empty gap states above the Fermi level. The method was first used by Den Boer (77.) to study glow discharge a-Si:H deposited in a sandwich structure, $n^+ - i - n^+$. He found a nearly uniform distribution of the states over a considerable energy range above E_F . In his approach, Den Boer (77) simplified the analysis by assuming a uniform distribution of injected charge, a simplification he found to introduce an inaccuracy

of no more than a factor of 2. The author adopted a step-by-step procedure and derived the following expression for the density of states.

$$g(E_F) = \frac{2\epsilon_s \Delta V}{ed^2 \Delta E_F} \quad (2.40)$$

where ΔV and ΔE_F are, respectively, changes in voltage and Fermi level energy occurring as a result of charge injection.

(ϵ_s is the semiconductor permittivity and d the sample thickness).

A more elaborate method was introduced by Nespurek et al (78). This method requires an accurate knowledge of the slope of the J-V characteristic as a function of voltage. Nespurek et al (78) expressed the density of states in the following relation:

$$g(E_F) = \frac{\epsilon_s b_1 b_2 V}{2ed^2 (m-1)} \quad (2.41)$$

where $m(v) = \frac{d(\ln J)}{d(\ln V)}$

b_1 and b_2 are parameters obeying the following conditions,
 $1 < b_1 < 2$ and $\frac{1}{2} < b_2 < 1$

In earlier work, Rose (74) discussed the case of an exponential distribution of trapping states which can be related analytically to the J-V characteristics. This was followed by a more detailed treatment by Mark et al (79) who used a density of states distribution described by the following equation:

$$g(E) = \frac{N_C}{kT_C} \exp\left(-\frac{E_C - E}{kT_C}\right) \quad (2.42)$$

which leads to the J-V relation in the S.C.L.C. regime

$$J_{SC} = k V^r.$$

The parameter T_C is an effective temperature which characterises the distribution and N_C denotes the total number of states, which can be determined from the coefficients k and r in the above equation.

As pointed out by Fritzsche in a recent review paper (72), the first results were obtained in an approximate manner which ignored the spatial dependence of a number of physical quantities, a simplification which has been shown to be ~~not very~~ accurate by the analysis of Weisfield (73) and Solomon et al (80).

Weisfield (73) presented an analytical treatment of the S.C.L.C. problem in which he expressed all spatially variable quantities in terms of the local Fermi level shift $u(x)$. The analysis still requires the validity of the following assumptions.

- 1) The sample is uniform and the mobility μ is spatially uniform and independent of position and field.
- 2) The gap state density $g(E)$ varies slowly and continuously over energies of order kT so that zero temperature Fermi Dirac statistics are valid. The charge density $\rho(x)$, in this case depends solely on the local shift in the quasi-Fermi energy

$$\rho(x) = \int_0^{kTu(x)} g(E_{F0} + E) dE = \rho(u(x)) \quad (2.43)$$

- 3) The population of free electrons is in quasi-equilibrium with the charge trapped in the deep

levels above the equilibrium Fermi level E_{f_0} and the density of free electrons is described by Boltzmann statistics i.e.

$$n(x) = n_0 \exp u(x) \quad (2.44)$$

where $u(x) = \frac{\Delta E_F}{kT}$ is the shift in the quasi Fermi level energy,

- 4) The current density J is uniform and described by electron drift (neglecting diffusion elements).
- 5) Poisson's equation relates the local field $F(x)$ to the charge density $\rho(x)$.

$$\frac{dF(x)}{dx} = \frac{\rho(x)}{\epsilon_s} \quad (2.45)$$

To derive the density of states $g(E)$, Weisfield (73) solved the inverse problem. In this $g(E)$ is determined explicitly from the J - V characteristic. To do this, he introduced a set of parameters α, β, γ and obtained an expression for $g(E)$ described by the following equation.

$$g(E_{F_0} + \Delta E_F) = \frac{V \epsilon_s}{ekTd^2} \left[\alpha(2-\alpha) + \frac{\gamma - \beta(3-2\alpha)}{1-\alpha+\beta(2-\alpha)} \right] \quad (2.46)$$

where $\alpha = \frac{d(\log(V))}{d(\log(J))}$ $\beta = \frac{d^2(\log(V))}{d(\log(J))^2}$ $\gamma = \frac{d^3(\log(V))}{d(\log(J))^3}$

ϵ_s is the semiconductor permittivity.

d is the sample thickness.

The above relation is valid provided that $g(E)$ does not vary rapidly with energy, i.e.

$$kT \frac{d(\log g(E))}{dE} \ll 1$$

Following along the lines presented by Den Boer (77) and Nespurek et al (78), MacKenzie et al (81) used the S.C.L.C. method

to resolve the controversial problem of the density of states presented by the conflicting results of D.L.T.S. measurements (68, 69, 70) and their field effect results. As predicted, MacKenzie et al obtained a low value of density of states near E_F , which, they interpreted as reflecting the true bulk properties of their glow discharge material. However, they showed total disagreement with D.L.T.S. results in the shape of the $g(E)$ curve.

In a thorough analysis, Solomon et al (80) rewrote the S.C.L.C. equations in terms of dimensionless variables and derived a simple formula for the density of states described by this relation i.e.,

$$g(E_F) = \frac{\epsilon \epsilon_0 V_C}{ekTd^2 \ell} \quad (2.47)$$

where V_C , the onset voltage, can be determined from the normalized J-V characteristic, (J-V characteristic expressed in reduced units j and v , defined by $j = \frac{J}{J_C}$ and $v = \frac{V}{V_C}$)

ℓ is a parameter introduced to describe the steepness of the J-V curve, $g(E)$ is written as $g(E) = \exp\left(\frac{E - E_C}{kT_g}\right)$ and $\ell = \frac{T_g}{T}$
 d is the thickness of the sample.

In this analysis, the fit of experimental data to a theoretical model is achieved by adjusting only two parameters i.e. the onset voltage V_C and ℓ the steepness of the distribution.

Solomon et al (80) concluded that the results are not sensitive to the form of $g(E)$ but depend exclusively on the value of the density of states at the Fermi level $g(E_F)$, a conclusion which has been brought into question by other workers (82.)

Our own discussion of S.C.L.C. analysis is given in Chapter 6.

Measurement	Preparation Method.	$g(E_F)$ ($eV^{-1}cm^{-3}$)	g_{SS} $eV^{-1}cm^{-2}$	Reference.
Field Effect	G.D.	2×10^{17}	-	Madan et al (26')
	Evap.	1.10^{19}	-	Malhuttra et al (85)
	R.F.Sputt.	$\sim 5.10^{17}$	-	Vaclav Smid et al ('86)
C-V on Schottky barriers.	G.D.	6.10^{15}	10^{13}	Wronski et al (57)
	G.D.	5.10^{16}	-	Hirose et al (64)
C- ω on Schottky barriers.	G.D.	10^{17}	-	Beichler et al (18)
	G.D.	2.10^{15}	-	Tiedje (65)
	R.F.Sputt	$9.9.10^{15}$ - $4.4.10^{17}$	2.10^{12}	Gibb et al (22)
D.L.T.S.	G.D.	8.10^{15}	-	Cohen et al (69.)
S.C.L.C.	G.D.	5.10^{15}	-	Solomon et al (80)
	R.F.Sputt	3×10^{14} - 10^{16}	-	Weisfield (73)
	Evap.	$\sim 10^{17}$	-	Gangopohvay et al (84)
E.S.R.	G.D.	10^{17}	7.10^{12}	Knights et al (43)

Summary of published values of the bulk localized state density and surface states density at the Fermi-level for a-Si.

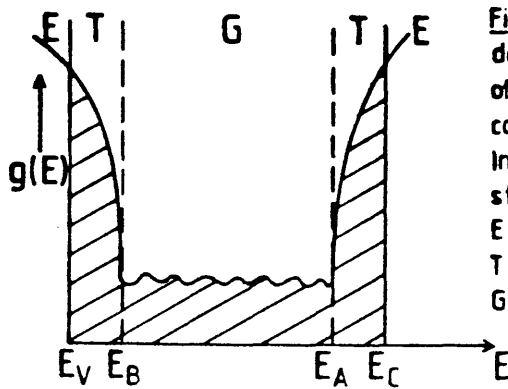


Fig 2.1.a. Schematic density of state distribution of an amorphous semi-conductor.

In the shaded parts the states are localised.
 E - extended states,
 T - tail states,
 G - gap states.

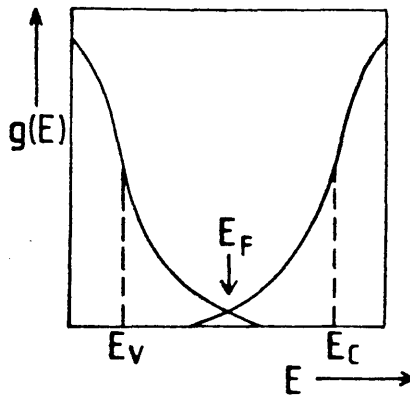


Fig 2.1.b. C.F.O. model for density of electron states in an amorphous semi-conductor.

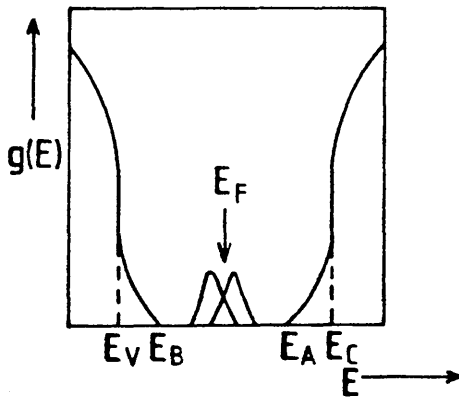


Fig 2.1.c. Defect band model proposed by Mott.

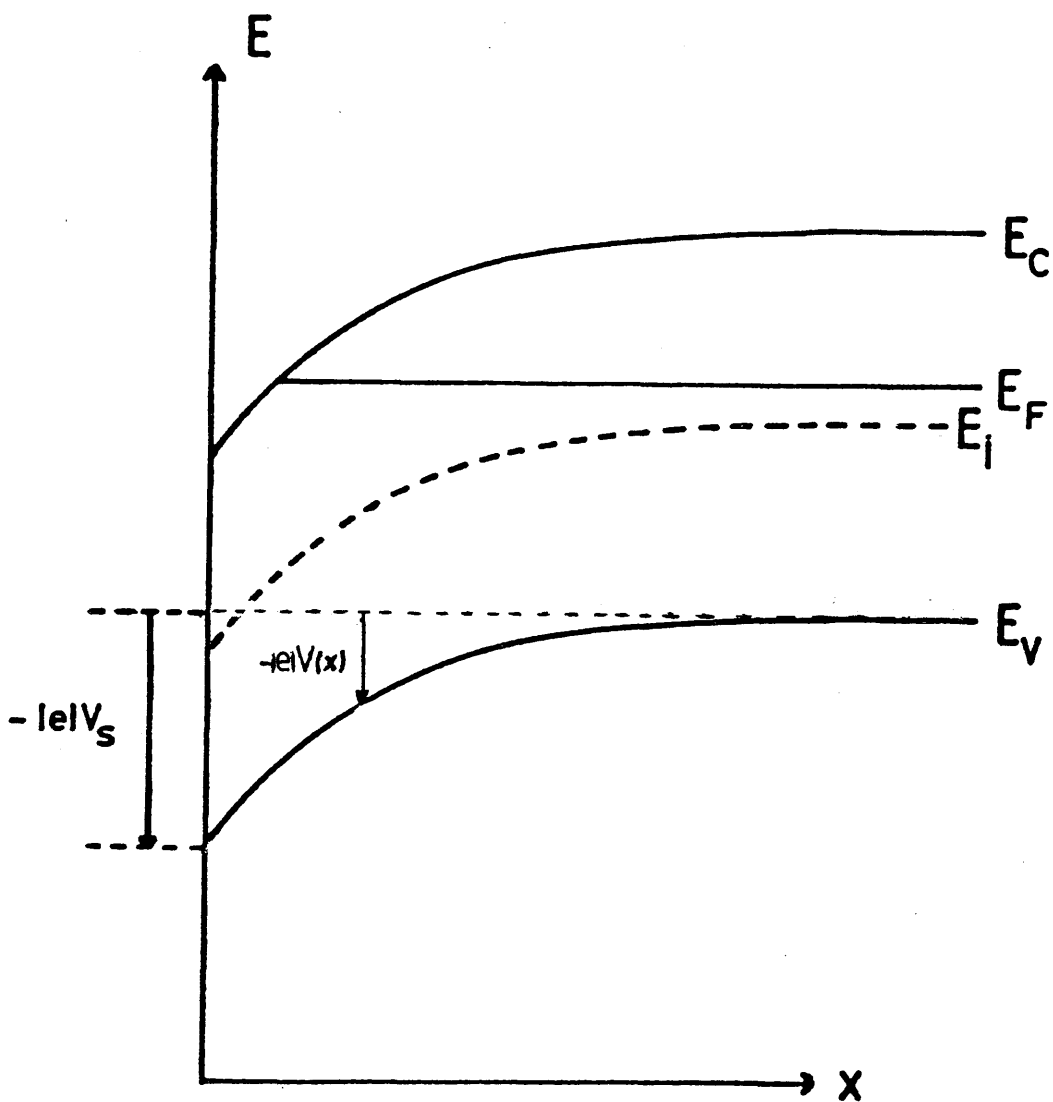


Figure 2.2. Band-bending diagram for n-type semiconductor (surface accumulation regime)

where E_c is the conduction band edge energy
 E_v is the valence band edge energy
 E_F is the Fermi level energy
 E_i is the intrinsic or mid-gap energy
 $V(x)$ is the electrostatic potential.

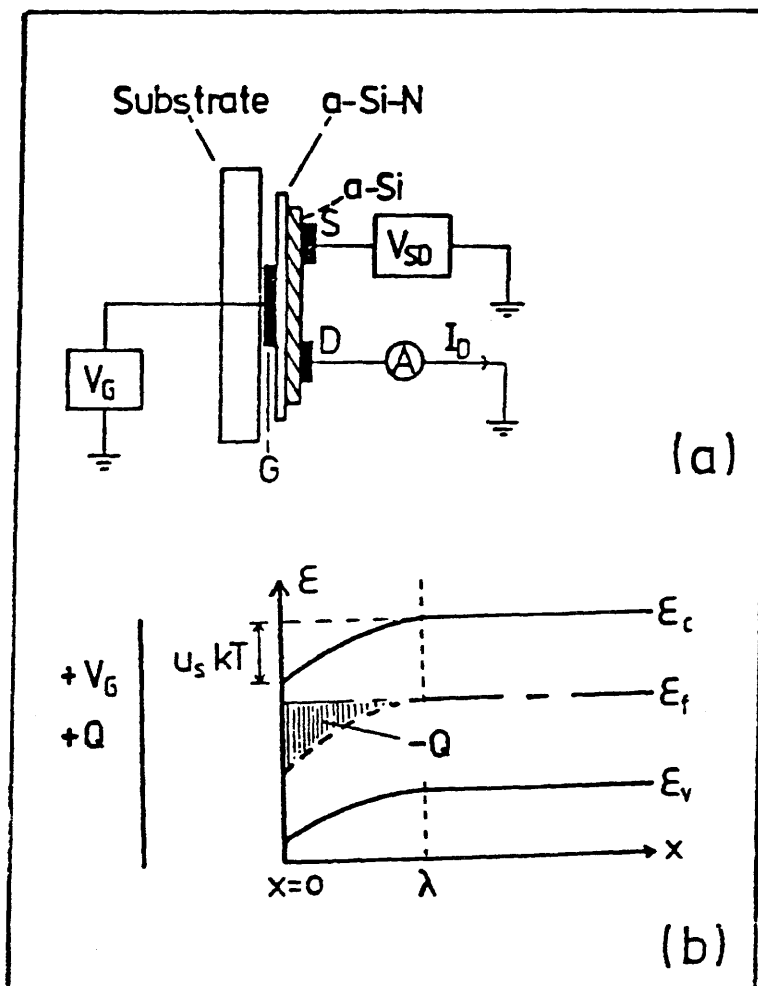


Figure 2.3 (a) sample geometry used in the field effect experiments. S,D and G represent the source, drain and gate electrodes.

(b) electron energy E plotted against the distance from the a-Si/dielectric interface at $x = 0$. $U_s kT$ denotes the magnitude of the band bending at the interface λ its extent into the semiconductor. Q and $-Q$ represent the total charge induced on the gate and in the a-Si respectively by the positive gate voltage V_G (after ref. 27, 28).

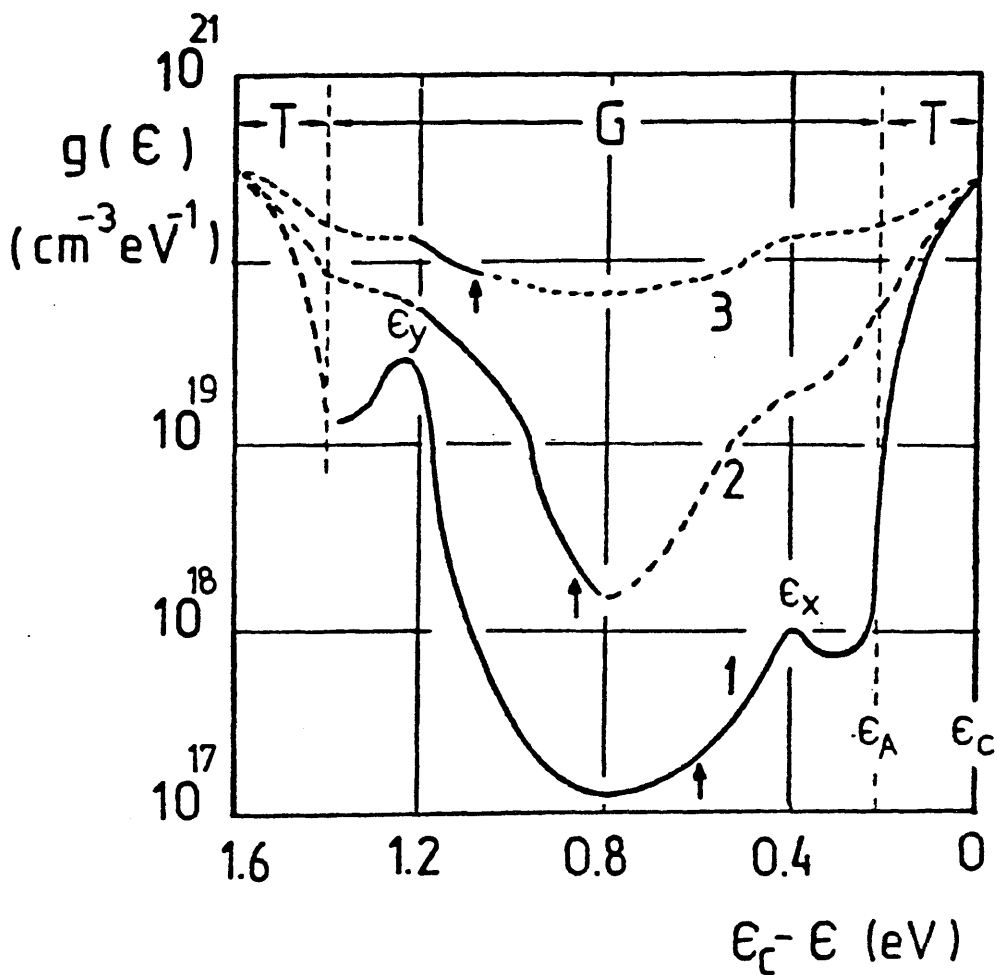


Figure 2.4

Density of state distribution for a-Si samples. Curve 1, glow discharge samples $T_g=520K$; curve 2 glow discharge samples $T_g=350K$; curve 3, evaporated samples. The full lines indicate results obtained from field effect experiments and the arrow in each curve shows the position of the Fermi level, E , extended states; T; tail states; G, gap states (after ref. 35, 28).

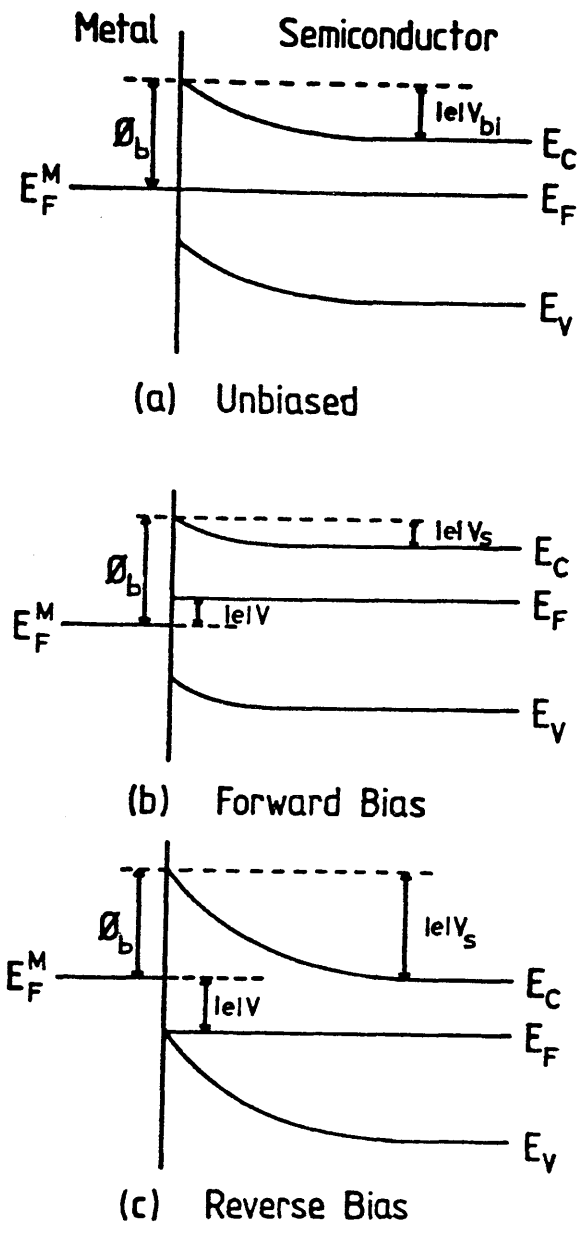


Figure 2.5 Band-bending diagram for metal/semiconductor junction (a) under zero bias (thermal equilibrium), (b) forward bias and (c) reverse bias.

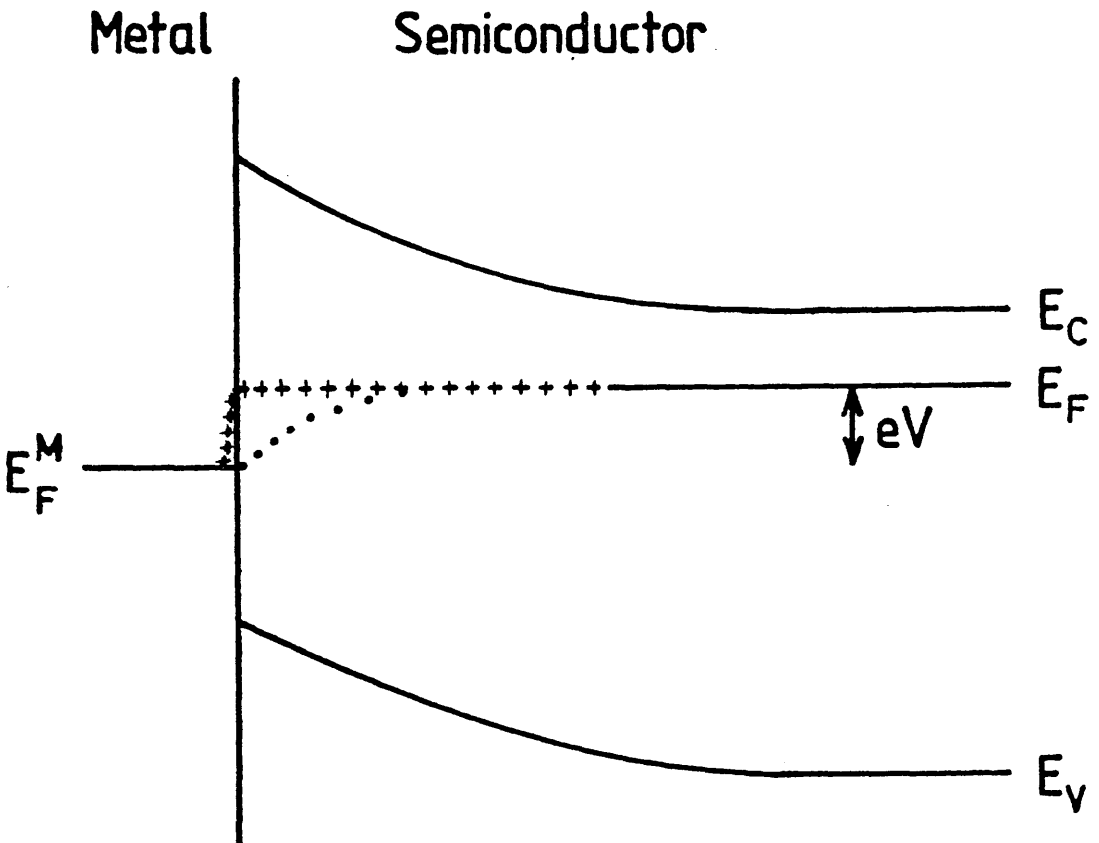


Figure 2.6

Illustrates the predicted behaviour of the electron quasi-Fermi level for forward biased Schottky barrier

(a) Thermionic emission theory (+ + + +)

(b) Diffusion theory (••••)

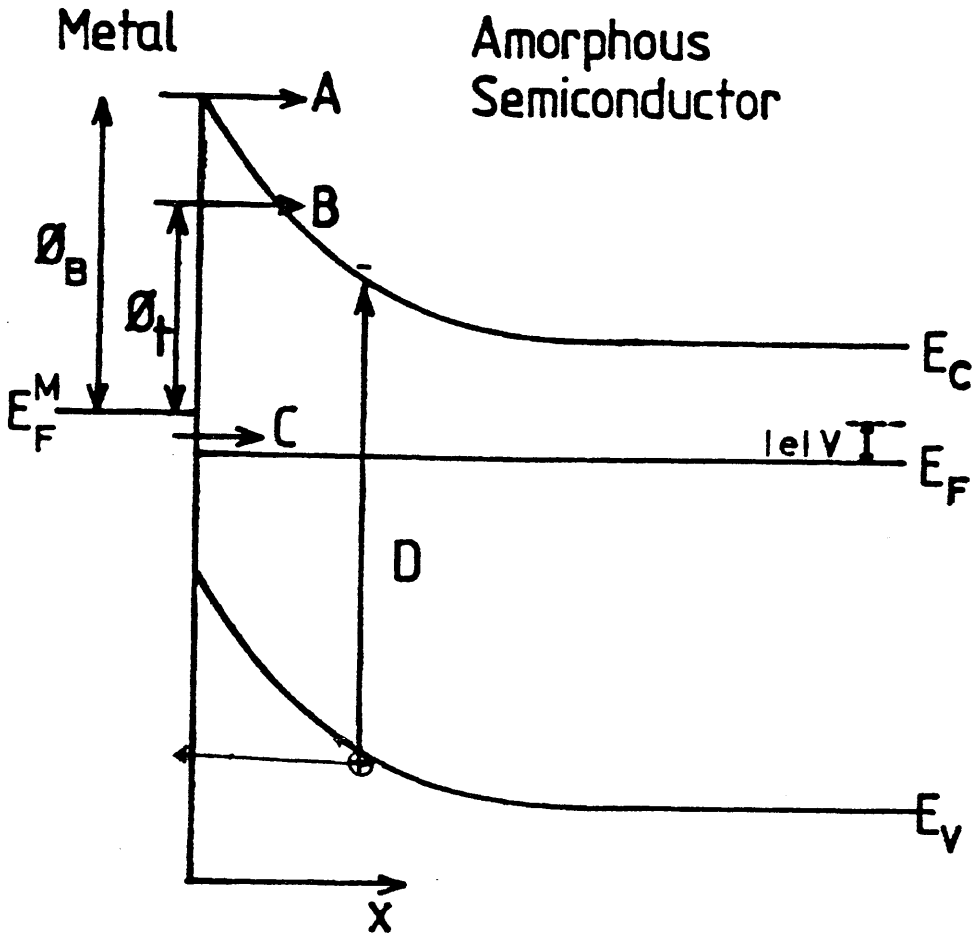
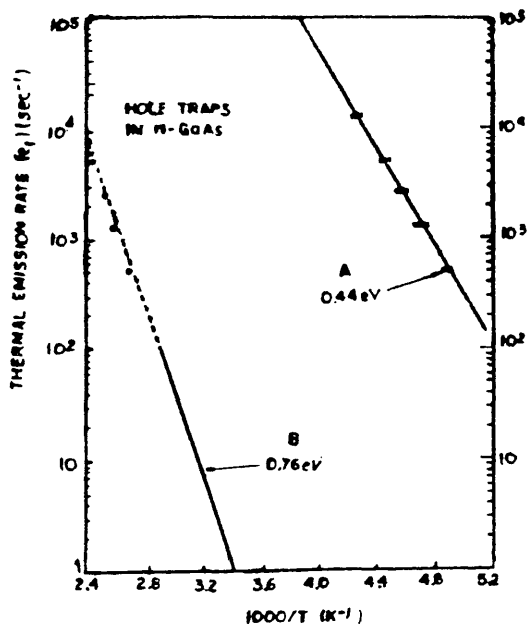
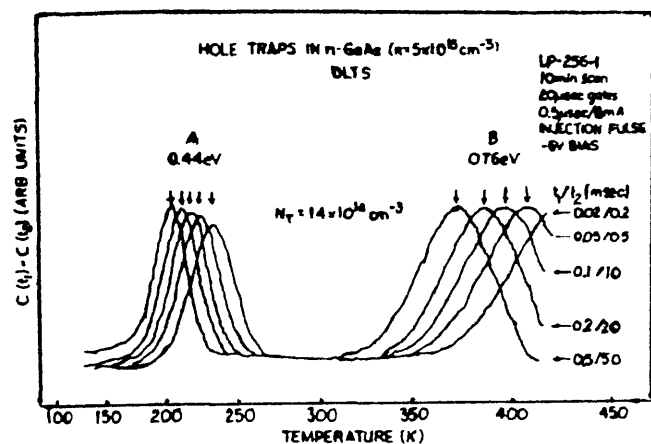


Figure 2.7

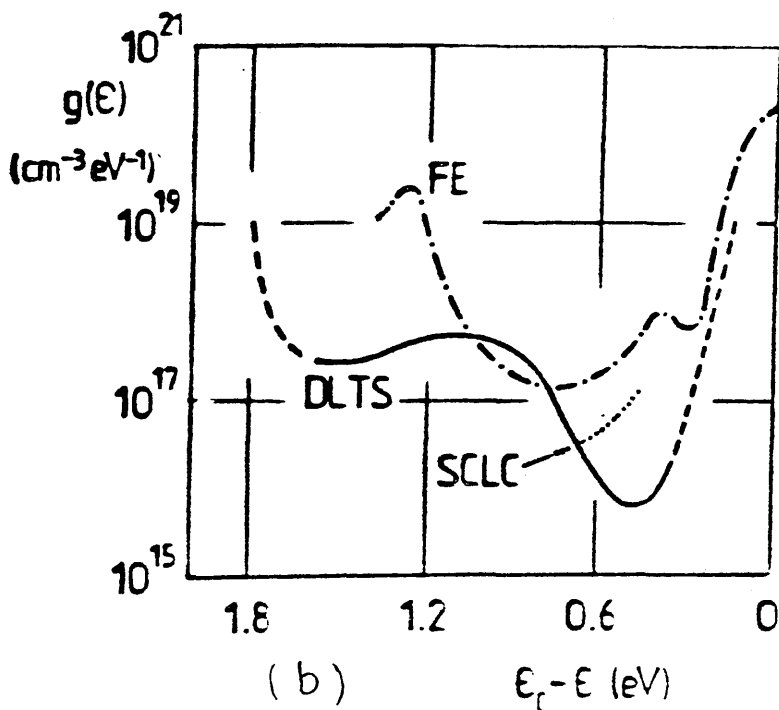
Illustrates possible current transport mechanisms through reverse biased Schottky barrier.

- (A) Thermionic emission
- (B) Thermionic field emission
- (C) Field emission
- (D) Electron-hole generation in barrier region.



(a)

Fig.2. Thermal emission rates vs $1000/T$ determined from the DLTS spectra in Fig. 1. The solid lines are determined from careful fixed-temperature measurements of the capacitance transients; the dotted lines are extrapolations of this data. The error bars on the DLTS data represent the uncertainty in locating the peaks in the spectra. (reference 125)



(b)

Figure 2.8

Shows the results obtained from DLTS experiment (a) the crystalline case (Ref. 125). (b) comparison of the density of states distribution for a-Si samples determined from field effect (FE) space-charge limited current (SCLC) and (DLTS)

CHAPTER 3.

In this chapter we describe the experimental techniques used. First we describe the sample preparation procedure. In this, a survey of R.F. sputtering technique is presented, followed by a discussion of the R.F. magnetron sputtering technique used to obtain the samples discussed in later chapters. We then present the measurement procedures adopted in this work.

3.1 Sample Preparation

3.1.1 A review of the sputtering process. (87)

Since our main objective is to study the electronic properties of hydrogenated amorphous silicon prepared by the R.F. sputtering technique, we will compare some properties of material sputtered with a magnetron source with those of material prepared with the conventional method and try to isolate the critical factors which control these properties. To start with, we give a brief description of the two processes to highlight the major differences between them.

In conventional D.C. sputtering, a plasma from an inert gas is formed in the target region. By biasing the target negatively, the positive ions in the plasma are accelerated towards the target. At a very low energy of bombarding particles (less than 5eV) the interaction is limited to the outermost surface layer of the target material and hardly anything is likely to happen. At sufficiently high energy, the removal of atoms begins. In the case of a conducting material target, the large negative bias applied to it can in itself be enough to enhance and sustain the plasma through the ionizing role of electrons emitted from the target surface. The plasma formation is governed by

many factors including bias voltage, gas pressure and the geometry of the discharge region. The D.C. sputtering has been used successfully for metallic targets. For insulating materials, however, it is useless because of a rapid accumulation of positive charge on the target surface which repels positive ions leading to a situation where the discharge cannot be maintained. To overcome this situation, a large radio frequency signal is applied between the substrate electrode and the target.

In this R.F. sputtering method, plasma excitation is accomplished by the R.F. fields which accelerate the plasma electrons to ionizing energies. It is advantageous to work at a high frequency (usually 13.56MHz) for more efficient plasma excitation. In this case, unlike the D.C. sputtering, the assistance of secondary emitted electrons is not required.

In the case of equal area electrodes, because of the high mobility of electrons with respect to the ions in the plasma, the applied R.F. voltage initiates the displacement of electron population. This flow of electrons creates a permanent electron deficit in the plasma in the vicinity of the electrodes. Subsequently, an electron depleted positive ion sheath is formed which remains positive with respect to the electrodes most of the time. As a result, a negative D.C. bias can be measured at either one of the two electrodes. This D.C. bias causes any ion which is close to the electrodes to be accelerated. In this situation, both electrodes undergo ion bombardment. If one or both electrodes is covered with a target material, then this can be removed and deposited on the substrate.

In an asymmetrical situation, where the area of one of the electrodes is greater than the other, the D.C. voltage will remain equal at both electrodes if the supply is D.C. coupled, since no D.C. drop can occur in the external circuit. However, due to the difference in the area, the number of electrons collected per half cycle at both electrodes is not equal leading to an asymmetric A.C. current. If a blocking capacitor is inserted in the R.F. circuit, it will be charged up by the asymmetric current and the D.C. biases at the electrodes will diverge. As a consequence the negative potential of the smaller electrode increases whereas that of the larger one decreases. With large electrode area ratio, the D.C. bias at the larger electrode can be reduced to below the threshold value. At this point no sputtering process takes place.

As discussed above, the capacitor can be made internal to the system by covering the smaller electrode with the insulator to be sputtered. With this geometry, insulating materials can be sputtered from the target and deposited on substrates placed on the other electrode. This is the basis of the asymmetrical parallel plate R.F. zero discharge devices which were first developed by Davidse and Maissel (88). The larger electrode in these systems consists of the grounded shield around the target, the grounded substrate holder, and all the other plasma-exposed grounded parts in the system (89). This is the operating principle of the R.F. sputtering used in this laboratory.

We have seen that the plasma formation is sensitive to many parameters some of which are very important. We now discuss the effect of introducing a permanent magnetic field in the

- 40 -

system, to give R.F. magnetron sputtering.

3.1.2 R.F. Magnetron Sputtering

The basis of magnetron sputtering was discovered by Penning (90) and further developed by Kay and others (91, 92, 93, 94). Basically, the planar magnetron source is in the classical D.C. or R.F. sputtering configuration, consisting of a planar cathode and its surrounding dark space shield. To this is added a permanent magnet behind the cathode. The magnet is disposed so that there is at least one region in front of the cathode surface where the locus of magnetic field lines parallel to the cathode surface is a closed path. In this region the magnetic field is normal to the electric field. Bounding this region the magnetic field lines enter the cathode surface. Ideally at the point of entry the field lines are normal to the cathode surface.

The amount of information about R.F. magnetron sputtering is limited and no detailed picture of the process has been given, other than that the discharge has a low impedance and insulators could be sputtered at high rates. Because of the low impedance, higher power densities are possible at low applied voltages. R.F. power supplies of 13.56 MHz developed for conventional sputtering are also suitable for R.F. magnetron sputtering. For a given power dissipation of 100 W, the D.C. voltage drops from 1.3 KV to 300 V. Because of the relatively high capacitance of the electrodes, a 1.25 KW system that incorporates planar magnetron electrodes (identical to our system) should be tuned using four 100 pF capacitors in series as a blocking capacitance. This is sufficient to compensate for the

lower planar magnetron plasma impedance.

As in the conventional method, a glow discharge is generated between the target and the substrate and two distinct regions are formed, a plasma ion sheath at the vicinity of the target and the remainder of the plasma region. During the process, ions bombard the target surface and cause the emission of secondary electrons. The latter penetrate a region where there is a crossed electric and magnetic field. The electron motion in this region can be described by the classical law of electromagnetism. When the electron emerges from the plasma sheath region, it is no longer affected by the electric field, instead, its motion is dictated only by the effect of the magnetic field and so follows a helical path about the lines of flux. The resulting effect is to direct back electrons into the plasma sheath region from which they are reflected. Thus the electrons are trapped by the magnetic and electric fields so that they cannot escape from the region adjacent to the surface target except by diffusion. Consequently, the electrons emitted from the target have to travel a very long path, compared to the short path length from target to substrate that these electrons have normally in a conventional sputtering system. The advantage of a such operating system is that each electron emitted from the target has a very high probability of causing ionization of the gas and therefore a high density plasma is obtained. The presence of a magnetic field at the target effectively confines the energetic charged species emitted from the target, thus preventing their bombardment of the substrate on which the films are being deposited. The low sputtering voltage, characteristic of this process yields

lower energy of the bombarding particles, which in turn, leads to minimal damage of the substrate and hence better quality films.

3.1.3 R.F. System

The R.F. sputtering unit commercially available from NORDIKO Ltd., is shown in Figure (3.1). All samples investigated throughout this work were produced using this system. The R.F. signal is provided by a stable crystal oscillator circuit whose resonant frequency is doubled to produce a 13.56 MHz waveform which is then amplified to give a maximum power output of 1.25 KW. Illustrated in Figure (3.2) is the equivalent circuit of the remainder of the system supplied by the generator. The circuit consists of the filter circuit which removes unwanted harmonics, an impedance matching unit and the load corresponding to the various mechanisms involved in this process. The matching unit is composed of a variable inductor which forms one side of a transformer whose mutual coupling can be varied. The elements beyond this component represent schematically the generated discharge, a blocking capacitor and stray earth capacitances all of which can be simplified to an LC combination. The matching unit, has two functions. First, it serves to tune the load impedance seen by the generator to have a resonant frequency of 13.56 MHz. Second, it ensures that the output impedance of the power supply is a purely resistive 50Ω so that no R.F. power output is reflected back to the generator. Due to the low impedance of the plasma in this R.F. magnetron system, the blocking capacitor mentioned previously consists of four

100 pF capacitors in series (i.e $C_B = 25\text{pF}$). As discussed in an earlier section, the insertion of a blocking capacitor is not essential if insulators are being sputtered, since in this geometry any form of target material can be sputtered without significant change in the R.F. circuit.

The magnetron source, routinely used during course of this project, was silicon (99.999% pure) bonded to a copper backing plate which was then screwed firmly to the electrode. The electrode was the NE400 (4 inch diameter) and a direct replacement for the conventional electrode. A grounded shield covered the periphery region of the target to prevent any contamination from the backing plate edges. It was always adjusted to be between 1 and 2 mm clear of the target surface. Cooling water was supplied to the electrode at adequate inlet pressure and the outlet led to an adjacent free drain at atmospheric pressure. The presence of three separate positions in the system made it possible to sputter in situ three different materials on any sample. To improve thickness uniformity, the substrate electrode was placed vertically above the target electrode ~ 6 cm apart. The substrate electrode could be held stable either at room temperature (or slightly below) through water cooling or at higher temperature up to a maximum of 650°C through resistive heating of a coil clamped to the back of the substrate electrode. All the components in the vacuum system were earthed including the substrate electrode, with the exception of the target electrode.

A vacuum better than 10^{-7} torr is routinely achieved in the chamber by means of an Edwards 160/700 M water cooled diffusion pump, with water cooled baffle backed by an Edwards EDM20 two stages rotary pump. The pressure is monitored

using a Penning gauge mounted in the discharge chamber. The vacuum can be further improved using liquid nitrogen trapping through a Meissner coil incorporated into the chamber. This is a common practice which condenses high pressure vapours such as water vapour from both the base vacuum during pump down and sputtering. The coil is mounted round the substrate electrode in order to remove contaminants which might be incorporated during deposition.

Prior to material deposition, the target is always presputtered for sufficient time (typically 30 min.). This is used to prevent the deposition of foreign species on the substrate while sputtering the target. Presputtering is necessary to remove oxygen from the damaged surface layer. Occasionally mechanical polishing of the target is also necessary. The procedure consists of placing a metal shutter in the plasma region between the two electrodes. The shutter is incorporated into the chamber and externally controlled.

A set of well defined copper masks firmly attached to a grounded and externally controlled plate can be moved into position close to the substrate and aligned in order to achieve the successive sequences for the forming of thin film sample.

3.2 The gas mixture

Figure (3.3) shows the gas supply arrangement of the system. As discussed earlier, an inert gas is needed to initiate the plasma. For this purpose, argon gas (99.999% pure) is chosen and supplied from a cylinder. For reactive sputtering, the active gas is hydrogen (99.995% pure) also supplied from a cylinder. For the forming of a hydrogenated amorphous silicon film, argon and hydrogen are pre-mixed in a tank to the desired pressure ratio. A mercury column

manometer is used to monitor the gas pressure (50-500 torr) at this point. Prior to mixing the gas, the lines and the tank are always evacuated by a rotary pump. For this, the pressure is monitored by a Pirani gauge inserted in the lines. The flow of sputtering gas into the chamber is controlled using a needle valve, and its value can be monitored by a gas flowmeter (GEC-Marconi Series 1100) incorporated to the line. However, since this is only directly calibrated for nitrogen, accurate values are only available by monitoring the change in tank pressure with time. Typically, flows are approximately $0.1 \text{ torr litre s}^{-1}$.

Before allowing the sputtering gas into the chamber, the throttle plate, externally controlled, is moved to partially close the pumping part in the chamber. This is a precautionary measure, always taken to prevent the danger of the diffusion pump stalling at high gas pressure. The chamber pressure is monitored by a micromanometer Furness Controls Ltd, ^{type} pressures ranging from 5-15mtorr were used in our experiments.

To check the atmosphere inside the chamber, an ANAVAC.2 quadruple mass spectrometer unit is available. It is placed just below the throttle plate, above the throat of the diffusion pump. The instrument is set up to analyse the constituents of the base vacuum in the chamber. It is a low resolution quadruple mass spectrometer capable of separating the ions formed by bombardment of the gases with electrons. Thus it enables to detect the presence of impurities. A typical mass spectrum is shown in Figure (3.4). With liquid nitrogen in the Meissner coil, the partial pressure of water vapour measured is reduced significantly, to the approximate

level of the other background gases. The major species detected in the background are hydrocarbons carbon monoxide and water vapour.

3.3 Thermal evaporation

A thermal evaporation source is mounted on a metal plate which is externally controlled such that the source can be moved away from the plasma region during sputtering or positioned, at will, below the substrate. This is an additional facility which allows thermally evaporated metal contacts to be deposited on the sample without exposure to atmosphere.

3.4 The insert

It is the aim of this work to investigate the electrical properties of a-Si:H. These are found to be very temperature dependent. Thus, a primary concern is to ensure adequate control over the sample temperature and to vary this parameter over a wide range of values from liquid nitrogen temperature up to 450 K. Moreover, to satisfy the experimental conditions required the sample temperature should be kept very stable for long periods, in order to probe the electrical behaviour of the sample satisfactorily. Since the material under investigation (a-Si:H) is a highly resistive material, thus any electrical connections made to the sample must have as near infinite ($>10^{13}\Omega$) leakage resistances as possible, both to earth and each other. This is essential in order to study properly the electrical behaviour of the material. It is also advantageous to carry out measurements in a clean environment which is, at least, evacuated by a rotary pump. This reduces possible effects associated with gas absorption

onto exposed sample surfaces, and also helps to extend sample life and the stability of its behaviour by stopping oxygen or nitrogen diffusion into the matrix.

The insert used in our experiments was designed to satisfy all these conditions. As shown schematically in Figure (3.5), it was composed of an outer stainless steel sleeve sealed at the bottom and an inner thin copper-nickel tube. To the bottom end of this tube was attached the sample holder and the top end was terminated by a brass plate which mated with a flange on the outer sleeve, forming a vacuum seal with the use of an 'O' ring. The system was evacuated through a copper tube piercing the brass plate. The sample was mounted on the sample holder which consisted of a copper block on which electrical connections were made by means of a set of pins fixed on a nylon block screwed into the sample holder. From these pins, short wires were used to make contacts to the sample. Copper wires were connected to the other ends of the pins and led through the brass plate by means of feedthrough. The connections were kept separate such that the inter-lead leakage resistances were greater than $10^{14}\Omega$. The temperature was monitored by a resistance thermometer. It consisted of a copper coil of resistance about 30Ω wound on a copper bobbin which had been previously calibrated at the temperature of melting ice and boiling liquid nitrogen. The thermometer was designed to measure the resistance of the coil and maintain it at a pre-set value by regulating the power fed to the heater. The latter consisted of Eureka wire wound around the copper block. The temperature could be raised up to 450 K or lowered by immersing the stainless steel tube in a bath of liquid nitrogen. A commercial Oxford

Instruments temperature controller (DTC2) was used to achieve temperature stability at any selected value between 77 K and 450 K. The unit balances heat input supplied through the heater with losses to the outside environment. Temperature stability of better than ± 0.1 K over eight hours was achieved. The electrical connections for this control system were also led up the inner tube of the insert to the brass plate through a single feedthrough sealed with epoxy cement.

It is worth mentioning that all measurements in this work were carried out in darkness in order to avoid photoconductive effects.

3.5 Sample geometry

3.5.1 Schottky barrier structure

Each sample was deposited on two glass slides. One slide was used for Schottky diode measurement and the other one for optical and thickness measurement. Figure (3.6) illustrates the film deposition order for the electrical sample. First a layer of molybdenum was sputtered in pure argon, to form the bottom contact, then a thin layer of unhydrogenated amorphous silicon ($250\text{-}500\text{\AA}$) was deposited to provide ohmic contact. This was followed by the layer of hydrogenated amorphous silicon (a-Si:H) to be investigated. The top contact was made by thermally evaporated Al. As mentioned previously, thermal evaporation could be made in situ. However, experience showed that exposure to air prior to metallization led to better rectifying behaviour for the Schottky diode. We ascribe this to oxidation of the damaged surface layer of the film.

The D.C. conductivities of the samples were measured

using two different electrode arrangements. A sandwich structure was used for transversal measurement through the film and a planar gap cell for measuring along the film. This method helped to determine the existence of layers in the film having different conductivity which may arise due to contamination.

For these samples the deposition temperature was held at around 250°C in all cases.

3.5.2 S.C.L.C. structure

As discussed in Chapter 2 this technique was developed to characterize bulk properties of a-Si:H material.

The procedure consisted of preparing a number of samples grown under the same conditions. In this, a total number of 4 samples were produced in a single run, the deposition parameters of which were kept unchanged while sample thicknesses were varied. To satisfy this requirement, a set of 5 masks was chosen to achieve the different sequences for the forming of samples. These are shown in Figure (3.7).

In this structure, the central region, nominally hydrogenated amorphous silicon is sandwiched between thin highly injecting layers, 250-500Å^o thick. The amount of atomic hydrogen needed to passivate the dangling bonds was provided by a freshly made gas mixture (argon/hydrogen ratio) discussed previously. The injecting layers were unhydrogenated amorphous silicon (a-Si) sputtered in pure argon. Both the top and the bottom electrodes were made of Chromium (Cr), also sputtered in pure argon. Before each deposition the target was pre-sputtered for a sufficient time to clean target surfaces. All samples examined by this technique had a symmetric configuration and were deposited with no intermediate exposure

to air. As for Schottky diode experiments we have produced different types of samples during which the total pressure was varied. In this, we used the following figures i.e., 7.5 μm (5 μm for argon + 2.5 μm for hydrogen) and 15 μm (10 μm for argon + 5 μm for hydrogen). The deposition temperature in all cases was held constant at around 250°C.

3.5.3 The measuring circuit

The measuring circuit used for both Schottky diode and S.C.L.C. experiments was the same and it is illustrated in Figure (3.8). In this, both D.C and A.C measurements can be carried out by choosing the appropriate connections. The circuit elements were contained in the same box, but both A.C and D.C signals were kept separate using a suitable switching system.

For D.C measurement, a voltage of either sign was allowed such that the D.C conductivity of the sample could be measured in either direction. The D.C voltage applied to the sample was monitored by a Keithley 179 TRMS digital multimeter and the collected D.C current was measured using a Keithley 616 electrometer.

For A.C measurement, the superposition of a D.C voltage on the A.C signal was made possible by inserting a series combination of 1 μF capacitor with a $10^7\Omega$ resistor which isolated the oscillator from the D.C signal and hence minimized transient effects when the D.C level was changed. Similarly, a $10^6\Omega$ resistor helped to prevent A.C voltage from reaching the D.C supply. The Keithley 179 used to monitor the superposed D.C voltage is always removed when the A.C response of the sample is being measured.

The accuracy of the capacitance measurement was better than 2% in the frequency range from 1Hz to 1KHz. However, large systematic errors were found in conductance data at high frequencies. This effect could lead to errors of an order of magnitude in conductance, though the capacitance error was less than 5%. Due to this effect and other error sources, the highest frequency measured during this experiment was 10KHz.

In the case of A.C measurements the frequency dependence of both the capacitance and conductance of the diode was probed. In this, the modulation in current, due to changes in sample admittance was detected by monitoring the voltage drop across the fixed resistor R of value $10^5 \Omega$. This non-inductive resistor was symmetrically inserted onto the A and B terminals of the lock-in amplifier to ensure its impedance was purely resistive. The lock-in amplifier used to monitor the voltage drop was a Brookdeal 9503.SC operating in the frequency range extending from the low frequency limit of 0.20Hz to the high frequency limit of 200KHz. The A.C signal source was a Levell TG 200 DM oscillator. The voltage applied to the sample was kept at (7.50 ± 0.05) mV r.m.s. to ensure the barrier perturbation was small and constant. The applied voltage was monitored using Channel A on the lock-in amplifier where the voltage between point A and earth is displayed. In the (A-B) mode, the in-phase and out of phase (quadrature) components of the voltage dropping on the resistor R could be measured then analysed to give the sample conductance and capacitance. These are described respectively by the following expressions:

$$G = \frac{1}{R} \left(\frac{V_{A-B}}{V_A} \right) \text{ in phase} \quad (3.1 \text{ a})$$

$$C = \frac{1}{\omega R} \left(\frac{V_{A-B}}{V_A} \right) \text{ quadrature} \quad (3.1 \text{ b})$$

However, owing to external contributions from the measuring circuit, both quantities required further analysis. The capacitance was corrected to remove the effect of the stray capacitance to earth of the co-axial cable between A and the sample itself. For the conductance signal, the correction consisted of removing the finite shorting conductance to earth of the A input of the lock-in amplifier.

A Racal 9835 Universal counter was used to check measurement frequencies. These were adjusted to achieve accuracy better than 0.1%.

3.6 Thickness Measurements

As shown in Chapter 6, the sample thickness is a very important parameter, therefore it must be determined as accurately as possible. For this reason we have adopted three different methods of thickness measurement.

3.6.1 Varian \AA Scope

This method is currently used in the laboratory. It involves the Tolansky Technique.

In ideal conditions, film thicknesses in the range 30-20,000 \AA could be measured using the instrument to a specified resolution of 30 \AA . However, experience showed that for sputtered films, the accuracy was not satisfactory, because of the difficulty in obtaining the sharp film edge

needed for this type of measurement. The values obtained tended to present the lower limit of the actual thickness at the centre of the film, due to spatial variations crossing from film edge to film edge. The errors involved can be as high as 15%.

3.6.2 Thickness measurement using optical response.

Another alternative is to measure the exact optical response of the sample in the area needed. The arrangement used is illustrated in Figure (3.9) and discussed in detail in the next section. The method consists of measuring the transmittance and the reflectance of the sample as a function of the wave-length of a light beam from a source. The fringes obtained are analysed in terms of minimum and maximum response indexed respectively n and $(n+\frac{1}{2})$. These are plotted on the vertical axis against $\frac{1}{\lambda}$ (where λ is the wave-length). The plot is linear with the gradient directly related to the sample thickness by the following relation:

$$d = \frac{1}{2x\eta \cdot \text{gradient}} \quad (3.2)$$

where η is the reflective index of the material.

To confirm the results obtained by this method, we carried out thickness measurement on a Talystep surface profiler in the Electrical Engineering Department of Glasgow University.

3.6.3 Mechanical method

For this method we used the Talystep which is a stylus instrument designed specifically for accurate measurement of thin film deposits. It measures the thickness by traversing the stylus either across a test groove formed in the deposit, or over the edge of the film. Vertical movement of the

stylus is amplified electronically and recorded as a graphical representation of the differences in the level between the surfaces of the substrate and the deposit. The measuring unit was a standard conical $12.5\mu\text{m}$ radius for step height measurement.

In general, the agreement between the optical method and mechanical method performed on the same sample is good. Typical errors are less than 10%.

3.7 Other Measurements

3.7.1 Electron Microscopy Analysis

It is well established that a-Si:H prepared by R.F. sputtering techniques in an argon atmosphere contains significant concentrations of embedded argon. So far most of the work has been performed on material sputtered by the conventional method (CRAVEN et al (95)). In this context, a similar method was undertaken to investigate some aspects of the structural behaviour of a-Si:H produced by R.F. magnetron sputtering technique . In this experiment, the samples consisted of KCl substrates coated with a-Si:H films which were lowered into a dish of freshly distilled water so that small sections of thin film were released and floated on the surface. These fragments were then floated onto G200 Copper or Titanium microscope grids and left to dry. The grids were then introduced into an electron microscope to be examined. This analysis was used to determine the concentration of included gas in the matrix and to reveal some other structural aspects of the material. Similarly, the use of small angle scattering technique (S.A.S) helped to investigate film homogeneity by looking at small angle scattering in the diffraction pattern.

We acknowledge the help of our colleague N. Hadji for carrying out this analysis.

3.7.2 Infra-red Absorption

Infra-red measurement was undertaken at Heriot-Watt University using a Perkin Elmer Spectrometer. For this examination, the samples were prepared by the R.F. magnetron sputtering technique. As for other measurements, two types of samples were investigated. These consisted of a-Si:H material deposited on polished silicon wafers to a thickness greater than $1 \mu\text{m}$ with the total pressure of $7.5 \mu\text{m}$ ($5 \mu\text{m}$ for argon + $2.5 \mu\text{m}$ for hydrogen) and $15 \mu\text{m}$ ($10 \mu\text{m}$ for argon + $5 \mu\text{m}$ for hydrogen). The measurements were carried out using a clean silicon wafer as a reference in order to remove substrate effects.

3.7.3 Optical Measurement

As discussed previously, in order to get a better insight into the material, various measurements were undertaken, the results of which were correlated to provide the amount of information needed to compare the properties of our material with those of material reported in literature.

In this spirit, optical absorption measurements were performed to determine the optical band gap of the sputtered material, and to check for the possible presence of oxygen contamination in the films. The band theory states that the valence band and the conduction band are separated by a forbidden band, i.e. the band gap. A photon of energy greater than the energy gap can excite an electron from the valence to the conduction band. Such photons are strongly absorbed by the sample. However, photons of energy less than the band gap cannot produce transitions and are not absorbed. Hence the

absorption measurement of light as a function of photon energy can be used to determine the band gap.

According to the theory, the optical absorption α is equal to $\frac{4\pi K_2}{\lambda}$ and the complex refractive index (of the semiconductor) $N_1 = K_1 - iK_2$. All external optical parameters are influenced by both K_1 and K_2 , including the reflectivity R_e and the transmittivity Tr . An exact analysis of the optical properties may be made, but the resultant expressions for R_e and Tr are extremely complicated even for normal incidence. As a first approximation to the exact expressions, the phase coherence across the absorbing film can be neglected so that the expressions for R_e and Tr can be simplified. The simplifications can be extended further if the "thick limit" approximation is considered where $\alpha d \gg 1$ (α being the optical absorption coefficient $\alpha = \frac{4\pi K_2}{\lambda}$, d being the thickness of the a-Si:H film and λ the wave-length). The equations for transmittance Tr and reflectance R_e that are measured become:

$$Tr = \frac{(1-R_1)(1-R_3)\exp(-\alpha d)}{(1-R_2R_3)} \quad (3.3 a)$$

$$R_e = R_1 \quad (3.3 b)$$

where R_1, R_2, R_3 are reflectances from various interfaces

Thus

$$R_1 = \frac{(K_1-1)^2 + K_2^2}{(K_1+1)^2 + K_2^2} \quad \text{air/silicon} \quad (3.3 c)$$

$$R_2 = \frac{(K_1-N_2)^2 + K_2^2}{(K_1+N_2)^2 + K_2^2} \quad \text{silicon/substrate} \quad (3.3 d)$$

$$R_3 = \frac{(N_2-1)^2}{(N_2+1)^2} \quad \text{substrate/air} \quad (3.3 e)$$

where N_2 is the substrate (corning 7059 glass) refractive index.

N_2 was estimated from transmittance versus wave-length measurements on a plain slide and was found to be 1.51 ± 0.01

The thick limit is much the simplest in which to analyse data and a computer program was available to obtain K_1 and K_2 from the measured R_e and T_r data using the above equations. As mentioned above, it is possible to calculate the band gap of the amorphous material by assuming a parabolic form of conduction and valence bands separated by an energy gap E_g .

In this case the following relation is derived i.e.

$$(\kappa\omega)^2 \epsilon_2 = A(\kappa\omega - E_g)^2 \quad (3.4)$$

where $\epsilon_2 = 2K_1K_2$ is the imaginary component of the dielectric constant.

The relation above is often expressed as

$$\alpha\kappa\omega = B(\kappa\omega - E_g)^2 \quad (3.5)$$

where A and B are constants but the form (3.4) is more accurate.

3.7.3.1 Experimental Arrangement

A sketch of the arrangement used for this experiment is shown in Figure (3.9). In this, the sample was mounted on an accurately machined carriage, enabling the sample to be moved, reproducibly, in and out of the light beam. The light source was a quartz-halogen bulb which was chopped at 110 Hz and passed through a precision prism monochromater (Hilger & Watts D285); which selected the measuring wavelength. Input and output slit widths and aperture size on the

monochromator were chosen to optimize resolution. Light from the exit slit of the monochromator was then focussed onto the sample. The optical detector was a photomultiplier tube. For transmittance measurement, the latter was positioned behind the sample and the light intensity passing through the sample was compared with the light intensity passing when the sample was removed. The transmittance T_r was given by the ratio of these two quantities $T_r = \frac{I_t}{I_o}$. For reflectance measurement the photomultiplier was moved to an other position such that the reflected beam could be detected. In this experiment, the light intensity reflected from the sample I_R was compared with the light intensity reflected from a neighbouring region of the substrate on which aluminium was deposited. The reflectance of amorphous silicon was then deduced from the known reflectance of aluminium using the relationship $R_c = \frac{I_R}{I_{Al}} \cdot R_{Al}$. The photomultiplier output was measured using a lock-in amplifier (Brookdeal 9501) referenced from the optical chopper.

3.7.4 Hydrogen Evolution Apparatus

The general arrangement of the apparatus built for this measurement is shown in Figure (3.10). It was composed of a roughing line, the chamber and the ion pump. To make the ion pump start, evacuation of the system down to pressure lower than 10^{-4} torr was required. For this purpose, a sorption pump was used the body of which was immersed in a dewar of liquid nitrogen and chilled for sufficient time before operation. A Pirani gauge was inserted in the line to monitor the pressure of the system. After each pumping cycle the sorbed gases were expelled to atmosphere through a

vent valve incorporated in the system. The ion pump line was separated from the chamber by an ultra high vacuum valve and a control unit was available to measure the ion pump pressure. Pressures in the range 10^{-8} - 10^{-9} torr were routinely achieved after 24 hours of pumping. To remove the unwanted gases, the system was baked for several hours up to 200°C while maintaining the sample temperature just above room temperature by means of a cooling system.

3.7.4.1. The Insert.

The insert consisted of a cylindrical block of copper sealed to a thin walled tube of stainless steel designed to allow heat transfer to the sample from a heater inserted into the tube and fixed at the rear of the sample holder making a satisfactory thermal contact.

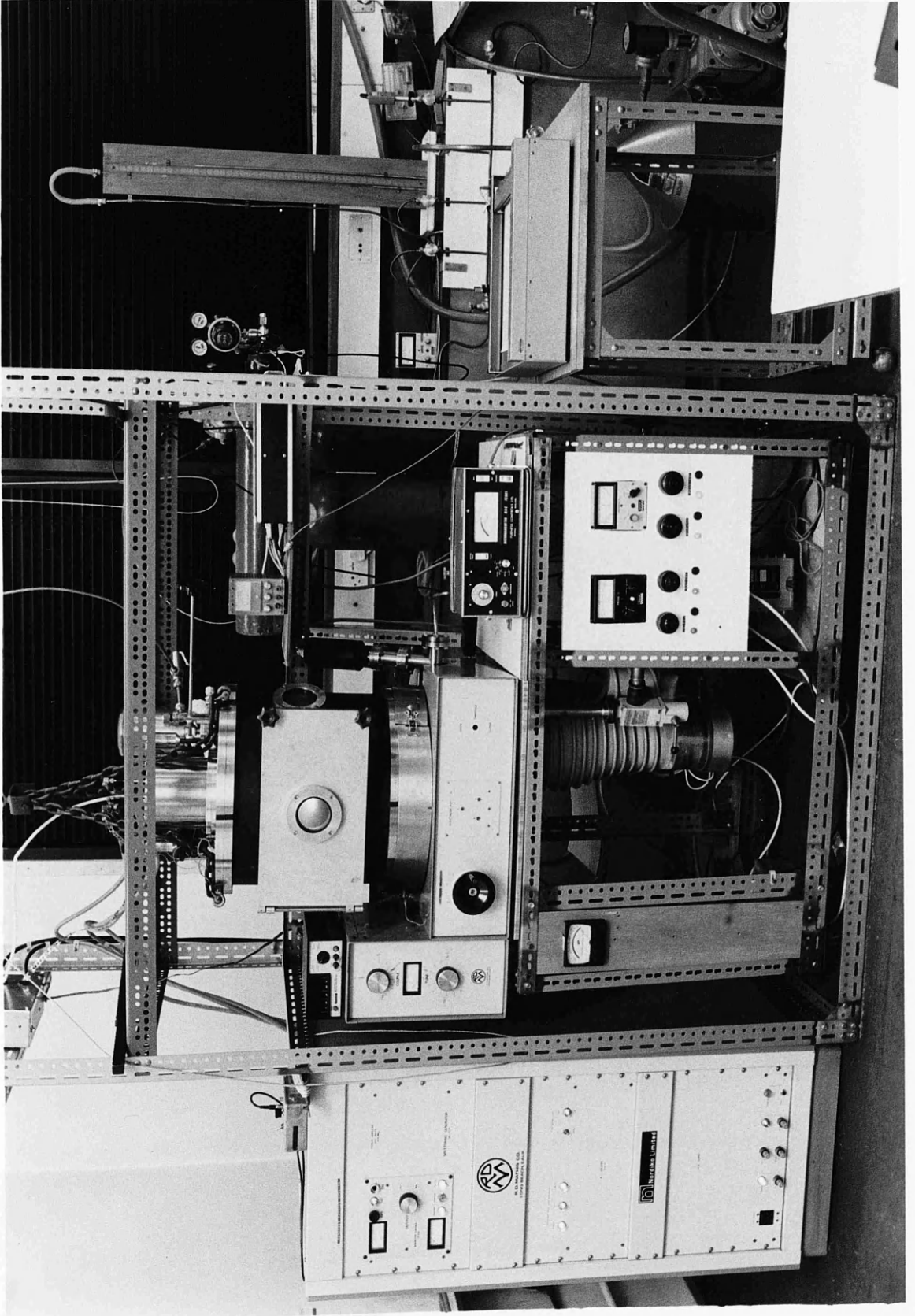
The temperature was monitored by means of a thermocouple. The latter was composed of two wires incorporated to the insert through two sealed holes. The wires were isolated inside the insert by ceramic tubes to avoid shorting.

To prevent radiation effects, two separate shields were incorporated. The inner shield was made of thin copper foil fitted with small holes on the wall designed for outgassing. The outer shield consisted of a stainless steel cylinder fixed at the top of the insert. A linear motion drive unit was used to allow the evolved gases to build up in the chamber by placing an orifice of 2mm across the line to the ion pump.

The heater consisted of a nichrome wire of resistance about 5 ohms wound on boron nitride ceramic placed at the rear of the sample holder and connected to a D.C power supply

provided to give the current needed to raise the sample temperature up to 550°C.

The analyser was an ANAVAC 2 unit capable of measuring the pressure in the range 10^{-5} - 10^{-11} mbarr. It analyses the total pressure into partial pressure in the mass range 2-60 a.m.u. The detector was used continuously to trace the components present in the system, concentrating on the region around mass 2. Heating rates were adjusted to be around 4°C/min.



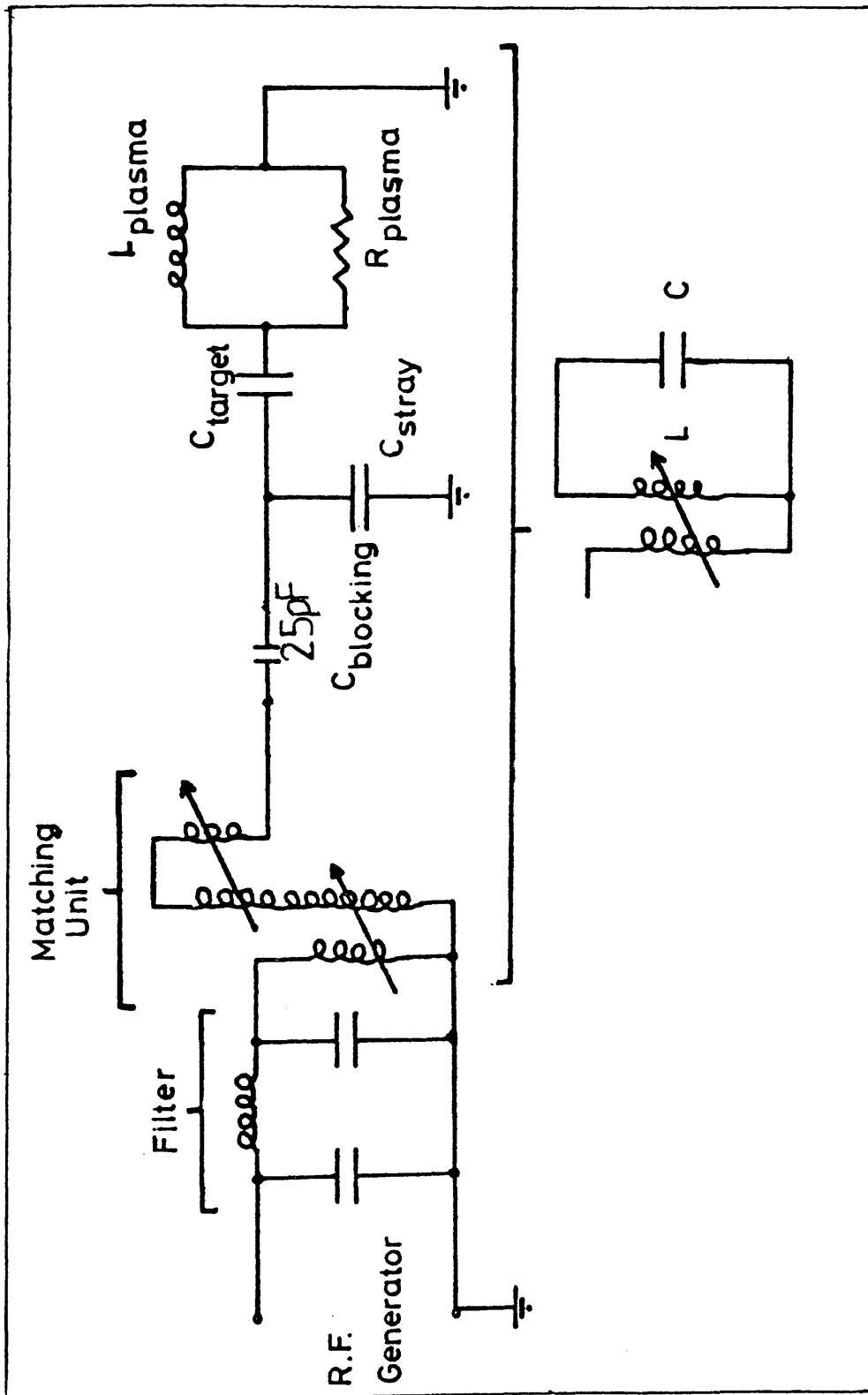


Figure 3.2 The equivalent circuit of the R.F. System

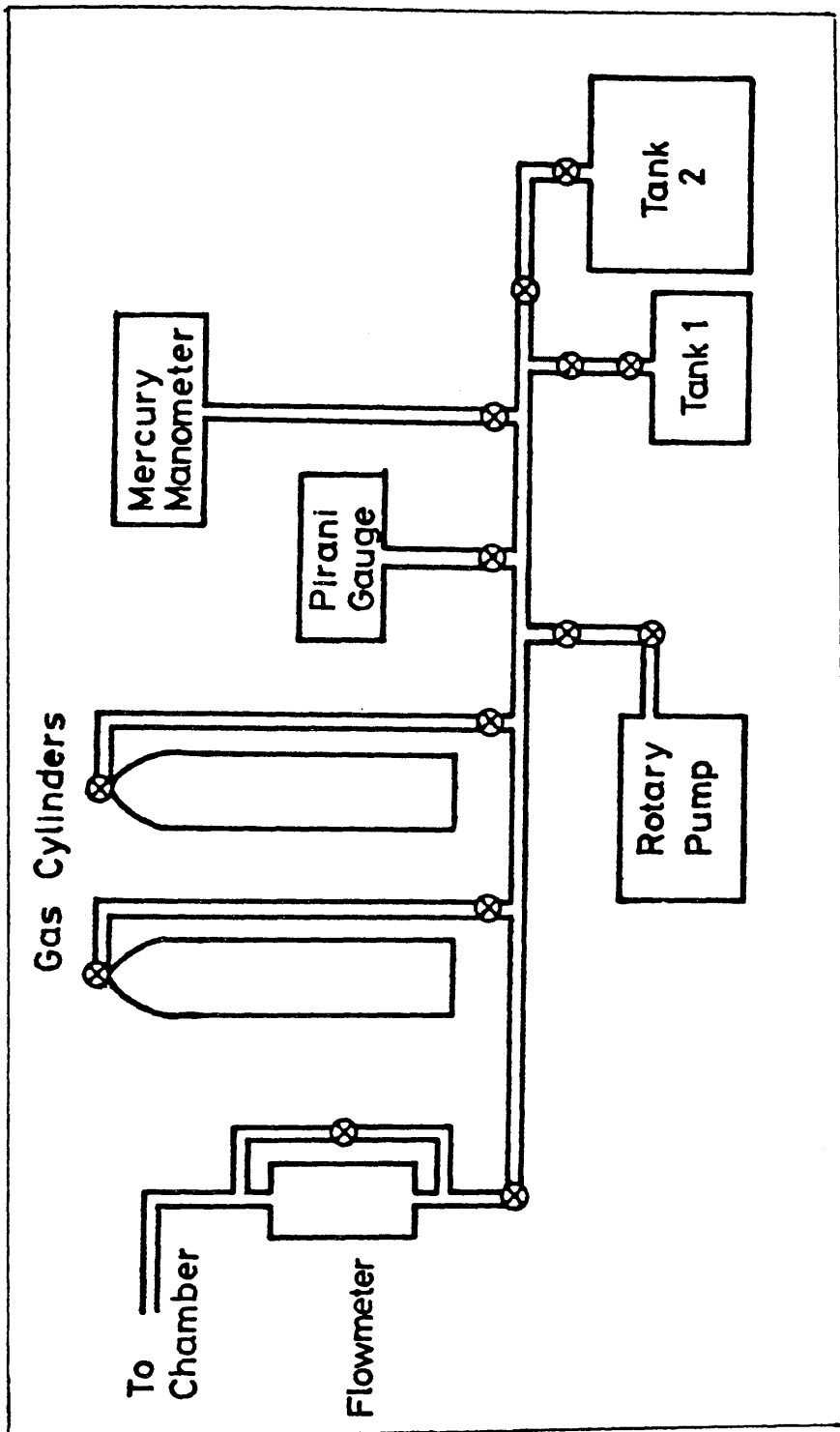


Figure 3.3 The gas supply arrangement of the system

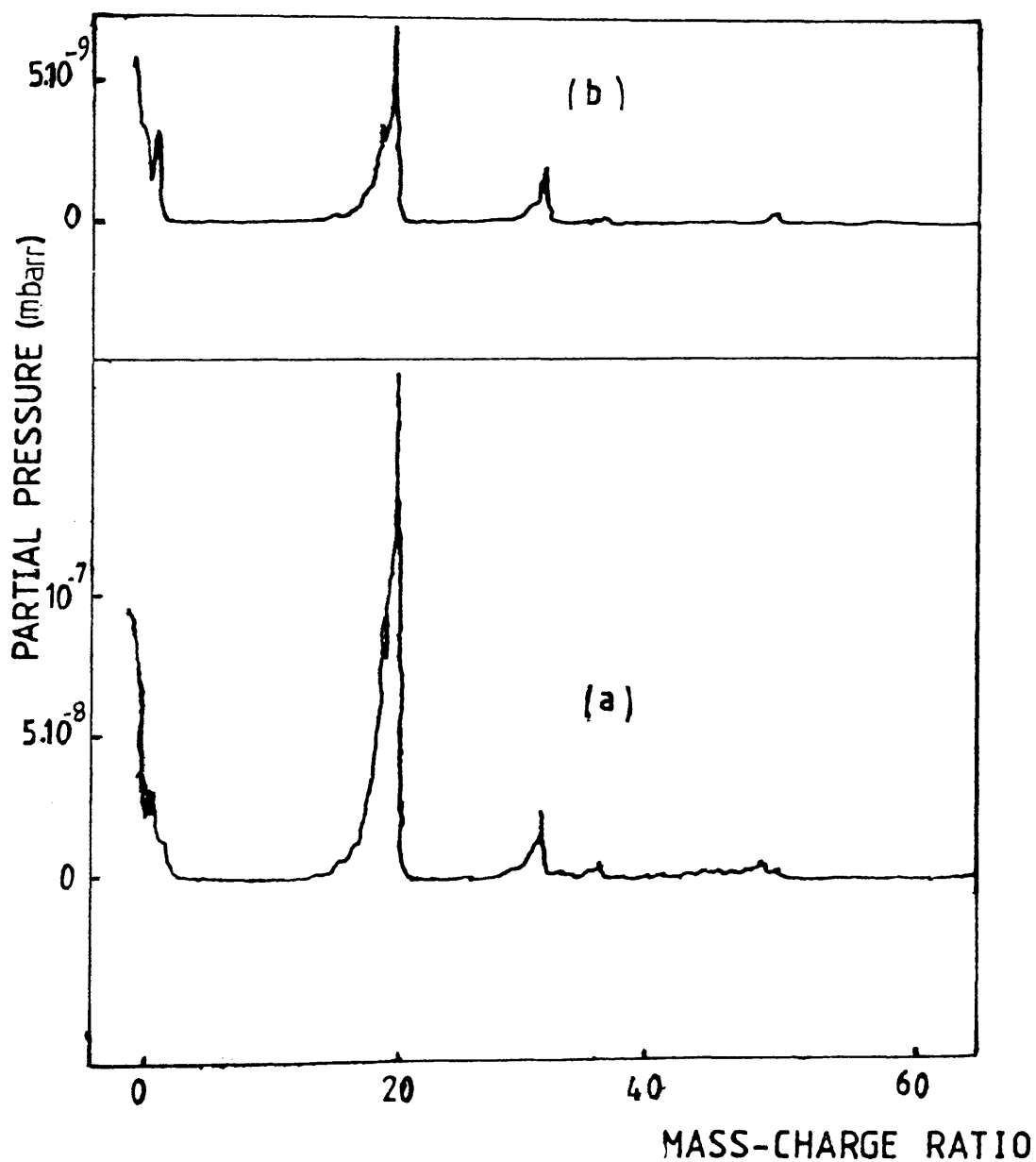


Figure 3.4 A typical mass spectrum of the chamber atmosphere

(a) without liquid nitrogen in the Meissner coil.

(b) with liquid nitrogen.

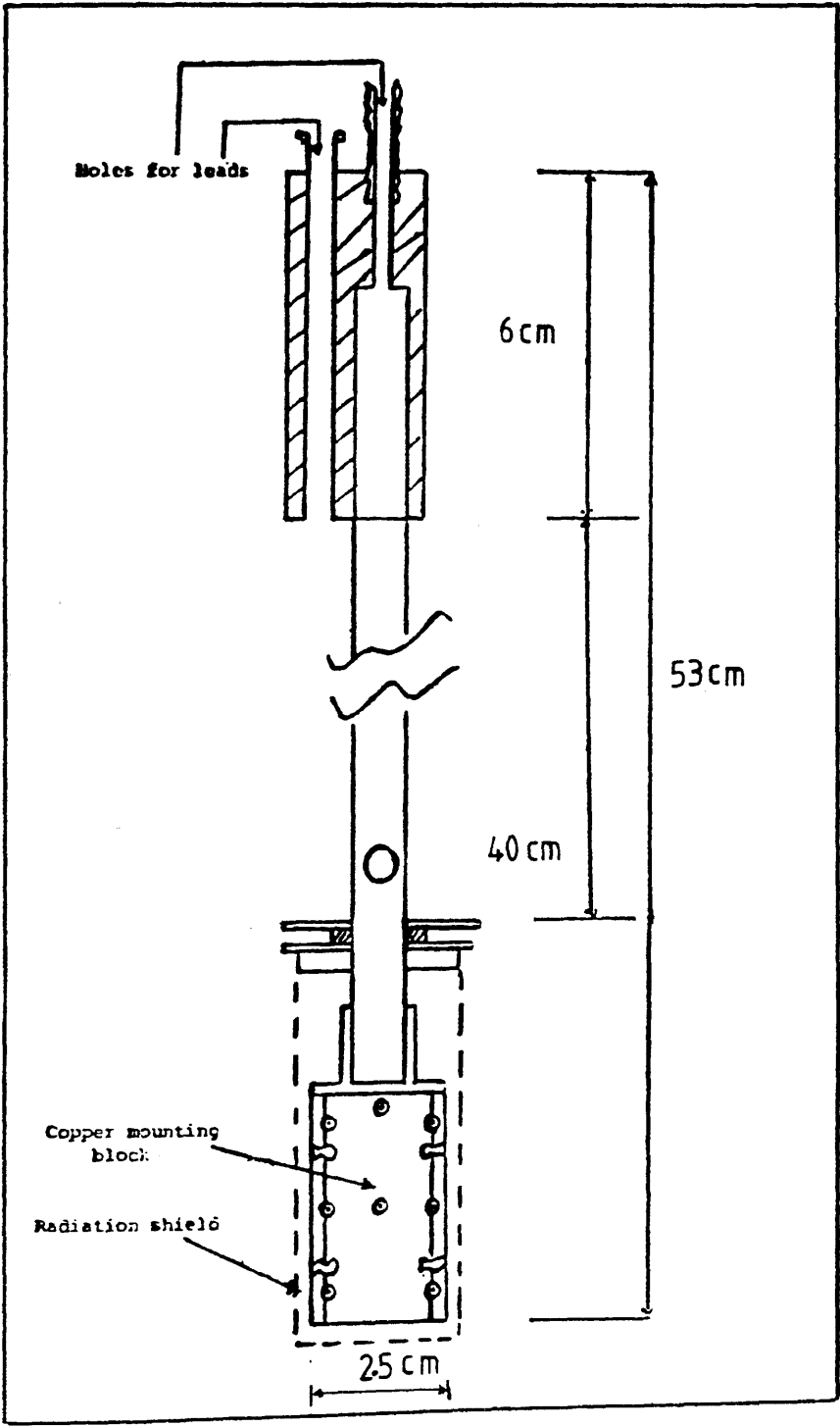
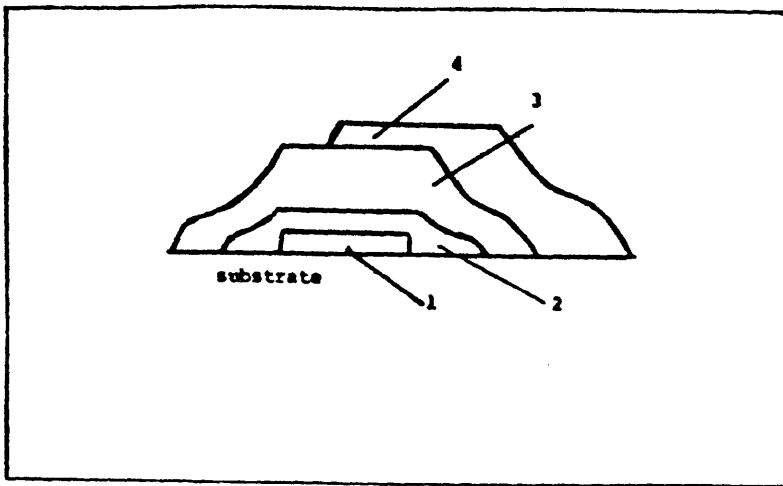


Figure 3.5

A schematic description of the insert used for electrical measurements. The sample is mounted on the copper block shown on the graph.



Schematic section through the sample

- (1) Molybdenum (thickness $\sim 200\text{\AA}$)
- (2) Unhydrogenated silicon (thickness $\sim 5.00\text{\AA}$)
- (3) Hydrogenated a-Si
- (4) Al top contact thickness $\sim 200\text{\AA}$

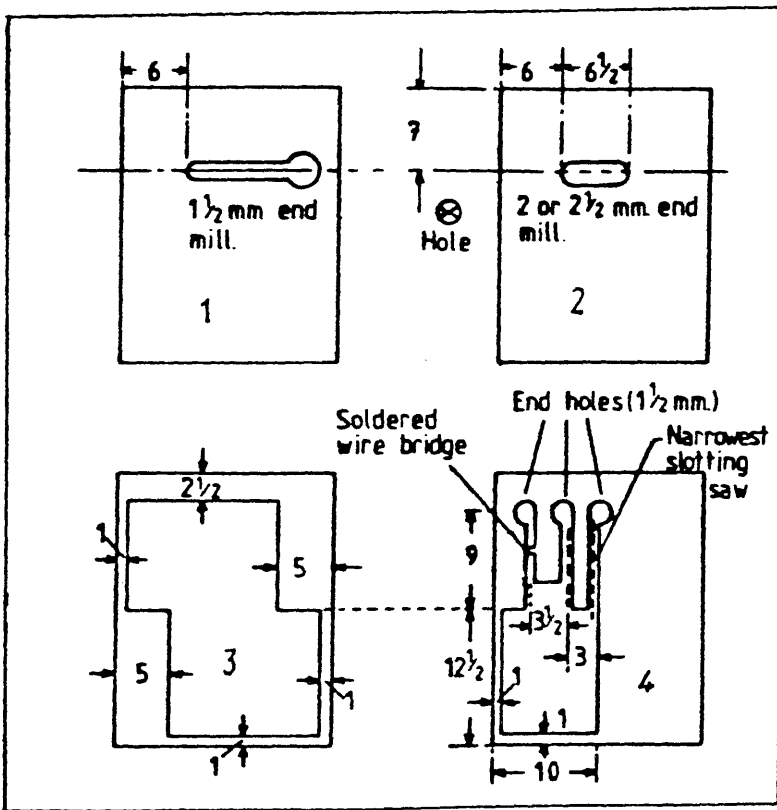
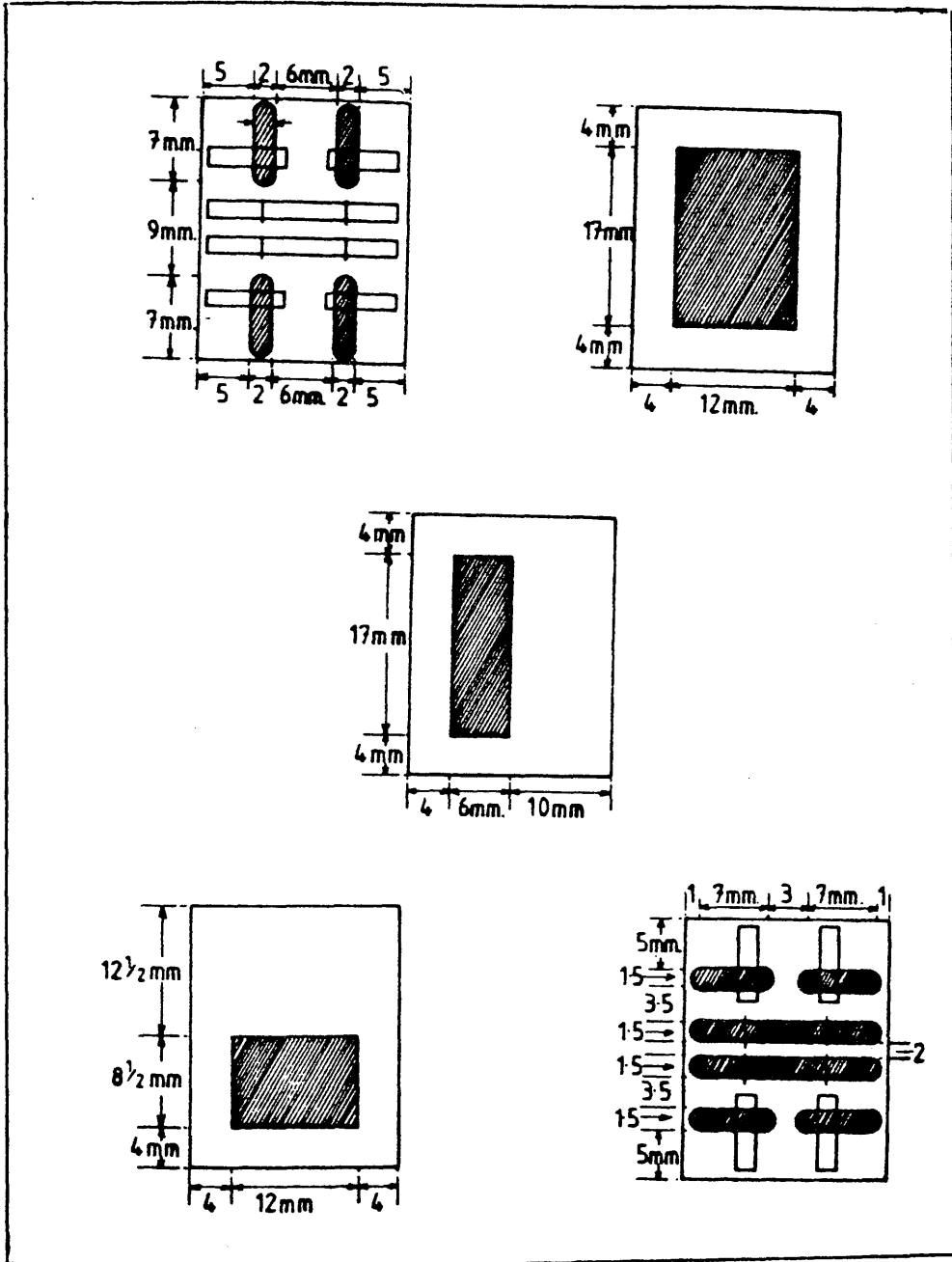


Figure 3.6

The Schottky barrier structure
 (a) schematic description of different layers of the film
 (b) the masks used for the forming of the sample. All dimensions in mm.

Figure 3.7 The masks used for SCLC samples.

All dimensions in mm.



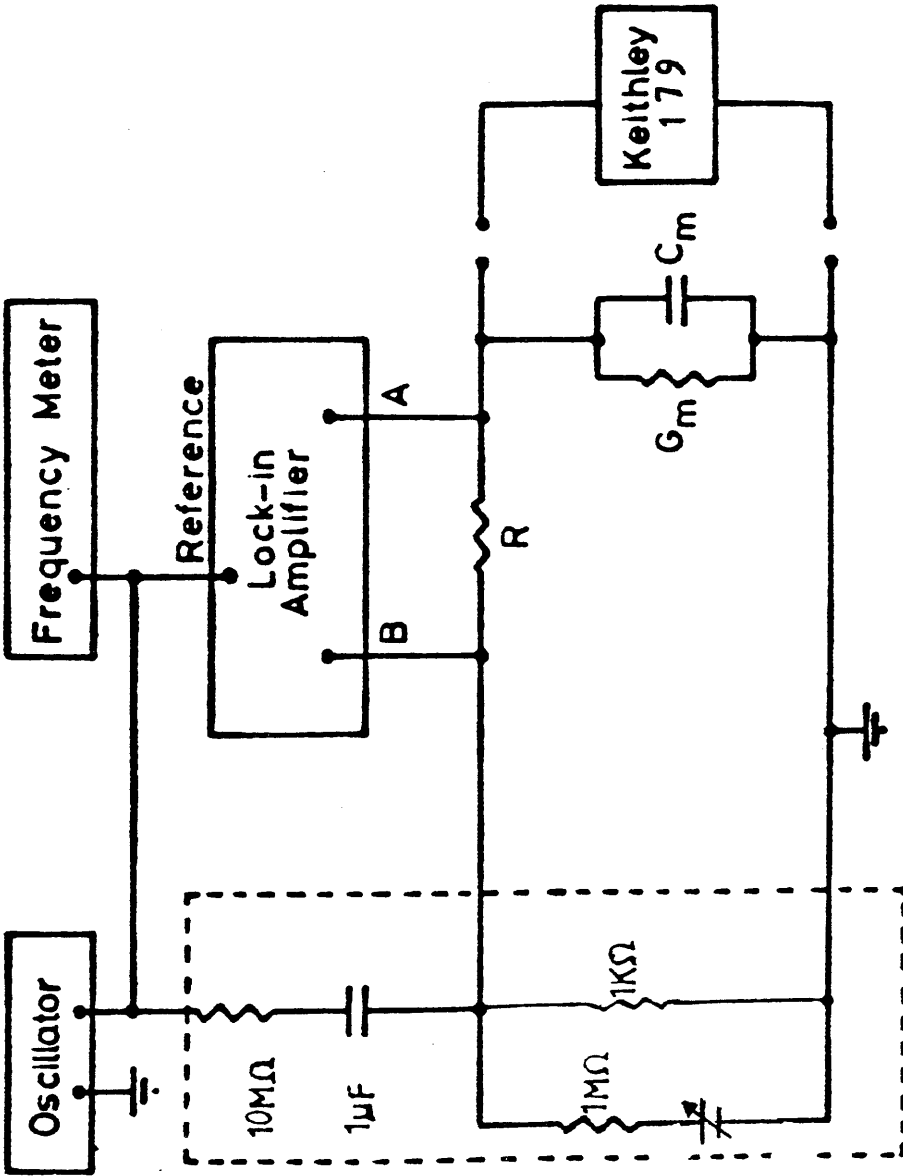


Figure 3.8 The a.c. circuit used for Schottky barriers measurements

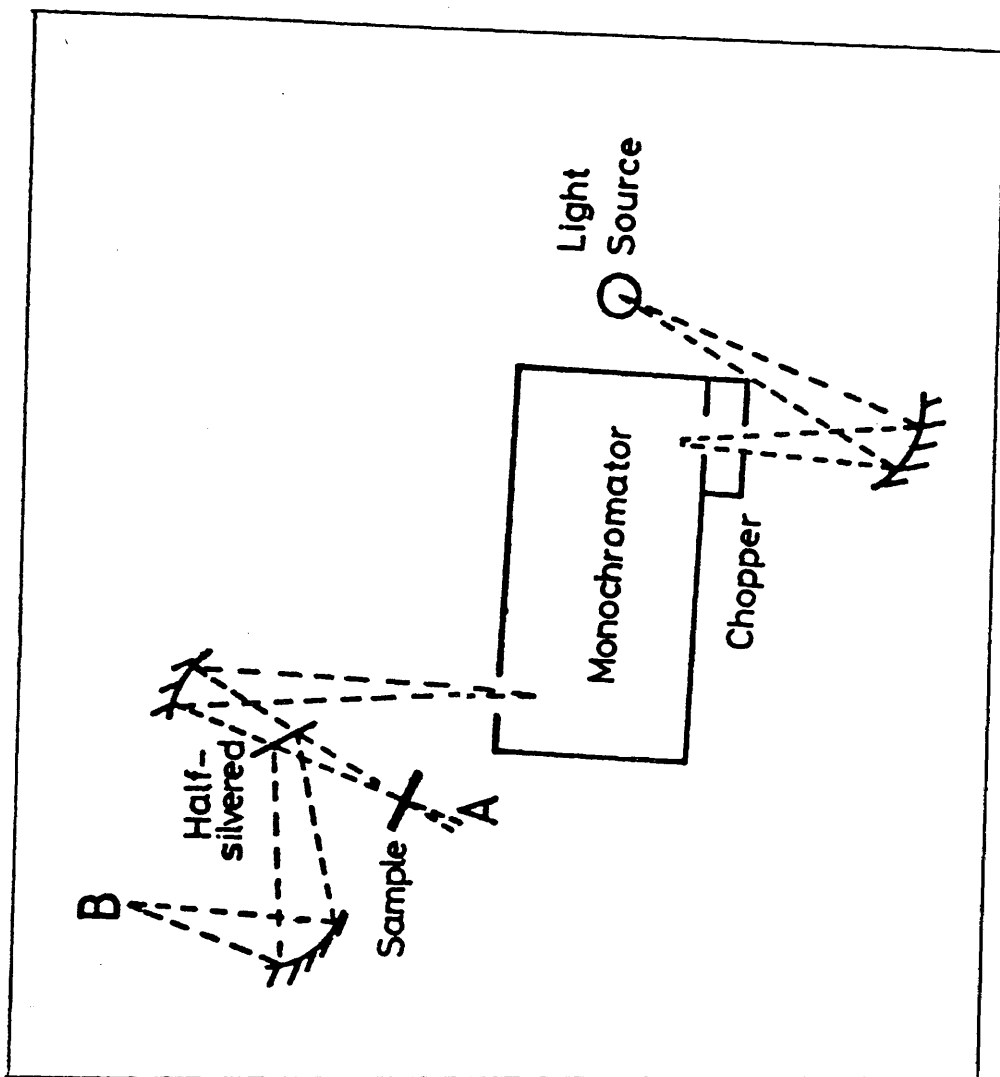
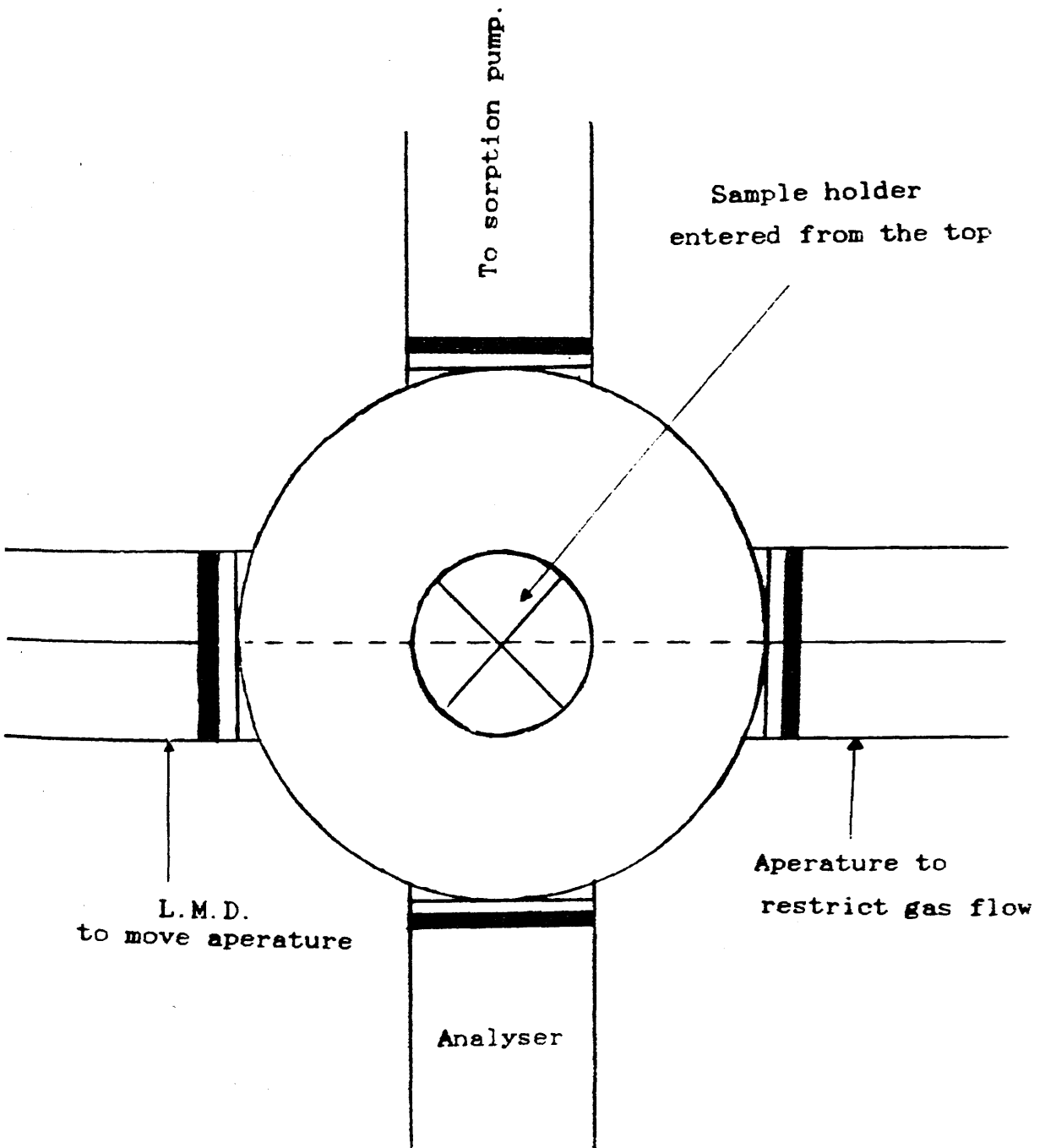


Figure 3.9

Optical arrangement used to measure the optical response of the samples.

Figure 3.10

Schematic arrangement of the hydrogen evolution apparatus. The six ports of the system are located along three mutually perpendicular axes



Tube for heater



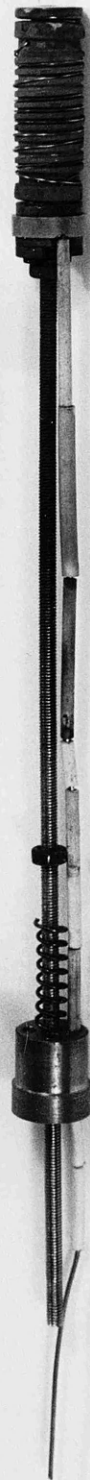
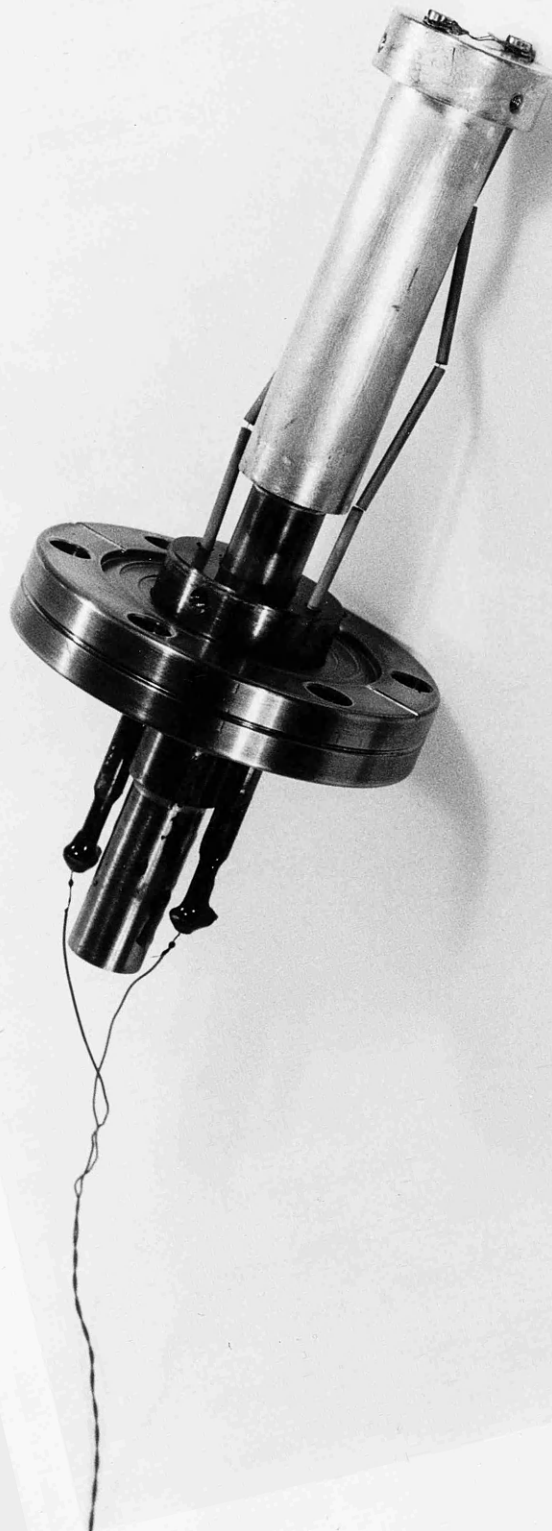
Vacuum Flange

Thermocouple Leads

Sample Mount

Heater

The insert used for H_2 Evolution
Experiment



CHAPTER 4.

FILM CHARACTERISATION.

4.1 General Description

Unlike glow discharge or to a lesser extent R.F. sputtered a-Si:H, the amount of information about R.F. magnetron sputtered a-Si:H is limited and no detailed picture of the material has been given other than that the technique is suitable for high rate deposition. Earlier results obtained by the Sheffield group (96) (97) (98) (99) were encouraging, particularly for multi-junction electronic devices such as a-Si MOS transistors and FETs. The incentive for carrying out these measurements lies in the fact that the sputtering process is sensitive to many parameters whose influence on film properties are usually interlinked. As discussed previously, we have chosen, in this work, to demonstrate the effect of reducing the target voltage by introducing a permanent magnet into the R.F. system. All the characteristics of the material will be examined in terms of this major change. Initially we hoped to investigate the effect of changing most parameters involved in this process, however, owing to the limited period of time available, some of these changes had to be sacrificed. Therefore it was decided to keep the deposition temperature constant and vary the sputtering gas pressure. To this end, the R.F. power input to the chamber was adjusted around 100W to give a constant value of 300V for the target voltage for all depositions. The partial pressure of hydrogen was varied according to the amount of hydrogen chosen. This was quantified in terms of argon to hydrogen ratio $\frac{P_{\text{argon}}}{P_{\text{hydrogen}}}$.

To investigate the influence of argon partial pressure, two pressures were selected 5mtorr and 10mtorr. The sputtering pressure (total pressure) was determined by calculating the chamber pressure appropriate for an argon partial pressure of 5 mtorr or 10 mtorr added to a hydrogen partial pressure determined by the gas mixture chosen. The method adopted has been to change one of these parameters while keeping the others fixed. As has been pointed out (MISRA et al (100)), there is a genuine belief that the properties of a-Si:H vary from one laboratory to another and therefore a convincing method of characterisation of this material would be at best carried out on the same sample or on samples prepared under identical conditions. In this spirit, in order to examine the deposition rates among other properties of the material discussed in detail in Chapter 6, we have prepared a set of samples under the same conditions but differing in thicknesses. In the following section we review the effect of hydrogen on transport properties.

4.2 The effect of hydrogen on transport properties of a-Si.

It has been shown that the deliberate incorporation of hydrogen to a-Si could remove a substantial number of gap states associated with dangling bonds from the pseudo-gap of a-Si:H (101)(102). The process in which hydrogen modifies the properties of the material is not fully understood yet, nor is there any consensus on how much hydrogen is needed to improve the quality of the material. Several groups have investigated the hydrogen content and, in most cases, it has been found very dependent on deposition

conditions. The reported values for hydrogen content vary between 5 and 40% (103, 104, 105, 106). Equally important is the manner in which Si-H bonding configurations are formed within the films. In this connection Anderson et al (101) carried out an intensive study of a large number of non-magnetron sputtered samples and observed a decrease in the D.C. conductivity with increasing hydrogen content which they interpreted as an indication of states being eliminated by additional hydrogen. However, the authors pointed out that the minimum hydrogen content required to remove the majority of states from the gap varies greatly with the preparation conditions of the material. For a low T_s ($< 200^\circ\text{C}$) specimen, a hydrogen content of nearly 10 at % was required. By contrast for a high T_s ($> 325^\circ\text{C}$) specimen only 3 at % was needed to achieve the same result. The influence of the deposition temperature seems to be important mostly in allowing more or less hydrogen incorporation for a given pressure of hydrogen. However, as pointed out by the authors, not only is the addition of hydrogen effective in reducing the density of states in the gap, but its effect on the density of states distribution extends beyond the mere compensation of defects associated with dangling and reconstructed dangling bonds. Anderson et al also pointed out that an excess of hydrogen can create defects in the film in one of the two ways:

(i) by occupying a site in the network which would have been a viable site for a silicon atom, terminating the network at that point and forcing it to grow round the hydrogen atom as best it can, or

(ii) by forming multiply bonded SiH_x complexes which

also force the network to depart from a regular random fully coordinated tetrahedral arrangement.

To illustrate the effect of hydrogen on transport properties of magnetron a-Si:H prepared by the technique described in Chapter 3, we reproduce the results of the D.C. conductivity measured on two different types of samples. Figure 4.1 shows the D.C. conductivity as measured at room temperature plotted against the activation energy for a number of samples sputtered in 5 mtorr and 10 mtorr argon plus the appropriate hydrogen partial pressure of the gas mixture. In this, films deposited in pure argon exhibit large conductivities which, for temperatures up to 300 K, follow the theoretical $T^{-1/4}$ behaviour predicted for a variable range hopping mechanism (Mott (1)). For samples prepared in 5 mtorr argon pressure, the D.C. conductivity as measured at room temperature decreases with increasing hydrogen content, similarly to the behaviour observed by Anderson et al (101) and discussed above. At low temperatures for high hydrogen partial pressures, the samples became highly resistive and details of sample behaviour become difficult to observe, but the evidence suggests that the room temperature conductivity becomes independent of hydrogen concentration.

Figure 4.1 also shows the D.C. conductivity at room temperature as a function of activation energy for a number of samples sputtered in 10 mtorr argon pressure with hydrogen partial pressure varied between 2 mtorr & 5 mtorr. As the hydrogen partial pressure is increased, the D.C. conductivity as measured at room temperature on these samples also increases, suggesting that instead of removing states from

the gap, extra states are being created. This is precisely what capacitance measurements to be discussed in Chapter 5 reveal for this category of sample. In addition, the density of states estimated from capacitance data on sample MS28 $\left(\frac{P_{\text{argon}}}{P_{\text{hydrogen}}} = 5 \right)$ suggests that less hydrogen is needed to achieve similar results given by samples MS13 and MS20 discussed in Chapter 5. In this context, there is a real possibility that the point made by Anderson et al and outlined above can be justified. However, further work is required in order to clarify the situation.

In order to assess the effect of hydrogen we carried out a direct measurement of hydrogen evolution in magnetron sputtered a-Si:H, the discussion of which is given in the following section.

4.3 Hydrogen Evolution

To study the release mechanism of hydrogen in a-Si:H we used the hydrogen evolution technique described in Chapter 3. When films of a-Si:H are heated to above 500°C in an isolated chamber of a given volume, the hydrogen is evolved. Its presence is detected by the mass spectrometer analysis and monitored as a function of temperature as the heating rate is adjusted around 4°C/min. To account for the residual elements remaining in the system, the background pressure related to outgassing of the system is analysed prior to sample examination. The kinetics of this process, which may give information about the way in which hydrogen is incorporated are not discussed here, but we concentrate on hydrogen evolution with increasing temperature. Figure 4.2 shows the results obtained from two samples deposited at room

temperature in 5 mtorr argon with an additional hydrogen pressure of 2.5 mtorr. In common with other groups (107) (108), we observe a dominant peak between 350°C - 360°C which suggests that, at this temperature, hydrogen atoms gain enough energy to dissociate from the structure, resulting in the hydrogen evolution process. The absolute hydrogen content cannot be estimated since the system has not been calibrated. The main information in Figure 4.2 is about the mechanism of hydrogen incorporation and release which may explain why the quality of the material depends critically on the degree of compensation of defects by hydrogen of which losses may occur by effusion over a long time of operation or during the hot process of deposition. As illustrated in Figure 4.2 the results indicate that hydrogen incorporation is easily accomplished by low temperature deposition. It is instructive to compare these results with those obtained by Beyer et al (107) for magnetron sputtered a-Si:H. For this purpose, we reproduce the results of Beyer et al (107) in the inset of Figure 4.2. As shown the agreement between these results is good, in the temperature range probed. The relationship between the hydrogen release mechanism and Si-H bonding configurations has been discussed (108) (109) and it is believed that the low temperature peak around 360°C shown in Figure 4.2 is associated with hydrogen effusion from SiH_2 complexes and the high temperature peak above 550°C reported by several groups (107) (108) is related to Si-H complexes. In the following we discuss some infra-red results to gain better understanding of our samples.

4.4 Infra-red Absorption

To assess the role of hydrogen, we examined the optical absorption in the infra-red of two samples prepared in 7.5 mtorr and 15 mtorr total pressure. Figure (4.3a, b) shows respectively the spectra of the films obtained. In both cases, we observe three absorption bands. The first occurs near 2000 cm^{-1} , the second a broader absorption near 650 cm^{-1} and a third band at 890 cm^{-1} associated with SiH_2 bending. Incidentally the spectra of Figure (4.3b) corresponding to the 15 mtorr sample shows a structure near 1050 cm^{-1} , which is attributed to oxygen contamination. Consequently, the absorption feature occurring at 2090 cm^{-1} and attributed to dihydride modes, becomes somewhat ambiguous whilst the 2000 cm^{-1} mode is completely absent.

A more clear picture of the infra-red absorption is given by the spectra of figure (4.3a). For this sample no sign of oxygen is present, hence unambiguous conclusions can be drawn. In this case, the absorption features occurring at 2090 cm^{-1} and 890 cm^{-1} and attributed to dihydride modes are, again, dominant but both the 2000 cm^{-1} and 690 cm^{-1} features are present.

It is believed that the predominance of dihydride bonding over monohydride, frequently reported for sputtered material, is responsible for ^{the} low quality of this material compared to glow discharge material. However, the characteristics of our magnetron material presented in later chapters suggest that the reason is most probably to be associated with surface layer properties of the film rather than bulk configurations.

Information about the absolute hydrogen content may be obtained from infra-red spectra. The results indicate a hydrogen content of about 14 at % for the sample prepared in 5 mtorr argon added to 2.5 mtorr hydrogen pressure. As outlined above, the hydrogen content of the other sample could not be deduced due to oxygen contamination.

4.5 Analysis by Electron Microscopy

In order to get a better insight into the material, we have attempted to characterise its structural behaviour. For this, a variety of structural techniques have been used to investigate amorphous silicon produced in this laboratory. Most of the work has been performed on material prepared by the conventional technique (95). It is only recently, that attention has been directed to R.F. magnetron sputtered material. As a result, structural information is only available in a limited number of areas.

(1). Argon Concentration:

As discussed in Chapter 3 the standard technique employed for sample preparation is that of R.F. sputtering in an argon gas. Therefore, it is not surprising that we find significant concentrations of embedded argon in the R.F. sputtered films. No active role has ever been proposed for this included gas, but it is an important impurity nonetheless, and it is easy to study in the electron microscope. EDX microanalysis carried out in this laboratory on orthodox sputtered material (95) showed that the concentration of argon in the films increases with increasing film thickness and decreasing deposition temperature. It is believed that the thickness dependence is likely to be related to argon loss from those voids which connect with the film surface, since argon is assumed to be included inhomogeneously in microvoids. The variations of argon concentrations with deposition temperature T_s suggest that the void volume decreases with increasing T_s . The analysis also showed that non-magnetron sputtered films contain about 5% of argon.

The data obtained for magnetron sputtered samples suggests a concentration of argon of about 1% or less. These values correspond to films sputtered in 5 mtorr argon pressure. There are indications that for high argon pressure the concentration may be even lower (110).

(2) Small angle scattering (S.A.S) Structure:

One of the best ways of investigating film homogeneity is by looking at small angle scattering in the diffraction pattern. Such measurements have been made for some years on non-magnetron sputtered material and reveal appreciable information about the void structure. This analysis shows a structure with a radius of gyration of around 5 Å. The voids have a higher electron density than the surrounding silicon and are thus attributed to argon inclusion. The early data obtained from magnetron sputtered films suggests that the main argon bearing inclusions are somewhat smaller. If one associates the deep localised states with these features in the small angle scattering, this observation is consistent with the lower density of states seen in the magnetron sputtered film (See Chapters 5 and 6). In addition to these small inclusions larger scale structure with radius of gyration around 10 Å is also seen. This is rather similar to that observed in glow discharge a-Si:H, consistent with the other general similarities observed between the two materials (96) (97).

material	argon content	S.A.S scale
non magnetron sputtered	5-7%	4-6 Å
magnetron sputtered	< 1%	~10 Å
glow discharge	0	10 Å

4.6 Optical Absorption:

Another method of characterising R.F. magnetron sputtered a-Si:H prepared by the technique described in Chapter 3, is to investigate its optical response. As discussed in Chapter 3, we have chosen to study the transmittance and reflectance of the material in order to draw some conclusions about the optical properties in which we are interested. For sputtered material, the thicknesses of the samples can vary significantly over quite small distances. Therefore it is essential to ensure that the area of the sample is being studied in both reflectance and transmittance measurements. As shown in Figure 4.4 which illustrates typical results from the optical absorption measurement, the interference fringes in reflectance and transmittance signals are accurately in antiphase, clearly indicating that the optical response does correspond to the same area of the sample. At high photon energies, absorption in the film becomes very significant and the transmittance signal becomes negligible. The interference effects in the reflected signal also die out as the interfering beams are increasingly attenuated in the film.

Following the analysis scheme presented in Chapter 3, we consider the relation between the imaginary part of the dielectric constant ϵ_2 and the photon energy $\hbar\omega$ in order to deduce the energy gap.

$$\hbar\omega \sqrt{\epsilon_2} = A (\hbar\omega - E_g)$$

where $\epsilon_2 = 2K_1 K_2$ and A is constant

The plot of $k\omega\sqrt{\epsilon_2}$ against $k\omega$ is displayed in Figure 4.5 for the data described above. The intercept on the $k\omega$ axis gives the optical gap E_g . Although ϵ_2 depends on K_1 and K_2 which are both affected by interference, in the region of relatively strong absorption where the analysis is valid, these effects are insignificant. The uncertainties in thickness, particularly significant in sputtered material, may lead to errors in the analysis. These, again, may be shown to have little effect on the results (I.Gibb, Ph.D thesis)¹²⁶. The errors are therefore small and the optical gap derived from data above is 1.98 ± 0.02 eV.

Several groups have discussed the effect of hydrogen content on the optical gap (111,112,113) and pointed out that increasing hydrogen content causes enlargement in the optical gap. In this context, the value of 1.98 ± 0.02 eV obtained from data discussed above, is consistent with the published results. In many cases the band-gap increases to a limiting value of ≤ 2 eV at the highest hydrogen contents.

As shown by the D.C. conductivity data discussed previously and from other reported data (101), increasing hydrogen content reduces both the density of localized states across the gap generally and at the band edges particularly causing the optical gap to increase (102). Transport data (101) shows the effect of hydrogen as being essentially on the valence band edge with the conduction band being relatively unaffected.

Sample	Pargon F ₂ hydrogen	total pressure (mtorr)	d(μm)	E _A (eV) ±2%	σ ₀ (Ωcm) ⁻¹	σ _{Rt} (Ωcm) ⁻¹	E _g (eV)
MS7	2.5:1	7	0.45	0.95	15.75	1.7510 ¹⁵	/
MS9	2.5:1	7	0.40	0.92	13.50	4.8.10 ¹⁵	/
MS11	2.5:1	7	0.5	0.98	1.3.10 ³	3.0510 ¹⁴	/
MS5	5:1	6	0.6	0.7	2.3	4.10 ¹²	/
MS13	2.5:1	7	0.5	0.90	34.5	2.6010 ¹⁴	/
MS16	2:1	7.5	0.5	0.68	1.4	2.4410 ¹²	1.88
MS19	2:1	7.5	0.45	0.90	29.5	2.2510 ¹⁴	1.98
MS20	2:1	7.5	0.4	0.75	1.5	1.310 ¹³	1.98
MS24	2:1	7.5	0.40	0.92	72.3	3.4.10 ¹⁵	/
MS25	2.5:1	14	0.35	0.90	727.8	5.6010 ¹³	/
MS26	2:1	15	0.35	0.70	3.93	6.9510 ¹²	/
MS27	3:1	13	0.34	0.78	4.07	3.24.10 ¹³	2ev
MS28	5:1	12	0.48	0.88	83.42	6.42.10 ¹⁴	/
MS31	2:1	15	0.45	0.80	7.6.10 ³	2.8010 ¹⁰	/
MS30	2.5:1	14	0.45	0.73	14.	7.7610 ¹²	1.96
MS33	2.5:1	14	0.40	0.80	68.	2.510 ¹²	/
MS34	2.5:1	14	0.42	0.90	842.	6.5210 ¹³	/

Table 4.1 summarises the results of the samples examined
deposition temperature T_s ~ 250°C

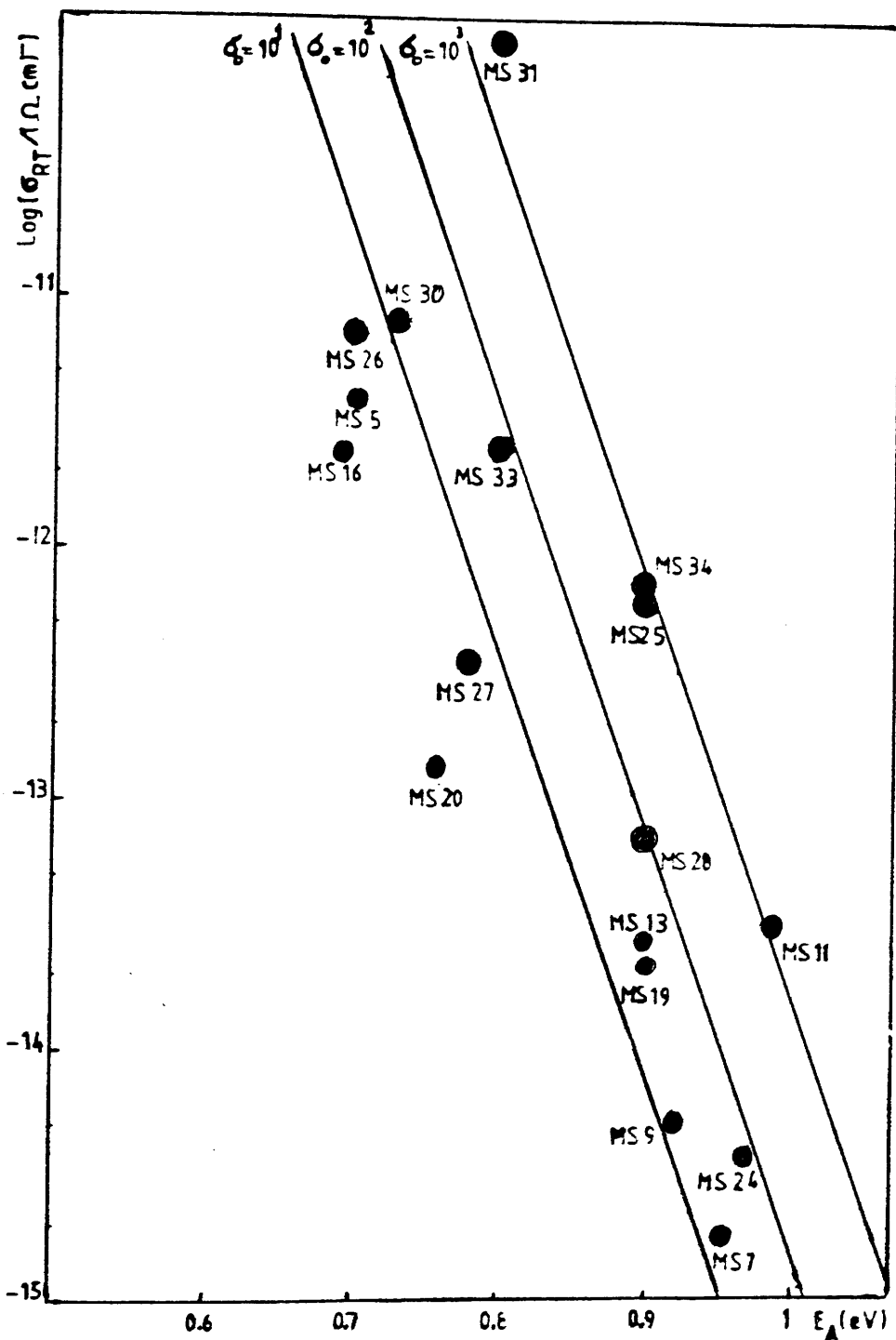
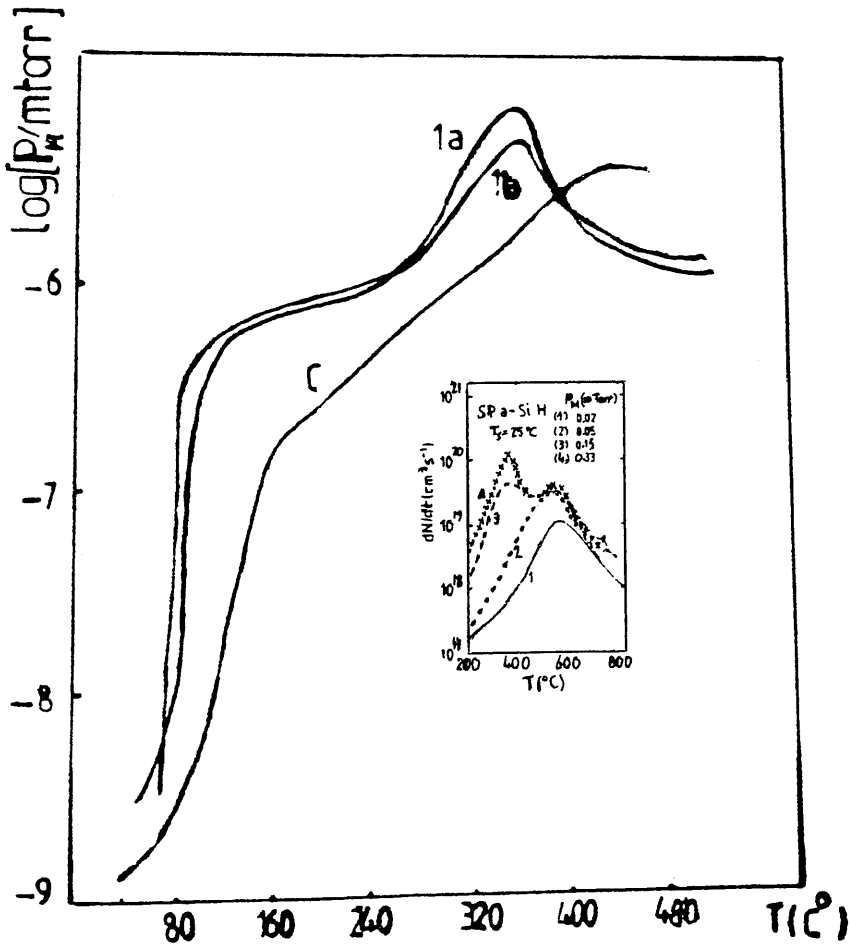


Figure 4.1 The d.c. conductivity as measured at room temperature against the activation energy for the samples summarised in table 4.1. Note the correlation with σ_0 .

Figure 4.2

This figure illustrates the hydrogen evolution as a function of temperature for two samples (1a) and (1b); C refers to the background pressure. The inset shows the hydrogen evolution rate for SP a-Si:H films. Film thickness, $d \sim 0.3 \mu\text{m}$ (after ref. 107)



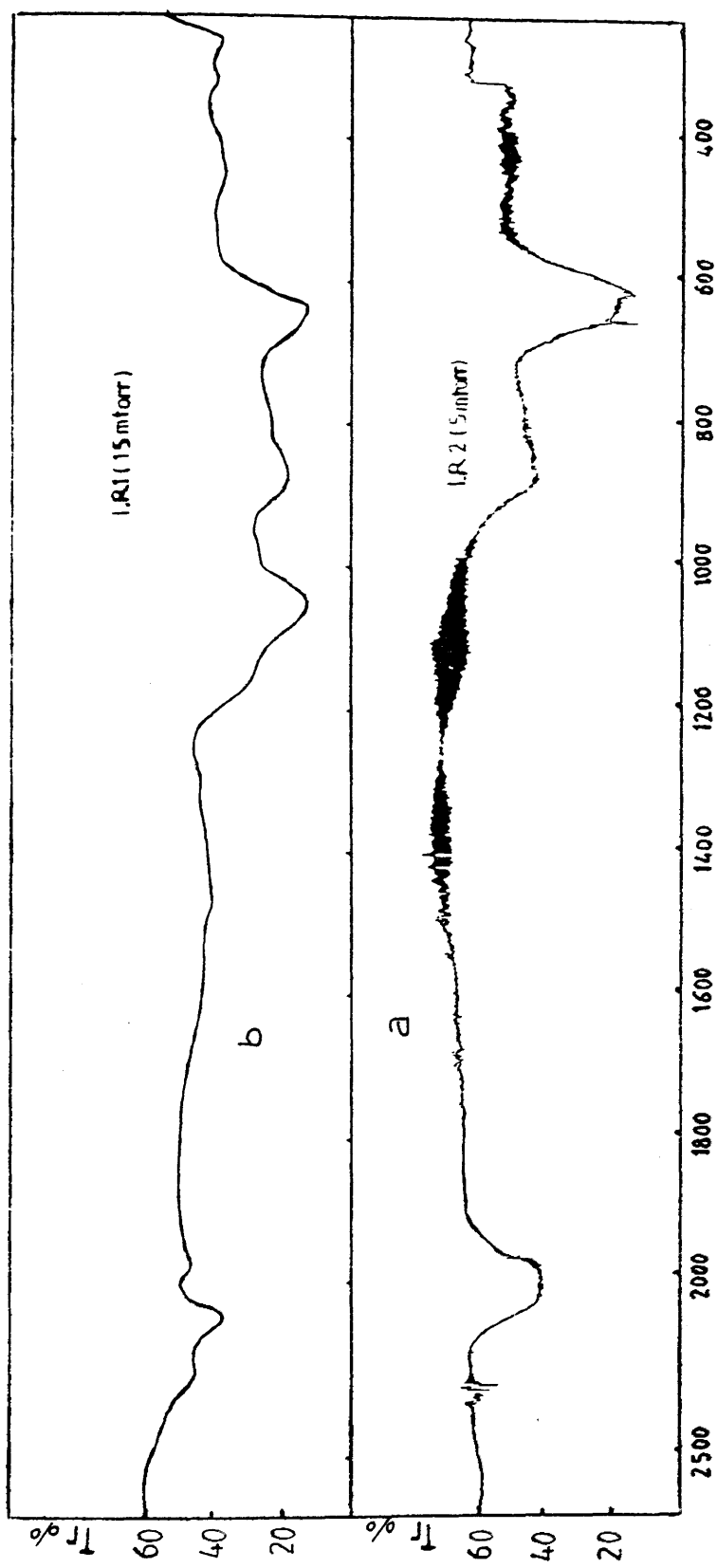


Figure 4.3 Infra red transmittance as a function of wavenumber for two samples.

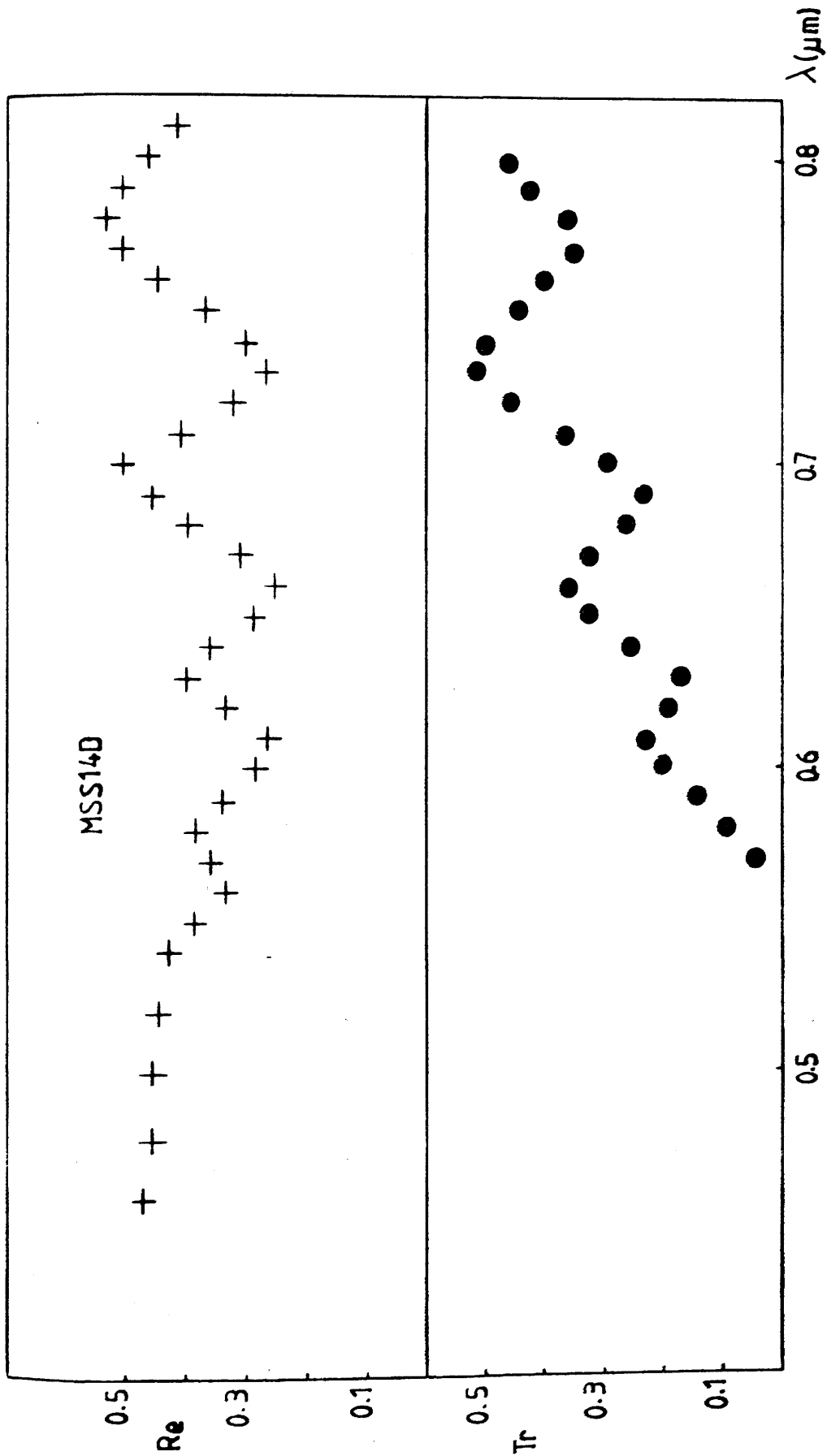


Figure 4.4 Optical Reflectance, Re , and transmittance, Tr as a function of wavelength for sample MSS14.

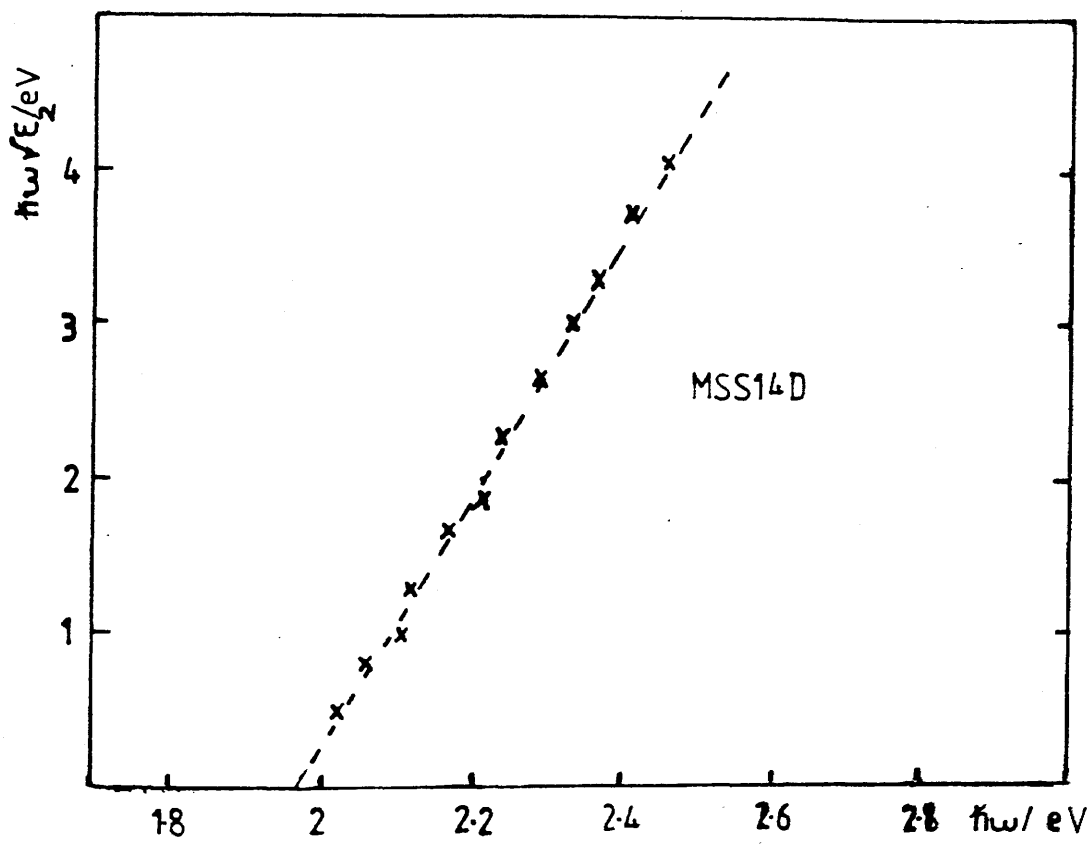


Figure 4.5 Optical absorption as a function of photon energy for MSS14.

CHAPTER 5.

Schottky Barriers.

In this chapter, the D.C. characteristics of Schottky barriers on hydrogenated amorphous silicon produced by R.F. magnetron sputtering are described, together with a detailed study of their related A.C. properties. In the first section, we give details about D.C. behaviour. The following sections are concerned with the study of the A.C. response of Schottky diodes.

5.1 D.C. Properties of Schottky Barriers

A typical I.V. characteristic from one of our samples is shown in Figure (5.1), where V is the voltage applied to one electrode with the other one earthed. The expected rectifying behaviour is clearly exhibited indicating the formation of the Schottky barrier between the amorphous semiconductor and the metal (as described in Chapter 2).

In common with other groups, the forward bias region is that mostly used for investigation. For this sample, this region can be divided into two distinct parts. At lower biases region, in the range 0-0.15 V. The I.V. characteristic is approximately exponential in nature as predicted by theory where the barrier dominates the resistance, the behaviour of which is outlined in the review Chapter. For higher values of bias, in the range 0.15-0.5 V, the plot becomes linear, evidence for bulk resistivity becoming significant and band bending negligible (Thompson et al (59), Gibb et al (22)). The amount of band bending can be estimated from the onset voltage of this second regime.

In reverse bias, in general, currents are much smaller, in agreement with the standard Shockley theory (114). However, unlike the theoretical prediction, the trend towards a constant saturation value I_0 is not observed. Instead, the current increases slowly and approximately linearly with voltage. In some samples, leakage currents become more important at high reverse bias. This causes deviation from linearity.

A failure to saturate to a constant current is seen often in both crystalline (30) and amorphous (58) (22) semiconductor junctions. It can be ascribed to various effects, such as generation in the depletion region or variation in barrier height. It is also observed for non-uniform junctions (115) the aspects of which are discussed in the review chapter. It is worth mentioning that this form of the I-V characteristic is typical of R.F. sputtered a-Si prepared in the laboratory and has been reported previously (I.G. Gibb, PhD., thesis)¹²⁶.

Other samples exhibited a third regime in the far forward region where the current increased more rapidly with voltage than linearly, similar to the SCLC structure discussed in Chapter 6. This type of behaviour was also observed in past experiments on a-Si:H produced by the conventional method (I.G. Gibb, PhD., thesis)¹²⁶. These changes may be associated with the space charge limited current effects.

Table 5.1 gives a summary of the relevant D.C. parameters characterising the samples investigated. Among other

parameters, a knowledge of the ideality factor n is needed to characterise our junctions. For this purpose, an analytical method was used in which the effect of bulk resistance was first removed. Since the current I is constant, therefore the drop voltage across the barrier can be simply deduced from $V_{\text{barrier}} = V_{\text{total}}(I) - V_{\text{bulk}}(I)$. This was done by determining the gradient from the far-forward bias region of the I-V plot which should give an estimate of bulk conductance G_{bo} . Then, a parallel of the same gradient drawn through the origin provided a good estimate of the barrier contribution, excluding, of course, the bulk effect as shown in Figure (5.1). A plot of $\ln \frac{I}{1 - \exp\left(\frac{-eV}{kT}\right)}$ versus V_{barrier} at different temperatures for the same sample is shown in Figure (5.2). As discussed in Chapter 2, it should be linear with slope $\frac{e}{nkT}$. Indeed, a linear region at low voltages is clearly visible for all temperatures measured. Values of n calculated from the gradients of these lines and accurate to approximately 10% vary from 1.43-1.15. In some samples n values are temperature dependant. In a review paper, Niamanich et al (115) discussed deviation of the ideality factor from unity. In his view, if the current transport is diffusion limited, then significant recombination process may occur causing an increase in the ideality factor. On the other hand, in the absence of recombination mechanism, n values can still approach unity despite the fact that the current is diffusion limited. There is also the case of a non-uniform junction in which the barrier height may change from place to place and the I-V characteristic is dominated by lower barrier height

regions. The ideality factor, in this case, can still be close to unity.

In crystalline semiconductors (30) n values around 1.3 which are independent of temperature are related to the presence of ^{an} interfacial layer of the order of 20Å. Not only does this cause deviations from ideal D.C. behaviour of the junction but it also affects its electronic properties. There is growing evidence that surface effects may well be the key element for further understanding of amorphous properties (Fritzsche (38) Street et al (116)). Such an explanation may well also apply in this case as a thin surface layer is likely to be formed on the film during exposure to atmosphere prior to metallization. As outlined in Chapter 3, oxidising the surface layer presented the only option for ensuring the rectifying behaviour of the Schottky diode. The results of an independent measurement (SCLC) also carried out during this work led to similar conclusions (Chapter 6). These observations are in agreement with the theory developed to treat properly the contact effects investigated in Chapter 6. Higher values of n with a larger scatter with temperature were also observed on some samples. For a low mobility material such as a-Si:H, it is not fully understood which effects dominate the behaviour, implying that further effects may become significant with temperature. Overall, n values found in this work are in good agreement, within acceptable error of 10%, with those reported by other workers (22, 58, 59, 63)...

We have seen above various effects which may cause deviations from ideal behaviour, we now go on to study some other D.C. parameters.

Examining the plot $\frac{I}{1-\exp(\frac{-eV}{kT})}$ in Figure (5.2), the intercepts of the linear region with I axis correspond to the value of I_0 the pre-factor in equation (2.31). As a result of lack of information about the electron effective mass in a-Si:H and because of the disorder that leads to localized band tail states, it is not possible to calculate directly the Richardson constant in the equation of the current flow. Thus, the main information to be derived from the temperature dependence of I_0 is the barrier height at zero bias. It is then in principle possible to distinguish between diffusion and thermionic emission theories as discussed in Chapter 2. It is not clear a priori which of these two transport mechanisms dominates. It has frequently been suggested that because of the low mobility in a-Si:H, it is likely that diffusion limited transport should dominate. However, on the contrary, many workers have reported thermionic-emission characteristics (Thompson et al (59) Gibb et al (22)).

To describe the temperature dependence of I_0 , we reproduce Figure (5.3). It can be seen that a satisfactory straight line fit can be obtained from both I_0 versus $\frac{10^3}{T}$ and $(\frac{I_0}{T^2})$ versus $\frac{10^3}{T}$ plots. However, the results are different indicating either the barrier height $\phi_b = 1.13$ eV using diffusion theory or $\phi_b = 1.04$ eV with thermionic-emission theory. The same ambiguity was found by Deneuille

and Brodsky (58) when they showed with their glow discharge material, that it is often difficult to differentiate between the two mechanisms.

In some cases, the samples investigated showed a poor quality behaviour. These samples have n values more scattered with temperature (from Table 5.1, n values of MS27 vary between 1.20 - 1.60) and the corresponding $\frac{I_0}{T^2}$ versus $\frac{10^3}{T}$ plots exhibit no clear activation energy behaviour. According to the theory developed by Crowell and co-workers (56, 61, 62) for crystalline semiconductors, a simple activated behaviour can be observed by extrapolation of data points to high temperatures. This type of behaviour is indicative of thermionic field emission transport mechanism across the barrier and it has been reported previously in this laboratory (Gibb et al (22)). In this case the process may be described in the following model. As the temperature is raised, ϕ_t the energy at which the maximum tunnelling current occurs also increases, to the limiting value ϕ_b . As illustrated in Figure (5.3), the values of $0.86 \pm 3\%$ eV and $0.91 \pm 3\%$ eV quoted for MS27, represent the lower limits for ϕ_b under thermionic emission and diffusion theories respectively. In this case, the tangents to the curve should provide ϕ_t as a function of temperature. Further investigation of this type of sample reveals that there is a likely reason for thermal field emission currents to be dominant.

The A.C. response and the resulting capacitance data (in the following sections) lead to the conclusion that the high densities of localized gap states seen in these samples

are responsible for such behaviour. This may be interpreted in the following manner. As $g(E_F)$ increases, the barrier width decreases and, assuming the barrier height remains approximately constant, the probability of tunnelling increases. The process is enhanced by the presence of surface states which contribute to the total density of localized gap states in the Fermi region (as discussed in Chapter 2).

A further examination of the I-V characteristic provides useful information about the D.C. properties of the sample. From the low bias region when the voltage becomes very small (i.e. $\frac{I}{V} \Big|_{V \rightarrow 0}$), the series D.C. combination of bulk conductance with the barrier conductance ($\frac{G_{bo} G_{so}}{G_{bo} + G_{so}}$) can be estimated. This is used to calculate the value of G_{so} needed to make the corrections for the equivalent circuit discussed in section 5.3. As mentioned earlier, the bulk conductance G_{bo} is obtained from the far forward region of the I-V plot. Similarly, by choosing a voltage lying in this region, the bulk activation energy can be derived. This quantity, under adequate conditions, should be in agreement with that deduced from co-planar conductivity measurement made on the same sample.

5.2 A.C. Properties of Schottky Barriers

To study the A.C. properties of Schottky barriers formed on magnetron sputtered hydrogenated amorphous silicon, we use the formalism developed for Schottky barriers on a-Si:H produced by the conventional technique⁽²²⁾. In this model, it is assumed that the effects associated with the movement

of mobile charge stored in the extended states are negligible. It follows that the A.C. response of the Schottky barrier may be understood by examining the effect of a small perturbing voltage on the deep states in the barrier region. The mechanism is based on a trap release model and may be conveniently represented by Figure (5.4) which shows the A.C. half cycle in which the front contact is negatively biased. By applying a small perturbing potential dV to the barrier, the diffusion potential V is diminished by a certain amount, this results in the transfer of more electrons to the Fermi level in the back contact of the barrier. By their departure the outgoing electrons leave empty states which result in an extra charge implying an additional capacitance being detected. Therefore, measurement of the differential capacitance should provide valuable information about deep states in the barrier region. The process is modelled in two stages. First, to empty a state requires a certain amount of time for an electron to be excited from its original state in the barrier region to a state in the conduction band at the edge of the Schottky barrier. The second stage is concerned with the drift of the electron to the back contact at de-excitation. Consequently, to empty a state requires the assistance of both processes.

To quantify stage 1, we use the standard perturbed rate equation method, leading to a Debye response for the process of the form $(1 + i\omega\tau)^{-1}$, where ω is the A.C. driving angular frequency, i is $\sqrt{-1}$ and the relaxation time τ is given by

terms of the relaxation rates for the processes A → B and B → A by

$$\frac{1}{\tau} = \frac{1}{\tau_A} + \frac{1}{\tau_B} \quad (5.1)$$

The contribution of the state A to the charge released from the barrier as function of angular frequency ω , depends on the real part of the response given by $(1 + (\omega \tau)^2)^{-1}$.

The escaping rate into the conduction band is governed by thermal excitation, thus it is a function of the activation energy $(E_C - E_F) + eV(x)$. Because of the barrier profile, this rate changes with position. As a result, the quantity $\tau(x)$ can be written in this form:

$$\tau(x) = \tau_0 \exp \frac{E_C - E_F + eV(x)}{kT} \quad (5.2)$$

where $V(x)$ is the barrier potential profile

τ_0 is an empirical rate parameter described by the following expression

$$\tau_0^{-1} = N_c v_{th} S_n \quad (5.3)$$

where N_c is the number of states at the conduction band edge

v_{th} is the carrier thermal velocity

S_n is the electron capture cross section for the deep traps.

The analysis is now extended further to cover the total A.C. response, for which we need to make assumptions about the density of the deep states in the Schottky barrier region. As usual, we test a simplified picture, that of a density of states g_0 uniform in space and energy. In this

case, assuming the Schottky barrier is determined by the deep states, the number of states per unit area emptied between x and $x + dx$ is given by:

$$N = g_o eV(x) dx \quad (5.4)$$

$$\text{and } \rho(x) = g_o e^{2V(x)} \quad (5.5)$$

Therefore the Poisson's equation becomes:

$$\frac{d^2V(x)}{dx^2} = - \frac{\rho(x)}{\epsilon} = - \frac{g_o e^{2V(x)}}{\epsilon} \quad (5.6)$$

Solving equation (5.6) leads to an exponential profile of the barrier i.e.

$$V(x) = V_s \exp(-x/L) \quad (5.7)$$

$$L = \frac{1}{e} \left(\frac{\epsilon}{g_o} \right)^{\frac{1}{2}} \quad (5.8)$$

where ϵ is the static permittivity of the a-si:H and L is the Debye length

By substituting equation (5.7) into equation (5.2) we obtain two important quantities i.e.

$$\tau'_o = \tau_o \exp \left(\frac{E_c - E_F}{kT} \right) \quad (5.9)$$

$$\tau''_o = \tau_o \exp \left(\frac{E_c - E_F + eV_s}{kT} \right) \quad (5.10)$$

These two quantities refer to the release times corresponding to those states at the onset of the barrier and those at the metal interface respectively. They, therefore represent the limits in the range of release times to be expected in any particular junction. In addition, these quantities are temperature dependent and

have activation energies related respectively to that of the bulk and the barrier height ϕ_b .

It is convenient to consider the perturbing signal dV_s to be of the same form as the interfacial potential V_s namely $dV_s \exp(\frac{-x}{L})$. In physical terms, this implies that all the deep states in the barrier are fully responding to the applied A.C. signal. This can be seen as only a first approximation (as is discussed below). Using equations (5.2) and (5.7) we can calculate the charge dQ perturbed in the barrier by the exciting potential dV_s and hence the differential capacitance of the barrier.

$$\frac{dQ}{A} = \int_0^d g_0 |e|^2 dx \frac{1}{1+\omega^2 \tau^2} dV_s \exp(\frac{-x}{L}) \quad (5.11)$$

where A is the cross sectional area defined by the electrodes and d is the thickness of a-Si:H layer.

Reordering and changing variables we obtain the corresponding capacitance formula (see p 93)

$$C_s(\omega) = \frac{1}{A} \frac{dQ(\omega)}{dV_s} = \int_{\tau_0'}^{\tau_0''} \frac{g_0 |e| kT L}{V_s \tau (1+\omega^2 \tau^2)} d\tau \quad (5.12)$$

where $C_s(\omega)$ is the differential capacitance per unit area.

On integration this becomes

$$C_s(\omega) = C_0 \left[1 - \frac{kT}{2\tau |e| V_s} \ln \frac{1+(\omega\tau_0'')^2}{1+(\omega\tau_0')^2} \right] \quad (5.13)$$

A detailed picture of $C_s(\omega)$ as a function of $\ln(\omega)$ in the limit of $d \gg L$ described by equation (5.13) is illustrated in Figure (5.5). Three main regions may be identified.

a) At low frequencies described by the inequality $\omega < (\tau''_0)^{-1}$, all states respond to the modulation and the capacitance saturates at a value

$$C_s = C_0 = g_0 L |e|^2 \quad . \quad (5.14)$$

Using equation (5.8) we can recognise the more usual expression ϵ/L equivalent to the D.C. capacitance of the barrier.

b) At intermediate frequencies where $(\tau''_0)^{-1} < \omega < (\tau'_0)^{-1}$, C_s has an approximate linear dependence on $\ln(\omega)$, decreasing with increasing frequency.

c) At high frequencies, described by the inequality $\omega > (\tau'_0)^{-1}$ the barrier capacitance is very small and becomes negligible.

It is interesting to examine the intermediate frequency region. Here, the extrapolations of the linear region intercept the $C_s=0$ axis at $\omega=(\tau'_0)^{-1}$ and the $C_s=C_0$ line at $\omega=(\tau''_0)^{-1}$. Also shown in Figure(5.5) is the predicted dependencies of C_s on (a) temperature and (b) potential V_s . It is clearly visible that as the temperature is raised the gradient of the linear region increases reflecting the relative temperature dependencies of τ'_0 and τ''_0 discussed previously. The variation of V_s causes the rotation of the linear region about a fixed τ'_0 value. It should be noted that the diagram shown describes not only the situation where V_s is varied by changing the metal contact and hence the work function, but also where V_s is changed by application of an external potential. This involves three assumptions:

- (i) The interface state density is negligible,
- (ii) The quasi-Fermi level, ξ_e remains flat throughout the barrier region implying thermionic-emission theory (see Chapter 2),
- (iii) The occupation of the deep states is determined only by the electron quasi-Fermi level.

As we shall see all these assumptions will be called into question later in data analysis.

The associated conductance (per unit area) for this model can be obtained by KRAMERS-KRONIG transformation of the capacitance expression, equation (5.13), or by integrating directly the imaginary part of the Debye response in a similar manner as for the capacitance $C_s(\omega)$. Using the former method, we obtain:

$$G_s(\omega) = \frac{2\omega^2}{\pi} \int_0^{\infty} \frac{C_s(u)}{u^2 - \omega^2} du \quad (5.15)$$

This becomes after simplifications:

$$G_s(\omega) = \frac{g_o |e| kTL}{V_s} \omega \left[\tan^{-1} \omega \tau_o'' - \tan^{-1} \omega \tau_o' \right] \quad (5.16)$$

Therefore, for frequencies in the range $(\tau_o'')^{-1} < \omega < (\tau_o')^{-1}$ $G_s(\omega)/\omega$ is expected to be roughly constant, falling off as ω^{-2} at higher or lower frequencies. Using equations (5.13) and (5.16) we can express the frequency dependence of the conductance $G_s(\omega)$ in the following relation and

$$\frac{G_s(\omega)}{\omega} = \frac{\pi}{2} \frac{dC_s}{d \ln(\omega)} = \frac{g_o |e| kTL}{V_s} \quad (5.17)$$

in the frequency range $(\tau_o'')^{-1} < \omega < (\tau_o')^{-1}$, provided $\tau_o' \ll \tau_o''$,

The quantities $\frac{dC_s(\omega)}{d\ln(\omega)}$ and $\frac{G_s(\omega)}{\omega}$ vary with frequency in a manner shown in figure (5.6). From this Figure drawn for two ratios of τ''_0/τ'_0 it can be seen that as the value of τ''_0/τ'_0 falls, the multiplying factor in equation (5.17) also falls.

The relationship between capacitance measurement and a constant density of states model predicted by equation (5.13) was pioneered and applied to amorphous silicon Schottky barriers by Beichler et al (18). However, their formalism was limited to the derivation of equation (5.13).

5.3 The Equivalent Circuit

The relationship between the measured capacitance and conductance of the sandwich sample and the properties of the Schottky barrier is described by the equivalent circuit summarised in diagram (5.7). In this C_s and G_s refer to trap release from the Schottky barrier. The drift of the electrons and subsequent de-excitation is modelled by the bulk conductance of the remainder of the film G_{bo} in series with the barrier. G_{so} refers to the current flowing over the barrier from the metal. At the lowest frequencies when $\omega \rightarrow 0$, the D.C. barrier conductance may be identified with G_{so} in series with the bulk conductance G_{bo} . C_g is the geometrical capacitance of the Schottky barrier which corresponds to charge stored in the metal electrodes, when the potential is applied.

Two effects which may become significant under specific conditions have been omitted.

- (i) Frequency dependent processes occurring at the Fermi-level (see Chapter 2).
- (ii) Contact resistance.

It is of interest to examine the advantages and limitations of this equivalent circuit. It follows that the measured frequency dependent admittance can be expressed in this form

$$G_m(\omega) = \frac{G_t G_{bo} (G_t + G_{bo}) + G_{bo} \omega^2 C_s^2}{\omega^2 C_s^2 + (G_t + G_{bo})^2} \quad (5.18)$$

Similarly the measured frequency dependent capacitance is:

$$C_m(\omega) = \frac{C_s G_{bo}^2}{\omega^2 C_s^2 + (G_t + G_{bo})^2} + C_g \quad (5.19)$$

where $G_t = G_s(\omega) + G_{so}$ is the total conductance of the barrier region.

There are conditions under which equations (5.18) and (5.19) can be reduced to simple forms. For instance, if we take the situation where the barrier is large (i.e. V_s is large), in this case the total conductance of the barrier will tend to be much smaller than G_{bo} the bulk conductance, particularly at measuring temperatures close to room temperature. Subsequently, the measured conductance and capacitance become respectively $G_m = G_t = G_s(\omega) + G_{so}$ and $C_m = C_s(\omega) + C_g$. As a result of these simplifications, the wanted quantities G_s and C_s become less complicated to derive. These are the conditions under which past experiments of this kind have been conducted.

However, according to Figure (5.5), it appears that (i) operating at low temperature (where $\omega\tau_0'' \gg 1$) with finite minimum frequency can lead to the situation where not all states respond, hence the complete behaviour of the barrier can be missed. Operating at low frequencies also leads to valuable information about the interface to be lost. At high temperatures, on the other hand, it is possible to measure the whole barrier, but unfortunately the simplified analysis equations developed for the low temperature case cease to operate.

(ii) For low density of states $g(E)$, the Debye length L becomes of the order of the sample thickness $d(L \gtrsim d)$ and the expression for the saturation capacitance C_0 is different. In this case, a different procedure is considered to derive a new form for C_0 . In the limit where $d \sim L$, the Poisson's equation is written as:

$$\frac{d^2V(x)}{dx^2} - \frac{V}{L^2} = 0 \quad (5.20)$$

The barrier profile, in this case takes the following form

$$V(x) = V_s \frac{\sinh((d-x)/L)}{\sinh(d/L)} \quad (5.21)$$

and

$$\frac{dV(x)}{dx} = -\frac{V_s}{L} \frac{\cosh((d-x)/L)}{\sinh(d/L)} \quad (5.22)$$

Matching the boundary conditions:

$$\text{at } x=0, \quad F = -\frac{dV}{dx} = \frac{V_s}{L} \coth \frac{d}{L} \quad (5.23)$$

and at $x=d$ $F = \frac{V_s}{L} \operatorname{cosech} \frac{d}{L}$ (5.24)

where F is the electric field at $x = 0$ and $x = d$,

By examining the field at $x = 0$ and for larger values of $\frac{d}{L}$ ($\frac{d}{L} \rightarrow \infty$), the charge stored in the barrier becomes simply (using equation (5.24)),

$$Q = \frac{\epsilon V_s}{L} \quad (5.25)$$

and the corresponding capacitance (per unit area) takes the following form:

$$C_s = \frac{Q}{V_s} = \frac{\epsilon}{L}$$

This is precisely the D.C. barrier capacitance obtained previously.

In the limit where $\frac{d}{L} \gg 1$ and at low frequencies,

$$\frac{C_o}{C_g} = \frac{d}{L} \coth \frac{d}{L} \quad (5.26)$$

where C_o is the saturation capacitance obtained at high temperatures and at low frequencies, expressed in the following form:

$$C_o = C_g \left(\frac{d}{L} \coth \frac{d}{L} \right) \quad (5.27)$$

As mentioned previously, more suitable simplifications are needed to make the analysis equations, derived for the low temperature case, operative in the high temperature case. For this, we make the assumption that the following inequality holds i.e.

$$G_t, G_{bo} \gg \omega C_s$$

This is likely to be the case at high temperature especially at low frequencies. In this case the equations 5.18 & 5.19 become:

$$G_m(\omega) = \frac{(G_t \cdot G_{bo})}{G_t + G_{bo}} \quad (5.28)$$

$$C_m(\omega) = C_s(\omega) \left(\frac{G_{bo}}{G_t + G_{bo}} \right)^2 + C_g \quad (5.29)$$

For small values of ω , G_t may be replaced in the above expression by G_{so} . These equations illustrate the fact that as the temperature is increased and G_{bo} becomes more significant with respect to G_t , the resulting effect will be to reduce the measured quantities.

In past experiments, various forms of equivalent circuits were considered to model the effects of extra capacitance. Generally a C_b term in parallel with G_{bo} in Figure (5.7) is attributed to bulk capacitance effects. This also implies a geometrical capacitance element defined by the total width of the barrier region, usually denoted by ϵ/w . This approach does not describe adequately the mechanism involved. The argument lies in the fact that, provided equilibrium is reached, very much more charge is stored in deep states than in the conduction band, hence charge there can be neglected which makes the inclusion of the C_b term unnecessary. This is particularly true for undoped material.

In view of what has been deduced so far for the response of a Schottky barrier assuming a perturbing signal of the form $dV_s \exp(-\frac{x}{L})$, it is worthwhile to stress that

this is only true at very low frequencies, where all the states can respond to the applied potential. At frequencies above $(\tau_0'')^{-1}$ it is necessary to introduce a more detailed analysis at the cost of complexity. A more elaborate approach to solve this problem is to use the abrupt cut off model discussed in Chapter 2 (Spear et al (50)); in this we define a critical position Ψ in the film where $\omega\tau(\Psi)=1$. For $x<\Psi$, the states do not respond to the perturbing signal and for $x>\Psi$, they do.

As discussed previously, a complete solution by this method, takes into consideration the properties of the back contact and as before equation (5.21) is valid i.e.

$$V(x) = V_s \frac{\sinh((d-x)/L)}{\sinh(d/L)} \quad (5.21)$$

where d is the total film thickness. Replacing this result into equation (5.2) leads to the following expression of $\Psi(\omega)$ i.e.

$$\Psi(\omega) = d - L \sinh^{-1} \left(\frac{kT}{eV_s} \sinh\left(\frac{d}{L}\right) \left[-\ln(\omega\tau_0') \right] \right) \quad (5.30)$$

A solution of the Poisson's equation for $x<\Psi$ shows that the perturbing potential drops linearly across this region of the barrier where there is no change of charge stored, whereas for $x>\Psi$, it is exponential as before. Here, the charge stored in a Schottky contact may be obtained by examining the field at $x = 0$, and the differential capacitance measured by the perturbation may be described as:

$$C = C_0 \frac{1}{\frac{\Psi}{L} + \tanh\left(\frac{d-\Psi}{L}\right)} \quad (5.31)$$

where C_0 is defined as before ($C_0 = |e|^2 g_0 L = \frac{\epsilon}{L}$).

(i) At low frequencies ($\omega < (\tau_0'')^{-1}$), $\Psi = 0$ and assuming that the applied field is fully screened from the back contact (i.e. $d \gg L$), $C \rightarrow C_0$ as before.

(ii) At high frequencies ($\omega > (\tau_0')^{-1}$) and $\Psi = d$, $C \rightarrow C_0 \frac{L}{d} = \frac{\epsilon}{d}$ the geometrical capacitance of the film C_g .

(iii) If $d \sim L$ then ^{the} capacitance measured is intermediate between C_0 and C_g as described by equation (5.26)

(iv) If $C_0 \gg C_g$, then the equivalent circuit of Figure (5.7) together with simple fit procedure provide a convenient interpolation method. In this approximation, the total capacitance becomes:

$$C = C_g + C_s(\omega)$$

and the corresponding conductance is $G = G_s(\omega)$

where $C_s(\omega)$ and $G_s(\omega)$ are obtained from equations (5.13) and (5.16) respectively with the saturation capacitance of $(1 - \frac{L}{d})C_0$ instead of C_0 . Hence the C_0 values quoted for the samples examined by this method may be in error by up to a factor $\frac{L}{d}$, typically 30% or less. In this work we use this approximation to investigate our samples.

5.4 Analysis of A.C. Results.

In the previous sections, we discussed the theory established with its advantages and weaknesses. In the following sections, the analysis scheme will be put to use.

A simple understanding of the resulting capacitance data taken at several temperatures can be gained from Figures (5.8 - 5.10) drawn to illustrate the measured capacitance for some of our representative samples such as MS13, MS20 and MS28. These were prepared under different conditions as summarised in table (5.1). As shown in these diagrams, all the features predicted by the Schottky barrier theory outlined in section (5.2) can be qualitatively recognised. At high and low frequencies, the capacitance tends to limiting values. At intermediate frequencies there is a region of linear dependence which, if extrapolated to the frequency axis, has an intercept value related to τ'_0 as described previously. The temperature dependence is clearly visible in these figures. The intercept frequency shifts to a higher value by an amount determined by the bulk activation energy as discussed later in this chapter. The gradient of the linear region also increases. As mentioned above, at high frequencies we observe the geometrical capacitance C_g invariant with frequency and temperature and merely shifts the curve up from the frequency axis by a constant amount. This quantity is the first to be corrected for during analysis and its value can be obtained experimentally both from high frequency/low temperature data and from physical measurement of sample thickness and area. In general, these are in agreement to within 20%, the uncertainty arising because of the inaccuracy in the thickness measurement (as discussed in Chapter 3) and because of variations in the permittivity ϵ for a-Si:H. For comparison we reproduce in Figure (5.11) capacitance data taken from material prepared in the same R.F. sputtering

system, but without the magnetron source (using reference (22)).

Referring to the same diagrams, it can be seen that limiting values at low frequencies in the magnetron samples ($C_o = e^2 g_o L$) suggest that the measured densities of gap states are significantly lower than for the non-magnetron samples as is expected following the improvement in the preparation technique. This first inspection of raw data is, indeed, confirmed later when the full analysis scheme is applied. This involves further corrections to be made. These results may be connected with major changes occurring in the plasma gas deposition. As discussed in Chapter 3, the self induced bias is reduced significantly and, as a result, the species which are removed from the target become less energetic and deposit smoothly on the substrate causing less damage, hence a better quality material is obtained. In connection with this technique, the Sheffield group has observed a similar effect (96, 97, 98, 99).

In common with other groups, our samples are seen to be sensitive to preparation conditions. Although no systematic study of the deposition parameters was carried out during this work, however, the results discussed in Chapter 4 indicate that hydrogen incorporation is an important factor to account for, as are the deposition temperature, sputtering gas pressure and gas flow etc.. To demonstrate the influence of some of these parameters, we have chosen to examine three samples whose deposition conditions of gas mixture and sputtering gas pressure were varied as shown in table (5.1). Samples MS13, MS20 and MS28 have respectively argon to hydrogen

ratios of 2:1, 2.5:1 and 5:1 respectively. The corresponding hydrogen partial pressures were varied with respect to these ratio as discussed in Chapter 4.

It is of interest to question the reliability of the technique adopted for the measurements of capacitance and conductance of Schottky barriers in this work. Difficulties experienced in capacitance measurements are due to errors in capacitance data obtained using the technique described in Chapter (3.5.3). The errors tend to increase at low frequencies. In general, typical errors are less than 2% for capacitance. The errors arise due to slight phase errors in the lock-in amplifier, since under these conditions, the admittance is almost purely real (i.e. conductance).

Because of the inherent correlation between capacitance and conductance of the Schottky barriers as described by this model, conductance measurements were simultaneously taken with capacitance data. Figures(5.12-5.14) show the corresponding conductances for samples MS13, MS20 and MS28.

At low frequencies, the conductance tends to constant value which can be identified from the equivalent circuit in Figure (5.7) as the quantity $\frac{G_{bo} \cdot G_{so}}{G_{bo} + G_{so}}$, the series D.C. conductance combination. These values correspond within experimental error (2%) to those measured from a D.C. I-V characteristic of the same sample at the relevant temperature.

At high frequencies, the measurements tend not to

follow the simple theory which predicts a saturation value corresponding to $\frac{G_t G_{bo}}{G_t + G_{bo}}$. This saturation occurs either when $G_t \gg G_{bo}$, when its value is simply G_{bo} , or when G_t itself saturates as predicted by equation (5.16) i.e.

$$G_t = \frac{g_o |e| kTL}{V_s} \left[\frac{1}{\tau'_o} - \frac{1}{\tau''_o} \right] \quad (5.32)$$

Since the analysis involves the use of the measured conductance $G_m(\omega)$, some error is contributed to the calculated high frequency capacitance due to the increasing quantity $G_m(\omega)$.

When the analysis scheme is applied to the Schottky barrier, it can yield very useful information. The combination of both D.C. and A.C. has been proven to be an efficient tool in revealing much of the Schottky barrier properties. From D.C. measurements, values of G_{so} and G_{bo} can be estimated (see the discussion in section 5.1). This, in turn, makes it possible to remove the effects arising from the equivalent circuit. For most measurements, the inequality $G_t, G_{bo} \gg \omega C$ holds. Thus, using the simplified form equations (5.28-5.29) a simple correction can be made for the capacitance. In general, the resulting corrected curve is acceptable within experimental error. However, for fitting of the theoretical curve, the complete expressions (5.18-5.19) were needed. This required an iterative calculation for each frequency and a computer program was written for this purpose. The fit was done on trial and error basis using the computer program which generated theoretical values for $C_s, G_s, G_s/\omega$ and $\frac{dc}{d \ln(\omega)}$

given values for C_0 , τ'_0 , V_s and T .

Numerical differential methods were used to generate $\frac{dc}{d\ln(\omega)}$ terms from the measured or calculated capacitance values, whereby the value at any point is the mean of the gradients to the two neighbouring points. However, due to noise in the capacitance data, the method is less accurate, but the overall shape can be recognised.

To assess the validity of the model used to describe the Schottky barrier behaviour, the experimental curves are in most cases, fitted to theory. As can be seen, the same theoretical parameters fit the data for all relevant temperatures scanned, bearing in mind that τ'_0 , is temperature dependent, therefore it must be modified. For measurements taken with applied D.C. voltages, the value of V_s is varied to fit the analysed data, using the values of τ'_0 and C_0 deduced for the zero bias data fitting at the same temperature.

5.5 Temperature Dependence

In the course of Schottky barrier investigations, it was felt necessary to extract as much information as possible in order to understand various aspects arising from various effects such as temperature, frequency, D.C. bias, etc.. Accordingly, figures (5.15-5.22) emphasize the features expected when the analysis scheme, described earlier, is adopted to the data of samples MS13, MS20 and MS28 at the relevant temperature shown on the graphs. Also shown are computer generated fits to the data. It is clear that the theoretical parameters which give a good fit at one

temperature also predict very well the temperature dependence of the barrier. For MS13, the V_s value of 160 mV compares well with that derived from barrier height measurements from the I-V characteristic as described in Chapter 2. The C_o value ($C_o = e^2 g_o L$) of 550 pF/mm² corresponds to a density of gap states $g_o = 1.46 \times 10^{16} \text{ eV}^{-1} \text{ cm}^{-3}$. The associated τ'_o values are plotted against reciprocal temperature in Figure (5.23) together with bulk conductivity data as measured in the ohmic region on the same sample. The respective activation energies are 0.90 eV \pm 2% and 0.88 eV \pm 2%, in good agreement as predicted by theory. A representative plot of $\frac{dc}{d(\ln(\omega))}$ and $\frac{G_s}{\omega}$ for this sample at 410 K together with the theoretical fit is shown in Figure (5.24). The theoretical parameters fit the general shape of the curve reasonably.

We go on now to investigate the effect of hydrogen content on the density of gap states. For this purpose, we have chosen three different gas mixtures illustrated by samples MS13, MS20 and MS28. As discussed previously, these are in terms of argon to hydrogen ratios 2:1, 2.5:1 and 5:1 respectively.

We refer now to the data of MS20(2.5:1) displayed in Figure (5.9). Again we apply a similar procedure and obtain theoretical fits. The results are as illustrated in Figures (5.18-5.20) which reflect the expected behaviour of this sample as scanned at three different temperatures i.e., 415 K, 400 K, and 375 K. Again, the trend is similar as predicted by the model. However there is tendency for details of the barrier to be missed out if the measuring temperature is further reduced, and the response of the

barrier is shifted towards the low frequency region. Judging from the data, it can be seen that this sample has a value of $C_0 = 200 \text{ pF/mm}^2$ ($C_0 = e^2 g_0 L$) and a corresponding density of gap states $g_0 = 1.26 \cdot 10^{16} \text{ eV}^{-1} \text{ cm}^{-3}$. The V_s value of 140 mV used to obtain the best fit is in agreement with that deduced from D.C. measurement as deduced from thermionic emission theory. The plot of $(\tau'_0)^{-1}$ values against reciprocal temperature shows a thermally activated behaviour with the activation energy equal, within experimental error, to that of bulk conductivity data taken on the same sample.

In a similar manner, a simple plot of $\frac{dC_s}{d(\ln(\omega))}$ and $\frac{G_s}{\omega}$ with theoretical fit is also shown for this sample in Figure (5.25-5.26). As pointed out earlier, the results are more scattered but the general shape is satisfactory.

When the analysis scheme is applied to the sample MS28 and the theoretical fit to the curves are obtained, the results are as displayed in Figures (5.21-5.22). As can be seen, for this sample whose gas mixture is 5:1 (a less hydrogenated film), a V_s value of 140 mV is used to obtain theoretical fits. This value is in agreement with that deduced from the I-V characteristic using again thermionic emission theory. The C_0 value of 228 pF/mm^2 corresponds to a density of states $g_0 = 1.19 \cdot 10^{16} \text{ eV}^{-1} \text{ cm}^{-3}$. In a similar manner as before, the agreement between this simple theoretical model and experimental results is good and the correspondence has been found for other relevant samples.

At this stage, it is worth concluding that a detailed picture of the density of gap states near the Fermi-level, based on C-T- ω measurements is obtained from the results of the samples investigated. The model gives a good fit to experimental data at the points at which it can be tested. However, the influence of measurement noise on the data and related artefacts due to processing of the data make the numerical differential methods used to generate $\frac{dC}{d(\ln(\omega))}$ less impressive. The high frequency deviations in the conductance data contribute to increases in the calculated capacitance, and therefore a premature decrease in capacitance gradient and also an increase in the calculated conductance. In the low frequency region, capacitance values have large errors due to the phase effect described earlier. The errors tend to be amplified by the analysis scheme. The analysis also introduces errors in the conductance data at low frequency, due to the limits of accuracy of the data, since the method involves subtraction of the G_{s0} value.

Examining the resulting capacitance data of these representative samples, it seems that there are signs indicating that deposition in a high partial pressure of hydrogen is likely to ensure a better quality of material. This suggestion is consistent with the values of the density of states measured in these samples. However, it is not possible to confirm this idea unambiguously on the basis of a limited number of results. To determine the role of hydrogen and its influence on amorphous silicon requires that a systematic study of a large number of samples be

conducted. Given the complexity of the growth process, we suggest that all the parameters involved in the deposition process are of concern.

As discussed in the earlier section, some of the samples produced were of poor quality. They do have A.C. response similar to that described previously, but it has been found difficult to obtain satisfactory theoretical fit over a range of temperatures as discussed earlier. These samples exhibit a number of similar characteristics.

1. The sample capacitances are higher indicating higher density of states, possibly as high as $10^{17} \text{eV}^{-1} \text{cm}^{-3}$.
2. The barrier heights as measured from both D.C. and A.C. measurement are smaller than expected.
3. The geometrical capacitance values C_g , as measured at low temperature are strongly frequency dependent and larger than the pure capacitance deduced from the geometry of the samples.
4. D.C. currents through the samples are not singly activated at low temperatures.

The typical behaviour of these samples is illustrated by the capacitance data of MS27 shown in Figure (5.28). Information about the bulk density of states in these samples was extracted by averaging the corrected saturation capacitance at the various measurement temperatures. Similarly V_s values were obtained from the averaged gradients of the capacitance data as summarised in table (5.2). Unlike previous samples discussed above (i.e. MS13, MS20, MS28), the

results of sample MS25, MS26 and MS27, the characteristics of which are outlined above and summarised in table (5.2), do not fulfil the conditions predicted by the model. Moreover, there is poor agreement between ϕ_b as measured from D.C. measurements and ($\phi_b = \Delta E + V_s$) deduced from capacitance measurements. However, there is evidence for this category of samples, that thermionic field emission currents are dominant in D.C. conductance data as described in section (5.1). The presence of a high density of states in these samples may be related to a tunnelling conduction mechanism (Chapter 2), which takes place at measuring temperatures above room temperature. But, the presence of other mechanisms which may contribute to the characteristics outlined above cannot be excluded.

5.5.1 Attempt to escape frequencies and trapping cross sections.

The exploration of capacitance-temperature dependence makes it possible to derive a characteristic frequency associated with emission from states at the Fermi-level in the bulk of the film. This frequency is activated with the same activation energy as the D.C. conductivity and described by a similar form of equation namely

$$v = v_0 \exp\left(-\frac{E_c - E_F}{kT}\right) \quad (5.33)$$

where the parameter v_0 is given by standard deep states kinetics and is directly proportional to capture cross section as illustrated by the following relation:

$$v_0 = S_n N_c kT v_{th} \quad (5.34)$$

here S_n is the capture cross section
 N_c is the density of states in the conduction band
 v_{th} is the thermal velocity

In this context, it is instructive to summarise the relevant information about defect centre energies reported in the literature and their correlation with "the attempt to escape frequency ν_0 ". Two distinct schools of opinion exist about the identification of defect centre energies (117). The first school places the neutral D^0 state between 1.2 and 1.3 eV below E_C and D^- at about 0.85 eV below E_C . The second one leads to consistently higher energy values with D^0 between 0.9 and 1 eV and D^- between 0.5 and 0.6 eV below E_C . The energy scale associated with these states is, in most cases, defined in terms of thermal release probability. This, in turn, involves the attempt to escape frequency of the electron which is, as shown in equation (5.34), directly related to the capture cross section S_n .

The most interesting feature in equation (5.33) is the dependence of the parameter ν on both temperature and energy. This can be very decisive and, indeed, as pointed out by TANAKA and OKUSHI (118), some of the uncertainty found in the attempt to escape frequency and in the resulting energy of the dangling bond state might arise from the fact that the parameter ν_0 is often assumed to be independent of energy. In connection with ^{the} ν_0 factor, we present some results obtained from samples examined in this work. In figure (5.29) we illustrate the variation of the attempt to escape frequency ν_0 with energy for the set of samples described in Table (5.2). It is clearly visible that this quantity does change with activation

energy in a reproducible manner and it is governed by thermal release mechanism described by equation (5.33). We ascribe this behaviour to the states D° and D^{-} located in the gap. We also use equation (5.34) to derive values for capture cross section. Subsequently, the upper states are D^{-} with S_n of the order of 10^{-15} cm^2 and the lower states are D° with $S_n \sim 10^{-12} \text{ cm}^2$.

For comparison, we reproduce the energy dependence of ν_0 values quoted for orthodox material prepared in the same R.F. system (Gibb et al (22)). The results shown are in agreement with those reported by Kida et al (119) using current transient spectroscopy.

TABLE 5.1 A summary of D.C. characteristics of the samples investigated.

Sample	P argon P hydrogen	Total pressure mtorr	Activation Energy (eV)	ϕ_b diffusion theory(eV)	ϕ_b Thermionic emission theory(eV)	$V = \phi_b - E_A$ (mV)	Ideality Factor n 10% errors
MS13	2.5:1	7	0.90±2%	1.13±3%	1.04±3%	140 (T.E) 230 (D.T)	1.43(410K) 1.31(392K) 1.15(375K)
MS16	2:1	7.5	0.67±2%	0.86±3%	0.79±3%	120(T.E.T) 190 (D.T)	1.25(400K) 1.26(375K) 1.35(350K)
MS20	2:1	7.5	0.75±2%	0.90±3%	0.84±3%	140(T.E.T) 200 (D.T)	1.60(415K) 1.30(400K) 1.10(375K)
MS24	2:1	7.5	0.92±2%	1.10±3%	1.04±3%	120(T.E.T) 180 (D.T)	1.21(400K) 1.25(375K) 1.45(355K)
MS25	2.5:1	14	0.90±2%	1.07±3%	1.04±3%	140(T.E.T) 170 (D.T)	1.25(400K) 1.16(375K) 1.20(350K)
MS26	2:1	15	0.70±2%	0.86±3%	0.81±3%	110(T.E.T) 160 (D.T)	1.70(400K) 1.62(375K) 1.55(350K)
MS27	3:1	13	0.78±2%	0.91±3%	0.86±3%	80(T.E.T) 130 (D.T)	1.20(400K) 1.30(375K) 1.60(350K)
MS28	5:1	12	0.88±2%	1.07±3%	1.02±3%	140(T.E.T) 190 (D.T)	1.50(305K) 1.15(400K) 1.26(375K)
MS32	2.5:1	14	0.80±2%	0.98±3%	0.93±3%	130(T.E.T) 180 (D.T)	1.10(406F) 1.10(400K) 1.18(375F)
MS34	2.5:1	14	0.90±2%	1.13±3%	1.06±3%	160(T.E.T) 230 (D.T)	1.20(400K) 1.12(375K)

A.C. DATA.

Sample	P argon - P hydrogen	Total Pressure mtorr	Activation energy (eV)	V_s (mV)	g_o (eV ⁻¹ cm ⁻³)
MS13	2.5:1	7	0.9±2%	163	1.46 10 ¹⁶
MS16	2:1	7.5	0.68±2%	130	7.4 10 ¹⁶
MS20	2:1	7.5	0.75 ±2%	132	1.26 10 ¹⁶
MS24	2:1	7.5	0.92±2%	146	8.20 10 ¹⁵
MS25	2.5:1	14	0.9±2%	79	-
MS26	2:1	15	0.70±2%	67	-
MS27	3:1	13	0.78±2%	103	-
MS28	5:1	12	0.88±2%	132	1.19 10 ¹⁶
MS32	2.5:1	14	0.80±2%	127	1.45 10 ¹⁶
MS34	2.5:1	14	0.91±2%	130	3.62 10 ¹⁵

errors
~2%

errors
~5%

TABLE 5.2 Illustrates a summary of A.C. results obtained from Schottky barriers. Deposition temperature $T_s = 250^\circ\text{C}$.

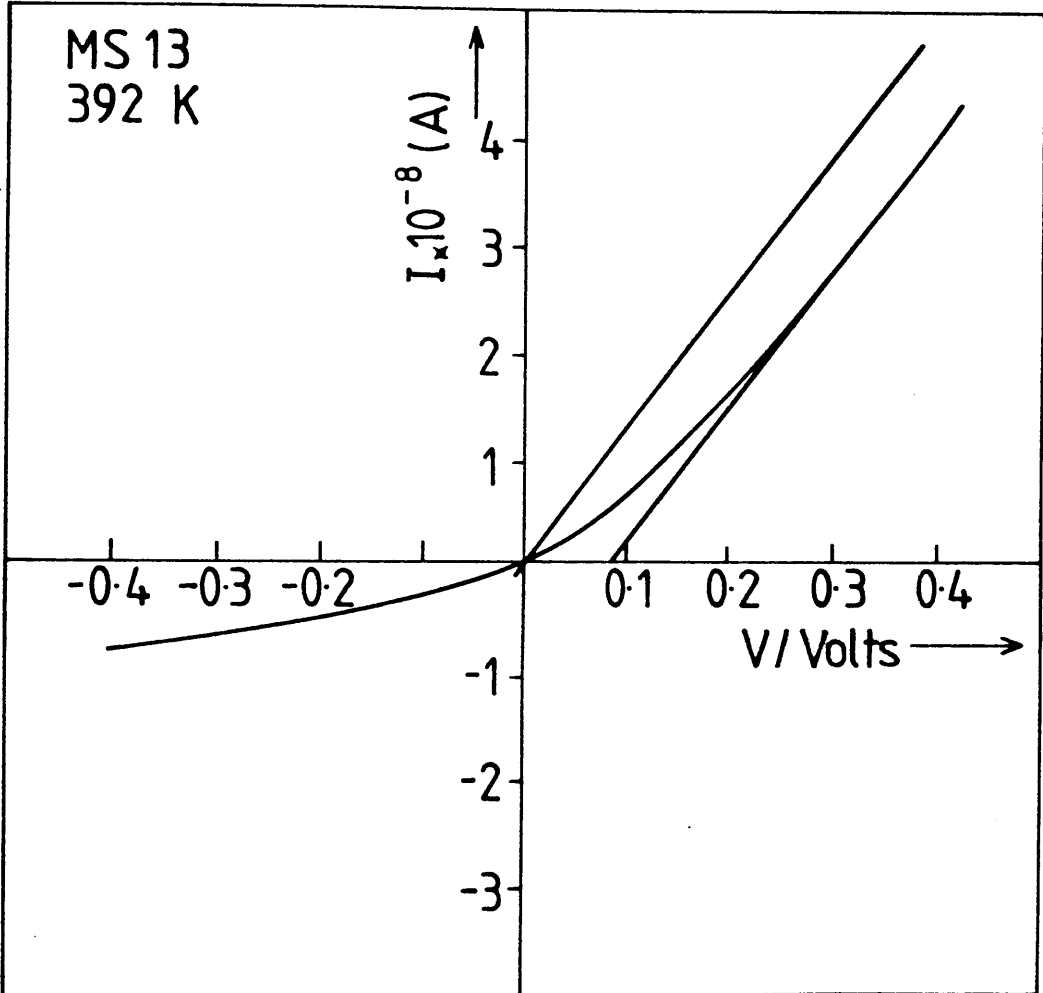


Figure 5.1

Current as a function of bias voltage for sample MS13 at 392K. Note the parallel line through the origin used to remove bulk effect as explained in section 5.1

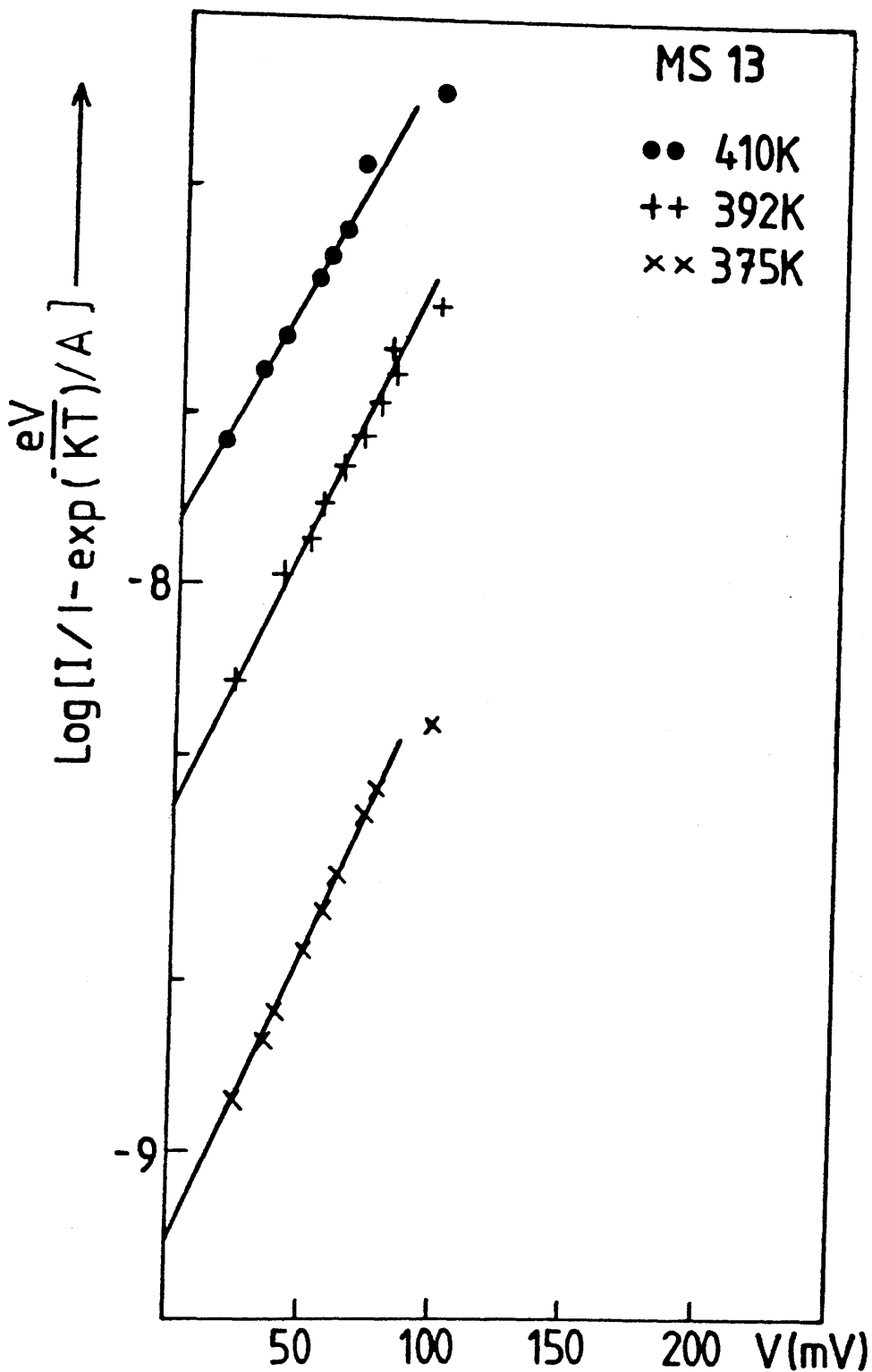


Figure 5.2

The effect of temperature on current voltage plots for sample MS13.

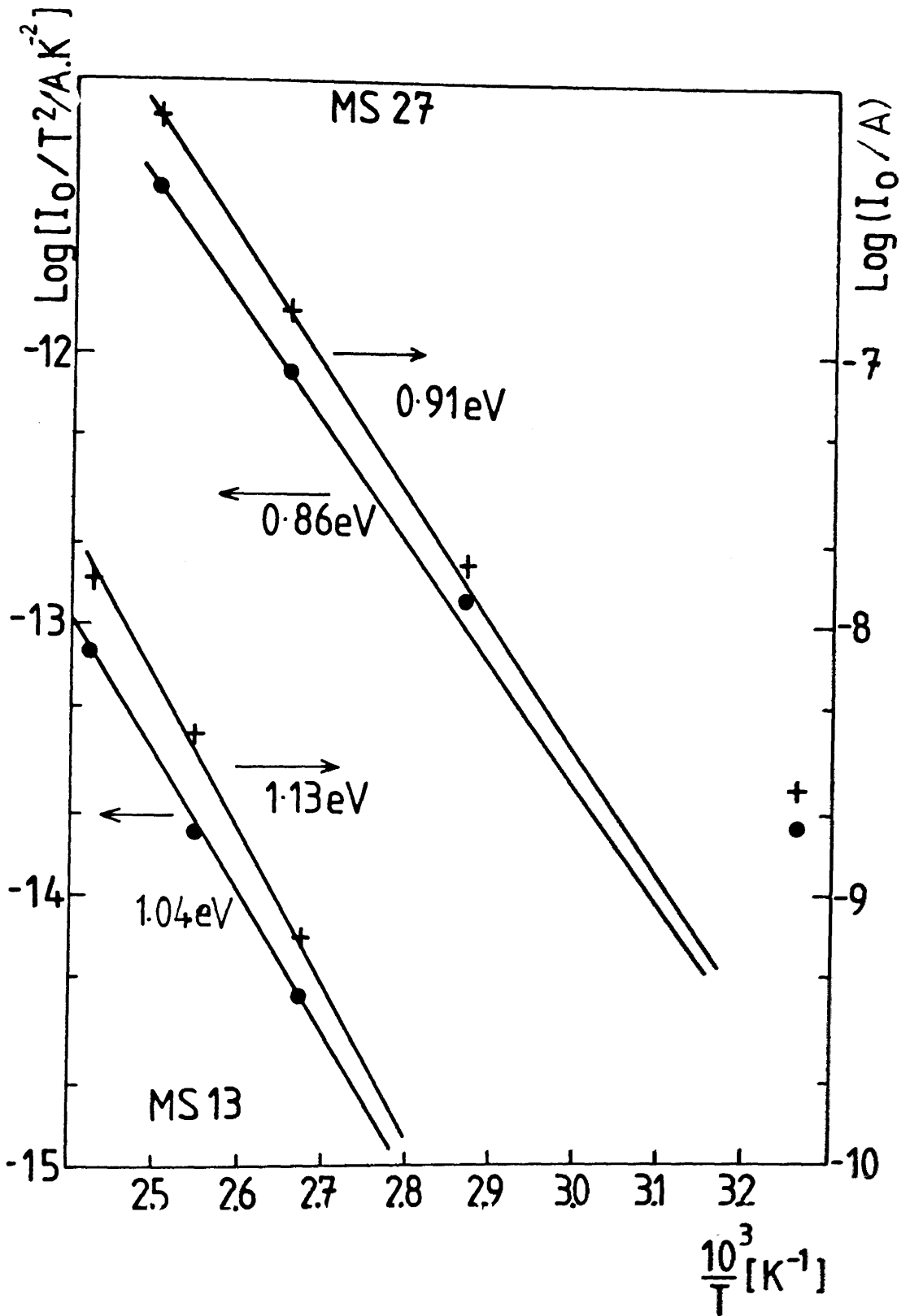


Figure 5.3 The temperature dependence of current pre-factor, I_0 for samples MS13 and MS27.

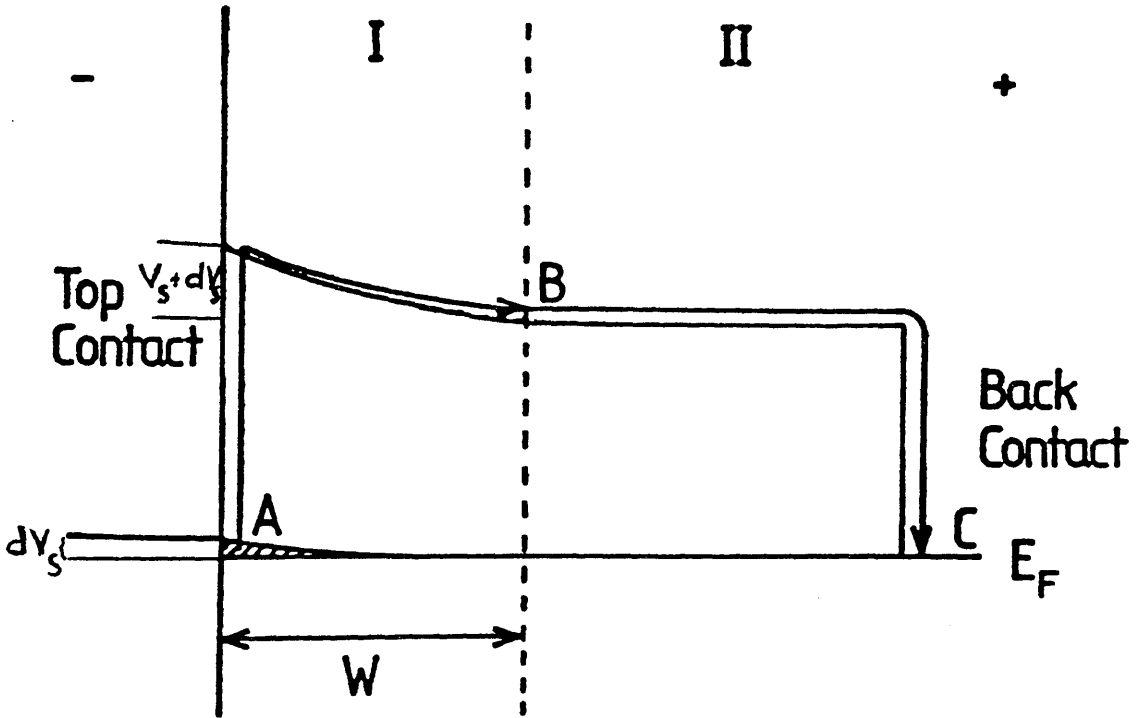
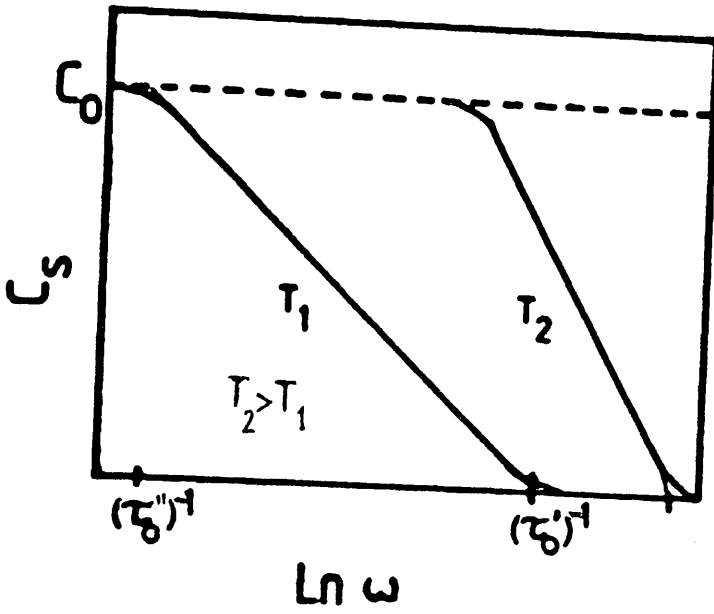
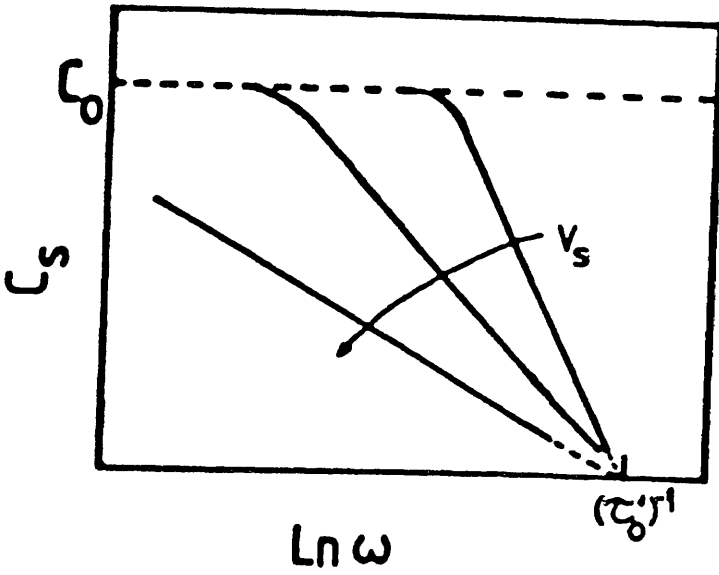


Figure 5.4 Illustrates the path of electron transfer in a Schottky barrier after a small perturbation.



(a)



(b)

Figure 5.5 The predicted dependence of the Schottky barrier Capacitance - frequency plot on (a) measuring temperature and (b) interface potential, V_s as described by equation 5.13

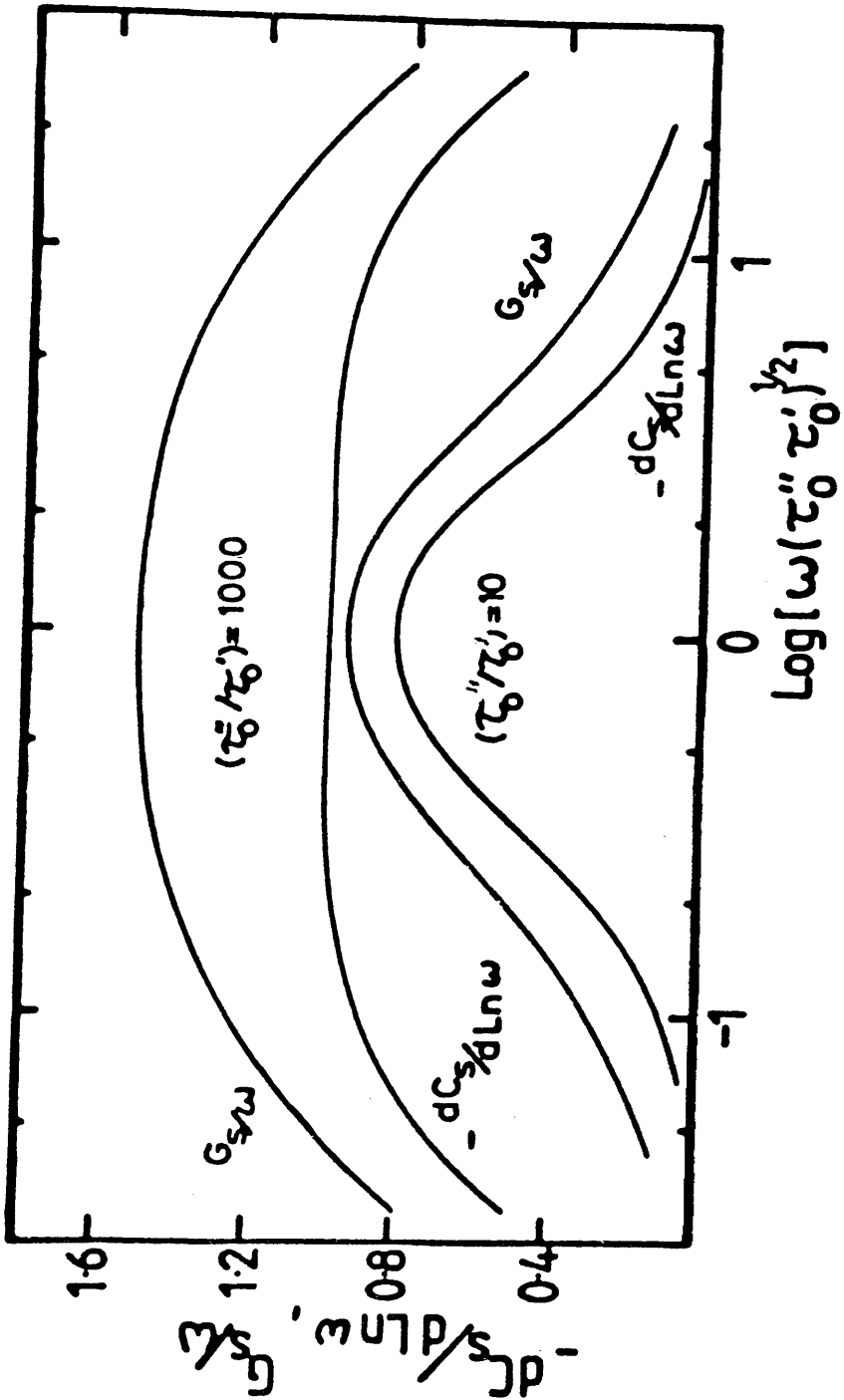


Figure 5.6 Variation of the quantities $\left(\frac{-dC_s}{d \ln(\omega)}\right)$, $\frac{G_s(\omega)}{\omega}$ with frequency for two values of (τ_0''/τ_0') . The frequency axis has been normalised and the vertical scale is in units of the quantity $\frac{g_0 |e| KTL}{V_s}$

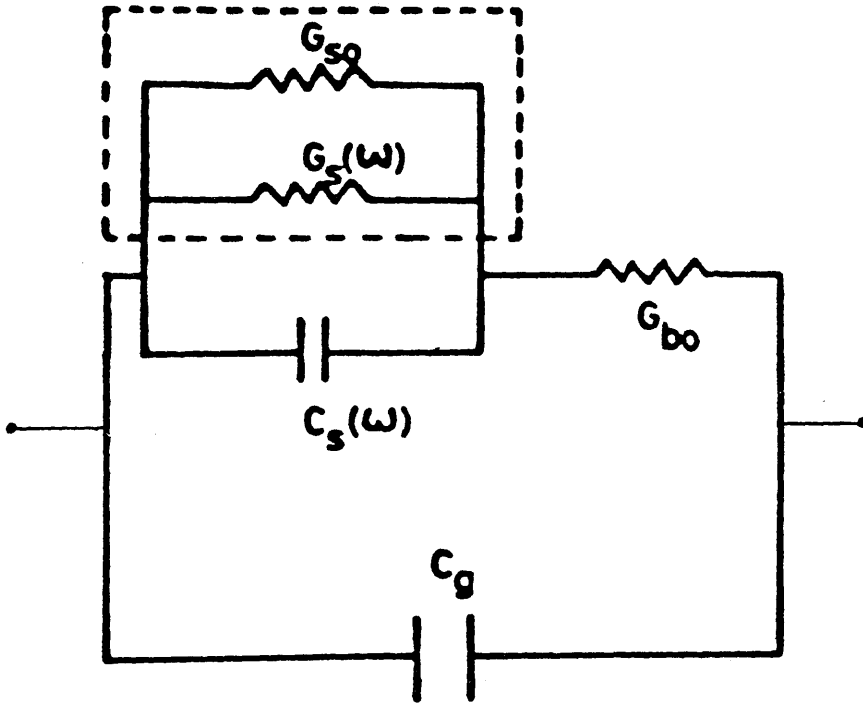


Figure 5.7 The equivalent circuit used for analysis of Schottky barrier admittance measurements

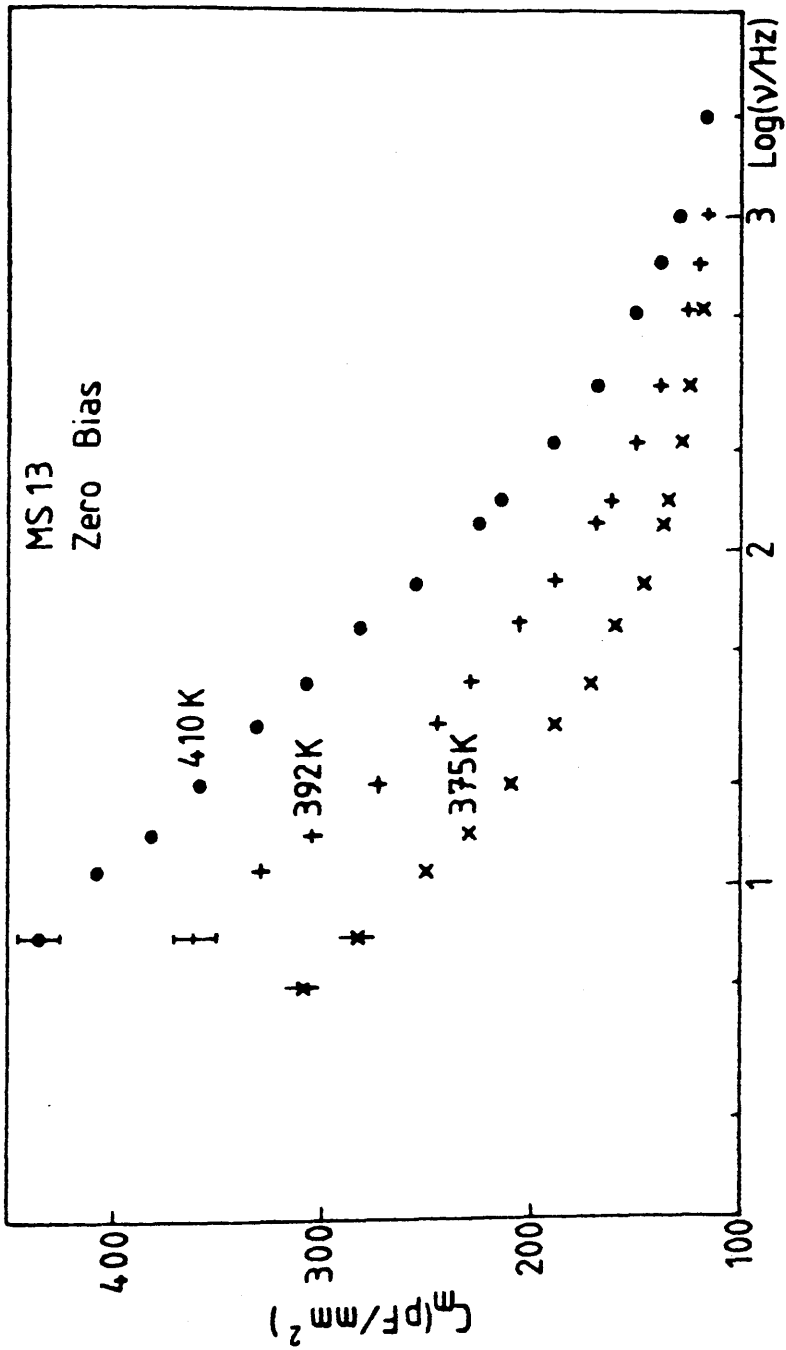


Figure 5.8 Effect of temperature on the measured capacitance-frequency plot for sample MS13.

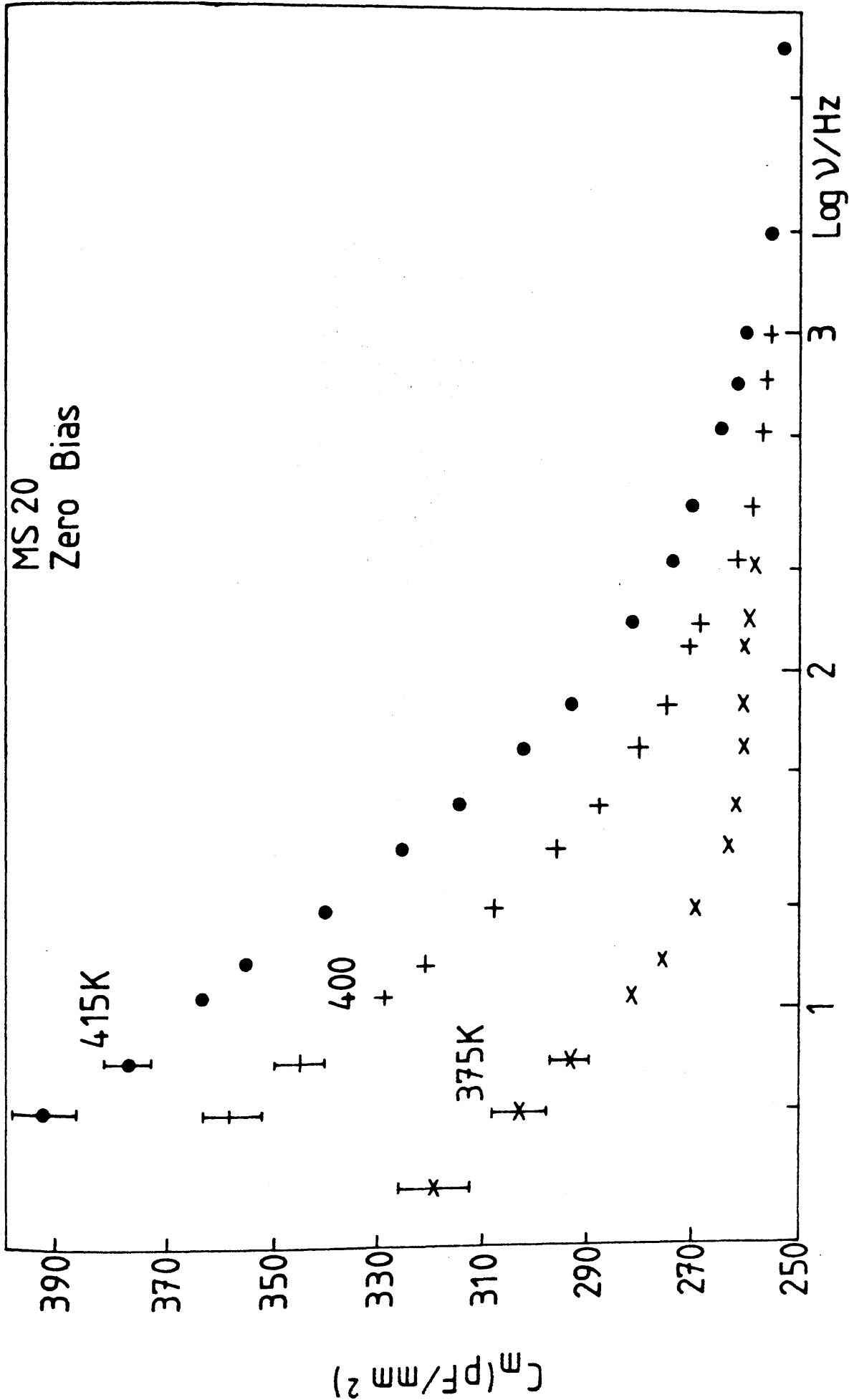


Figure 5.9 Effect of temperature on the measured capacitance-frequency plot for sample MS20.

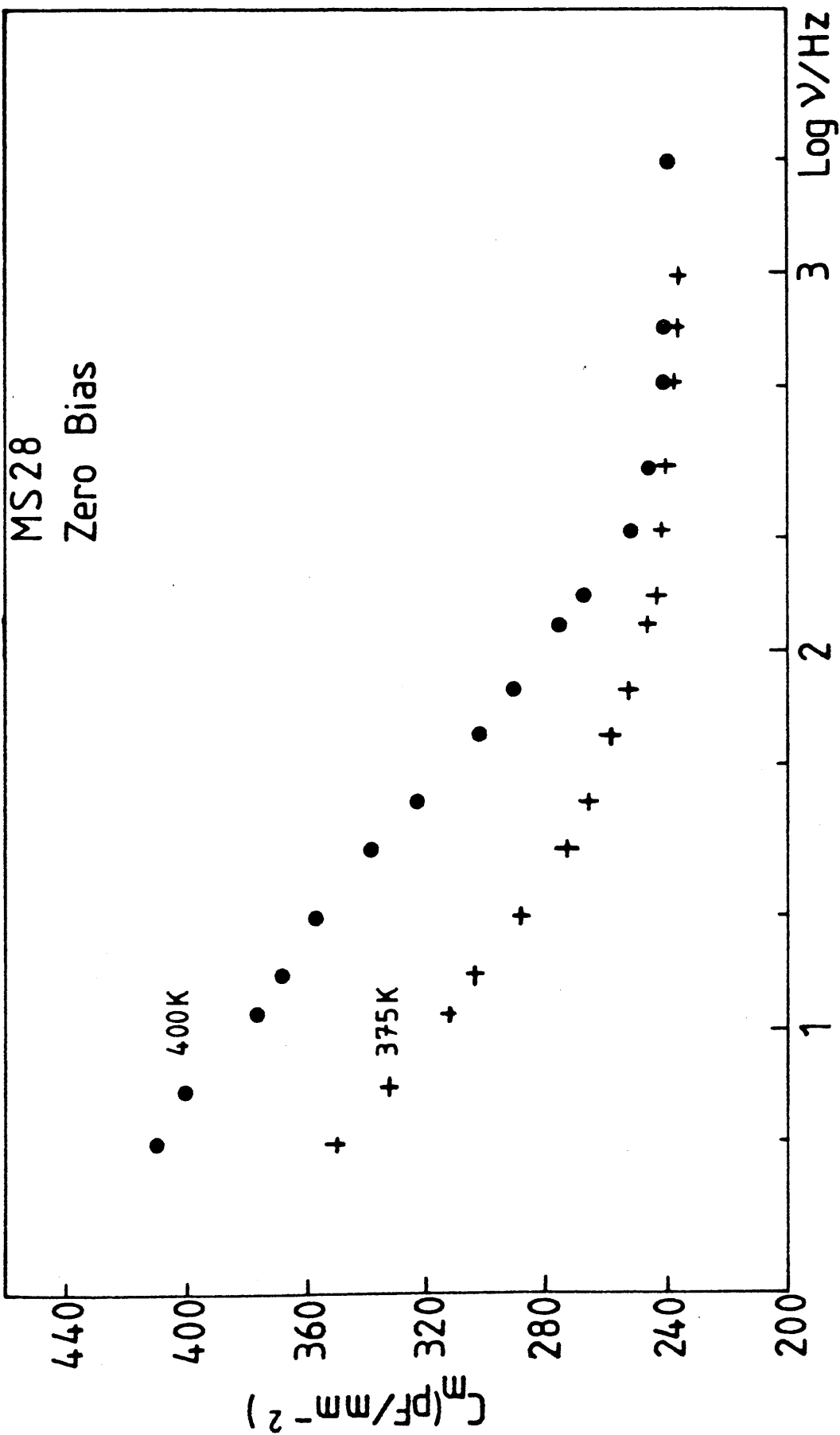


Figure 5.10 Effect of temperature on the measured capacitance-frequency plot for sample MS28.

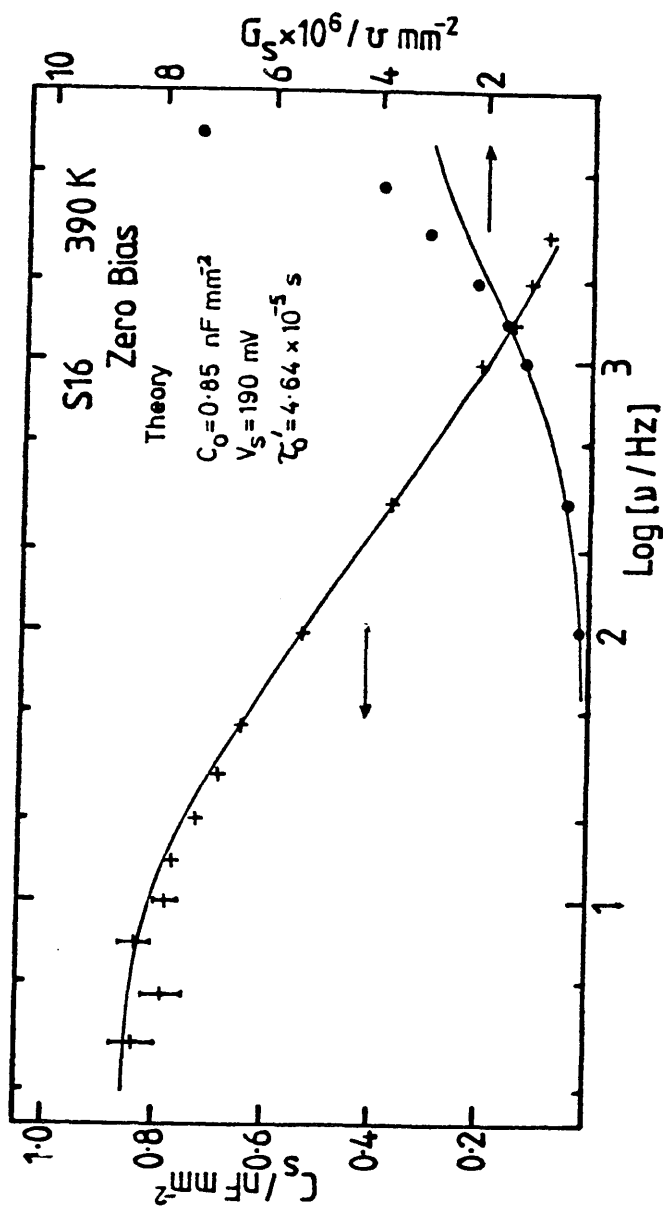


Figure 5.11 The effect of temperature on the measured Capacitance for representative sample produced by the conventional technique after reference 22.

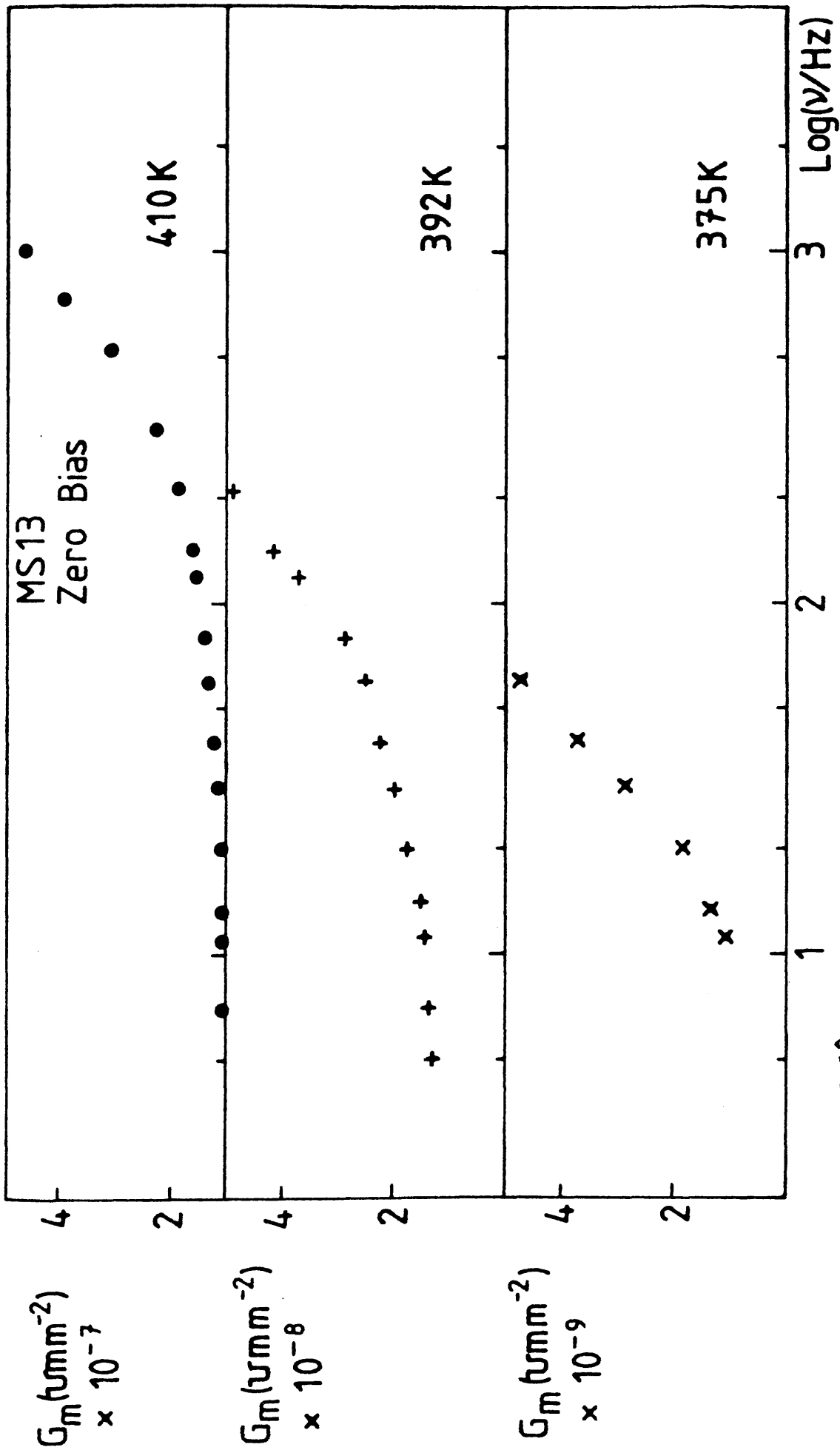


Figure 5.12

Effect of temperature on the measured conductance-frequency plot for sample MS13.

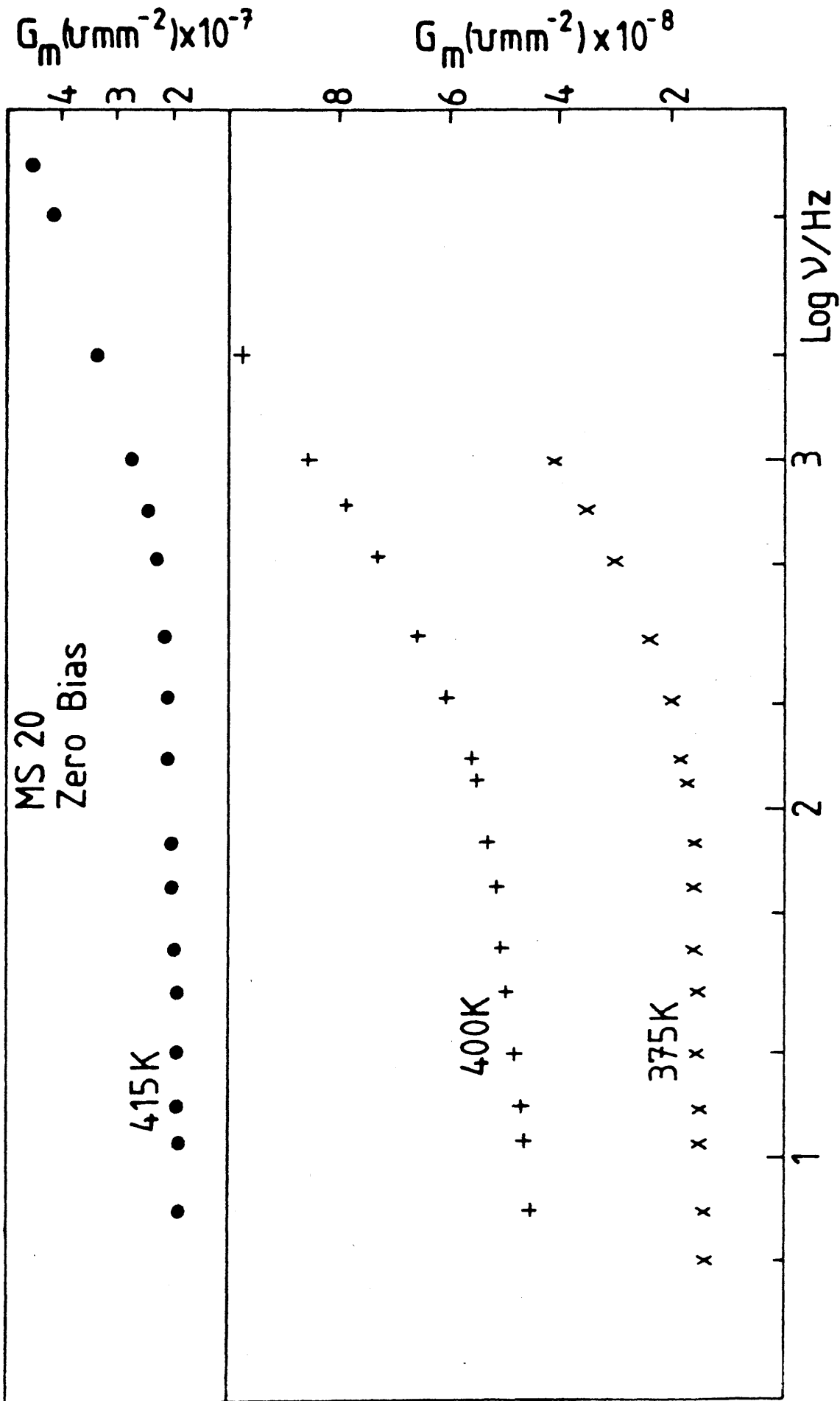


Figure 5.13 Effect of temperature on the measured conductance-frequency plot for sample MS20.

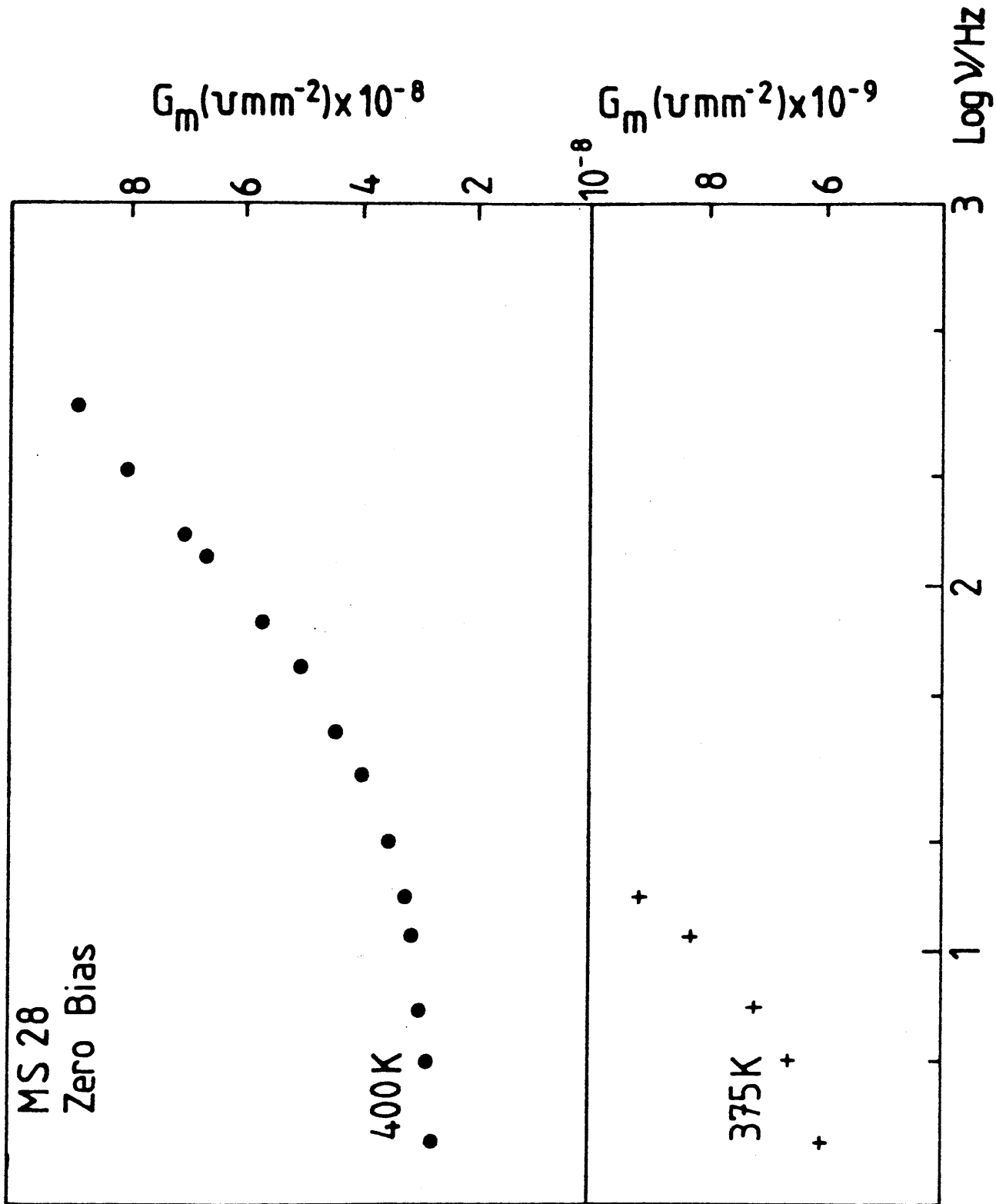


Figure 5.14

Effect of temperature on the measured conductance-frequency plot for sample MS28.

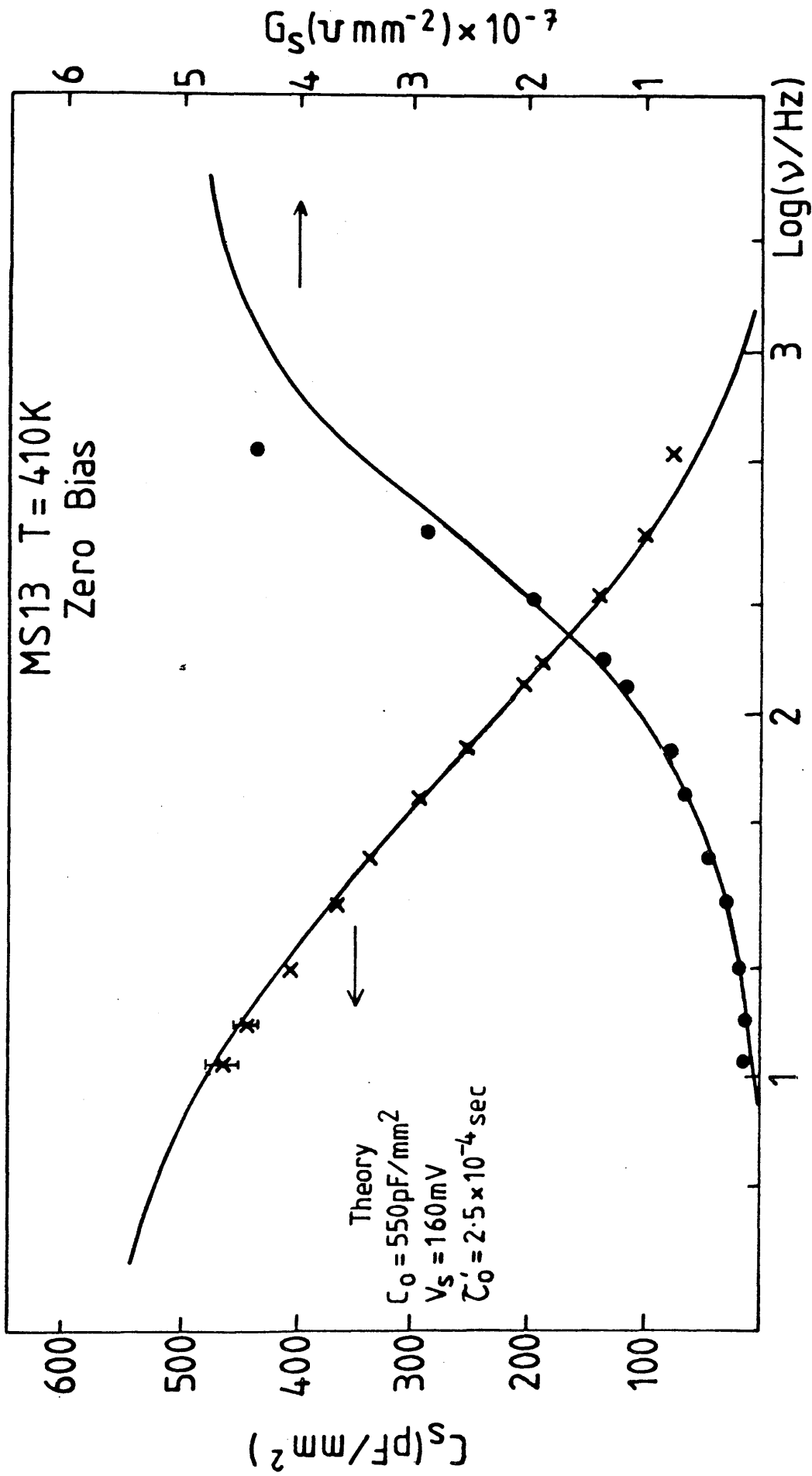


Figure 5.15 Schottky barrier capacitance and conductance as a function of frequency for MS13 at 410K with theoretical fit.

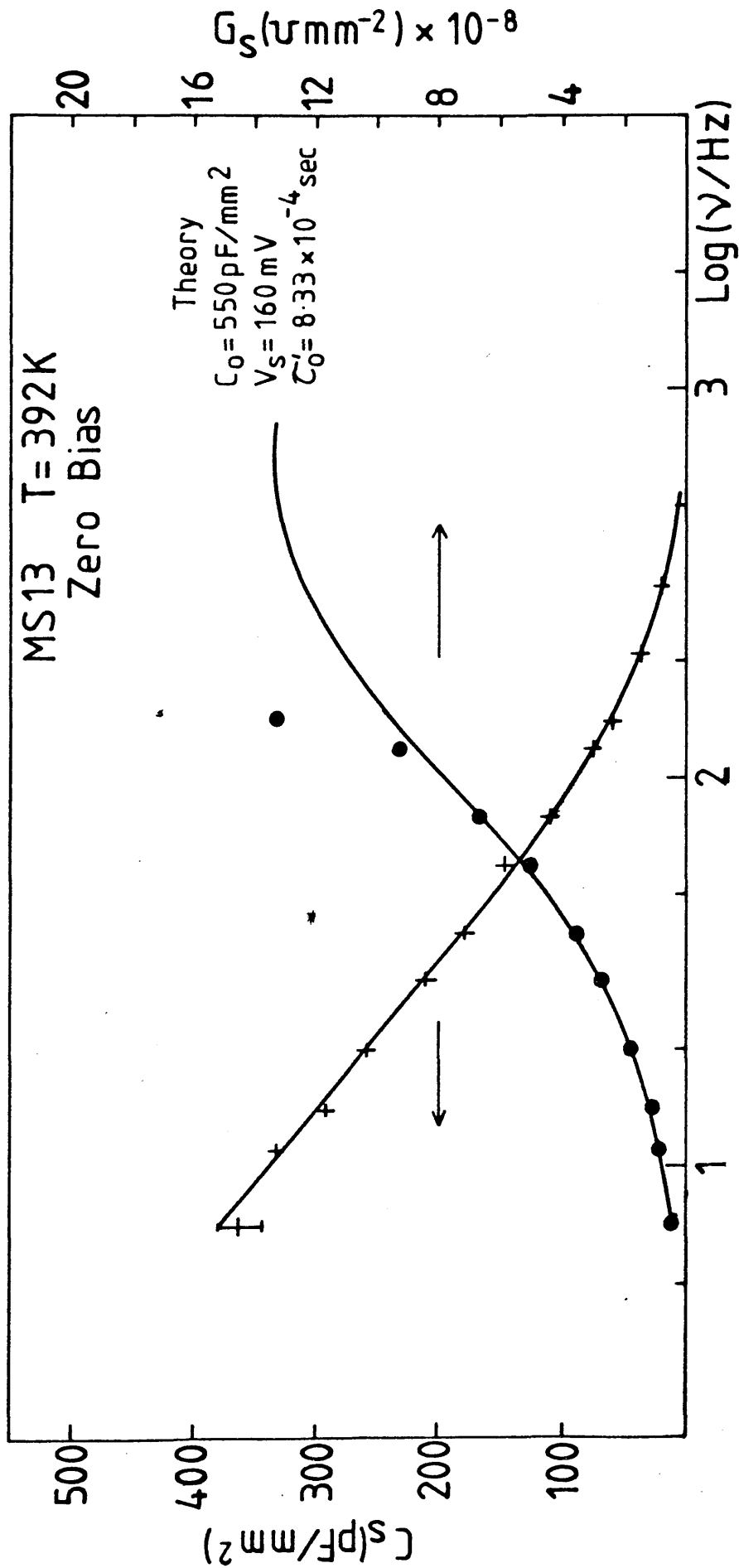


Figure 5.16 Schottky barrier capacitance and conductance as a function of frequency for MS13 at 392K with theoretical fit.

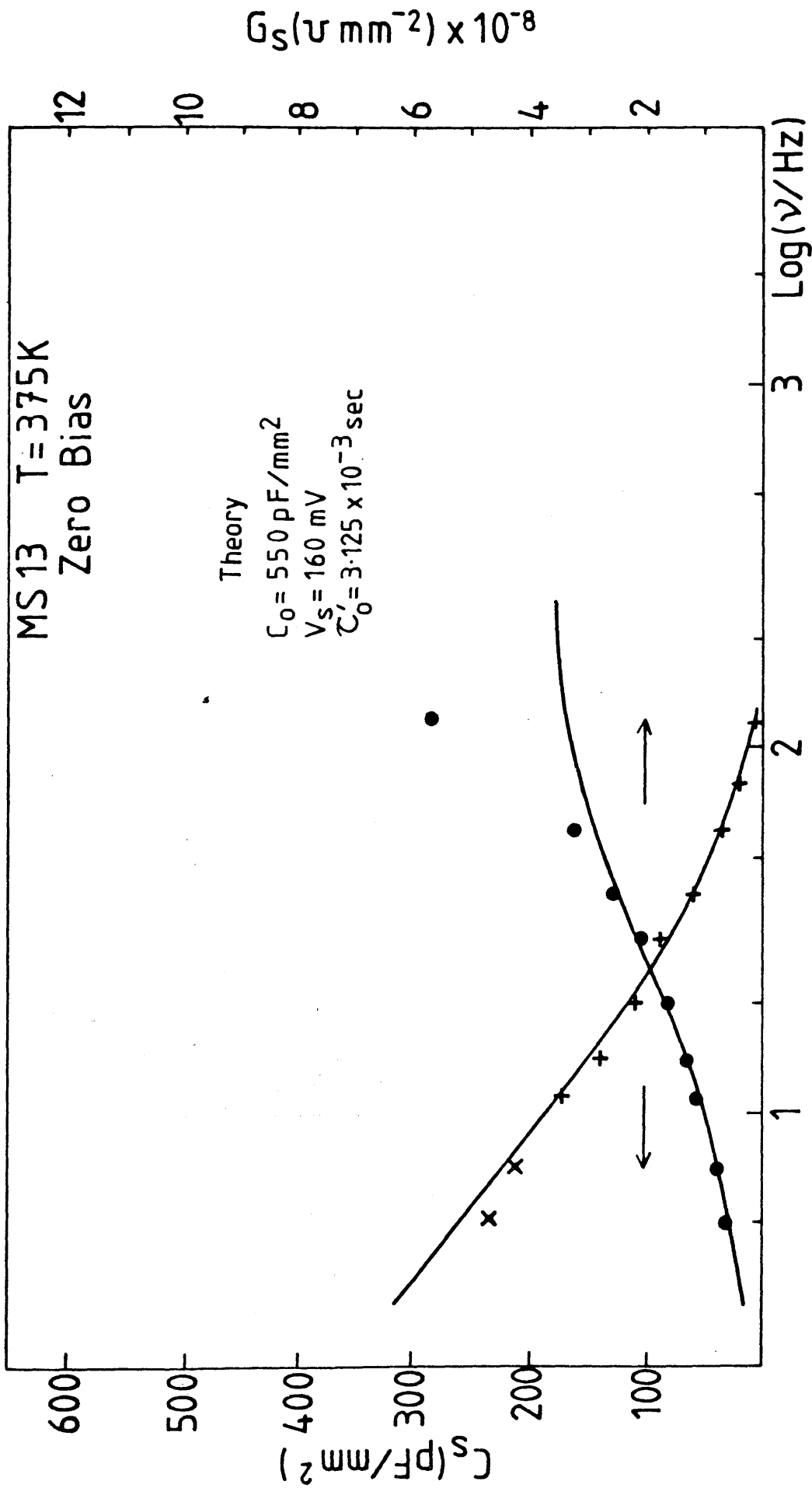


Figure 5.17 Schottky barrier capacitance and conductance as a function of frequency for MS13 at 375K with theoretical fit.

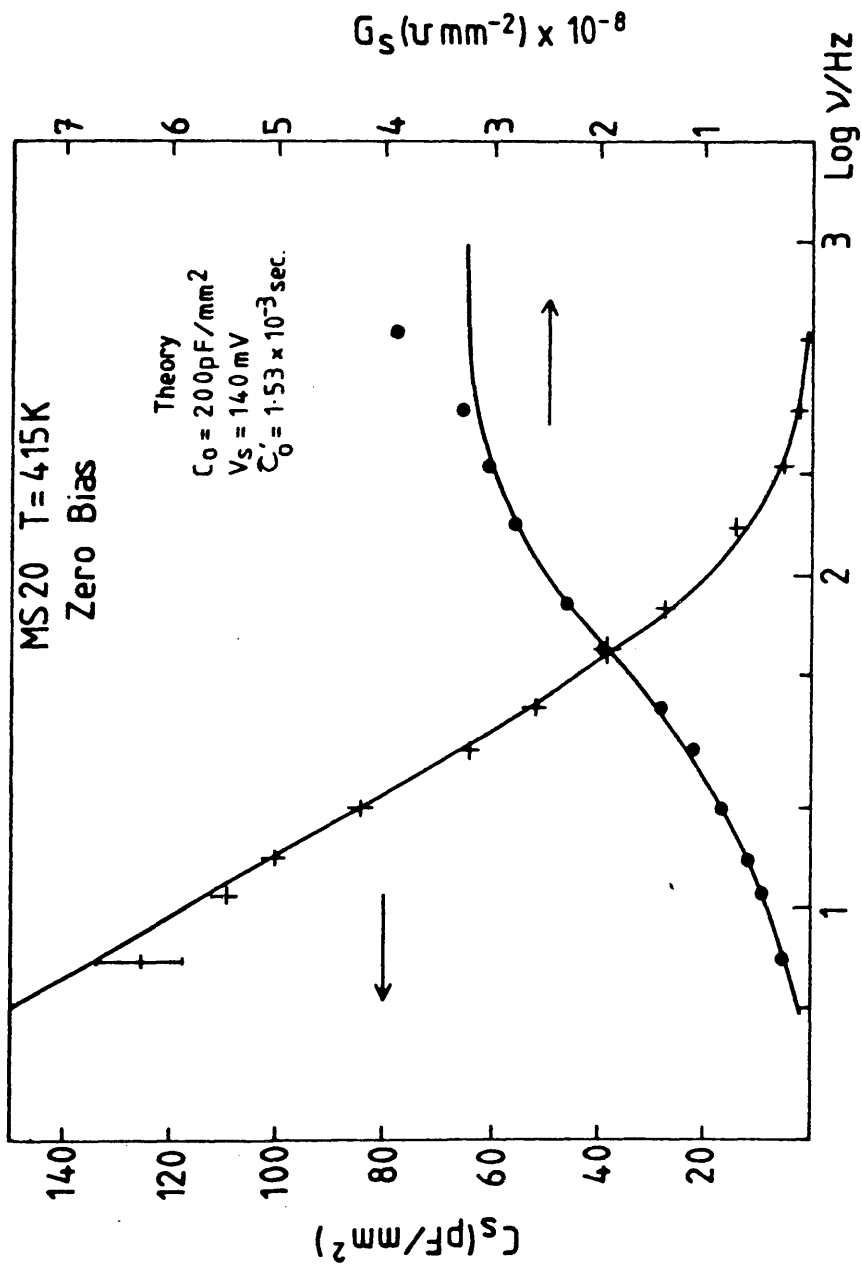


Figure 5.18 Schottky barrier capacitance and conductance as a function of frequency for MS20 at 415 K with theoretical fit.

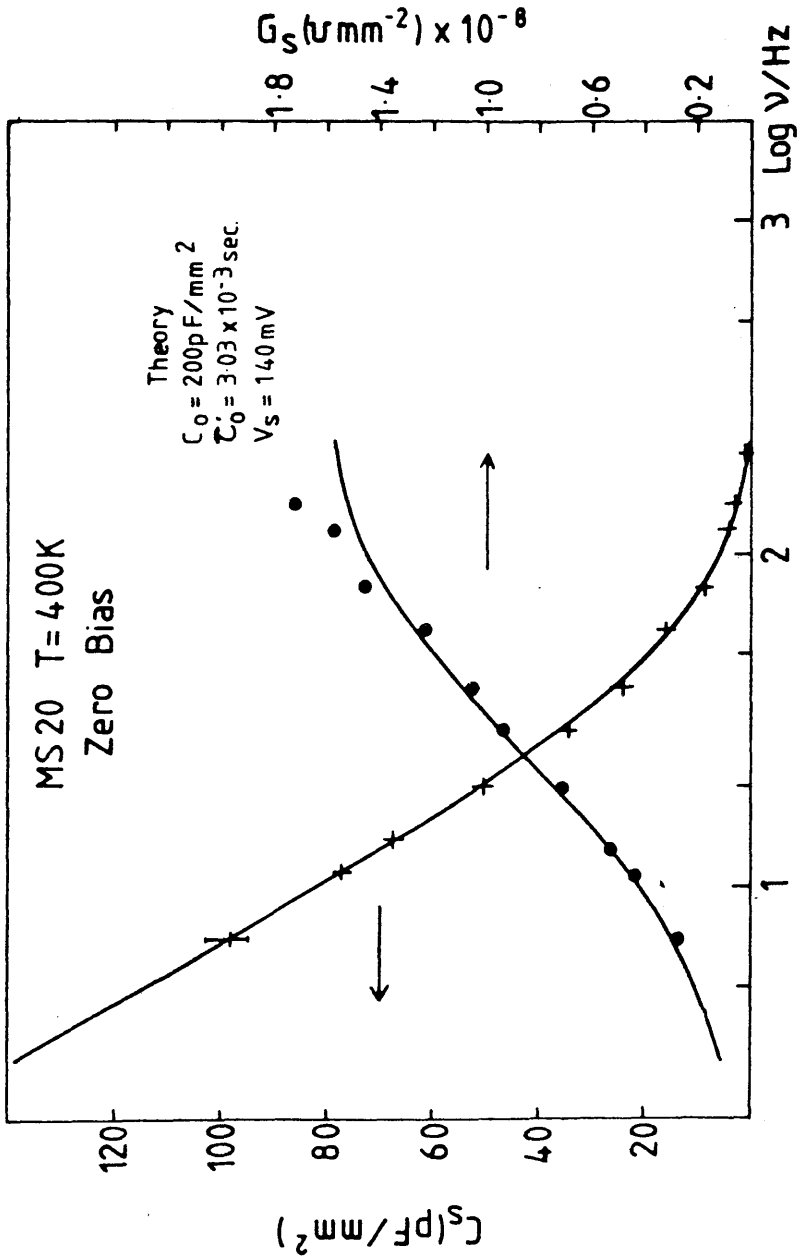


Figure 5.19

Schottky barrier capacitance and conductance as a function of frequency for MS20 at 400K with theoretical fit.

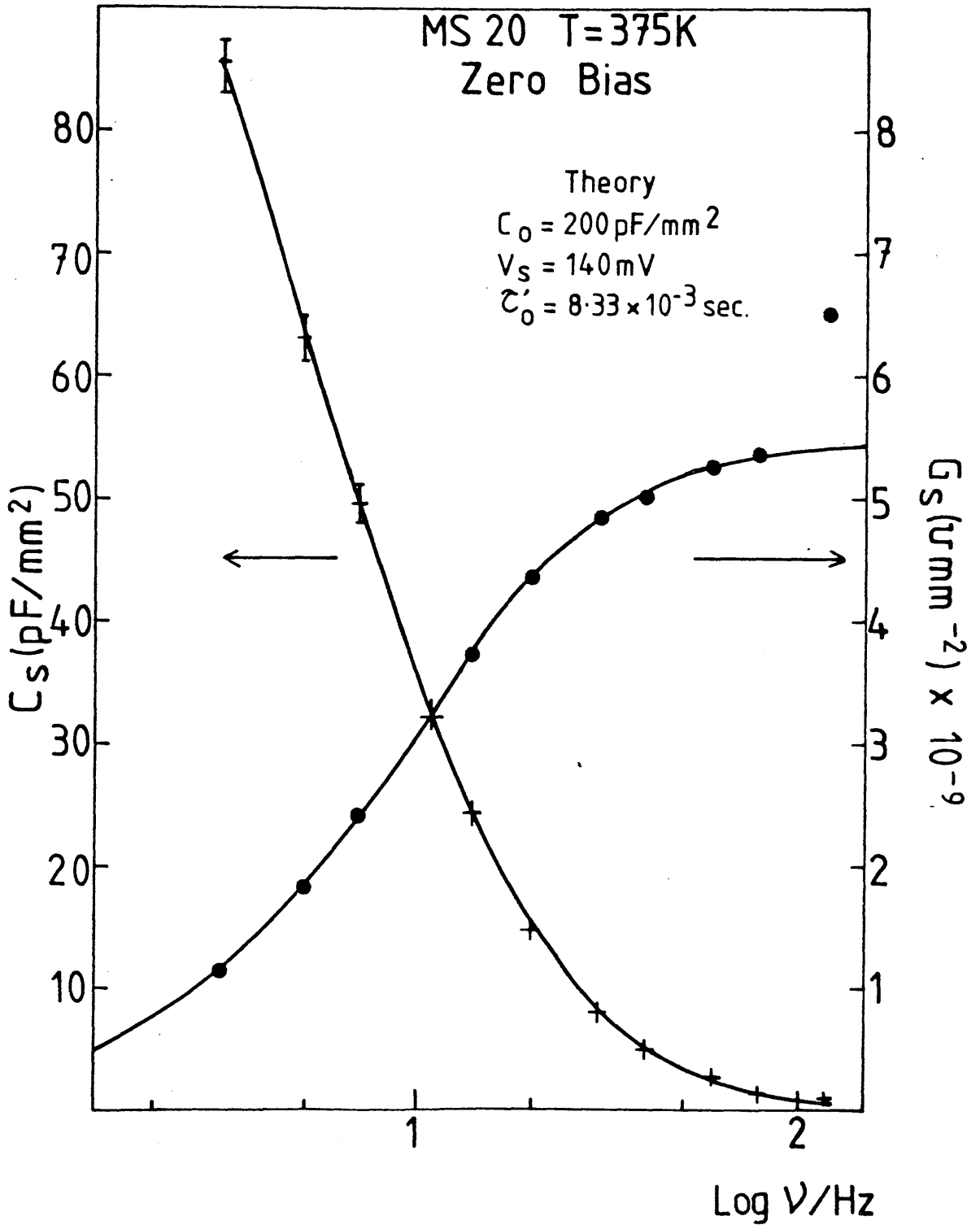


Figure 5.20 Schottky barrier capacitance and conductance as a function of frequency for MS20 at 375K with theoretical fit

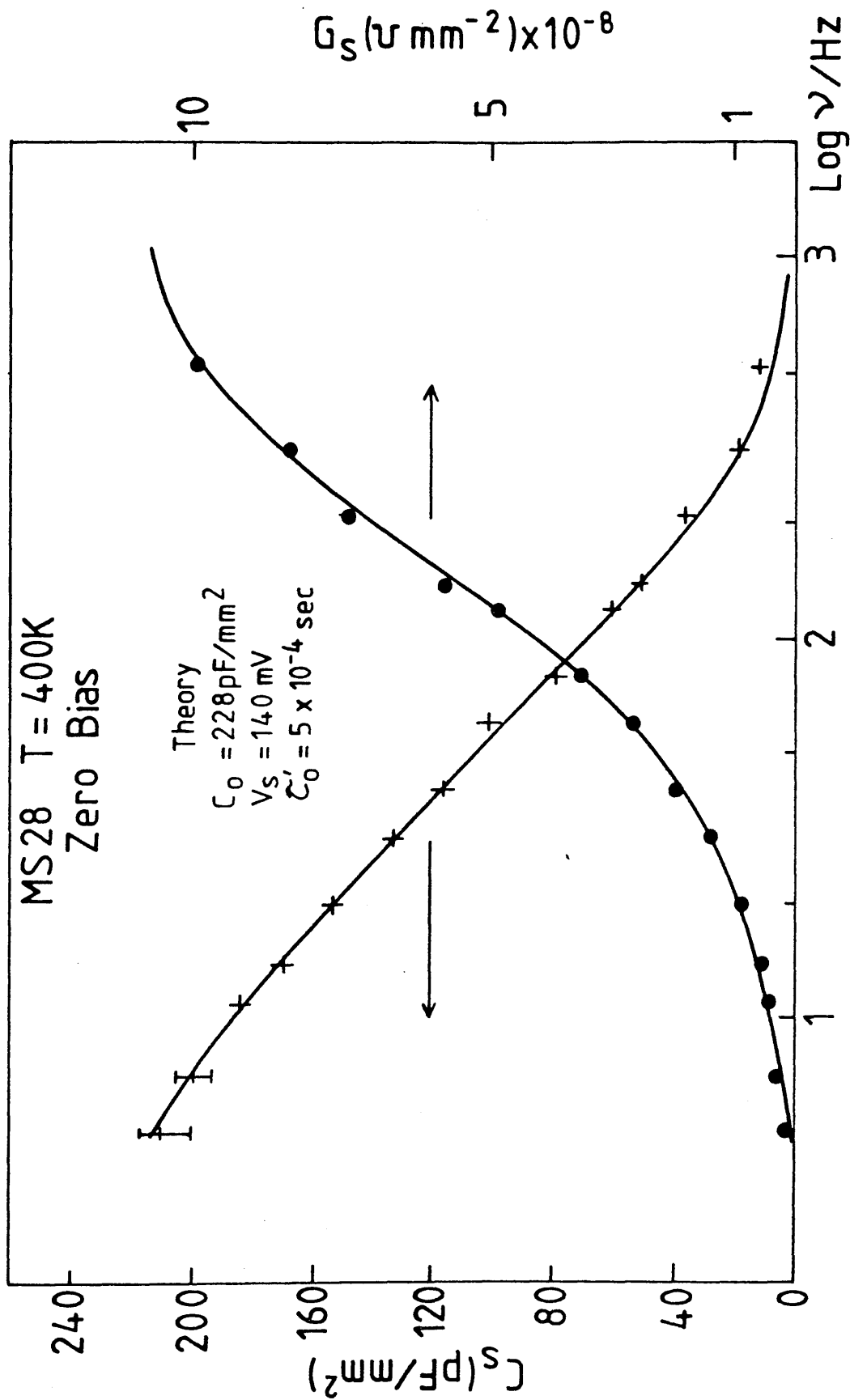


Figure 5.21 Schottky barrier capacitance and conductance as a function of frequency for MS28 at 400K with theoretical fit.

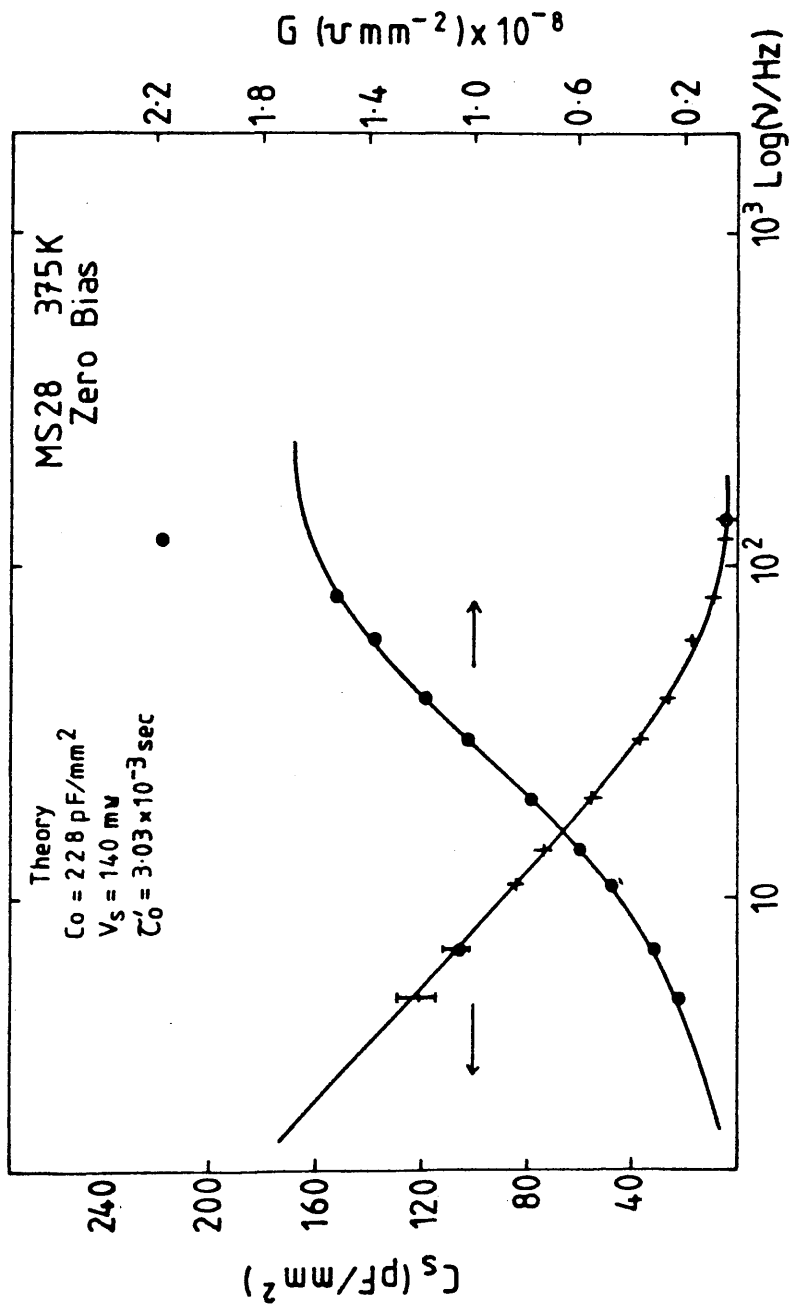


Figure 5.22 Schottky barrier capacitance and conductance as a function of frequency for MS28 at 375K with theoretical fit.

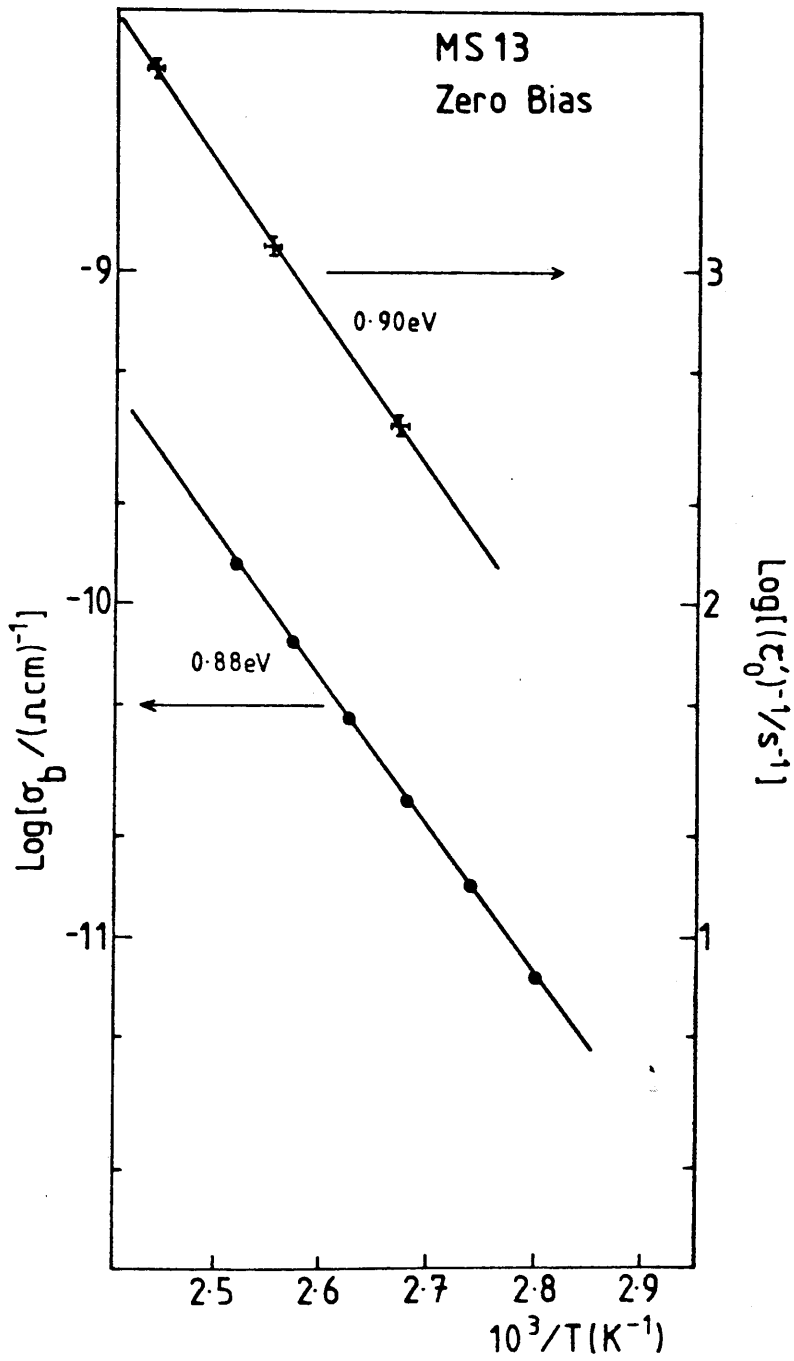


Figure 5.23 Comparison of temperature dependence of bulk conductivity and $(\tau_0)^{-1}$ for MS13

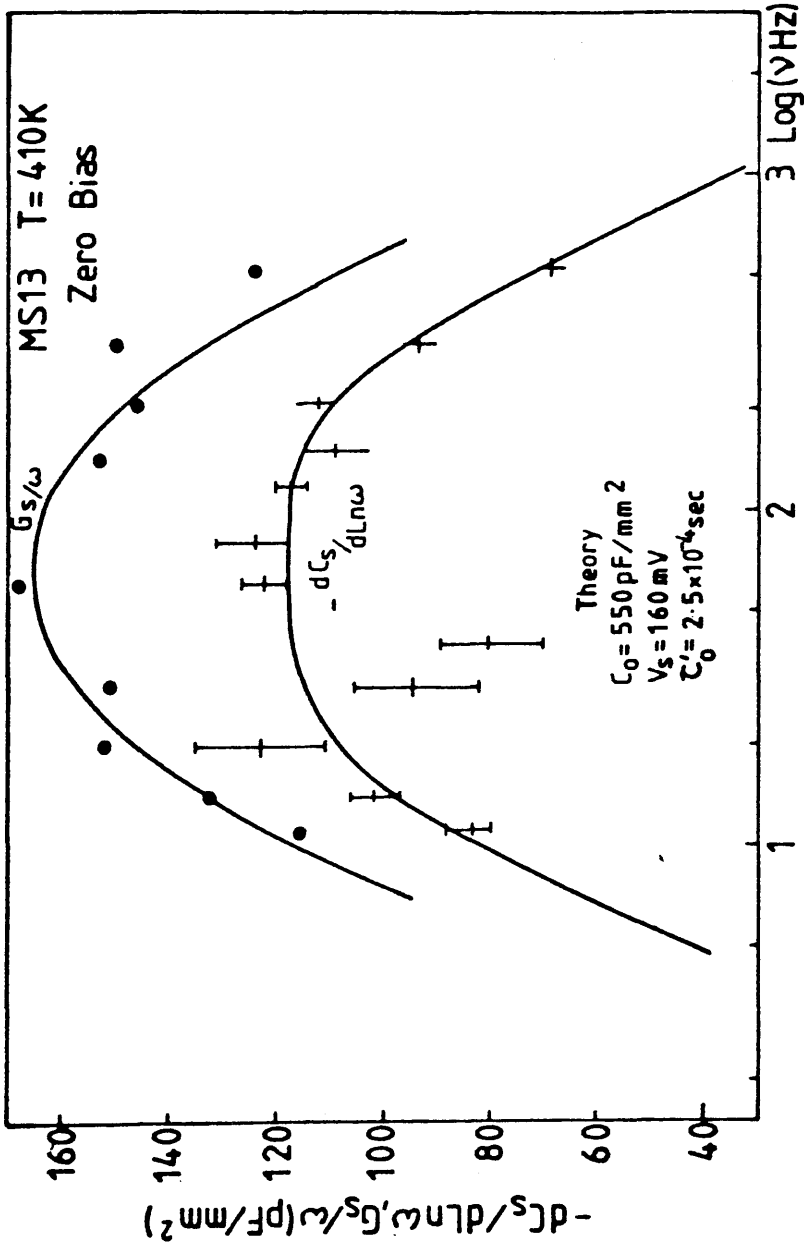


Figure 5.24 Variation of $-\frac{dC_s}{d(\ln(\omega))}$ and $\frac{G_s}{\omega}$ with frequency for MS13 at 410K with theoretical fit.

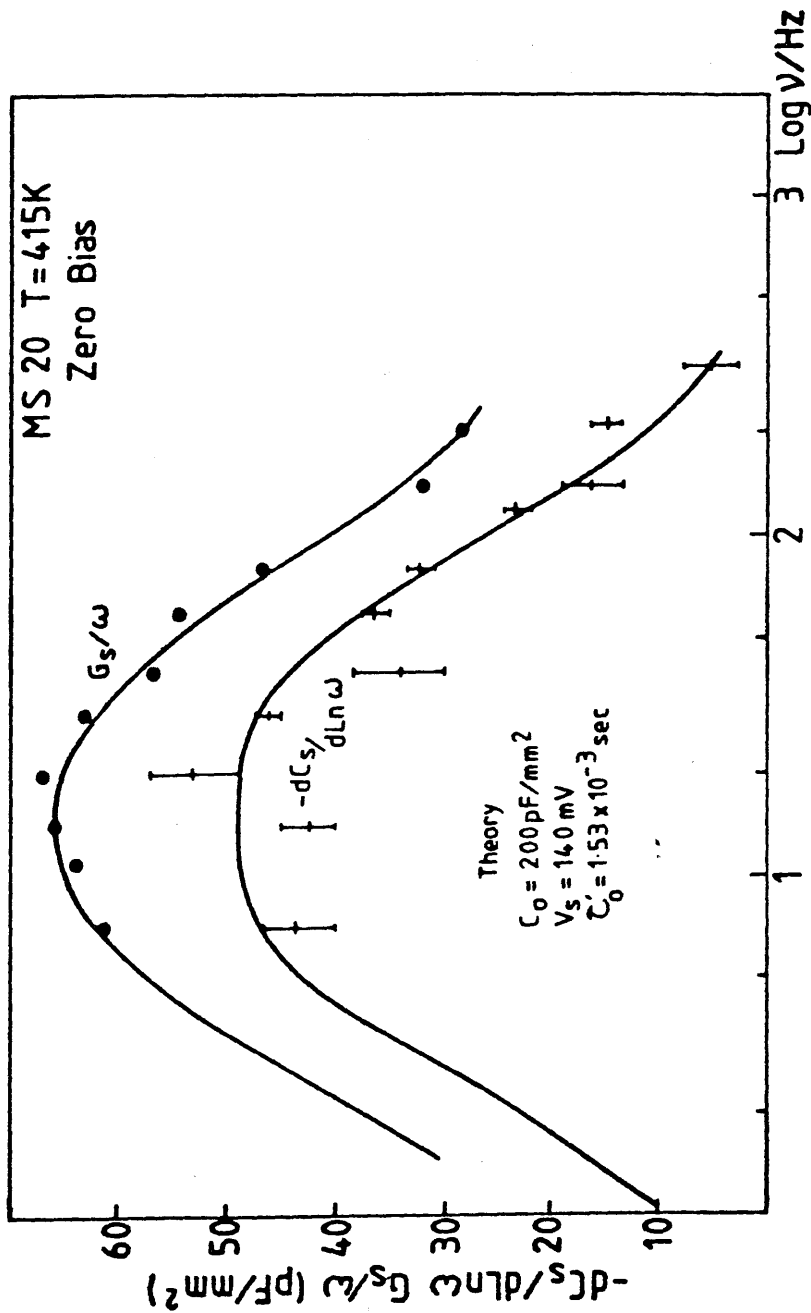


Figure 5.25 Variation of $-\frac{dC_s}{d(\ln(\omega))}$ and $\frac{G_s}{\omega}$ with frequency for MS20 at 415K, with theoretical fit.

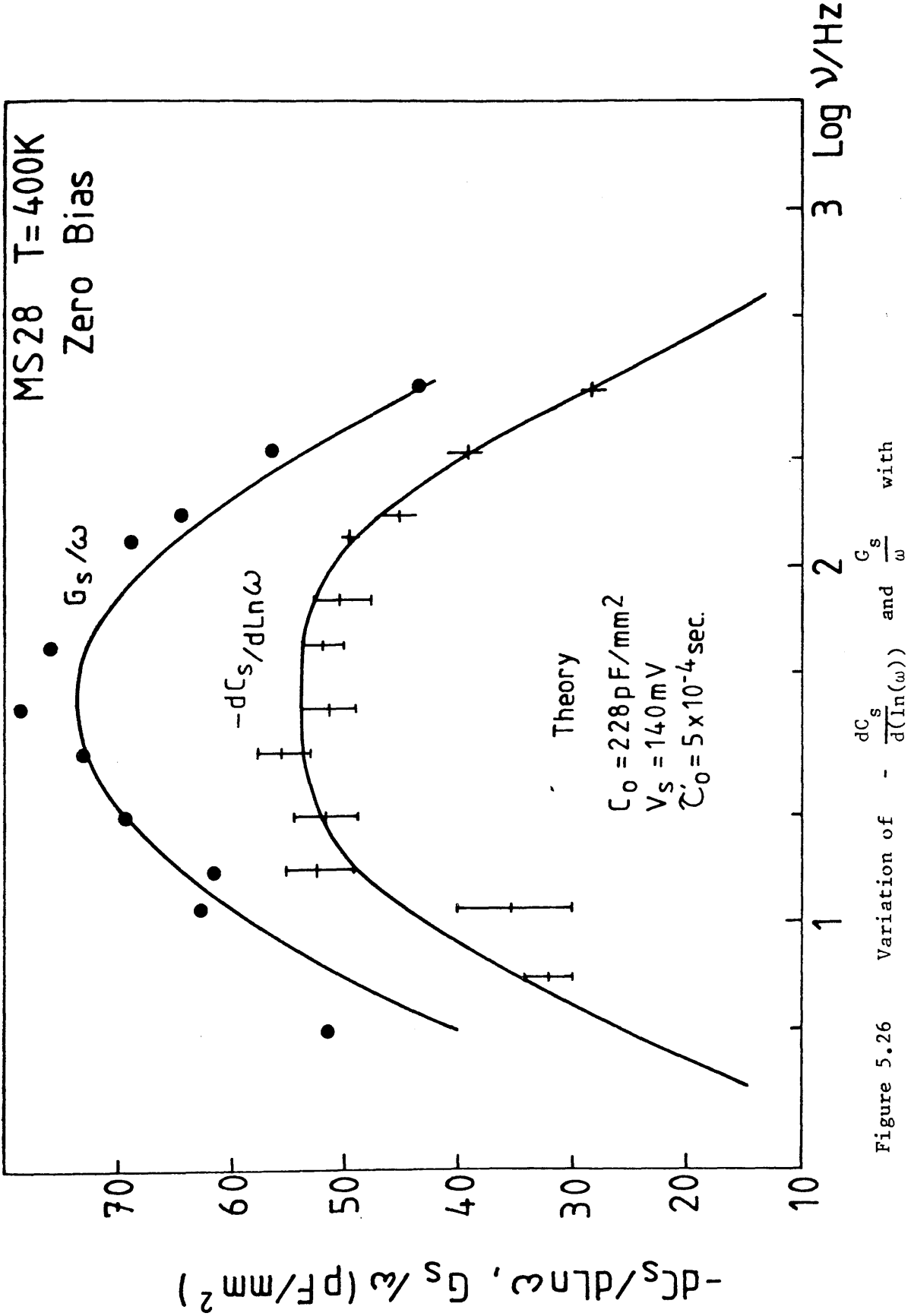


Figure 5.26 Variation of $- \frac{dG_s}{d(\ln(\omega))}$ and $\frac{G_s}{\omega}$ with frequency for MS2 at 400K, with theoretical fit.

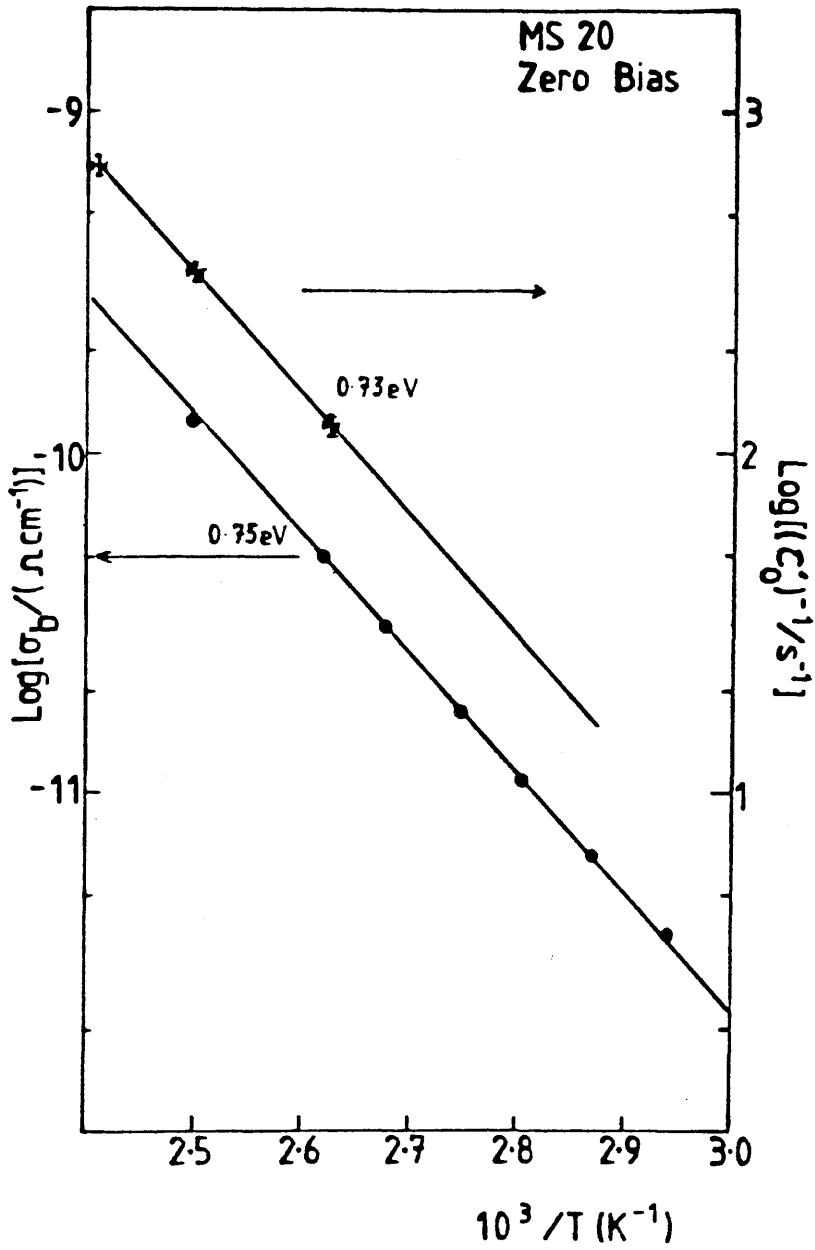


Figure 5.27 Comparison of temperature dependence of bulk conductivity and $(\tau_0)^{-1}$ for MS20

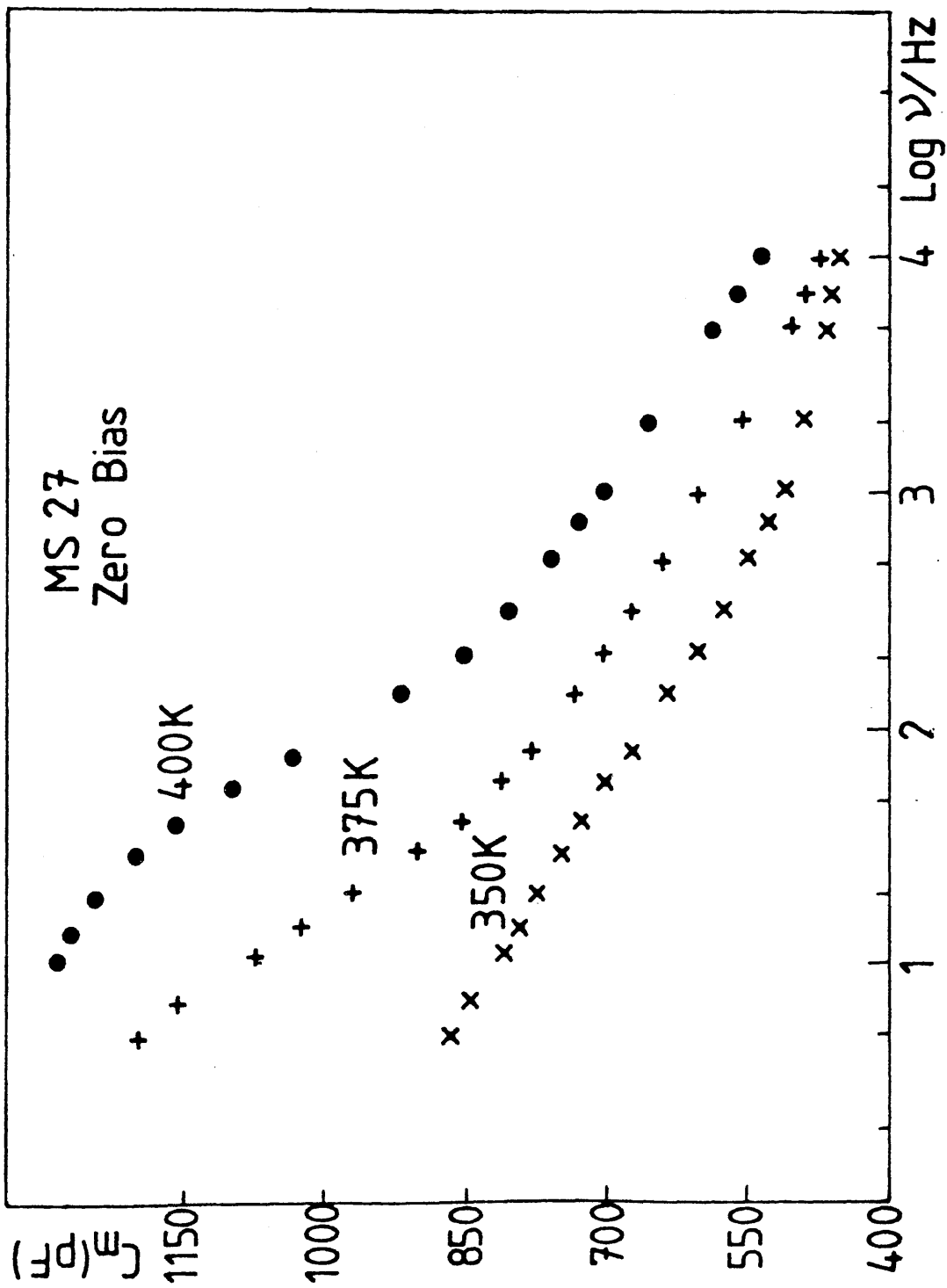


Figure 5.28 Effect of temperature on the measured capacitance-frequency for sample MS27

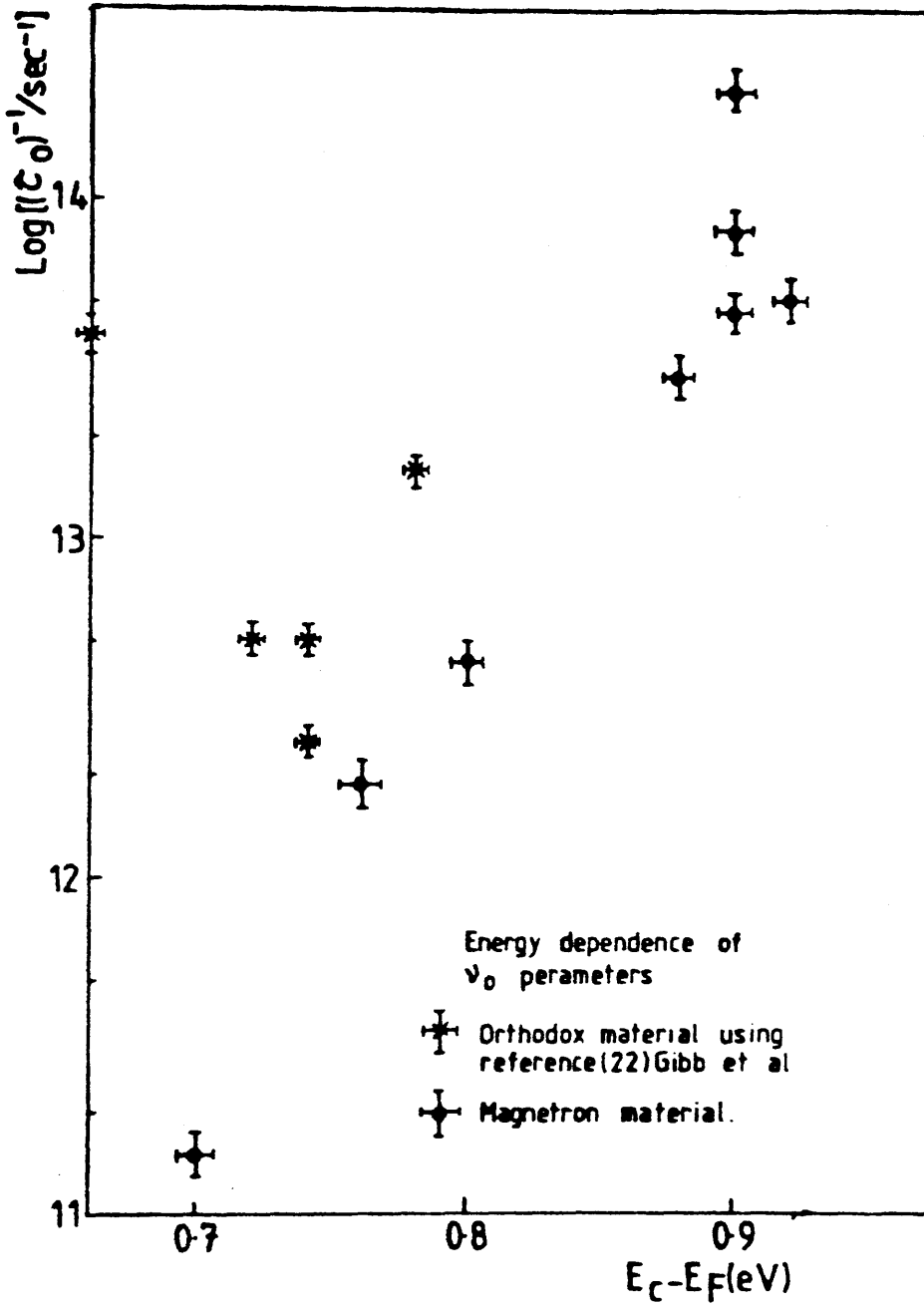


Figure 5.29 E.C. Activation energy

CHAPTER 6. - SCLC EXPERIMENT.

In this chapter we concentrate on the study of the density of states in a-Si:H prepared by the technique described previously and we present the space charge limited current (SCLC) method.

6.1.1. The SCLC mechanism

As discussed in the review chapter, in this experiment, a voltage applied across a thin diode causes an electrode to inject a non-equilibrium density of electronic charge which occupies the empty gap states above the Fermi level E_F close to the injecting contact. At high voltage, a large electron current is drawn and the extra charge extends across the entire sample thickness. Most of the carriers decay into states above E_F filling traps, but a small fraction is thermally promoted to the conduction band edge E_C , increasing the current measured. It is this fraction reflecting bulk enhancement mechanism which is analysed in this experiment to provide information about the density of states above the equilibrium Fermi level.

As outlined in Chapter 2, the basis of SCLC theory was first introduced by Rose (74) and Lampert (75) and summarised by Nespureck et al (76). Later, Weisfield (73) and Solomon (80) refined the analysis and made a great deal of progress. In our view, the physical mechanism of the SCLC is formulated adequately by the approach of Weisfield (73). In the following sections we will concentrate on this formalism and develop some other aspects of SCLC analysis. Starting from the elementary equations, the potential use of SCLC

analysis as a reliable method of determining the density of states is shown.

6.1.2 SCLC Formulation

In this, we consider that the current carrying electrons in the band are assumed to have a constant mobility μ_0 and to obey Boltzmann statistics, so that when the Fermi level is shifted by an amount Δ towards the conduction band the electron density increases from n_0 to $n(x)$ where

$$n(x) = n_0 \exp\left(\frac{\Delta(x)}{KT}\right) = n_0 \exp(u) \quad (6.1)$$

$$\text{where } u = \frac{\Delta(x)}{KT} \quad (6.2)$$

The additional charge density introduced by this displacement of Fermi level can be written in the following form i.e.

$$\rho_0(\Delta) = -e \int g(E) \left[h(E, E_{F0} + \Delta) - h(E, E_{F0}) \right] dE \quad (6.3)$$

where $g(E)$ is the density of states in the film and $h(E, E_{F0})$ is the Fermi occupation function with a Fermi level E_{F0} .

However if we assume that states deep within the energy gap dominate the charge density, and that the density of states is only slowly varying there, then the additional charge density is concentrated between E_{F0} and $E_{F0} + \Delta$. Therefore ρ_0 may be approximated by

$$\rho_0(\Delta) = -e \int_{E_{F0}}^{E_{F0} + \Delta} g(E) dE \quad (6.4)$$

It is usual to express this equation in dimensionless form

$$\rho_0(u) = -eg_0KT \int_0^u \left[g(y)/g_0 \right] dy = -eg_0KT\rho(u) \quad (6.4a)$$

where y is the reduced variable $(E-E_{F0})/KT$, and g_0 is the density of trap states at E_{F0} . The electric field F across the sample varies according to Poisson's equation

$$\epsilon\epsilon_0 \frac{dF}{dx} = \rho_0(u(x)) \quad (6.5)$$

where ϵ is the dielectric constant of the sample.

The relationship between $F(x)$ and $n(x)$ may be described by the following equation i.e.

$$J = e \mu_0 n(x) F(x) \quad (6.6)$$

where J is the current density within the film which is constant at all points.

The corresponding voltage drop across the sample is given by

$$V = V(d) - V(0) = - \int_0^d F(x) dx \quad (6.7)$$

where d is the thickness of the film.

The equations (6.1) (6.4a) (6.5) (6.6) (6.7) define the standard theory of SCLC. It is convenient to express them in dimensionless form using the constants

$$F_C = -g_0 KTed / \epsilon\epsilon_0 ; V_C = -F_C d ; J_C = e n_0 \mu_0 F_C \quad (6.8)$$

when they become

$$\begin{aligned} \frac{n(x)}{n_0} = \exp(u) = \frac{j}{F} & ; \quad \frac{df}{dz} = \rho(u) & ; \quad v = - \int_0^1 f dz \\ \text{(a)} & \qquad \qquad \text{(b)} & \qquad \qquad \text{(c)} \end{aligned} \quad (6.9)$$

The reduced variables are defined by

$$f = \frac{F}{F_C} ; \quad j = \frac{J}{J_C} ; \quad v = \frac{V}{V_C} ; \quad z = x/d \quad (6.10)$$

To solve the equations numerically we need to make a substitution for u in equation (6.9b) using (6.9a), and integrate across the film to give $f(z)$. For this we require a boundary condition at $z = 0$. In common with other workers we assume that $f(0) = 0$; i.e. that there is an infinite reservoir of majority charge at the injecting contact at the origin, the discussions of which is followed in the next sections. In this case $f(z)$ is given by

$$\int_0^f \frac{df}{\rho(\ln(J/f))} = z \quad (6.11a)$$

Hence the quantity v may be obtained by the direct integration of $f(z)$ from equation (6.11a).

A different approach to the calculation of v is to re-express the differential term in (6.9b) as $-f \frac{df}{dv}$ and integrate to give

$$\int_0^{f_d} f df / \rho(\ln(j/f)) = -v \quad (6.11b)$$

where f_d is the reduced field at $z=1$. f_d can then be eliminated between (6.11a) and (6.11b) to give $v(j)$.

Weisfield (73) and Zmeskal et al (83) write similar integral equations, expressed in terms of the variable u . Expressed in reduced units these are

$$\frac{1}{j} = \int_{u_d}^{\infty} \frac{\exp(-u) du}{\rho(u)} ; \quad \frac{v}{j^2} = - \int_{u_d}^{\infty} \frac{\exp(-2u) du}{\rho(u)} \quad (6.12)$$

where u_d is the value of u at the back contact. The importance of equations (6.12a) and (6.12b) lies in the inversion procedure which can be deduced from them which is discussed in the following section.

6.2 Deduction of the Density of States

6.2.1 The Direct Method

In principle, it is possible to determine the density of states $g(E)$ near the fermi level by fitting procedures. For this purpose, we construct mathematical forms for various models which may describe the possible mechanisms characterising SCLC behaviour in a-Si:H. Having established these models, we calculate the corresponding current-voltage curves by numerical integration using computer programs. The main function of the programs used is the same. The exact solution of equation (6.9b), describing the electric field across the film, is obtained by numerical integration, then the corresponding voltage is obtained by direct integration of $f(z)$ as outlined in section (6.1.2). The values of the quantity v obtained by this method are then plotted in the form of $\log j$ versus $\log v$ in dimensionless terms. To derive the density of states $g(E_F)$, real experimental data, expressed in reduced units is fitted to the theoretical curves by adjusting the parameters of the model. Solomon et al (80) used this method to estimate the density of states $g(E_F)$ for their glow discharge material. However, on physical grounds, the method can be improved to take into account several other important points. It is worthwhile mentioning en passant that a spatially non-uniform

density of states has never been reported nor has any suggestion about the surface layers and their related problems. In the following paragraphs we will review the various models mentioned above.

Illustrated in Figure (6.1) are some possible forms of $g(E)$ which may account for the SCLC characteristics.

a) The constant density of states model.

As usual we consider a simple form of the density of states. We assume g_0 to be constant and large enough so that the space charge is concentrated in deep states i.e. $(n(x)-n_0) \ll g_0 \Delta(x)$ and $(n(x)-n_0)$ is negligible.

In this case, the charge density $\rho(u)$ becomes

$$\rho(u) = -e g_0 u$$

and using equation (6.5), we obtain

$$\frac{df}{dz} = \ln\left(\frac{j}{f}\right) \quad (13.a)$$

in reduced units.

Integrating and inverting, equation (13.a) leads to the following form

$$\frac{J}{d} = \frac{en_0 \mu g_0 KT}{\epsilon \epsilon_0} \mathcal{F}_1\left(\frac{V}{V_c}\right) \quad (6.14)$$

As a result, we obtain the more common scaling law which is valid for homogeneous samples. This means that for a series of films differing only by their thickness d , the $J(V)$ curve must satisfy at a given temperature the general law

$$\frac{J}{d} = \mathcal{F}_2\left(\frac{V}{d^2}\right) \quad (6.15)$$

By similar methods one can derive ^{curves for} exponentially increasing and decreasing $g(E)$. It is worth mentioning that we have

tested other forms of $g(E)$. In general, the corresponding $j(V)$ characteristics are controlled by two parameters the inset voltage V_C and the steepness of the curves ℓ , where ℓ is defined by the ratio of two given temperatures ℓ ^(See p 41). However, experimental data obtained suggests that a simple exponential decrease or increase of the density of states is unlikely to provide accurate analysis of a real SCLC mechanism in a-Si:H. To analyse adequately the temperature dependence of SCLC characteristics obtained, a new model of the density of states is needed. This will be discussed later when we introduce a more elaborate analysis of the SCLC characteristics.

6.2.2 Deduction of the Density of States from SCLC Characteristics (Inversion procedure).

As discussed in section (6.2.1), the simplest method for the determination of the density of states involves fitting procedures whereby an experimental curve is fitted to a calculated curve by adjusting some parameters. In this section, the inverse problem is solved and the explicit derivation of the density of states is obtained from experimental current voltage characteristics. Weisfield (73) has given the procedure to solve the inverse problem using equations (6.12a) and (6.12b) outlined above.

Explicit expressions for u_d and the charge density $\rho_o(u)$

$$u_d = \ln \left(Jd / n_o e \mu_o V (2-\alpha) \right) \quad (6.16a)$$

$$\rho_o(u_d) = -V \epsilon \epsilon_o \left[(2-\alpha) (1-\alpha) + \beta \right] / d^2 \quad (6.16b)$$

are derived, in terms of the logarithmic derivatives of the characteristic

$$\alpha = \frac{d \ln V}{d \ln J} ; \quad \beta = \frac{d \alpha}{d \ln J} ; \quad \gamma = \frac{d \beta}{d \ln J} \quad (6.17)$$

Then under the assumption that all the charge is concentrated at the Fermi level, i.e. that (6.4a) is satisfied, equation (6.16b) may be further differentiated to give an explicit expression for $g(u_d)$

$$g(u_d) = \frac{V \epsilon \epsilon_0}{eKTd^2} \left[\alpha(2-\alpha) + \frac{\gamma-\beta}{1-\alpha+\beta/2-\alpha} (3-2\alpha) \right] \quad (6.18)$$

Using (6.16a) and (6.18), the density of states may be deduced as a function of u from the experimental data. Zmeskal et al (³³) give an exactly equivalent expression for the density of states, but derive the u value to be associated with the $g(u)$ from an analysis of the temperature dependence of the SCLC characteristic. In this work we have used the Weisfield inversion procedure, which we believe to be accurate within the stated assumptions.

The approach, so far, has been to establish a theoretical formulation of SCLC. We have shown in section (6.1.2) that starting from elementary equations, various models of the density of states distribution can be described. In section (6.2.2) we have presented a more elaborate approach to deduce the density of states. To illustrate the integration method discussed in section (6.2.1) and the inversion procedures of section (6.2.2) we consider briefly the well known case of a constant density of trap states at the fermi level, for which the density of

states function $\rho(u) = -e^{-u/g_0} kT u$. In Figure (6.2) we plot the computation of $j(v)$ curve made using equations (6.11a) and (6.9c). Also given in this figure is an inversion of the computed characteristic made using versions of (6.16a) and (6.18) expressed in reduced forms

$$u_d = \ln(j/v (2-\alpha)) \quad (6.19a)$$

$$\frac{g(u_d)}{g_0} = v \left[\alpha(2-\alpha) + \frac{\gamma-\beta(3-2\alpha)}{1-\alpha+\beta/(2-\alpha)} \right] \quad (6.19b)$$

This double inversion gives an $g(u_d)/g_0$ in agreement with value assumed to better than 1%. It should be noted that

(i) In order to calculate accurately the derivatives of the characteristic it is necessary to take data points over a considerable range (an order of magnitude in current density in this case). This is indicated by the error bars on the u axis. In practice, the SCLC inversion procedure always involves a significant smoothing effect of this type and hence is only applicable to slowly varying density of states functions.

(ii) For regions of the characteristic where the deviations from linearity are small, the effects of truncation errors on the inversion process increase greatly leading to large errors in the $g(u)/g_0$ values. This effect is of course much more significant still when experimental data rather than numerically obtained values are inverted, as will be shown in the following sections.

6.2.3 The Role of States away from the Fermi Level in Determining SCLC Characteristics.

In this section we examine in more detail the consequences of some of the more critical assumptions made in deriving the SCLC equations. The removal of these assumptions is found to be of considerable importance in discussing data obtained from hydrogenated amorphous silicon films. We consider firstly, the role of space charge trapped in states far from the fermi level, in for example the localized states in the band tails. This problem has already been considered in some detail by Orton and Powell (120), using the constant u approximation to the exact SCLC solutions. Orton and Powell compute J-V characteristics numerically for a number of realistic density of states models (Classical F.E, DLTS, step and exponential models). Their curves are dominated at low voltages by states near the fermi level, but at high voltages they go over to the v^2 behaviour expected for shallow traps (Lampert and Mark (76)). It is straightforward to perform equivalent calculations using the full Poisson's equation as described in the previous section. For this we consider the model of the density of states distribution of the form shown in Figure (6.1. Curve 3) where the density of states increases in a step at an energy E above the fermi level to a value g_1 ($g_1 \gg g_0$). Assuming that Boltzmann statistics apply in the region of the step, it is straightforward to add the contribution from above the step to the charge density, giving

$$\rho(u) = u + \Gamma(\exp(u) - 1) \quad (6.20a)$$

$$\Gamma = \frac{g_1}{g_0} \exp - \frac{(E_1 - E_{F0})}{KT} \quad (6.20b)$$

Although the form of the density of states distribution described by equation (6.20) appears to be very limited, in practice any density of states which increases above E_1 at least as rapidly as $\exp(-\frac{E_1}{KT})$ leads to a similar form for ρ and thus to similar results. For example for the linear band tail considered by Orton and Powell (120), g_1 is replaced in (6.20b) by $g_1 \left(\frac{KT}{E_0}\right)$, where E_0 is the width of the tail and g_1 is now the density of states at $E_1 + E_0$. In Figure (6.4), $j-v$ characteristics computed for the ρ function in (6.20a) are plotted. These are similar to the curves given by Orton and Powell, though they are plotted in reduced form. For $\Gamma \ll 1$, the onset of non linearity defined by V_C is determined by the constant density of states g_0 and the v^2 behaviour begins when $\Gamma \exp(u) > 1$. It can be shown analytically that $j \sim \frac{g_0 v^2}{8\Gamma}$ in this region. Analytically, this becomes, using the relations below in reduced forms

$$\text{From (6.9b)} \quad \frac{df}{dz} = \rho(u)$$

$$\text{and} \quad -f \frac{df}{dz} = \rho(u)$$

$$\text{also} \quad \exp(u) = \frac{j}{f}$$

For $\Gamma = 1$ when this quantity is absorbed into the constant field V_C so that

$$V_C = \frac{eKTd^2 g_1 \exp(-E_1/KT)}{\epsilon \epsilon_0}$$

on integration, the equations above give

$$\frac{z+f}{j} = \ln\left(\frac{j}{j-f}\right) \quad (6.21a)$$

$$-v = j^2 \ln\left(\frac{j}{j-f}\right) - jf - \frac{f^2}{2} \quad (6.21b)$$

When solved for $z = 1$, these give $v(j)$, then

for $j \ll 1$ we obtain the usual ohm relation i.e. $j = -v$

and for $j \gg 1$ and integrating for the complete film $j = \frac{9}{8} v^2$

For $\Gamma > 1$, the onset voltage V_c is determined by the quantity ΓV_c (for low values of Γ) and the characteristic goes over immediately to a v^2 variation; the states in the step are completely dominant. The characteristics are thus strongly influenced by the value of the quantity Γ which from (6.20b) is temperature dependent. Hence an important prediction of this model is that the reduced current voltage characteristics will depend strongly on temperature (as opposed to the constant density of states case of Figure (6.2) where the $j-v$ characteristic is universal). This result is also implicit in the work of Orton and Powell.

The analysis of this model density of states is extended further by inverting the $j-v$ curve using the Weisfield procedure (equation 6.19). The results of such computations for two values of Γ are given in Figure (6.4) superimposed on the original density of states. Agreement between the original and the deduced density of states is rather poor; the computed values show a tendency to rise above the constant value. This result is not particularly surprising in that, by including the effect of states far

away from E_F , we have violated the assumptions under which the inversion procedure was derived. It is important though to emphasise this point. If the density of states includes a step close enough to E_F to contribute significantly to $\rho(u)$ then the results for $g(u)$ obtained from the inversion method are unreliable and it is not possible to deduce unambiguous information about the energy dependence of the density of states. As we shall see later, when the analysis scheme is put into practice, this problem is of considerable significance.

Fortunately there is a simple procedure for identifying when states far from the equilibrium fermi level need to be considered, and that is to look at the temperature dependence of the characteristics. If the shape changes rapidly with temperature, as in Figure (6.4), then such states are important and need to be accounted for. Some results of this type of analysis are given in the following sections.

6.2.4 The influence of spatial non uniformities in the film on the SCLC Characteristics

As discussed in the review chapter an assumption of some importance made during the standard analysis of the SCLC is that the film is spatially uniform and hence has the same density of deep gap states everywhere. This assumption is known however to be only a first approximation to the real behaviour; measurements of the transverse field effect in a-Si:H, which are sensitive to the density of states in the surface region, invariably produce g_0 values much greater than those obtained from bulk measurements such as those of

capacitance-frequency characteristics or from DLTS as discussed in the review chapter. We can show that a surface layer containing a higher density of states than the bulk will have a significant effect on the SCLC characteristics by performing another simple model calculation. We firstly integrate equation (6.11) for a number of different j values, and for surface layers of thickness 1% and 5% of the total at the injecting contact and different, enhanced but constant state densities. The spatial variation of the electric field for such composite films is compared in Figure (6.5) with that for equivalent films without the surface layer. For low values of j (the linear part of the SCLC characteristic) little difference is observed. However above $j \sim 1$, the high density surface layer allows the electric field to increase much more rapidly at small values of z .

As might be anticipated, this has no effect on the electric field profile in the bulk of the film, and only a minor effect at the back contact. When the $f(z)$ curves are integrated to give the voltage drop across the film, v , in the presence of the surface layer, will be greater than the value obtained without and hence the SCLC characteristic will be less non-linear, as shown in Figure (6.6).

In practice, if a set of real experimental data taken from a film with a large density of states at the injecting contact is analysed assuming that it is uniform using the methods described previously, then the density of states/

deduced will be higher than the bulk value. This is illustrated in the inset of Figure (6.6) where the density of states deduced by inversion is plotted against the integrated number of states in the film. There is an approximately linear relation between the two, and indeed the states in the surface layer contribute to the total with a relative weight compared with bulk states of approximately 2. This result has important implications for the scaling of SCLC data with film thickness. It is equally important for the results of Schottky barrier analysis performed on samples prepared under similar conditions but with exposure to atmosphere prior to metallization, as discussed in Chapter 5. Oxidising the surface, in this case, helps to neutralise the reactive part of it, and hence allows the rectifying behaviour of the Schottky diode to be observed. This suggests that the film properties at the surface are different from those in the bulk. Considerable evidence was found (Gibb et al (22)) for the presence of an enhanced density of states in a thin layer close to the metal-semiconductor interface. Such surface states are most probably responsible for the failure to observe a strong field effect in sputtered a-Si:H (as in the glow discharge material) unless the surface is specially treated (Weisfield and Anderson (34) Weisfield et al (121), I.G. Gibb, Ph.D thesis).¹²⁶ Powell and Pritchard (122) have also shown the effect of surface states and fixed charge, at both contacts, on the field effect conductance of amorphous silicon. Solomon et al (80) have shown that thin samples of a-Si:H have SCLC characteristics which imply a higher density of states than for thick samples. Our calculations imply

that Solomon's results may reflect a large number of states in a surface layer, which will have a more significant effect for thin films, rather than a higher uniform bulk density. There is no obvious way of distinguishing between these two models when a single SCLC characteristic is examined. However, the calculation does suggest one important test of any experimental data. Because the j-v curve is strongly influenced only by states at the injecting contact, different information can be obtained by measuring the characteristics in both forward and reverse bias directions. If they are symmetric, then it is likely that the bulk of the film is dominant; whereas any asymmetry is likely to reflect different surface conditions. In section (6.3.1) we give a discussion of our experimental data along these lines.

6.3 Analysis of Results

6.3.1 Sample Description and Measurement.

As discussed in Chapter (3.5.2), in order to produce several films of different thicknesses with identical properties, a set of five masks were used to give four different thicknesses by in situ masking. For all samples, the R.F. power was 100 W corresponding to 300 V D.C. target voltage and the temperature was held constant at around 250°C. A thin layer of unhydrogenated amorphous silicon (250 Å - 500 Å thick) of a low resistance was sandwiched between a-Si:H layer and the contacts, the latter were made of chromium (typical area 3mm²) with no exposure to atmosphere at any stage. The film thicknesses were measured by optical and mechanical techniques as described in Chapter 3. Usually,

these are in agreement to within 10% or less. The I-V characteristics of the samples were measured using the electrical circuit of Figure (3.8) within the temperature range between 250K and 400K, the exact temperature limits depending on the film conductivities. Some samples, although they had J.V characteristics close to those predicted by the standard SCLC experiment, showed only a weak temperature dependence. We ascribe this behaviour to shorting effects and exclude such samples from our analysis. Other samples showed I-V characteristics with strong temperature dependence. These samples were analysed using the theoretical methods of section (6.2.3). The optical gap of these samples as deduced by the Tauc construction is typically $1.95 \pm 3\%$ eV. The analysis procedure adopted in this investigation consists of, firstly, an examination of the I-V characteristics in both forward and reverse bias and then, secondly, a normalisation of these plots as required by the theory of SCLC discussed in section (6.1.2). Inversion or fitting to theoretical curves is then performed as suggested by the data.

Table (6.1) summarises some important details about the samples examined in this work. As illustrated, two types of samples are discussed. One group of samples nominally intrinsic have high activation energies around the mid-gap. Typical samples are MSS13B, MSS14B, MSS14A, MSS19C and MSS19D whose activation energies vary respectively between $0.85 \pm 2\%$ eV and $0.75 \pm 2\%$ eV. The other group nominally MSS16A, MSS16B, MSS16C, MSS16D and MSS19A has values of E_A around $0.60 \pm 2\%$ eV.

6.3.2 High Activation Energy Samples

Figure (6.7) shows the J.V characteristics, as measured at different temperatures indicated on the graph, of a typical sample MSS13B whose activation energy is 0.85 eV. As predicted, at low voltages the curves are approximately linear indicating the ohmic region of the plot. Above a critical voltage V_C , the curves deviate from linearity and the current density increases rapidly with applied voltage. In this region, for a given value of the current density the corresponding voltage is less than the ohmic voltage. This is termed the space charge region. For this sample, this region dominates the sample behaviour and no third regime is observed at high voltages. For other samples, the $\log J$ - $\log V$ curves change over at high voltage to a region of decreasing gradient which tends to the v^2 behaviour discussed in section (6.2.3).

When the characteristics of Figure (6.7) are plotted against eV/KT on a displaced current scale such that the ohmic region is common to all curves, the results are as shown in Figure (6.8). We discuss this data firstly by comparison with calculated j - v curves, as described in section (6.2.1). At the lowest temperature (304K) the data is in good agreement with the constant $g(E)$ curve of Figure (6.2). From a direct comparison of theoretical and experimental data we obtain $v = 0.34$ at $eV/KT = 12$ implying a density of states of around $2.5 \times 10^{16} \text{ eV}^{-1} \text{ cm}^{-3}$. At high temperatures however, the constant $g(E)$ model is less good. A better fit is provided by an exponentially increasing $g(E)$

with ℓ decreasing from $\ell = 10$ at 350K to $\ell = 5$ at 400K. Because ℓ decreases more rapidly than $\frac{1}{T}$, this analysis calls into question the validity of the simple model, except in the low temperature limit. We consider this again in the light of the low activation energy sample data, when the effect is more pronounced.

The inversion procedure used in this investigation and discussed in principle in earlier sections depends upon a fitting procedure whereby real data is taken from an experimental J-V plot then fed to a laboratory computer. The output provides the density of states $g(E+\Delta)$ as a function of fermi-level shift Δ caused by carrier injection. In principle, it is simple to use the computer program written to do the calculations necessary to derive values of $g(E)$ within the energy range probed by this technique. However, the method involves the use of an experimental quantity J/J_{Ω} (where J_{Ω} is the current density in the ohmic region) which also needs to be fed to the computer. Since the fermi-level displacement depends critically on J/J_{Ω} , it may be influenced by any residual Schottky barrier at the injecting contacts. Therefore, some errors may be introduced. A cubic fit is used to smooth the numerical data; without such smoothing large errors would enter.

In practice, a 10 point fit taken over 15-2 decades of J values is adequate for smoothing the results and the sum of standard deviations introduced is calculated in order to check the accuracy of the results.

When the inversion procedure is applied to the data of

MSS13B at temperature above room temperature around 325K, the value of the density of states obtained is $4.3 \times 10^{16} \pm 3\%$ $\text{eV}^{-1} \text{cm}^{-3}$. It remains approximately constant up to 0.1 eV above the fermi level. At higher temperature up to 400K, $g(E)$ increases with energy in agreement with our deduction from the comparison of the data with computed J-V curves.

6.3.3. Low Activation Energy Samples.

Figure (6.9) refers to the J-V characteristics, as measured at different temperatures shown on the graph, of a typical sample MSS16A with the activation energy around 0.60 eV. As shown, these characteristics are best understood by comparison with the calculated curves of the step model discussed in section (6.2.3). At low voltages, the plot is approximately linear indicating the ohmic region of the characteristic. This provides a measure of the temperature dependence of the D.C. conductivity of the sample. The intermediate region corresponds to the SCLC where the majority of the injected charge is trapped in deep states near the fermi level. At high voltages, the curves change over to the v^2 behaviour where we postulate that the dominant trapping occurs in states remote from fermi level.

As outlined in section (6.2.2), probing the density of states at both front and back contacts, provides appreciable information about film homogeneity and reveals important details about the density of states in the surface layer region. Assuming electron conduction is dominant, if a positive bias is applied at the front contact, the electrons will be injected at the back contact. In this case, the back contact effects

are studied. Similarly, the reverse bias will be used to monitor the front contact effects. When this method is applied to sample MSS16A and the corresponding characteristics are plotted against eV/KT as before, the results obtained are as shown in Figure (6.10a) under positive and negative bias, clearly indicating that the characteristics are not symmetric. Other samples (MSS16B, MSS16C and MSS16D) prepared under the same deposition conditions, show similar behaviour.

To test the scaling law for these samples we examine films of four different thicknesses which are made by the technique described previously. Figures (6.10a,b,c,d) shows their corresponding $j-v$ characteristics, normalised and expressed in the dimensionless forms. As illustrated, the curves as measured at the temperatures indicated are similar in shape, implying that the SCLC mechanism in region (ii) of the characteristics is solely controlled by one parameter V_C , the onset voltage at which the fermi level begins to move from E_F . Hence, we consider the scaling law to be obeyed if the parameter V_C scales with the thickness of these films as predicted by equation (6.8). However, referring to figure (6.10a,b,c,d) it can be seen that V_C is almost independent of the thickness d . The failure of scaling with the thickness together with the asymmetry observed in these films both imply surface states are present.

A direct implication of the asymmetry seen in these films is that the density of states $g(E)$ is not spatially uniform. From this evidence and the failure of the scaling law, it becomes conclusive that the SCLC mechanism is influenced by the surface layer properties of the films. This effect

becomes clearer when we determine the density of states using the inversion procedure for data taken from the forward and reverse bias characteristics at a given temperature.

In an earlier section (6.2.4), we have presented a theoretical study of the spatial non-uniformity in a-Si:H films. In this, we have shown the effect of the surface layers at the injecting contacts on the spatial variation of the electric field in the film. We have also demonstrated that the relative contribution from additional states at the injecting contact is approximately twice that expected if these states were distributed uniformly. Accordingly, we have analysed a set of real experimental data of samples MSS16A, MSS16B, MSS16C and MSS16D, the results of which are shown in table (6.2) below

Sample	d(μm)	E _A (eV)	T(K)	Positive bias			Negative bias		
				V/J (Ωcm ²)	g(E) (eV ⁻¹ cm ⁻³)	S.D.V.	V/J (Ωcm ²)	g(E) (eV ⁻¹ cm ⁻³)	S.D.V.
MSS16A	1.85	0.60	280	1.7910 ⁵	2.61.10 ¹⁵	4.2.10 ⁻²	1.1210 ⁵	9.710 ¹⁴	8.10 ⁻³
MSS16B	1.40	0.60	280	7.610 ⁵	4.710 ¹⁵	2.610 ⁻²	5.610 ⁵	1.8910 ¹⁵	2.10 ⁻²
MSS16C	1.00	0.60	280	1.2510 ⁵	1.1610 ¹⁶	0.15	1.2010 ⁵	3.610 ¹⁵	1.810 ⁻²
MSS16D	0.75	0.60	280	6.010 ⁵	1.4610 ¹⁶	6.10 ⁻²	4.10 ⁵	5.1010 ¹⁵	6.10 ⁻³

Table (6.2) Summarises the results obtained from low activation energy samples.

*SDV : Standard mean deviation.

The results show that the $g(E)$ values obtained from forward and reverse bias data are different in magnitude indicating that the surface properties at the back and the front contacts are being probed. As illustrated the $g(E)$ values corresponding to the injecting back contact (positive bias) are higher by a substantial amount, implying that surface states are dominant in the first layers of the film deposited. A further evidence of these effects is illustrated by the high values of $g(E)$ quoted for thin films which suggest that the surface states are more significant in thin samples. As the thickness d decreases from $1.85 \mu\text{m}$ in MSS16A to $0.75 \mu\text{m}$ in MSS16D, the density of states $g(E)$ increases from $2.16 \times 10^{15} \text{eV}^{-1} \text{cm}^{-3}$ in MSS16A to $1.46 \times 10^{16} \text{eV}^{-1} \text{cm}^{-3}$ in MSS16D under positive bias i.e. $g(E)$ increases by a factor more than 5. The discrepancy in $g(E)$ values as probed in both directions, suggests that these may be interpreted as upper limits of the true bulk contributions.

We now go on to discuss other aspects of these samples. Returning to the data of Figure (6.9), the change in the gradient occurring at high voltages may be explained at least qualitatively by the step model of the density of states discussed previously. At low temperatures, where a wide range of current values can be investigated, the characteristics turn over towards a v^2 region at high values of v . The data can be analysed by fitting it to the step model and then looking at the temperature dependence of the quantity Γ in equation (6.20b). Using the theoretical curves of Figure (6.4) calculated at different values of Γ in equation (6.20a),

experimental data can be fitted to one of these curves and hence Γ can be obtained at a given temperature. Since the quantity Γ is thermally activated, the plot of $\log \Gamma$ against reciprocal temperature should provide a direct measure of its activation energy. The latter determines the onset of the tail states, E_1 in equation (6.20b). The energy band between E_1 and E_C determines the band tail states width. The experimental evidence can be obtained if J-V characteristics of a sample are measured at sufficiently low temperatures in order to probe the v^2 region. However owing to the difficulties arising at low temperatures and outlined in Chapter 4, the data of sample MSS16A provides only a limited number of Γ values. When these are plotted against the reciprocal temperature the activation energy derived for Γ is around 0.40 eV giving 0.2 eV for the tail band states width as shown in Figure (6.11).

6.3. Summary of SCLC Results

We summarise the results obtained from a number of samples in Table (6.1). As illustrated, two types of samples have been examined. The samples deposited in high argon pressure (10 mtorr) yield low values of the density of states near fermi level. Our best film gives a D.O.S. value of $9.7 \times 10^{14} \text{ eV}^{-1} \text{ cm}^{-3}$ which is consistent with the results reported (73; 80, 84, 81). Where probed $g(E)$ shows a slight increase with energy and while our results agree in magnitude with the values of the D.O.S. obtained by DLTS technique, we have found no evidence that $g(E)$ decreases with energy just above E_F . The SCLC results are generally consistent with those obtained from the capacitance measurements

discussed in Chapter 5. A comparison of these two experiments is presented in Chapter 7.

We have also shown that the SCLC analysis can be used to investigate the surface layers at the injecting contacts. The results show that surface states are more significant at the rear contact.

We have also demonstrated that tail states can be detected by examining the temperature dependence of SCLC characteristics. In this we have found stronger temperature dependence in low activation energy samples and this is qualitatively in agreement with what one would expect if the temperature dependence is due to tail states near the conduction band edge E_C implying that small $E_C - E_F$ leads to smaller value of E_1 and hence larger value of Γ .

Sample	Total pressure (mtorr)	d (μm)	E_A (eV)	T (K)	V/J ($\Omega \text{ cm}^2$)	$g(E)$ $\frac{1}{\text{eV}^{-1} \text{ cm}^{-3}}$	SDV %	V/J ($\Omega \text{ cm}^2$)	$g(E)$ $\frac{1}{\text{eV}^{-1} \text{ cm}^{-3}}$	SDV %
MSS16A	15	1.85	0.60 \pm 2%	280	1.79.10 ⁵	2.61.10 ¹⁵	4.2%	1.1210 ⁵	9.710 ¹⁴	0.8%
MSS16B	15	1.40	0.60 \pm 2%	280	7.6.10 ⁵	4.710 ¹⁵	2.6%	5.610 ⁵	1.8910 ¹⁵	2%
MSS16C	15	1.00	0.60 \pm 2%	280	1.25.10 ⁵	1.1610 ¹⁶	14%	1.2010 ⁵	3.610 ¹⁵	1.8%
MSS16D	15	0.75	0.60 \pm 2%	280	6.0.10 ⁵	1.4610 ¹⁶	6%	4.010 ⁵	5.1010 ¹⁵	0.6%
MSS19A	7.5	2.00	0.60 \pm 2%	280	6.5.10 ⁸	7.710 ¹⁵	-	-	-	-
MSS19C	7.5	1.35	0.75 \pm 2%	320	1.6.10 ⁸	5.1.10 ¹⁶	5.8%	1.6510 ⁸	5.910 ¹⁶	30%
MSS19D	7.5	1.20	0.75 \pm 2%	300>0 320<0	1.10.10 ⁹	7.3.10 ¹⁶	3.9%	1.5510 ⁸	6.410 ¹⁶	10.1%
MSS14A	15	1.20	0.80 \pm 2%	320	1.3.10 ⁵	8.9.10 ¹⁵	2.5%	-	-	-
MSS14B	15	0.76	0.80 \pm 2%	320	3.10 ⁵	1.8610 ¹⁶	4%	-	-	-
MSS13B	7.5	1.10	0.85 \pm 2%	325	1.5.10 ⁶	4.310 ¹⁶	2.8%	-	-	-

Table (6.1). A summary of SCLC results.

deposition temperature $T_S \sim 250^\circ\text{C}$

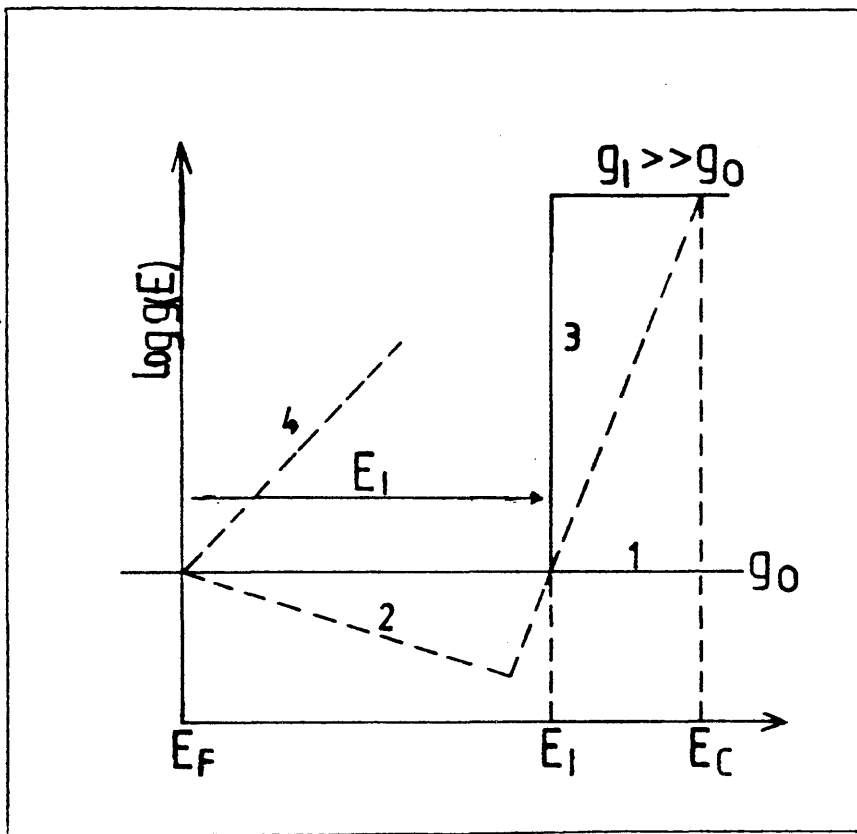


Figure 6.1

Various Forms of the Density of states $g(E)$

- (1) constant g_0
- (2) exponentially decreasing and increasing $g(E)$
- (3) the step model of $g(E)$
- (4) Exponentially increasing $g(E)$

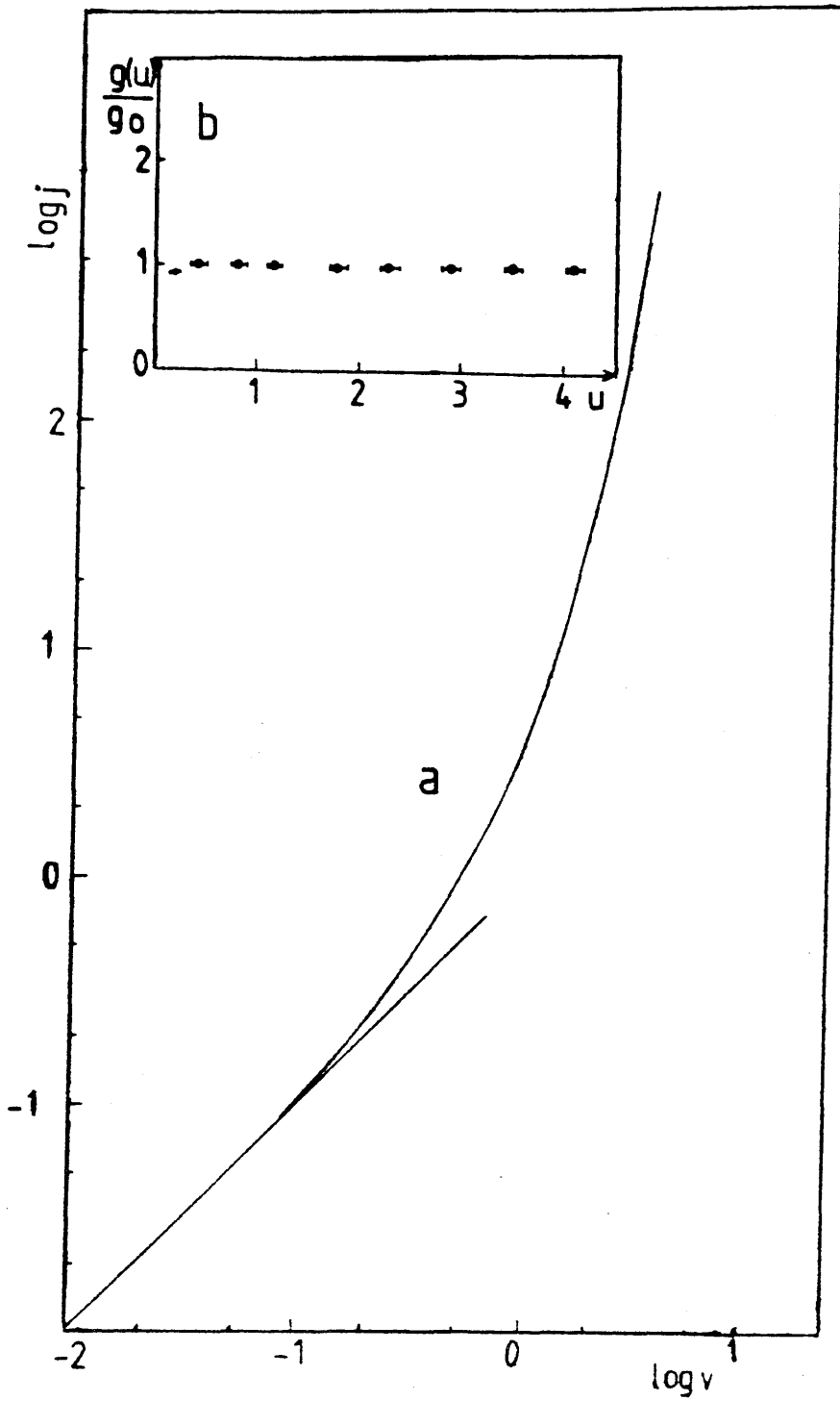


Figure 6.2 The constant density of states model
 (a) computed ($j - v$) characteristic
 (b) inverted ($j - v$) characteristic

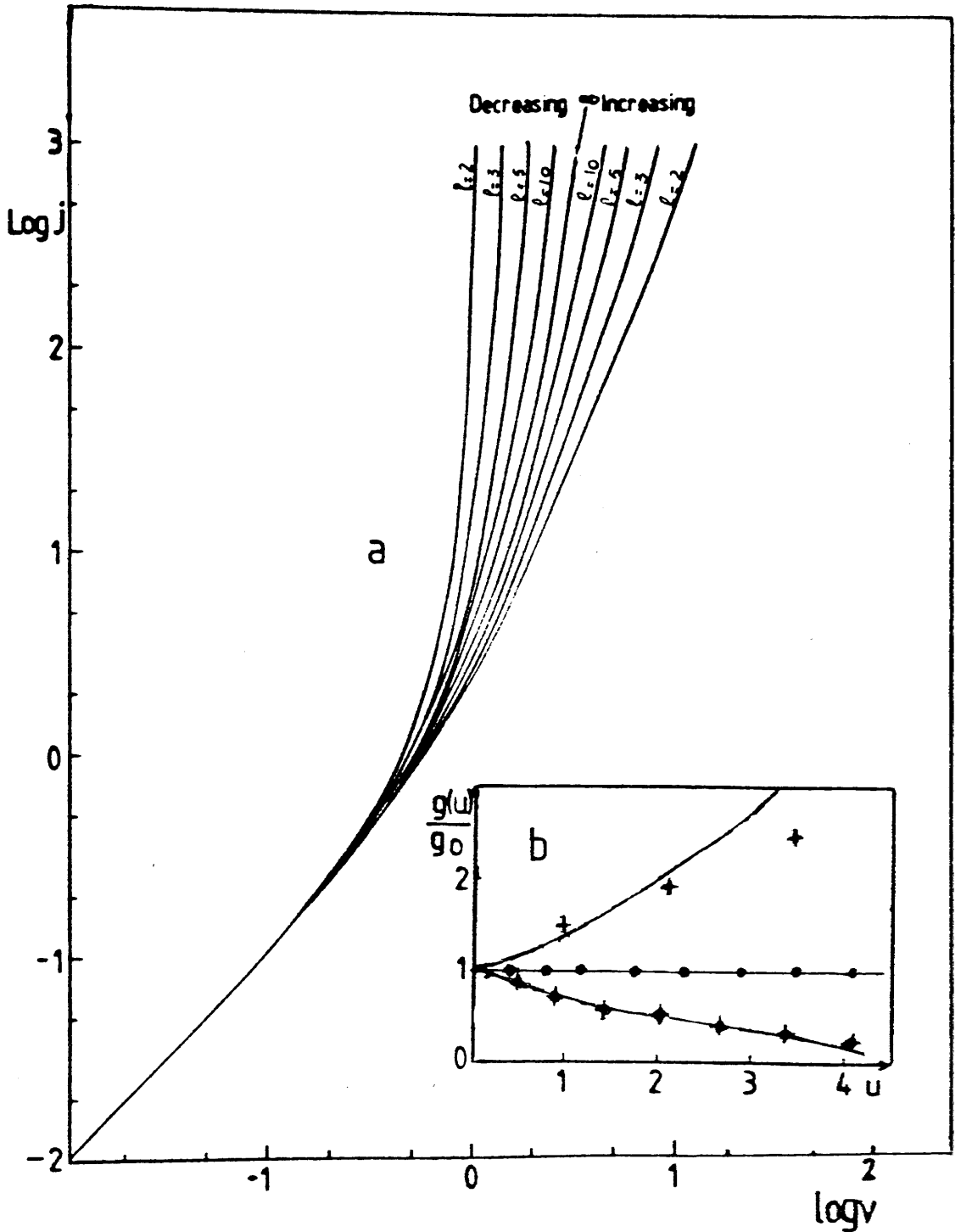


Figure 6.3 (a) Computed $j - v$ curves for Exponentially increasing and decreasing $g(u)$. The parameter is ℓ representing the steepness of the $g(u)$ curve defined by T_g/T (see p 41)

(b) The density of states determined by inverting $j - v$ curves

- constant $g(u)$, + Exponentially increasing $g(u)$ with $\ell = 3$, ♦ exponentially decreasing $g(u)$ with $\ell = 3$.

The solid lines are the $g(u)$ functions used to compute the $j - v$ curves.

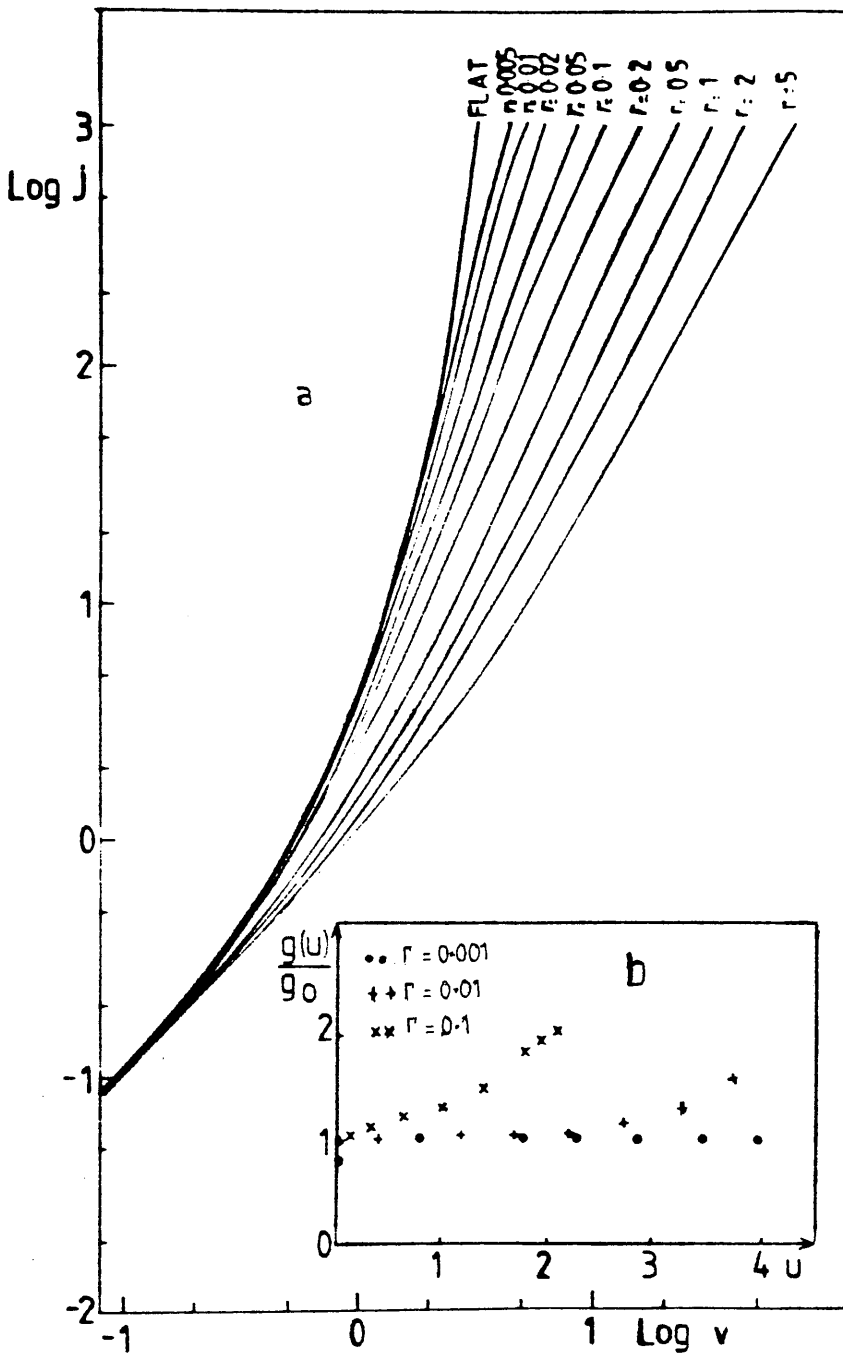


Figure 6.4

The step density of states model

(a) computed ($j - v$) characteristics in reduced forms

(b) Density of states determined by inverting $j - v$ curves.

For high Γ values false increases in $g(u)$ are calculated.

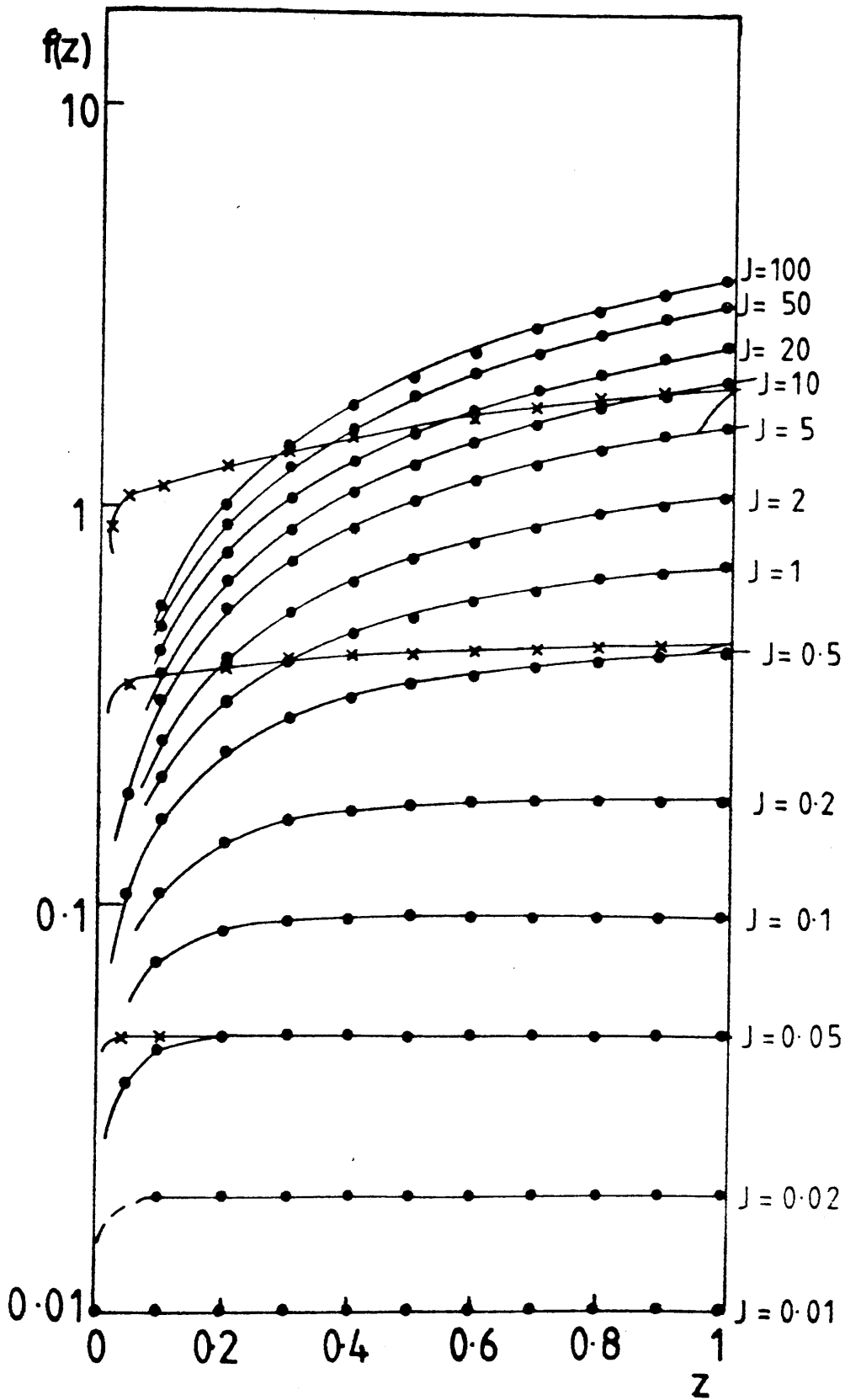


Figure 6.5 The effect of surface layers on the spatial variation of the electric field

$\times \times 10 g_0$ for $z < 0.05$, computed for $j = 0.05, 0.5, 5$.

$- 10 g_0$ for $z > 0.95$.

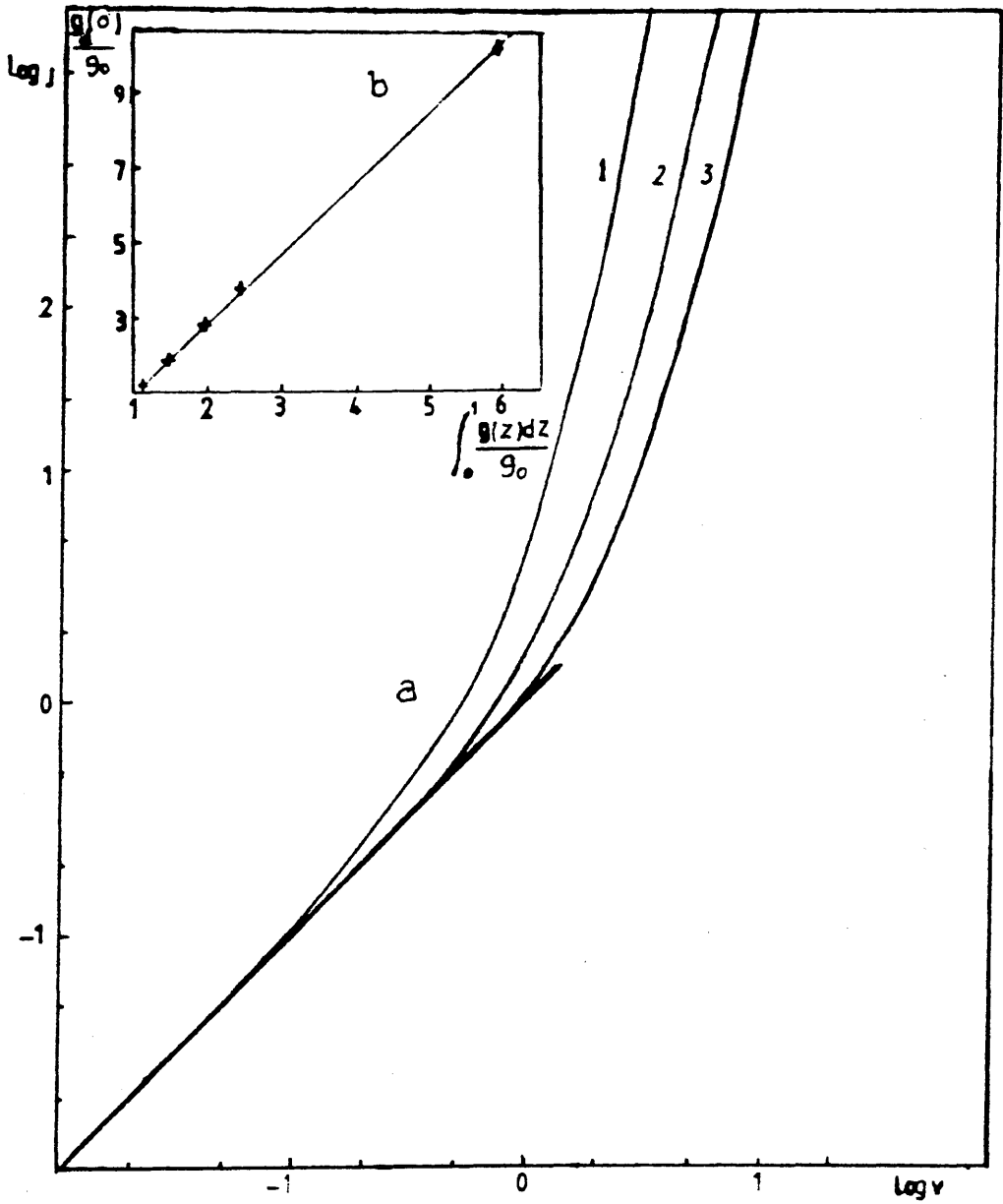


Figure 6.6 The effect of surface layers on the $j - v$ characteristics for a constant density of states model g_0 , (1) g_0 is constant
 (a) 2. $10 g_0$ for $Z < 0.05$
 3. $100 g_0$ for $Z > 0.01$
 (b) Effective density of states determined by inversion $g_d(0)/g_0$ plotted against average density of states in film

$$\int_0^1 g(z) dz / g_0$$

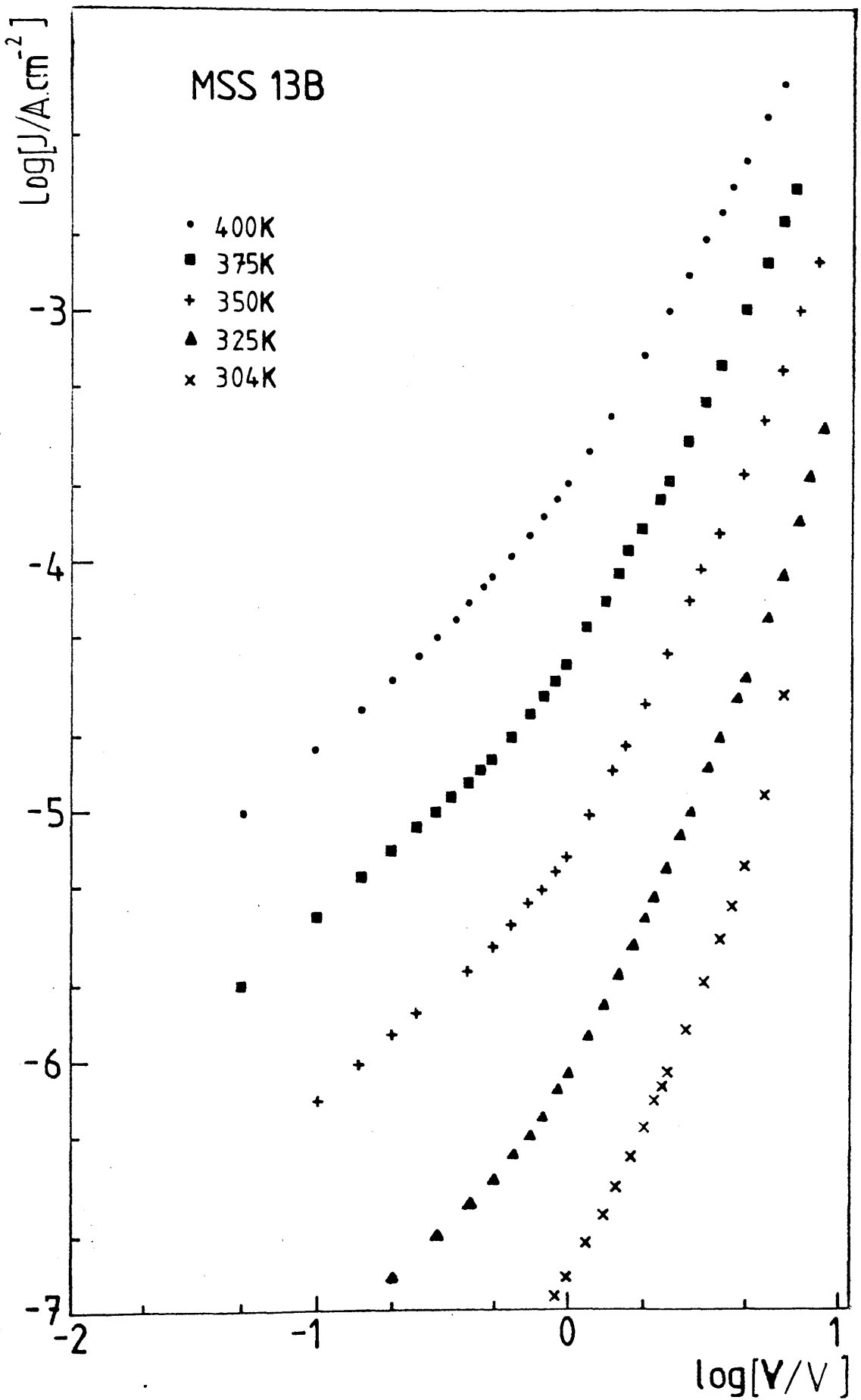


Figure 6.7

J-V characteristics as measured for MSS13B

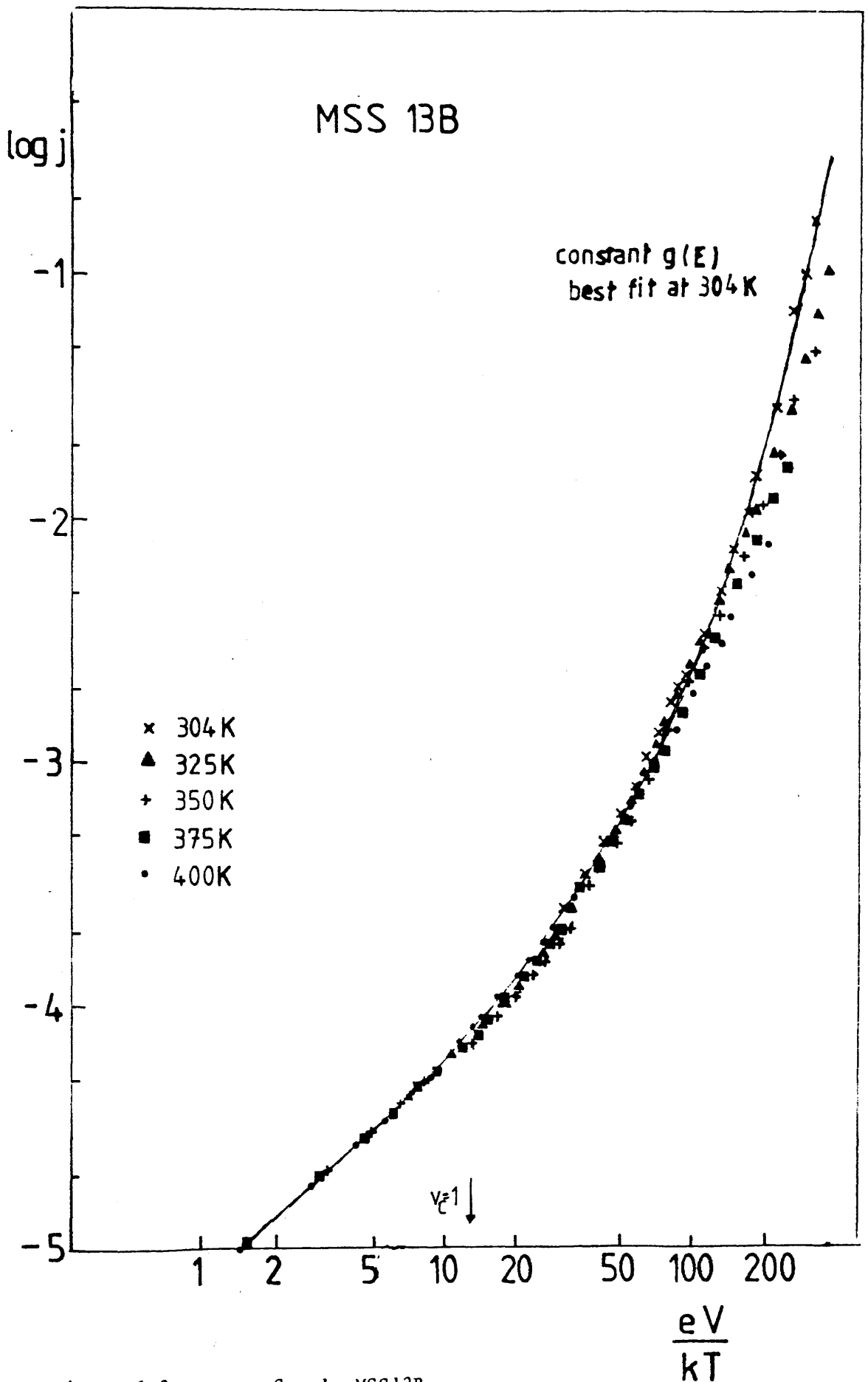


Figure 6.8

Sample MSS13B

$j(v)$ characteristics normalised and expressed in dimensionless forms

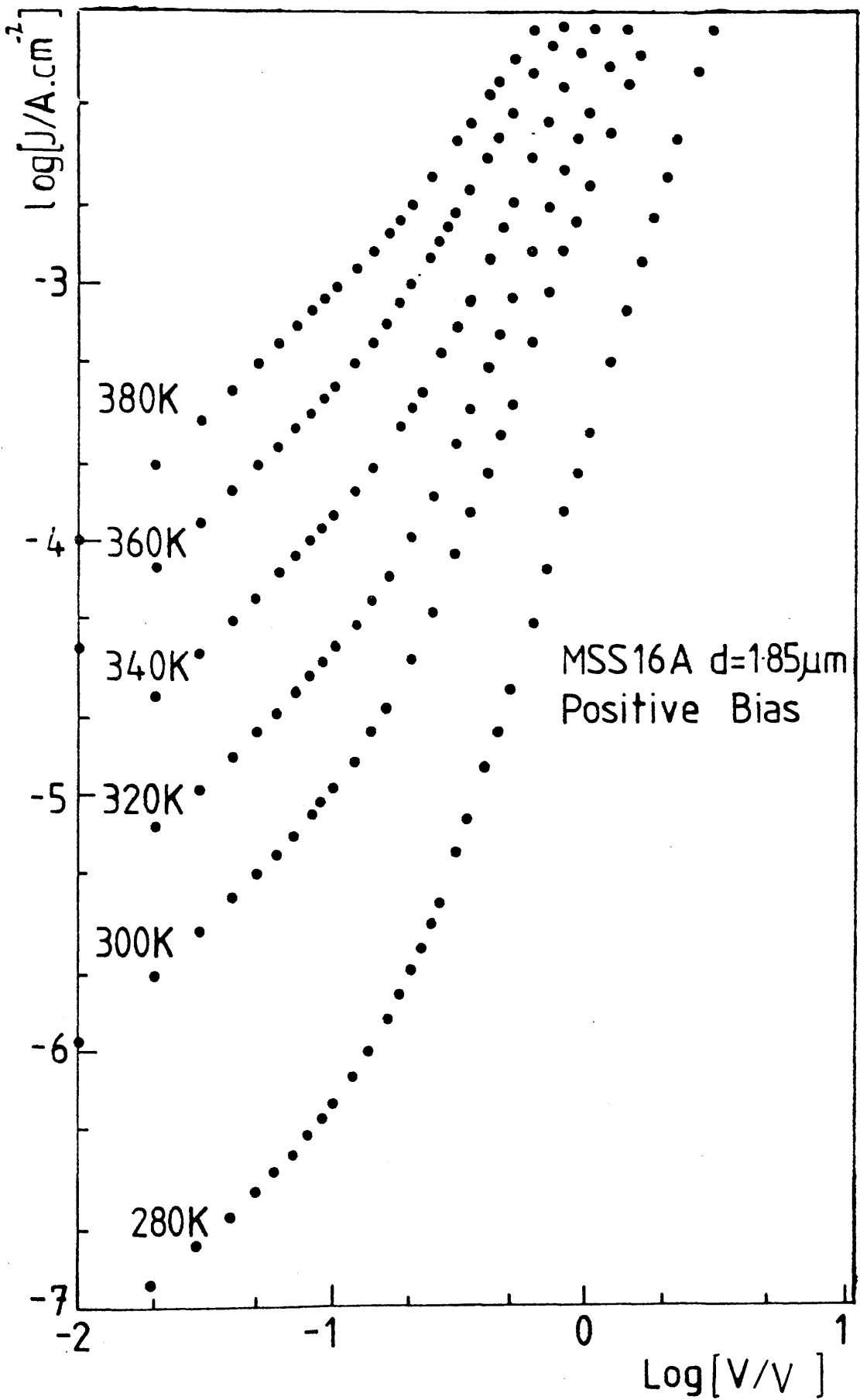


Figure 6.9

Sample MSS16A

(a) J-V characteristics as measured under positive bias

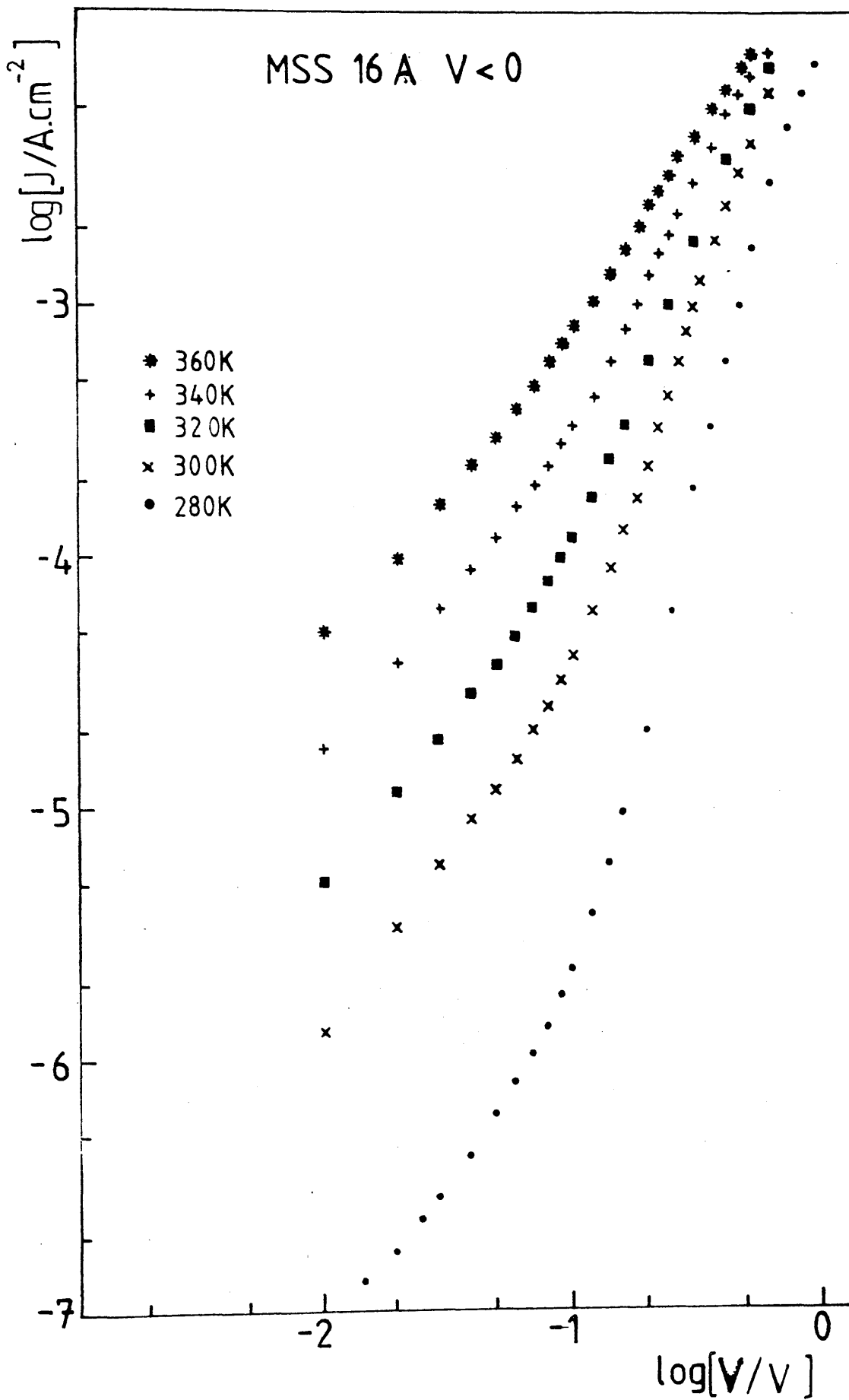


Figure 6.9

Sample MSS16A

(b) J-V characteristics as measured
under negative bias

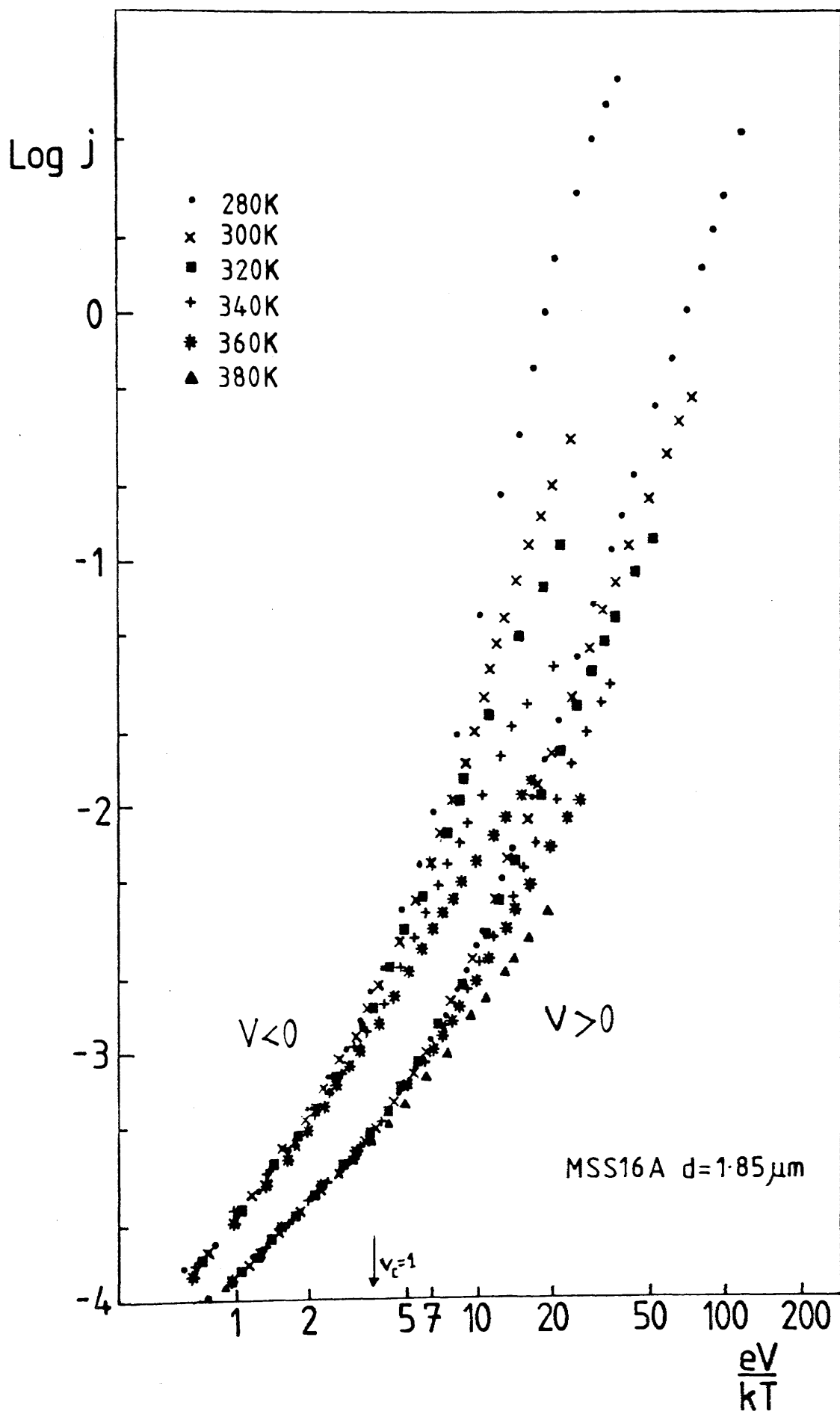


Figure 6.10

$j(v)$ characteristics normalised and expressed in dimensionless forms (a) Sample MSS16A

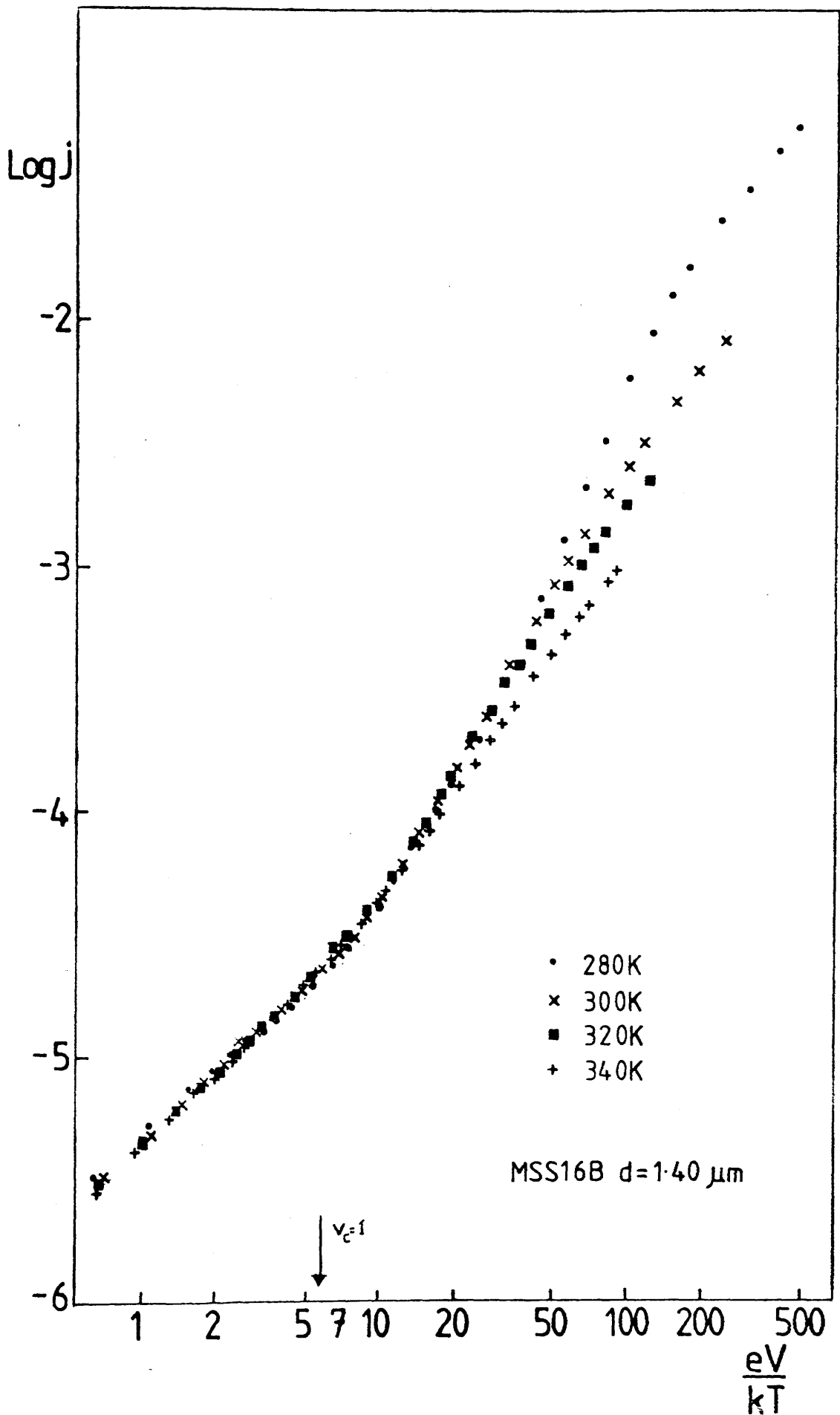


Figure 6.10

$j(v)$ characteristics normalised and expressed in dimensionless forms (b) Sample MSS16B

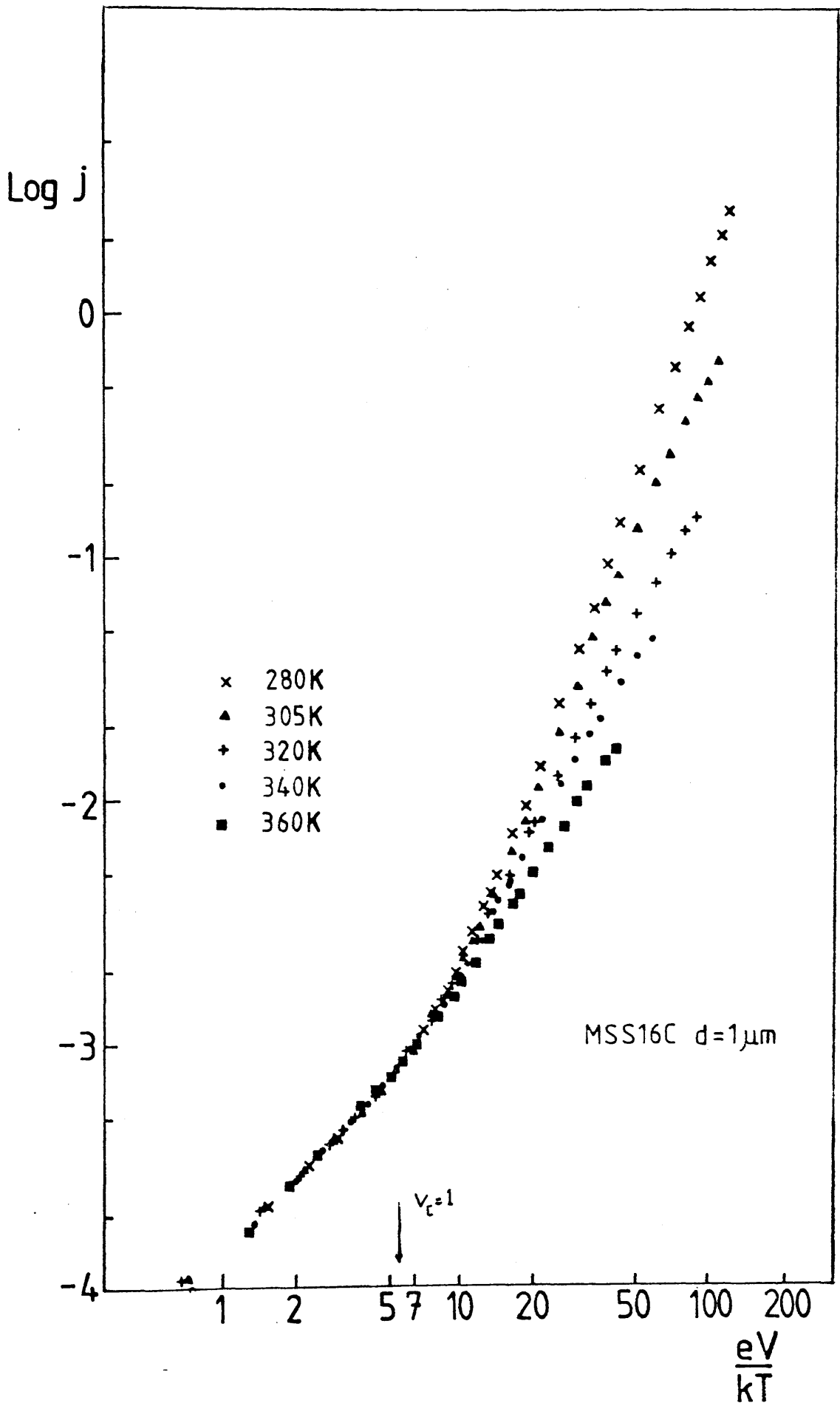


Figure 6.10

$j(v)$ characteristics normalised and expressed in dimensionless forms (c) Sample MSS16C

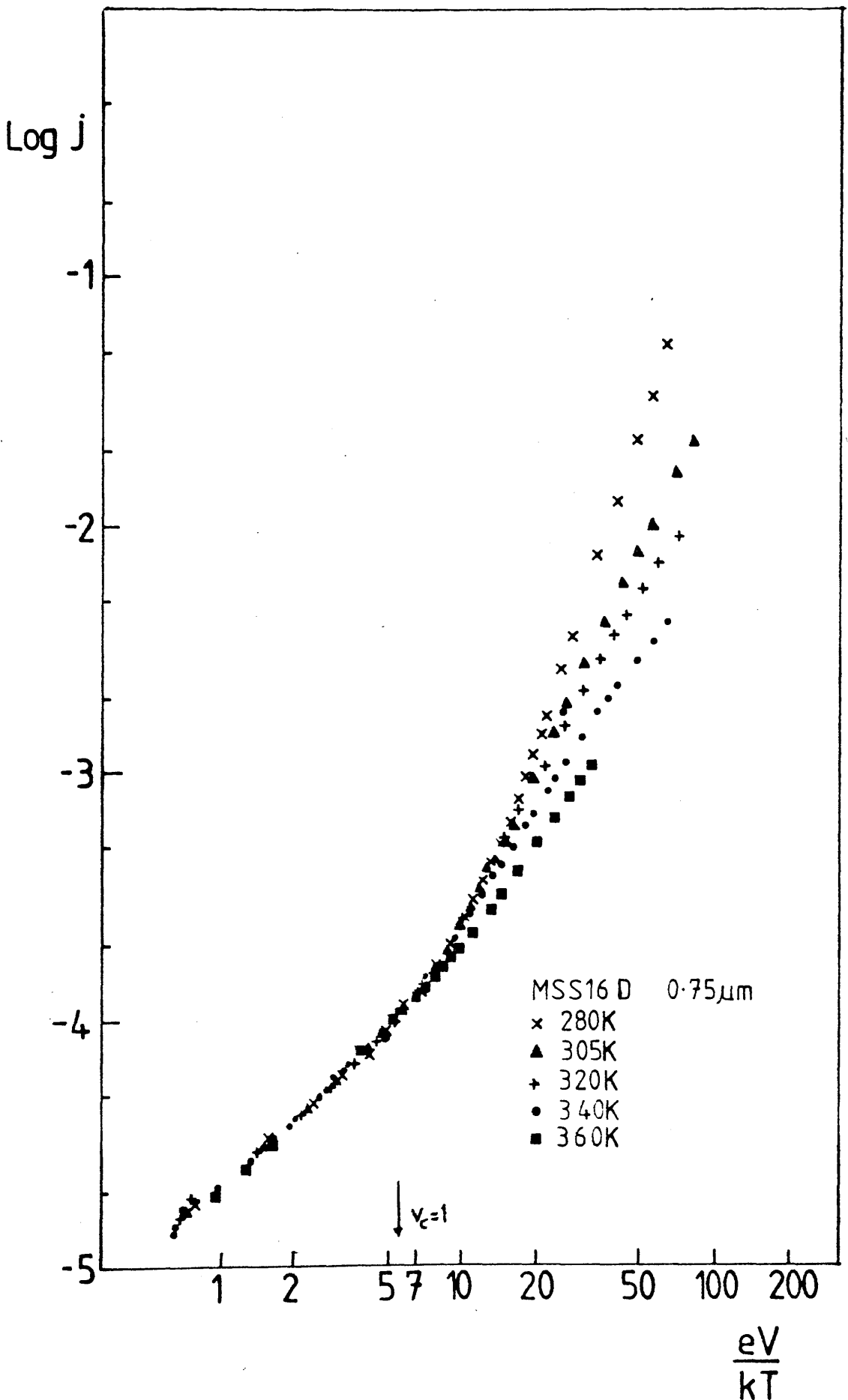
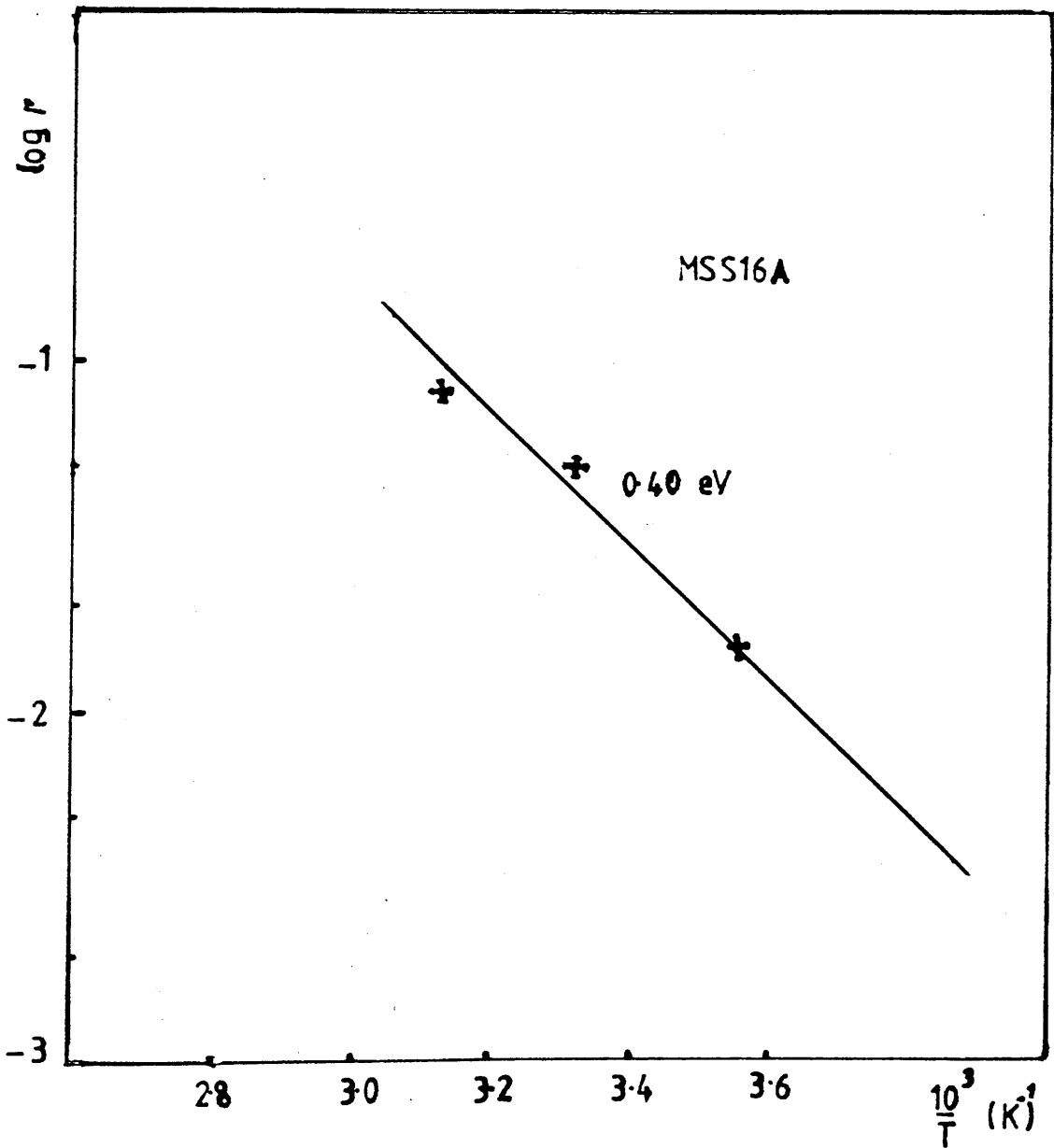


Figure 6.10

$j(v)$ characteristics normalised and expressed in dimensionless forms (d) Sample MSS16D

Figure 6.11

Illustrates the temperature dependence of the quantity Γ



CHAPTER 7.

SUMMARY AND CONCLUSIONS

It was the aim of this work to study the electronic properties of magnetron sputtered a-Si:H, in general, and to measure the density of its localised gap states, in particular. To this end, it was decided to measure $g(E)$ over a wide range of varying deposition parameters in order to assess the correlation between $g(E)$ and the preparation conditions. The measurement technique chosen to probe $g(E)$ was the admittance frequency measurement in Schottky barriers. Although results were obtained and appreciable information about deep localised states was extracted (see Chapter 5), it was felt necessary to undertake an other independent measurement in order to ascertain that these were truly representative of bulk properties. For this, the SCLC experiment was carried out and led to the results discussed in Chapter 6. In our initial attempt to derive $g(E)$ from SCLC characteristics, we used the simple method in which various models for $g(E)$ were constructed and its value near the fermi level was determined by fitting the model parameters. This method was found insufficient to explain real SCLC data. This meant that a more appropriate approach was needed. For this, we used the inversion procedure pioneered by Weisfield (73). To analyse experimental SCLC characteristics, the step model of $g(E)$ was developed. In the following paragraphs we summarise the main results obtained.

Given the limited amount of information available about magnetron material, it was decided to undertake several preliminary measurements in order to characterise our films. This preliminary work is described in Chapter 4. The procedure adopted was to compare basic electrical, optical and structural properties of our material with those of the material produced in other laboratories and by other techniques. It was clear that the electrical and optical characteristics of these films correlated with the deposition parameters. In common with other groups (123) (124), we found that the hydrogen content influenced the properties of these films. Electron microscopy analysis showed that argon concentrations were small ($< 1\%$) and larger scale structure with radius of gyration about 10 \AA was observed. This feature was found consistent with that observed earlier in glow discharge a-Si:H (95). From this preliminary work, it became clear that the introduction of a permanent magnet into the R.F. system led to a-Si:H with rather different properties to that prepared by orthodox sputtering.

The next step was to take the investigation further and examine the behaviour of localised gap states in this material. For this purpose, we studied in Chapter 5 the properties of Schottky barriers formed on magnetron sputtered a-Si:H. Our initial efforts to prepare Schottky barriers on magnetron a-Si:H by in situ metallisation were fruitless. To remedy this situation, it was decided to expose the films to atmosphere prior to metallisation. This was successful and led to the results analysed in Chapter 5. We deduce that

surface treatment is essential for preparing Schottky barriers in a-Si:H. Exposure to air to oxidise the surface was the option chosen. However, it is probable that oxygen treatment during the deposition process may be equally useful and could lead to high barrier height of Schottky barriers. This option was not tried.

To characterise our Schottky diodes, both D.C. and A.C. properties were analysed. In common with other workers (22) (58), we found it difficult, from D.C. characteristics of our Schottky diodes, to distinguish between diffusion and thermionic emission mechanisms for current flow. However, the values of the barrier heights deduced from the D.C. characteristics, using thermionic emission theory, were consistent with those derived from A.C. data. This suggests, that thermionic emission theory may be more appropriate to explain current mechanisms in our Schottky diodes. Also, some of our samples showed that thermionic field emission was a possible current flow mechanism in some poorer amorphous Schottky barriers.

Capacitance-frequency measurements performed on Schottky barriers made it possible to study their A.C. properties. The results obtained were analysed using a simple trap release model and a constant density of states approximation, after correction to remove bulk conductance and geometrical capacitance contributions. The agreement between theory and experiment was good at the temperatures scanned. This suggests that our initial approximation of a constant density of states g_0 is adequate to describe the behaviour in deep state depletion. This approach was complemented later by the

SCLC analysis, presented in Chapter 6, where it was found that $g(E)$ remains constant at low temperatures, at least, up to 0.2 eV below the conduction band edge E_c before it increases in a step model (See Chapter 6). In general, the density of state values obtained were around $10^{16} \text{eV}^{-1} \text{cm}^{-3}$. Other samples (MS25, MS26 and MS27) did not fit this simple theoretical model. These samples had a number of similar characteristics i.e.,

- (i) The geometrical capacitance C_g was not frequency independent.
- (ii) The barrier heights were lower than expected.
- (iii) The densities of states were probably as high as $10^{17} \text{eV}^{-1} \text{cm}^{-3}$.

This degraded behaviour was ascribed to an excess of hydrogen acting in the manner pointed out by Anderson et al (101). The values of the attempt to escape frequency derived using this analysis scheme were in the range between 10^{11}s^{-1} - 10^{14}s^{-1} .

It can be concluded from the final values of g_0 that the density of localised gap states in R.F. magnetron sputtered a-Si:H is substantially lower than that of material produced by the conventional R.F. sputtering techniques. The results of $g(E)$ obtained from several samples indicate that the density of states in R.F. magnetron material depends on hydrogen incorporation. It is of interest to point out that these values of g_0 are in good agreement with those reported by other groups performing similar experiments on R.F. magnetron sputtered a-Si:H (84, 96, 97).

As mentioned above, having decided to carry out another independent experiment part of the original aim of this work had to be sacrificed. Initially, it was intended to measure $g(E)$ over a wider range of preparation conditions but lack of time restricted this work. Fortunately, this was compensated by the ability of the analysis scheme developed in the SCLC experiment, to probe $g(E)$ far away from fermi level. As pointed out in the introduction, given the conflicting reports about $g(E)$ in amorphous silicon, we believe that unambiguous conclusions can only be made through a series of measurements carried out in parallel, at best, on the same samples or, at least, on samples prepared under similar conditions. In this spirit, we introduced the SCLC experiment.

Despite the theoretical reservations about earlier attempts to analyse SCLC data (Mackenzie et al (81), Solomon et al (80)), it is without doubt that the technique can be improved to yield unambiguous information about bulk properties of $a\text{-Si:H}$. In our initial attempt to analyse SCLC characteristics we used the simplest method whereby $g(E)$ was derived by fitting procedure involving the parameters V_c and ℓ of the characteristics similar to the method used by Solomon et al. This method was found to be inadequate in analysing real SCLC characteristics. One way of improving the analysis scheme was to use the inversion procedure given by Weisfield. In this the density of states near fermi level was derived from experimental data with accuracy of a few % within the relevant assumptions. This analysis was used to

examine the effect of surface layers having different properties at both front and back contacts. Significant evidence was found for these layers. This was consistent with the values of $g(E_F)$ deduced from the reverse and forward bias conditions. The densities of states derived from forward bias conditions were significantly higher than those obtained from the reverse case implying that surface states are more significant in the first deposited thin layers of the film in agreement with the observations of Solomon et al (80) and Powell et al (122). The effect of the back contact together with the failure of the scaling law found in our magnetron material led to the conclusion that $g(E)$ is spatially non uniform. Solomon et al (80) have shown, in their analysis of thin glow discharge films, that additional states are present in thin samples even of glow discharge material. The densities of states obtained in this work are in the range between $10^{15} \text{eV}^{-1} \text{cm}^{-3}$ - $10^{16} \text{eV}^{-1} \text{cm}^{-3}$ depending on film thickness. These values are consistent with those reported in literature (78, 80, 81, 84)

This highlights the fact that as far as bulk properties of magnetron sputtered a-Si:H are concerned, it is not easy to distinguish between these properties and those of a better quality glow discharge material. It can be concluded unambiguously that the main difference between these two materials lies on the role of the surface layers which are more prominent in magnetron material.

Following on, it becomes clear that R.F. sputtering technique has been improved by the use of a magnetron source leading to good bulk characteristics. However the presence

of the interface layer casts doubt over the prospect of device applications of this material, emphasising the fact that good bulk properties are not a guarantee of a better quality material. It is hoped that the interface layer can be eliminated by special surface treatment to make magnetron material a candidate for future technological development.

REFERENCES

1. Mott, N.F. and Davis, E.A. "Electronic Processes in Non Crystalline Materials" 2nd Edn. (Oxford University Press, Oxford 1979)
2. P.W. Anderson, Phys. Rev. 109, (1958), 1492.
3. Cohen, M.H., Fritzsche, H and Ovshinsky, S.R. Phys. Rev. Lett. 22 (1969), 1065.
4. Adler, D. Solar Cells 2 (1980), 199.
5. D.A. Anderson and W.E. Spear, Phil Mag. 36 (1977) 695.
6. C.R. Wronski and R.E. Daniel, Phys. Rev. B23 (1981) 794.
7. M. Hack, S. Guha and M. Shur, Phys. Rev. B30 (1984) 6991.
8. T. Kagawa, N. Matsumoto and K. Kumabe, Phys. Rev. B.28 (1983) 4570.
9. R.A. Street, Adv. Phys. 30, (1981) 593.
10. R.A. Street, D.K. Biegelson and J.C. Knights, Phys. Rev. B.24 (1981) 969.
11. H. Dersch, J. Stuke and J. Beichler, Appl. Phys. Lett. 38 (1981) 456.
12. H. Dersch, L. Schweitzer and J. Stuke, Phys. Rev. B.23 (1983) 4678.
13. N.F. Mott, Phil. Mag. 51, (1985) 1177
14. N.F. Mott, Phil Mag. 19, (1969), 835.
15. McKelvey, J.P. "Solid State and Semiconductor Physics" (Harper and Row, New York 1966), p. 489.
16. Sze, S.M. "Physics of Semiconductor Devices" 2nd Edn. (J. Wiley and Sons New York, 1981)
17. Barbe, D.F. J. Vac. Sci. Tech. 8 (1971) 102.
18. Beichler, J. Fuhs, W., Mell, H and Welsch, H.M. J. Non Cryst. Sol. 35-36 (1980) 587.

19. Mehra, R.M., Kathuria, A.K., Shyam, R., Sawar, A.L. and Mathur, P.C. Phys. Stat. Sol. 45 (1978), 1159
20. Solomon, I., Dietl, T and Kaplan, D. J. Phys. (Paris) 39 (1978), 1241.
21. Viktorovitch, P., and Moddel, G. J. Appl. Phys. 51, (1980), 4847.
22. I.G. Gibb and A.R. Long, Phil. Mag. 49 (1984) 565.
23. Mahan, J.E., and Bube, R.H. J.Non-Cryst. Sol. 24, (1977), 29.
24. Neudeck, G.W. and Malhotra, A.K., J. Appl. Phys. 46 (1975), 2662.
25. Spear, W.E. and LeComber, P.G. J. Non-Crystl Sol. 8-10 (1972), 727.
26. Madan, A., LeComber, P.G. and Spear, W.E. "Proc. 7th Int. Conf. in Amorphous and Liquid Semiconductors, Edinburgh (C.I.C.L. Univ. Edinburgh, 1977).
27. W.E. Spear "Amorphous and Liquid Semiconductors" Ed. J. Stuke and Brenig (Taylor and Francis, London 1974) p.1.
28. A. Madan, P.G. LeComber and W.E. Spear, J. Non-Cryst. So. 20, (1976), 239.
29. Spear, W.E. and LeComber P.G., Phil. Mag, 33 (1976), 935.
30. Rhoderick, E.M. "Metal-Semiconductor Contacts", (Clarendon Press, Oxford 1978).
31. Goodman, N.B. and Fritzsche H, Phil Mag. B.42 (1980), 149.
32. Goodman, N.B. Phil. Mag. B. 45 (1982), 407.
33. Powell, M.J. Phil. Mag. B.43 (1981), 93.
34. R.L. Weisfield and D.A. Anderson, Phil. Mag. B44, (1981), 83.

35. Spear, W.E. and LeComber, P.G., J. Non-Cryst. Sol. 8-10, (1972) 727.
36. Loveland, R.J. Spear, W.E. and Al-Sharbaty, A., J. Non Cryst. Sol. 11 (1973/74) 219.
37. Anderson, D.A., and Spear W.E., Phil Mag. 36, (1977), 695.
38. Fritzsche, H., Solar. Energy Mater. 3 (1980) 447.
39. Tanielian, M.H., Fritzsche, H. Tsai, C.C. and Symbalisky, E., Appl. Phys. Lett. 33 (1978) 353.
40. Ast, D.G., and Brodsky., M.H., J. Non Cryst. Sol. 35-36 (1980) 4548.
41. Solomon, I., and Brodsky, M.H., J. Appl. Phys. 51, (1980) 4548.
42. Rehm, W., Fischer, R., and Beichler, J. Appl. Phys. Lett. 37, (1980), 445.
43. Knights, J.C. and Biegelson, D.K., Solid State Commun. 22, (1977), 421.
44. L. Schweitzer, M. Grunewald and H. Dersch Sol.St.Comm. 39, (1981), 353.
45. Goodman, A.M. J. Appl. Phys. 34, (1963), 329.
46. Roberts, G.I. and Crowell, C.R. J. Appl. Phys. 41, (1970) 1767.
47. Beguwala, M., and Crowell, C.R., Solid State Electron 17, (1974), 203.
48. Losee, D.L., J. Appl. Phys. 46, (1975) 2204.
49. Dohler, G.H. and Hirose, M. (1977). In "Amorphous and Liquid Semiconductors" (W.E. Spear, Ed.) p.372 C.I.C.L. Univ. Edinburgh.
50. Spear, W.E., LeComber, P.G. and Snell, A.J. Phil. Mag. 38 (1978), 303.
51. Snell, A.J., Mackenzie, K.D. LeComber, P.G. and Spear, W.E., Phil. Mag. 40, (1979).

52. H.L. Fernandez-Lanque and J. Allison,, M.J.
Thompson, J. Appl. Phys. 54 (12), (1983) 7025.
53. Abram, R.A., and Doherty, P.J. Phil. Mag. 45, (1982)
167.
54. Powell, M.J., and Dohler, G.H. J. Appl. Phys. 52,
(1981), 517.
55. Bethe, H.A., M.E.T. Radiation Lab. Report 43-12 (1942)
56. Crowell, C.R. and Beguwala, M., Sol. St. Elec. 14,
(1971), 1149.
57. Wronski, C.R., Carlson, D.E. and Daniel, R.E., Appl.
Phys. Lett. 29 (1976), 602.
58. Deneuville, A. and Brodsky, M.H. J. Appl. Phys.
50, (1979), 4015.
59. Thompson, M.J., Allison, J. Al-Kaisi, M.M. and
Thomas, J.M. Rev. Phys. App. 13, (1978), 625.
60. Hurault, J.P., J. Phys. Paris, 32, (1971), 1121.
61. Crowell, C.R., and Rideout, V.L., Sol. St. Elec.
12, (1969), 84.
62. Rideout, V.L. and Crowell, C.R., Sol. St. Elec. 13,
(1970), 993.
63. Wronski, C.R., Carlson, D.E. Sol. St. Comm. 23,
(1977), 421.
64. Hirose, M., Suzuki, T. and Dohler, G.H. Appl. Phys.
Lett. 34, (1979), 234.
65. Tiedje, T., Wronski, C.R., Abeles, B. and Cebulka, J.M.
Solar Cells, 2 (1980) 301.
66. Viktorovitch, P and Jousse, D. J. Non-Cryst. Sol.
35-36 (1980), 564.
67. Viktorovitch, P. J. Appl. Phys. 52, (1981) 1392.
68. D.V. Lang, J.D. Cohen and J.P. Harbison, Phys. Rev.
B25, (1982), 5285.

69. Cohen, J.D., Lang, D.V., and Harbison, J.P.,
Phys. Rev. Lett. 45, (1980), 197.
70. Cohen, J.D. and Lang, D.V., Phys. Rev. B25, (1982)
5321.
71. N.M. Johnson and K.D. Biegelson, Proc. 17th Int.
Conf. Phys. Semicond. Eds. J.D. Chadi, W.A. Harrison
(Springer, N.Y., 1985), p. 817 ; D.K. Biegelson and
N.M. Johnson, A.I.P. Conf. Proc. 120 (1984) 32.
72. H. Fritzsche, Proc. of 11th Int. Conf. on Amorphous
and liquid semiconductors (Ed. F. Evangelisti and
J. Stuke, Rome 1985).
73. R.L. Weisfield, J. Appl. Phys. 54, (1983) 6401.
74. Rose, A., Phys. Rev. 97, (1955), 1538.
75. M.A. Lampert, Phys. Rev. 103, (1956), 1648.
76. M.A. Lampert and Mark "Current Injection in Solids"
(Academic, New York, 1970)
77. W. Den Boer, J. Phys. Paris, C4, 42, (1981) 451.
78. Nespurek, S., and Sworakowski, J., J. Appl. Phys.
51, (1980 a), 2098.
79. Mark, P., and Helfrich, W., J. Appl. Phys. 33,
(1962), 205.
80. I. Solomon, R. Benferhat and H. Tran-quoc, Phys. Rev.
B30, (1984), 3422.
81. K.D. Mackenzie, P.G. LeComber and W.E. Spear,
Phil. Mag. B.46 (1982), 377.
82. M. Hack and M. Shur, J. Appl. Phys. 54, (1983), 5858.
83. O. Zmeskal, F. Schauer and S. Nespurek, J. Phys. C.
Sol. St. Phys. 18, (1985), 1873.
84. S. Gangopadhyay, S. Iselborn, H. Rubel, B. Schroder
and J. Geiger, Phil. Mag. B.51, (1985), L.33.
85. Malhotra, A.K. and Neudeck, G.W. Appl. Phys. Lett. 28,
(1975), 47.

86. V. Šmid et al, Proc. of 11th Int. Conf. on Amorphous and Liquid Semiconductors, Ed. F. Evangelisti and J. Stuke, Rome, 1985.
87. Maissel, L.I. "Handbook of thin film Technology" Ed. L.I. Maissel and R. Glang (McGraw - Hill, New York 1970).
88. Davidse, P.O. and L.I. Maissel, J. Appl. Phys. 37, (1966) 574.
89. Vossen, J.L. and F.J. O'Neill, R.C.A. Rev. 29, (1968) 149.
90. F.M. Penning, Physica (Utrecht) 3, (1936) 873 US Patent 2, 146, 025 (1939).
91. E. Kay J. Appl. Phys. 34, (1963), 766
92. W.D. Gill and E. Kay, Rev. Sci. Inst. 36 (1965) 277.
93. Vossen, J.L. and Kern, W. "Thin Film Processes" (Academic Press, New York, 1978).
94. K. Wasa and S. Hayakawa, Rev. Sci. Inst. 40, (1969), 693 ; US Patent 3, 528, 902.
95. A.J. Craven, A.M. Patterson, A.R. Long and J.L.B. Wilson J. Non-Cryst. Sol. 77 & 78, (1985), 217.
96. A.R. Mirza, A.J. Rhodes, J. Allison and M.J. Thompson J. Phys. C4 (1981) 659.
97. P.K. Bhat, A.J. Rhodes, J.M. Searle and I.G. Austin, Phil. Mag. B47 (1983) L99-105.
98. Moafak, C., Abdulrida and J. Allison, Appl. Phys. Lett. 43(8) (1983) 768.
99. M.C. Abdulrida and J. Allison, thin solid films, 102, (1983) L.43.
100. D.S. Misra, A. Kumar and S.C. Agarwal, J. Non-Crysts. Sol. 76 (1985).
101. D.A. Anderson and W. Paul, Phil. Mag. B44, (1981) p.187.

102. Anderson, D.A., Moustakas, T.D. and Paul, W., (1977) Proceedings of 7th Int. Conf. on Amorphous and Liquid Semiconductors, Edited by W.E. Spear (Univ. Edinburgh: C.I.C.L.) p. 334
103. Brodsky, M.H., Frisch, M.A. Ziegler, J.F., and Lanford, W.A., Appl. Phys. Lett. 30, (1977 b), 561.
104. Zanzucchi, P.J., Wronski, C.R. and Carlson, D.E., J. Appl. Phys. 48, 5227.
105. Freeman, E.C. and Paul, W., Phys. Rev. B18, (1978) 4288.
106. Brodsky, M.H., Cardona, M., and Cuomo, J.J., Phys. Rev. B16, (1977 a), 3566.
107. W. Beyer and H. Wagner, J. Non-Cryst. Sol. 59-60 (1983) 161.
108. C.C. Tsai, H. Fritzsche, M.H. Tanielian, P.J. Gaczi, P.D. Persans and M.A. Vesaghi, reference as (102) p.339
109. D. Jousse and J. Said, Thin solid films, 124, (1985) p. 191-197.
110. W. Pawlewicz, J. Appl. Phys. 49 (11) (1978) 5595.
111. Cody, G.O., Tiedje, T., Abeles, B., Brook, B., and Goldstein, Y., Phys. Rev. Lett., 47 (1981) p. 1480.
112. J. Dixmier, P. Derouet, M. Essamet and Luridjani., Phil. Mag. B52 (1985), 943.
113. James B. Webb and S.R. Das, J. Appl. Phys. 54 (6) (1983) 3282.
114. W. Shockley, "The Theory of p-n junctions in Semiconductors and p-n junctions Transistors" Bell syst. Tech. J. 28, 435, (1949) ; Electrons and holes in semiconductors, D. Van Nostrand, Princeton, N.J. 1950.
115. Nemanich, R.J. "Semiconductors and Semimetals" Vol. 21 (Academic Press, 1984).
116. R.A. Street, M.J. Thompson and N.M. Johnson, Phil. Mag. 51, (1985), 1-17

117. P.G. LeComber and W.E. Spear, *Phil. Mag.* 53, (1986)
L1.
118. Tanaka, K., and Okushi, H., *J. Non-Cryst. Sol.*, 66,
(1984), 205.
119. Hirotsugu Kida, Kiminori Hattori, Hiroaki Okamoto and
Yoshihiro Hamakawa, *Proc. 11th Int. Conf. on Amorphous
and Liquid Semiconductors*, (Rome, Italy, 1985), Edited
by F. Evangelisti and J. Stuke.
120. J.W. Orton and M.J. Powell, *Phil. Mag.* B50, (1984) 11.
121. Weisfield, R.L. Viktorovitch, P., Anderson D.A., and Paul
W., *Appl. Phys. Lett.* 39, (1981), 263.
122. M.J. Powell and J. Pritchard, *J. Appl. Phys.* 54, (1983)
3244.
123. Takao Nagatomo, Shunji Moribe, Masaaki Uzur and
Osamu Omoto, *J. Appl. Phys.* 21, (1982), 209.
124. F. Demichelis, E. Mezzetti, P. Rava, A. Tagliaferro,
E. Tresso and G.A. Della Mea, P. Mazzoldi (as 71).
125. D.V. Lang, *J. Appl. Phys.* 45, (1974), 3023.
- 126) I. Gibb, Ph.D. thesis, University of Glasgow, (1983)
unpublished.

